Martin Schubert

**Fluctuations of temperature and turbulent
radial energy transport in the edge plasma
of the Wendelstein 7-AS stellarator**

Fluctuations of Temperature and Turbulent Radial Energy Transport in the Edge Plasma of the Wendelstein 7-AS Stellarator

Inauguraldissertation

zur

Erlangung des akademischen Grades eines

doctor rerum naturalium (Dr. rer. nat.)

an der Mathematisch-Naturwissenschaftlichen Fakultät

der

Ernst-Moritz-Arndt-Universität Greifswald

vorgelegt von

Martin Schubert

geboren am 11.5.1974

in Burghausen

Greifswald, im Juli 2005

Dekan: Prof. Dr. Jan-Peter Hildebrandt

1. Gutachter: Prof. Dr. Thomas Klinger

2. Gutachter: Prof. Dr. Ulrich Stroth

Tag der Promotion: 3.11.2005

Abstract

Transport relevant turbulent fluctuations of plasma potential U_{plasma}, density n_0, and electron temperature T_e have been measured simultaneously in the Wendelstein 7-AS stellarator edge plasma by applying the sweeping technique to a poloidal array of 15 cylindrical Langmuir probe tips.

Tip currents are measured with a temporal resolution of $20\,\text{ns}$. The voltage sweep frequency is $1.4\,\text{MHz}$ and the tip spacing is $2\,\text{mm}$. Saturation current I_{sat}, floating potential U_{float}, and T_e could be determined with a bandwidth of $1.4\,\text{MHz}$ in the frequency and of $15\,\text{cm}^{-1}$ in the wavenumber, while n_0 and U_{plasma} were deduced using a collisionless 1D model for both the presheath and the sheath.

The high bandwidth of the measurement was achieved by placing miniaturised differential amplifiers close to the probe tips. Profiles of the plasma quantities and their fluctuations were recorded in the scrape-off layer up to the last closed magnetic surface (LCMS). Individual probe characterstics can be adequately described by an exponential fit, but particular attention must be paid to the covariance of the fit parameters. Hence, cross-correlation and smoothing techniques were utilised during data evaluation.

Two-dimensional correlation functions have similar structure in all quantities, revealing turbulent structures with a poloidal extent of $1\,\text{cm}$ and a lifetime of $30\,\mu\text{s}$. Near the LCMS, U_{float} data additionally show counter-propagating structures, which indicate the vicinity of the shear layer. The Fourier transform of cross-correlations with the probe located near the LCMS reveals a broad-band uniform cross phase, which is small between n_0, T_e, and U_{plasma}, and close to $\pi/2$ between either of the pairs (U_{float}, T_e) and (U_{float}, I_{sat}). The latter confirms previous results from non-swept probes. Broad-band small phases between n_0 and U_{plasma} are also found in numerical simulations of drift-wave turbulence.

Profiles of the convected and the conducted perpendicular heat transport are calculated. Continuity of the energy transport is demonstrated, where near the LCMS, heat conduction via temperature fluctuations contributes to a large fraction. It is replaced by convection in the SOL. A significant change in the profile of the radial particle transport is well correlated with an abrupt change of the connection length.

A comparison with the confinement shows that the measured fluctuations carry roughly 28% of the total energy transport. Based on an extrapolation of the turbulence properties to experimentally unaccessible but transport relevant high frequencies and wavenumbers, it is consistent to assume that the turbulence is fully responsible for the perpendicular transport. An experimental verification requires an increased bandwidth in wavenumber and frequency.

Contents

Preface

This thesis is devoted to a very special aspect of plasma physics. A plasma is a state of aggregation just as the solid, the liquid or the gaseous state. Any material, any chemical element can be transferred into the plasma state. The reader who is not familiar with advanced illumination techniques or modern technical methods for the treatment of surfaces, this reader might think, that a plasma itself is already something very special, because all things in our environment apparently consist of either solids or liquids or gases. It is only during a thunder storm, when the air of our atmosphere is getting in touch with a plasma in a natural way. For some fraction of a second, lightning generates an electroconductive and intensely flashing plasma channel. One may disregard, however, for a moment the Earth and its weather and instead focus on the sky and the universe respectively. Scientists have come to the conclusion, that plasma is the usual state of matter there. The sun, all visible stars, the solar wind, interstellar nebulae, all these things completely consist of plasma. From this point of view solids, liquids and gases are very special indeed. Now, if the sun is plasma all over and if our life directly or indirectly depends on the sun, then this should be a good reason to study the properties of plasma.

Chapter 1

Introduction

This is an experimental investigation of turbulence at the boundary of a high temperature plasma by means of electric probes. The main focus will be on the turbulent transport of particles and energy, which plays a crucial role for plasma confinement in strong magnetic fields. So far, the mechanisms of the plasma turbulence are not understood in detail, since the small scales involved make the measurement very difficult. This work is one step, where the measuring tools have been further improved, so that a part of the plasma turbulence yet unknown can now be resolved experimentally. To make it more precise: The presented measuring method allows highly resolved and simultaneous observation of plasma density, temperature and electric potential. The experimental data of temperature fluctuations in particular have not been obtained before with similar spatial and temporal resolution. All measurements were carried out at the Wendelstein 7-AS Stellarator (W7-AS), which is located on the site of the Max-Planck Institute for Plasma Physics in Garching near Munich. The W7-AS was developed for fusion research.

In the beginning those basics are introduced, which are necessary to understand this work: The concept of magnetic confinement is outlined together with its application in fusion research. Some attention is drawn to the turnover of particles and energy inside a fusion machine and a spotlight is cast on the current theoretical understanding of the underlying mechanisms. At this point the turbulence comes into play. With the definition and the role of temperature fluctuations this chapter shall close.

1.1 Magnetic confinement of plasma

Plasma does not live peacefully together with other states of aggregation. To protect plasma facing components in the laboratory, one must utilise a method that separates the plasma from both the atmosphere and solid bounds. The most convenient way to achieve this is to set up a magnetic field with a particular geometry inside a vacuum chamber. Since plasma consists of charged particles, i.e. electrons and ions, a magnetic field will give rise to Lorentz forces on individual particles, provided that

they have got a velocity component perpendicular to the lines of the magnetic field. If the field is homogeneous with intensity B this yields the well-known gyro motion. Frequency f_c and gyration radius r_L at given velocity $v_\perp$, charge q and mass m are

$$f_c = \frac{|q|B}{2\pi\,m} \quad , \qquad r_L = \frac{v_\perp}{2\pi f_c} \quad . \qquad (1.1)$$

Note that there are several gyro radii due to the different masses of electrons and ions but also due to the velocity distribution at the temperature T. In a Maxwellian

$$f_{eq} = \pi^{-\frac{3}{2}}\, v_{th}^{-3}\, \exp(-v^2/v_{th}^2) \ , \qquad v^2 = v_\perp^2 + v_\parallel^2$$

with $v_\perp^2 = v_x^2 + v_y^2$ and $v_\parallel = v_z$ parallel to the magnetic field, the latter component is integrated [1] and yields the perpendicular distribution:

$$f_\perp = 2\,v_\perp\,v_{th}^{-2}\,exp(-v_\perp^2/v_{th}^2) \ .$$

The most probable, the average and the root mean square values of $v_\perp$ are

$$
\begin{aligned}
v_{\perp,mp} &= \tfrac{1}{\sqrt{2}}\,v_{th} &\approx& \quad 0.71\,v_{th} \ , \\
\overline{v_\perp} &= \tfrac{\sqrt{\pi}}{2}\,v_{th} &\approx& \quad 0.89\,v_{th} \ , \qquad v_{th} = \sqrt{\frac{2\,k_B T}{m}} \ , \\
v_{\perp,rms} &= \ v_{th} \ ,
\end{aligned}
\qquad (1.2)
$$

with k_B equal to the Boltzmann constant.

1.1.1   Natural magnetic confinement

From equation (1.1) it is obvious that gyro radii become small if B is increased. Thus, in a strong magnetic field, charged particles are pinned to a field line. Proper confinement however must include the direction parallel to the field line, where the particles still may move freely. There is an example in nature, where an inhomogeneity serves as a barrier. Consider the magnetic field line of a dipole as drawn in figure 1.1: Approaching the dipole, the magnetic field strength increases. The center of gyration of a particle starting in the equatorial plane with a finite $v_\parallel$ will follow the field line towards the pole and encounter a positive gradient of field strength. If the gyro radius is small compared to the gradient scale length $B/|\operatorname{grad}B|$, then the magnetic moment $\mu = m\,v_\perp/2\,B$ becomes invariant (see Chen [1974]), i.e. $v_\perp$ increases with B. Conservation of the kinetic energy $\frac{m}{2}(v_\perp^2 + v_\parallel^2)$ causes $v_\parallel$ to be depleted when the charged particle runs or rather spirals into the gradient. At the outmost point ($v_\parallel = 0$) the particle is reflected and the whole thing starts again in opposite direction.

---

[1] $\iiint_{-\infty}^{\infty} \ldots dv_x\,dv_y\,dv_z$ must be replaced by $2\pi \int_{v_\parallel=-\infty}^{\infty} \int_{v_\perp=0}^{\infty} \ldots v_\perp\,dv_\perp\,dv_\parallel$,
    this type of definite integral can be found in appendix A.2.1

Independent of this argumentation about $v_\parallel$ one has to be aware that the simple picture of a stationary gyration does not hold in an inhomogeneous field. A grad-B drift comes up, which has the sign of the particle charge and is perpendicular to the field direction and the gradient.

$$\mathbf{v}_{\nabla B} = \pm\frac{1}{2}\, v_\perp\, r_L\, \frac{\boldsymbol{B} \times \operatorname{grad} B}{B^2} \tag{1.3}$$

$\boldsymbol{B}$ is the field vector. The superposition of grad-B drift and gyration is valid, if r_L is small compared to the gradient scale length $B/|\operatorname{grad} B|$, while the ratio of r_L and this scale length determines the magnitude of the drift relative to $v_\perp$. In figure 1.1 the opposite grad-B drifts for ions and electrons are indicated.
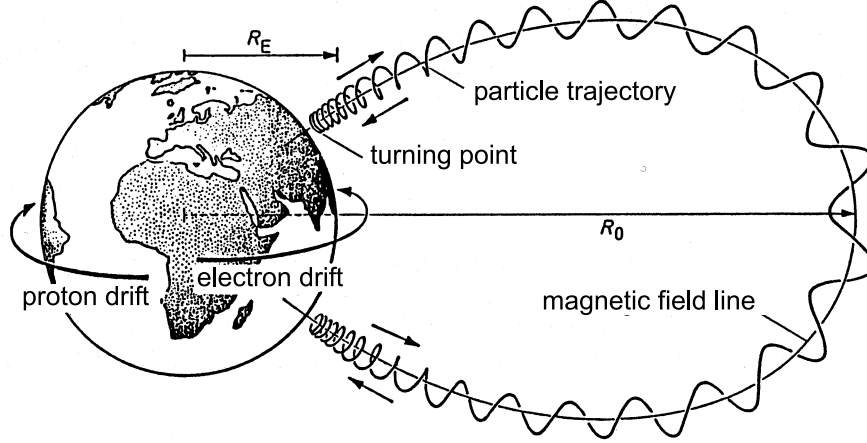
Figure 1.1: *Natural magnetic confinement [Schumacher 1993]. Charged particles from the solar wind that were scattered into the magnetosphere are trapped, i.e. confined in the Earth's magnetic dipole characteristic (R_E= 6378 km). The particles form the Van Allen radiation belts (Grimsehl et al. [1988]) up to $R_0 \approx 4\,R_E$. More far away, the dipole characteristics are perturbed by the impact of the solar wind. In the magnetosphere, the field vector points from the South to the North Pole.*

1.1.2   Toroidal magnetic confinement

Although the described magnetic confinement in a dipole characteristic seems to be complete, in the laboratory a different geometry is superior. It is the toroidal configuration which doesn't rely on a barrier in parallel direction but instead extends the parallel dimension to infinity by a circular closure. Figure 1.2 may impart an idea of the geometry: The magnetic surface has the shape of a torus, i.e. a doughnut or a closed flexible tube. One magnetic field line does not leave the surface, it rather
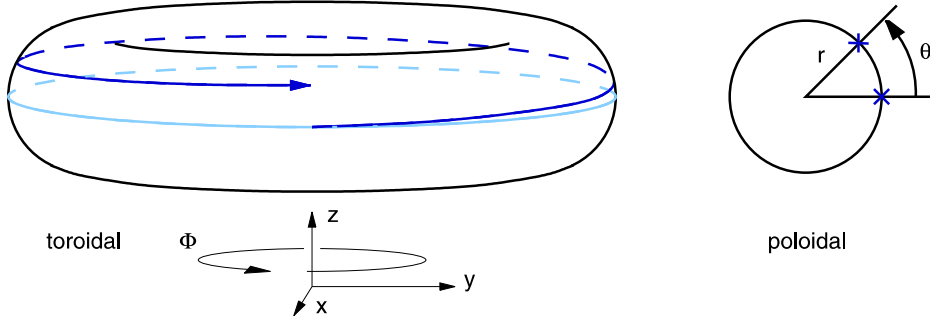
Figure 1.2: *Toroidal geometry with rotational transform of field lines. The equatorial plane is indicated in light blue. A field line (dark blue) starting at the equator departs in poloidal direction with increasing toroidal angle. To the right a single cross section is drawn together with the angle θ_1 after 1 toroidal turn. The drawing is roughly corresponding to $\iota \sim 1/8$.*

generates it by circulating with a slight helical twist. The latter is defined by the quantity ι :

$$\iota = \lim_{N \to \infty} \sum \frac{\Theta_N}{2 \pi N} \quad , \tag{1.4}$$

where Θ_N is the poloidal angle after N toroidal turns. In this context "poloidal" means the direction along the small circumference as shown on the right hand side of figure 1.2. Note that ι shouldn't be an exact rational number, otherwise the field line would close before the surface is densely covered.

Concerning the grad-B drift from equation (1.3) there is now a very favourable property of ι in a toroidal configuration: Although the field strength is inhomogeneous, i.e. decreasing from the inside towards the outside of the torus, particle drifts compensate on average. Consider an electron in figure 1.2, starting exactly on the surface at the equatorial plane outside the torus. If it has a positive $v_\parallel \gg |\mathbf{v}_{\nabla B}|$ it will follow the field line in toroidal and poloidal direction, meanwhile doing small gyrations. The drift will point in negative z-direction, that is into the volume of the surface, as long as the electron is above the equatorial plane. When the electron eventually crosses the equatorial plane, entering the lower half space, the downward drift now points out of the volume. Apart from a small intermediate drift excursion, the original location on the surface is restored after one poloidal turn.

To summarise, particle trajectories will closely follow the magnetic surface, they are confined to it. Since the argumentation holds for electrons and protons independently, the plasma volume will not be vertically polarised by the charge dependent grad-B drift. This is of particular importance because otherwise an $E \times B$ drift would deteriorate the confinement:

$$\mathbf{v}_{E \times B} = \frac{1}{B^2} \, \boldsymbol{E} \times \boldsymbol{B} \ . \tag{1.5}$$

Up to now only one surface was shown, but there is an arbitrary number of them. Geometrically they are all nested around the torus axis which is the core filament inside any surface's volume. It may appear that the toroidal configuration is axisymmetric, i.e. cross sections are invariant with respect to the toroidal direction. Indeed this is the case for plasma confining machines of the tokamak type (see Wesson [1997]), but the concept of nested magnetic surfaces can be generalised. In the next section the non-axisymmetric stellarator is introduced.

1.1.3 Stellarators

A stellarator [Spitzer 1958] establishes a toroidal magnetic configuration that develops from an external coil system only, including rotational transform of field lines. The stellarator can't be axisymmetric. To understand this it is sufficient to integrate the curl of the magnetic field vector over the area S_X of a cross section. According to the curl theorem this is equal to the line integral along the closed circumference ∂S_X. If there is a steady poloidal component of the magnetic field vector, then this integral should yield a non-zero value.

$$\iint_{S_X} \mathrm{rot}\, \boldsymbol{B} \cdot d\boldsymbol{S}_X = \oint_{\partial S_X} \boldsymbol{B} \cdot d\boldsymbol{x}$$

Due to Maxwell's law, however, integrating the curl of the magnetic field in one cross section is equal to the total current enclosed by the circumference plus the displacement current. Since the latter are both zero in a stationary vacuum magnetic field, an axisymmetric configuration with rotational transform is a contradiction.

$$\mathrm{rot}\, \boldsymbol{B} = \mu_0 \boldsymbol{j} + \mu_0 \epsilon_0 \cdot \frac{\partial \boldsymbol{E}}{\partial t}$$

Stellarators establish a rotational transform by a rather complex three dimensional structure. For the Wendelstein 7-AS machine this structure is displayed: Part of the coil system in figure 1.3 and the largest of the nested vacuum magnetic surfaces in figure 1.4.

To reduce the complexity when discussing plasma quantities in the 3D stellarator configuration, magnetic surfaces are labeled ψ. This label is a scalar function that depends in a complicated way on the cartesian coordinates of the laboratory system, but it can also be written as the function of only one parameter $\psi(r_{\mathrm{eff}})$, where r_{eff} is related to the small radius r of an equivalent axisymmetric configuration (like in figure 1.2). Mathematically, magnetic surfaces are defined by

$$\psi = const \quad \text{and} \quad \boldsymbol{B} \cdot \mathrm{grad}\, \psi = 0 \ ,$$

and the constraint is, that a curve which outlines the perimeter of one cross section is mapped into itself after one toroidal turn. In doing so, each point on the curve must be traced following the lines of the magnetic field.
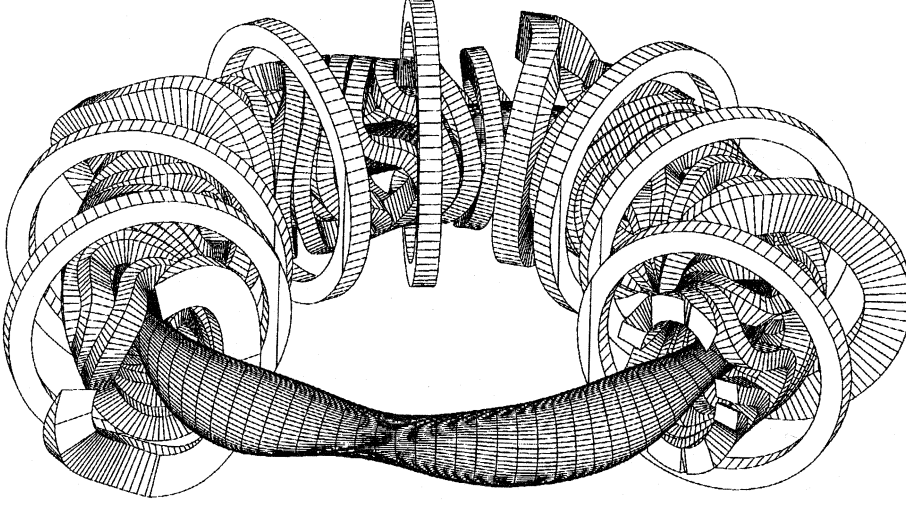
Figure 1.3: *Coil system and plasma of the Wendelstein 7 Advanced Stellarator (W7-AS). Actually there is a vacuum vessel in between the coils and the plasma surface. The vessel wraps the plasma closely and is omitted in this drawing.*
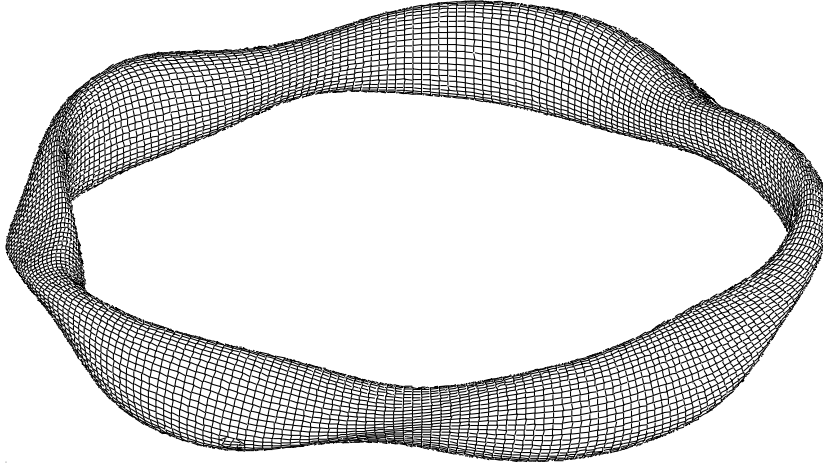
Figure 1.4: *Largest closed magnetic surface (LCMS) inside the vacuum vessel of W7-AS. The radius of the ring is $R_0 \approx 2\,\mathrm{m}$ (actually R_0 is the radius of the magnetic axis, i.e. the core filament inside the volume). The average radius of a cross section is $\sim 0.2\,\mathrm{m}$.*

In a stationary plasma state, it is generally a good approximation to regard the magnetic surfaces ψ as isosurfaces for plasma potential, density and temperature and all derived quantities. The reason is the following: One field line with non-rational rotational transform will reach any region of the surface. Particles move freely in direction parallel to the field line and the mean free path is usually so large, that it corresponds to several toroidal and poloidal turns. Thus, one particle encounters only particles that are confined close to the very same surface. The plasma thermalises within one surface and a representation of the plasma as a function of r_{eff} alone is adequate.

The remaining task is to find a good mapping between the magnetic surface label and the cartesian coordinate system of the laboratory, where all the machine components and the measuring systems are aligned. Normally, ψ is identified with the toroidal flux

$$\psi = \iint_{S_X} \boldsymbol{B} \cdot d\boldsymbol{S}_X$$

where S_X is the area of a cross section of the surface. Obviously ψ is linear in the field strength, and the ratio ψ/B has the dimension of an area. If an equivalent axisymmetric system is regarded, then the field strength varies according to

$$B = \frac{R_0\,B_0}{R_0 + r\cos\theta} \quad.$$

In this formula $x^2 + y^2 = R_0^2$ defines the core filament or the torus axis inside a magnetic surface (see figure 1.2 for the definition of x and y). R_0 is also called the "major radius", whereas B_0 is the field strength on axis ($r = 0$). Evaluating the toroidal flux yields

$$\psi(r) = 2\pi R_0\,B_0\,\left(R_0 - \sqrt{R_0^2 - r^2}\right) \;\approx\; r^2\pi\,B_0 \;,$$

provided that $r \ll R_0$. For a large aspect ratio R_0/r_{eff} the right hand side is a good approximation. Transferring this result to the W7-AS stellarator, which has got an aspect ratio of roughly 10, it becomes clear that the flux surface coordinate r_{eff} can be identified with the radius r from figure 1.2 that produces a circular cross section of the same area. Since in the W7-AS the cross section is a function of the toroidal angle Φ (it varies periodically), r_{eff} is simply defined via the arithmetic mean of the areas at two particular toroidal positions:

$$r_{\text{eff}}^2\,\pi \;=\; \tfrac{1}{2}\left(S_X(0) + S_X(\tfrac{\pi}{5})\right) \;. \tag{1.6}$$

The positions are chosen to be the center and the edge of one field period.

Although there is no simple symmetry, a stellarator may consist of several periods. There are five in the case of the W7-AS. Within each period there is a specific "stellarator symmetry": The cross sections of the period boundaries and the cross section in the center of one period are up-down symmetric, i.e. relative to the equatorial plane. Within one period there is a "flap" symmetry between the two halves. One half period can be produced from the other by a rotation around that radial axis, which is defined as the intersection line of the equatorial plane and the cross section in the period center. Applying this knowledge to W7-AS, one half period covers the toroidal angle from $0 \ldots \pi/5$. Since there are five periods and ten half periods, respectively, the toroidal closure is satisfied.

A general introduction into stellarator geometry and appropriate coordinate systems can be found in the comprehensive review by Boozer [2004].

So far the feedback of the plasma to the magnetic configuration was neglected. If the number of particles is increased, the picture of individual plasma particles moving in a vacuum magnetic field becomes invalid. Plasma pressure $p = n_0 \, k_B T$ builds up and, consequently, the plasma has to be described by a fluid model [Wobig 1997]. Given the ratio β between p and the pressure of the magnetic field $p_B = B^2/\mu_0$ is not negligible any more, then the magnetic field configuration is actually changed by the plasma. Typically this becomes important if $\beta \gtrsim 0.01$.

In the design phase before the construction of a stellarator, there are degrees of freedom for the magnetic geometry, which allows one to do an optimisation. Thus, the negative impact of an increasing plasma pressure can be reduced. For instance, magnetohydrodynamic (MHD) instabilities can be avoided [Nührenberg and Zille 1986], and it is possible to minimise the so-called Shafranov shift of the nested flux surfaces. From the engineering point of view the technical feasibility of the stellarator coil system is also an important point. Further optimisation criteria, such as the confinement of high energetic α particles, must be addressed, if finally the stellarator is intended to be used as a fusion reactor. The reviews of Wagner [1997] and Wagner and Wobig [2005] provide more details.

In the line of stellarators that have been put into operation up to now, the W7-AS plays an important role. It demonstrated the feasibility of modular coils and successfully tested the optimisation concept. Additionally, in the most recent experimental campaigns it has pioneered the island divertor as an exhaust concept [Grigull et al. 2001; Wagner et al. 2005].

1.2 Fusion and energy confinement

One strong motivation to exploit the physics of magnetic confinement is the option to utilise nuclear fusion reactions for the generation of energy. Such process with the most lightweight hydrogen isotope involved proceeds on the sun for billions of years. From today's point of view probably this reaction is technically viable:

$$D + T \rightarrow He + n + \Delta E \ .$$

The hydrogen isotopes Deuterium and Tritium form a Helium nucleus. One neutron and an amount $\Delta E \approx 17.6 \, \text{MeV}$ of energy are released. Safety issues must be addressed in such a technology [Raeder et al. 1995]. A significant reaction rate is only achieved if the Deuterium and Tritium nuclei have an average kinetic energy $\wp(10 \, \text{keV})$ [Schumacher 1993]. This corresponds to a D-T plasma thermalised at roughly $8 \cdot 10^7 \, \text{K}$. To maintain such a hot plasma and reliably keep it away from the environment, the toroidal magnetic confinement seems to be most promising.

While machines of the tokamak type (see [Wesson 1997]) are highly developed and close to the goal of producing net fusion power, yet the stellarator is the only machine type that is inherently capable of steady state operation. At the same time, since in a stellarator there is no externally driven plasma current, there are no

disruptions. This is the reason, why such large and sophisticated machines like the W7-AS are built and operated.

For the nuclear reactions to yield more energy than is necessary to set up the hot plasma, a threshold has to be exceeded. Given the thermal energy of Deuterium and Tritium corresponds to $13\,\mathrm{keV}$, the threshold reads

$$n_0 \cdot \tau_E \quad \gtrsim \quad 2 \cdot 10^{20}\,\mathrm{m}^{-3}\mathrm{s} \ , \tag{1.7}$$

where n_0 is the plasma particle density and τ_E the so-called energy confinement time. This time constant characterises the quality of heat insulation inside a plasma machine. Microscopically, τ_E is determined by the processes that transport the thermal energy across the lines of the magnetic field, from the hot plasma center (i.e. the axis) to the boundary. The magnitude of τ_E is determined experimentally from the ratio of the stationary kinetic energy content (in total) and the absorbed heating power. The higher τ_E, the higher will be the temperature inside a plasma machine with fixed heating power and plasma density.

Since the heating power balances the losses in stationary operation and since the loss is to some extent connected to the temperature gradient and thus to the scale length between the hot plasma center and the cold boundary, the size of the machine plays a decisive role. Extrapolating the confinement properties experimentally observed at present-day machines, the ITER project has been initiated. ITER is large enough to overcome the threshold (formula 1.7), e.g. see the ITER Physics Basis Editors and ITER Physics Expert Groups Chairs and Co-Chairs [1999]. But there is a second task: If the mechanisms that determine τ_E, i.e. the heat loss of a hot plasma in a magnetic confinement, are identified correctly, then the extrapolation becomes much more substantiated.

1.3 Understanding of the energy transport

Classical and neoclassical transport

Consider a diffusive approach to characterise the radial thermal conduction in the toroidal magnetic confinement of the W7-AS. The heat flow vector $\boldsymbol{q}$ is proportional to the temperature gradient and the constant of proportionality λ is expressed as the product of density n and heat diffusivity χ.

$$\boldsymbol{q} \ = \ - \lambda \,\mathrm{grad}\, T \ = \ - n\, k_B\, \chi \,\mathrm{grad}\, T \tag{1.8}$$

Under the assumption that flux surfaces are isosurfaces for the temperature, there is a temperature gradient only in the direction of $-\mathbf{e}_r$, where r is the coordinate along the minor radius as defined in figure 1.2. The temperature gradient is perpendicular to the lines of the magnetic field.

A very simple method to model the heat diffusivity is to interpret it as the ratio between stepsize squared and collision time. Since particles are forced to cyclotron

11

motion, the stepsize is assumed to be the gyration radius r_L. In the terminology of magnetic confinement the corresponding result is called the classical diffusion co-effecent. Applying equations (1.1) and (1.2) with root mean square perpendicular velocity, and using the self collision time (appendix A.1.2), the classical heat diffusivities for protons and electrons in a typical W7-AS plasma are ($\hat{T} = 1\,\mathrm{keV}$, $n = 10^{19}\,\mathrm{m}^{-3}$, $B = 2.5\,\mathrm{T}$, the temperature is supplied in eV $\rightarrow \hat{T} = k_B T / e$):

$$\chi_{p,\,class} \approx 1.4 \cdot 10^{-3}\,\mathrm{m^2\,s^{-1}} \ , \quad \chi_{e,\,class} \approx 3 \cdot 10^{-5}\,\mathrm{m^2\,s^{-1}} \ .$$

This is in strong contrast to the experimental values, which are of the order $1\,\mathrm{m^2\,s^{-1}}$ [Stroth et al. 1995].

The next logical step to improve the model is to include the correct geometry. It has already been pointed out that the field strength in a toroidal magnetic confinement is inhomogeneous, and that this leads to drift excursions of the particles relative to the magnetic surface. Thus, given a particle encounters another particle during such an excursion, and given this excursion is larger than the gyro radius, then the stepsize and the diffusivity are strongly enhanced. A model that includes all these effects is called neoclassical. Galeev and Sagdeev [1979] treat the theory in detail, and they also pay some attention to the peculiarities of stellarator geometry. Note that the simple diffusion laws for the flows of particles, energy and electric current have to be modified. In a toroidal plasma the full transport matrix has the form (adapted from [Stroth 2005]):

$$\begin{pmatrix} \Gamma_r \\ q_r / k_B T \\ n\, j_\Phi / \sigma_\parallel B \end{pmatrix} = -n \begin{pmatrix} D & D_{12} & D_{13} \\ D_{21} & \chi & D_{23} \\ D_{31} & D_{32} & \sigma \end{pmatrix} \begin{pmatrix} \left(L_n^{-1} - \frac{3}{2}L_T^{-1} - qE_r / k_B T\right) \\ L_T^{-1} \\ q\, E_\Phi / k_B T \end{pmatrix} \quad (1.9)$$

$$L_n = \frac{n}{\mathrm{grad}\, n \cdot \mathbf{e}_r} \ , \quad L_T = \frac{T}{\mathrm{grad}\, T \cdot \mathbf{e}_r}$$

where Γ_r and q_r are the collisional radial fluxes of particles and energy, respectively, j is the current density, $\sigma_\parallel = \eta^{-1}$ (see appendix A.1.3) the electric conductivity in direction of the magnetic field lines, E is the electric field and q the particle charge. The subscripts Φ and r denote the toroidal and the radial direction, respectively. Note that all matrix elements have the unit of a diffusion coefficient.

When applied to experimental results from the W7-AS, the neoclassical theory was successful in the plasma core [Maaßberg et al. 1993; Brakel 1997]. Profiles of electron and ion temperatures and of the electron density were measured. Heat diffusivity was deduced from the heating power and its localisation, using the profiles and observing the correct geometry. At the same time the heat diffusivity was modelled with neoclassical theory, again based on the measured profiles. In figure 1.5 the results of both approaches are compared for a W7-AS plasma which was heated with $800\,\mathrm{kW}$ microwave power. The deposition of the heating is determined by the location of the electron cyclotron resonance. In this case at $r_{\mathrm{eff}} = 0$, that
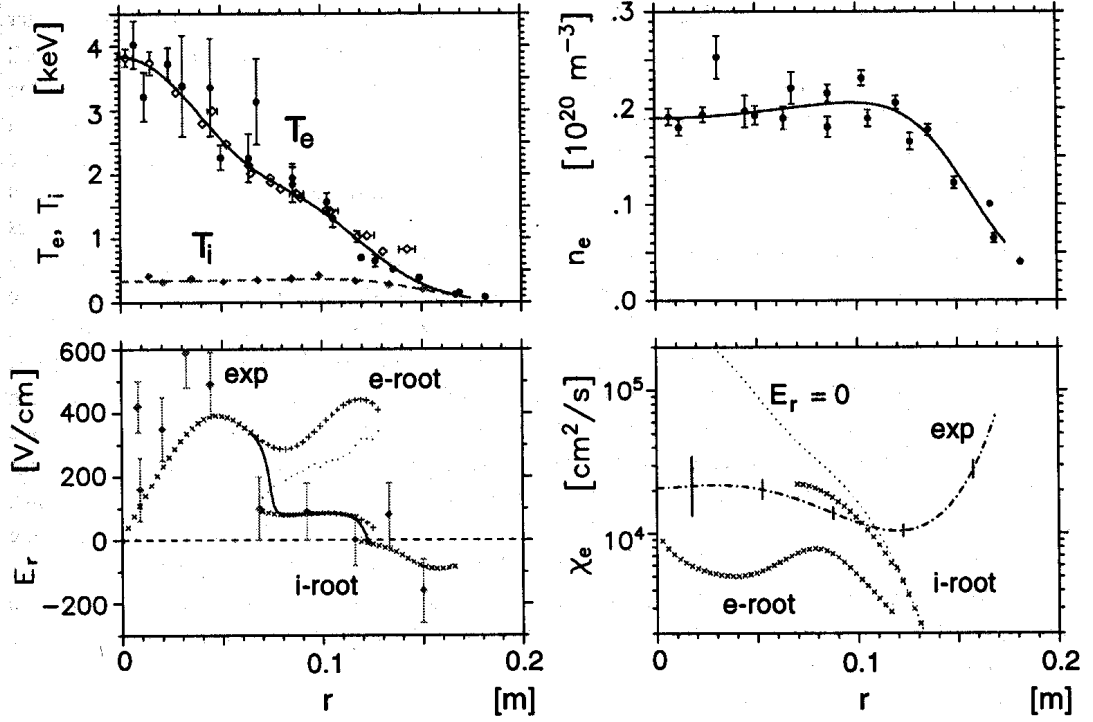
Figure 1.5: *Neoclassical theory and experimental W7-AS results [Brakel 1997]. Top row are measured profiles of temperature and density together with their fit functions. All x-axes are r_{eff}. Bottom row contains the comparison of E_r and of χ_e between the neoclassical prediction (plotted with small crosses, on the left additionally with a solid line indicating a transition) and experimentally obtained values (points with error bars on the left, dash dot line on the right).*

is on axis ($R_0 \approx 2\,\mathrm{m}$, cf. figure 1.4). The magnetic surfaces do not intersect any component inside the vessel until $r_{\mathrm{eff}} \approx 0.18\,\mathrm{m}$. Neoclassical theory predicts χ_e within a factor of 2 for $r_{\mathrm{eff}} \leq 0.12\,\mathrm{m}$. Outside this radius, i.e. towards the plasma boundary the prediction is by far too small compared to the measured heat diffusivity.

A separate topic is the radial electric field E_r. There is good agreement between the predicted and the measured one. E_r adjusts itself to balance ion and electron particle fluxes, since the plasma inherently remains quasi-neutral. This so-called ambipolarity is compatible with different theoretical solutions in different regions and, therefore, both the "electron-root" and the "ion-root" are plotted in figure 1.5. For stability reasons, the "ion-root" should be obtained by the plasma from its onset at $r_{\mathrm{eff}} = 0.07\,\mathrm{m}$, which is correctly predicted by the theory. More details can be found in [Brakel 1997].

To conclude, neoclassical theory is a powerful tool for modelling transport in the stellarator core. But the core is coupled to the boundary and in the boundary there is a lack of understanding. The search for a mechanism that could explain the transport in the boundary leads to the next section.

Turbulent transport in a plasma

Unlike interactions between individual particles, turbulence is a collective phenomenon. It is discussed in the fluid picture, the plasma is regarded as a two component liquid with density and temperature. Basic ingredients of the turbulence are: instability, nonlinearity and dissipation on a small scale compared to the machine size. Altogether a stationary state evolves with dynamical generation and decay of a set of substructures and an enhanced flow of energy.

There must be a source of energy to generate the turbulence. This is the inhomogeneity of state inside a plasma machine: In the very center (r_{eff}=0) the plasma has a high thermal energy and at the boundary this energy approaches the comparatively low thermal energy of the environment. Thus the plasma is not in equilibrium in a strict thermodynamical sense. The pressure gradient is the energy source that feeds the turbulence.

Generally, the turbulence at the boundary of fusion devices is electrostatic: the movement of turbulent structures is strongly dominated by electric field induced drifts [Liewer 1985]. Magnetic turbulence is prevented by both the comparatively low pressure and the high collision frequency at the plasma edge. The detailed interrelation can be found in [Schröder 2003]. Throughout this work, the effect of magnetic turbulence is neglected.

In the literature plasma edge turbulence is often regarded as "micro-turbulence", because the structures, which are frequently denoted as "vortices" or "curls" or "eddies" extend only a few centimeters in poloidal direction. Additionally their average lifetime is usually less than $0.1\,\text{ms}$. One should not forget, however, that the condition of a quasi-neutral plasma holds even in the turbulence. In other words, electron and ion charge density may differ only slightly and the sizes of the turbulent structures are still large compared to the Debye length, which is the characteristic scale for charge separation in a plasma. Subsequently, a picture of the turbulence shall be sketched, discussing the basic ingredients.

1.3.1 The drift wave picture

Consider a local disturbance $\tilde{p}$ of the plasma pressure in a strong magnetic field. The species to react first are the electrons. Being by far more mobile than the ions, they will flow away in parallel direction as indicated in figure 1.6, leaving behind the disturbance positively charged. In this new situation the lines of the electric field should be discussed. At first sight the electric field extends in parallel direction, too, connecting the positive charge and the electron excesses on both ends of the perturbation. But this structure is usually highly elongated so that one has to bear in mind the toroidal closure of the geometry and the rotational transform. If the elongation is comparable to the toroidal circumference, then the electron excesses are likely to be more close to the positive charge, but now separated in poloidal direction, that is perpendicular to the magnetic field lines. The electric field is
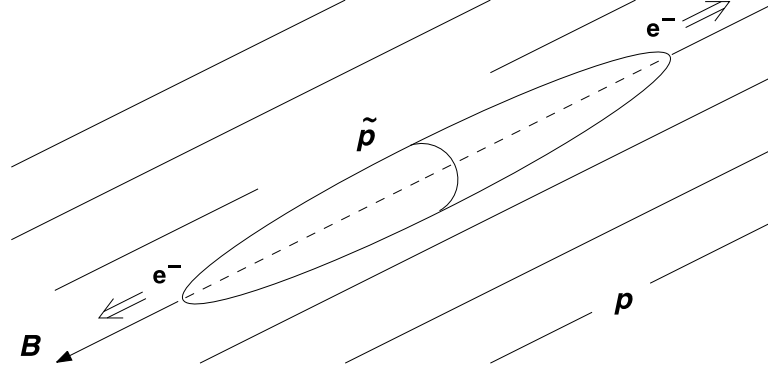
Figure 1.6: *An arbitrary initial pressure perturbation in a magnetised plasma and the dynamic reaction of the electrons. The proportions are not accurate. Experimentally it is known that such a structure extends at least several 10 m in parallel direction and only some cm perpendicular.*
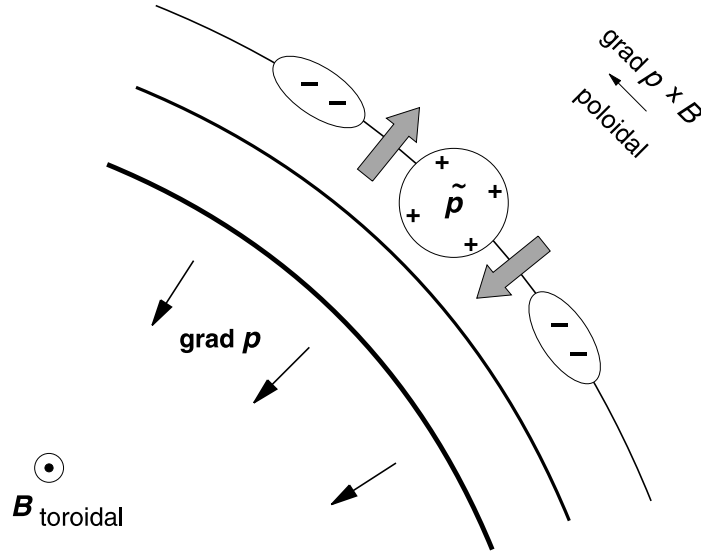
Figure 1.7: *Sector of a cross section in a toroidal magnetised plasma with radial pressure gradient (slim arrows). There is a pressure perturbation (large circle) at one magnetic surface. Since some electrons escaped, it is positively charged. Due to the toroidal geometry with rotational transform, the electron excesses (ellipses) on both ends of the perturbation come to lie close to the positive charge. The resulting poloidal electric fields generate opposite $E \times B$ drifts (broad arrows) in the pressure gradient. Thus a new positive pressure perturbation is created in direction of the electron diamagnetic drift and a negative opposite.*

consequently perpendicular with field lines starting from the positive charge and spreading in both poloidal directions. This condition gives rise to opposite radial $E \times B$ drift motions on the opposite poloidal boundaries of the initial disturbance. Figure 1.7 illustrates the situation.

At this point one should remember the background plasma with a strong pressure gradient. The opposite $E \times B$ drifts will shuffle high pressure plasma into the low pressure region on one side of the perturbation and vice versa on the other (see figure 1.7). Since the $E \times B$ drift is in good approximation ambipolar, a new pressure disturbance is generated, slightly shifted in poloidal direction. Again the electrons will react first at this new position and the whole thing starts over.

In this way the initial pressure perturbation propagates poloidally in direction of the electron diamagnetic drift (therefore it is called a drift wave), that is the direction of the vector cross product between electron pressure gradient and magnetic field

$$\boldsymbol{v}_{e,\,dia} = \frac{1}{e\,n_0\,B^2}\ \mathrm{grad}\,p_e \times \boldsymbol{B}\ . \tag{1.10}$$

Due to the low frequency of drift waves, ion inertia and thereby polarisation currents have to be taken into account

$$\boldsymbol{v}_{pol} = \frac{m}{Z\,e\,B^2}\,\frac{d}{dt}\boldsymbol{E}_{(\perp)}\ . \tag{1.11}$$

Note that the total or advective derivative of the electric field is defined for each vector component as the partial derivative plus the change by convection

$$\frac{d}{dt} \rightarrow \left(\frac{\partial}{\partial t} + \boldsymbol{v} \cdot \mathrm{grad}\right)\ . \tag{1.12}$$

The contribution of the polarisation current is proportional to the particle (ion) mass m and the inverse charge number Z^{-1}. During the initial state of a pressure perturbation electrons flow off in parallel direction and the change of the electric field has got its maximum, therefore an ion-dominated polarisation current exists perpendicular to the lines of the magnetic field. Following the equation of continuity in a quasi-neutral plasma the perpendicular ion current balances the parallel electron current.

Up to now the picture of a localised pressure perturbation in a toroidal closure with rotational transform has been used. This situation applies well to closed magnetic surfaces inside the plasma boundary of a fusion machine. The localisation implies already the superposition of different Fourier modes. Generally, drift waves exist in any magnetic configuration with a gradient of the plasma pressure perpendicular to the lines of the magnetic field. Sources and sinks for the transport relevant (via $E \times B$ convection) electric fields are poloidally adjacent half periods of the wave structure. Thus the picture is portable into the scrape-off layer of a fusion plasma, where closed magnetic surfaces do not exist any more. Magnetic field lines are intersected by so called limiters there. Due to this boundary condition, the electrons escaping from an initial perturbation flow onto the limiter and from there possibly into the poloidally adjacent regions. This has been analysed by Endler [1994]. To summarise, drift waves are characterised by parallel electron motion and perpendicular ion motion. Background plasma is convected by radial $E \times B$ drift arising from fluctuating poloidal electric fields.

1.3.2 Instability of the drift wave

Electrons that react to a density perturbation try to establish a local Boltzmann equilibrium where their energy is modified by an electrostatic potential. The inter-relationship between density and potential difference is

$$n_e = n_0 \exp(e\, U / k_B T_e) , \tag{1.13}$$

where n_0 is the electron density of the unperturbed background, T_e is the electron temperature, and $U = 0$ denotes a potential equal to that of the background plasma. Consequently the electrostatic field can be deduced by $\boldsymbol{E} = -\operatorname{grad} U$. Electrons are frequently called "adiabatic" if equation (1.13) is fulfilled anywhere. Assuming small amplitudes a first order expansion of the exponential function can be used. Thereby the electron density perturbation is a linear function of the potential difference

$$\tilde{n}_e = (n_e - n_0) \approx \frac{e\, n_0\, U}{k_B T_e} .$$

The fluctuating density $\tilde{n}_e$ may be re-written in Fourier space as an isothermal fluctuating electron pressure $\tilde{p}_e$ with wave number k and angular frequency ω. If there is a propagation into positive y direction the phase factor is $\exp(iky - i\omega t)$.

Now a small phase shift α between the fluctuation of the electric potential $U(k,\omega)$ and $\tilde{p}_e$ should be allowed, so that the slightly non-adiabatic relation between pressure and potential is in Fourier space:

$$U(k,\omega) = \frac{1}{e\, n_0} \tilde{p}_e(k,\omega) \, (1 + i\alpha) . \tag{1.14}$$

A positive phase shift $\alpha > 0$ corresponds to a phase lag of the potential against the density, i.e. in direction of the propagation U is delayed relative to $\tilde{p}_e$. The reason is obvious: Inertia and the collisional friction at the ions both prevent the electrons from an instantaneous adjustment to the Boltzmann distribution, thus the formation of the electric potential is retarded.

In order to eliminate U, the equation of continuity with $\boldsymbol{v} = \boldsymbol{v}_{E \times B}$ for the $E \times B$ convection is employed. Multiplying this equation with $k_B T_e$ and observing $\operatorname{div} \boldsymbol{v}_{E \times B} = 0$ (will be discussed in section 1.4.2), this reads

$$\frac{\partial}{\partial t} p = -\boldsymbol{v}_{E \times B} \cdot \operatorname{grad} p . \tag{1.15}$$

If the pressure gradient is in negative x direction and the magnetic field in positive z direction, then in Fourier space this is equal to

$$(\gamma - i\omega)\, p_e(k,\omega) = -\frac{ik\, |\operatorname{grad} p_e|}{B}\, U(k,\omega) \tag{1.16}$$

since the fluctuating $E \times B$ velocity is $-ikB^{-1}U(k,\omega)\,\mathbf{e}_x$. Substituting U from equation (1.14) it is easy to see that the modified wave factor $\exp(\gamma t + iky - i\omega t)$

is necessary, therefore $\partial/\partial t$ has already been replaced by $\gamma - i\omega$ in equation (1.16). The connection between the growth rate γ of the pressure perturbation and the phase shift α becomes

$$\gamma = \frac{k \,|\operatorname{grad} p_e|}{e \, n_0 \, B} \, \alpha \; .$$

It is also possible to verify the phase velocity from this approach. Both absolute value and direction of the electron diamagnetic drift (equation 1.10) are reproduced exactly

$$\frac{\omega}{k} = |\boldsymbol{v}_{e,\,dia}| = \frac{|\operatorname{grad} p_e|}{e \, n_0 \, B} \; .$$

But it should be noted that a drift wave's own propagation is usually not observable at the boundary of a fusion experiment. Additional radial electric fields from the intrinsic ambipolar particle fluxes (e.g. see lower left of figure 1.5) superpose and cause the background plasma to be convected poloidally. Both propagation direction and speed of the drift wave structures are determined by this background movement and the observable drift wave frequencies are spoiled. What remains untouched is the phase shift between the perturbations of pressure and potential. With $\alpha > 0$ the displacement of the pressure or density structure relative to the associated potential is always in electron diamagnetic direction.

1.3.3 Nonlinear behaviour and mode coupling

The nonlinearity has already been written down on the right hand side of equation (1.15) but it has been omitted in equation (1.16). Both $U(k,\omega)$ and $p_e(k,\omega)$ are represented in Fourier space. As long as the amplitude of the perturbation is small, the background pressure gradient is nearly unaffected. With growing amplitude, however, $\operatorname{grad} p_e$ will get a mode structure similar to that of p_e. In this case the feedback on p_e via the left hand side of equation (1.15) is a product of two fluctuating quantities, which turns into a convolution in Fourier space. Thus the term $|\operatorname{grad} p_e|\,U(k,\omega)$ on the right hand side of equation (1.16) must be re-written

$$g * U \; = \; \int\limits_{-\infty}^{\infty} g(\kappa)\, U(k - \kappa)\, d\kappa \tag{1.17}$$

where g denotes $\operatorname{grad} p_e$ and $g(\kappa)$ its Fourier spectrum. For simplicity only the transform in space is carried out.

It is intuitive to understand mode coupling by studying the properties of the convolution. Given there is a power spectrum of U with a few coherent waves and a spectrum of g (alias $\operatorname{grad} p_e$) with corresponding waves and an additional component for the background at $k = 0$, as illustrated in figure 1.8. The value of the convolution at value k is the integral U times g of a wavenumber shifted by k. That way satellite
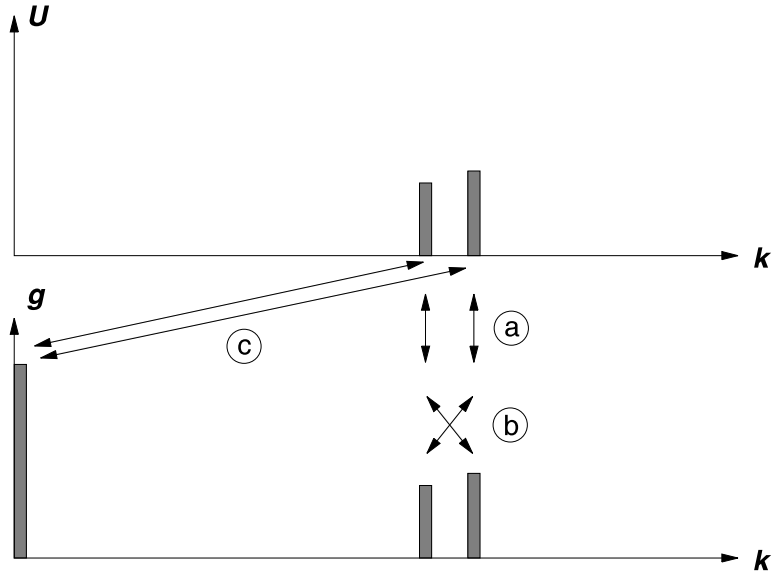
Figure 1.8: *Initial power spectra of fluctuating electrostatic potential and density gradient, utilised to demonstrate the formation of a turbulent spectrum. Exemplarily, the linear instability is modelled with two discrete modes. The gradient additionally has got a mean value.*
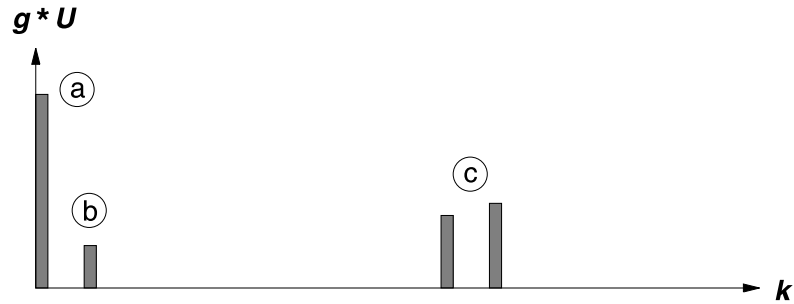
Figure 1.9: *Convolution of the two spectra from figure 1.8 as a result from nonlinear wave coupling. A satellite line (b) is generated.*

lines are generated in the new spectrum, whenever there is an overlap between any of the primary lines (see figure 1.9).

If the mode coupling is continued with ever new satellite lines, it is probable that a broadband range of modes comes up. In a fully turbulent (i.e. nonlinear) situation, generally none of the initial spectral lines can be identified any more. The spectrum is finally limited by dissipation processes at high k.

1.3.4 Dissipation and the turbulent spectrum

A universal form of turbulence spectra was proposed by the Russian mathematician Kolmogorov (see Frisch [1995]). These two basic assumptions are important to

19
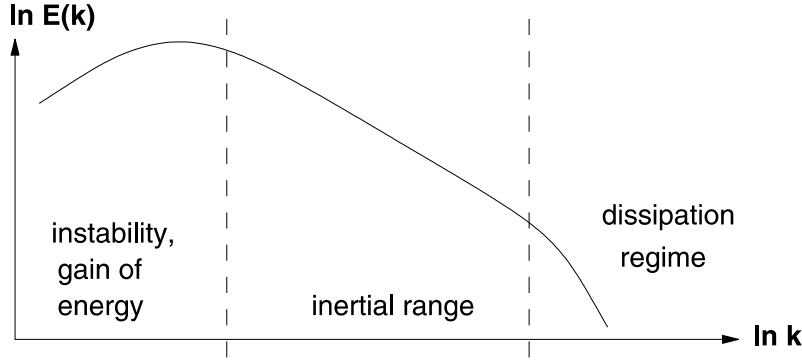
Figure 1.10: *General form of the spectrum of kinetic energy in turbulence.*

understand the properties of the kinetic energy wavenumber spectrum: First, there is a limited range of unstable mode numbers k. Usually this applies to low k (large structures). Second, at high k there is dissipation. All kinds of friction forces are proportional to the velocity of a particle or a fluid element. Velocity is the time derivative of the wave amplitude and thus clearly connected to ω and k respectively.

If the instability region and the dissipation region are separated in k, then there is a so-called inertial range in between with a characteristic spectral decay proportional to $k^{-5/3}$. At the limit $k \to 0$ the spectral power must be limited due to the finite system size. At high k the dissipation leads to an exponential decay much stronger than in the inertial range. Qualitatively this spectrum is drawn in figure 1.10.

Now the general form of a turbulence spectrum should be compared with a fully developed spectrum of drift waves in a magnetised plasma. First one should distinguish the different scales: On one hand there is the scale of the wave propagation or wave drift. This is the perpendicular scale which is usually small. On the other hand there is the scale in parallel direction which is large due to the high mobility of the electrons. The first (perpendicular) scale is relevant for the radial transport, since it determines the fluctuating poloidal electric fields. Therefore in the following all energy spectra are interpreted as a function of k which should be identical with the perpendicular wavenumber $k_\perp$. For convenience, the distinction between the poloidal and the exact perpendicular projected (with respect to the lines of the magnetic field) direction is often neglected. The approximation is tolerable if the angle between the lines of the magnetic field and the toroidal direction is small.

Dissipation is taking place along the path of the electrons that is parallel to the magnetic field lines. Reacting to the pressure perturbations, the electrons suffer from friction. Their propagation speed or the amount of friction power, however, depends on the dynamics of the wave and this again is dominated by the perpendicular wavenumber k (see also chapter 4 of Scott [2000]). Altogether there is an appropriate dissipation mechanism supporting the development of a spectrum similar to the one in figure 1.10 at high k.

In the low k region drift wave dispersion indeed provides the scale where the spectral power starts to degrade as shown right from the maximum in figure 1.10.

But an isolated inertial range with a clear Kolmogorov like decay would require a clear spectral separation from the dissipation regime. This is not always the case in the boundary of a fusion plasma and therefore one should not be too surprised, if the spectrum and particularly the spectral decay with k differs from the ideal one.

1.3.5 The dispersion scale

The dispersion of drift waves is obtained when the equation of continuity is written in a more accurate way than (1.15) for the ions. In next order the polarisation drift velocity (1.11) must be included, so that the equation reads

$$\frac{\partial}{\partial t} n_i = -\boldsymbol{v}_{E \times B} \cdot \operatorname{grad} n_i - \operatorname{div}(n_i \boldsymbol{v}_{pol}) \ .$$

It is sufficient to apply this extension to the example from section 1.3.2. Observing $n_0 = Z\, n_i$ the dispersion relation becomes

$$\omega = \frac{|\operatorname{grad} p_e|}{e\, n_0\, B} k \left(1 + \frac{m_i k_B T_e}{Z^2 e^2 B^2} k^2 \right)^{-1} = |\boldsymbol{v}_{e,\, dia}| \frac{k}{1 + \rho_{\mathrm{s}}^2 k^2} \quad . \tag{1.18}$$

The dispersion scale ρ_{s} depends on the characteristic combination of ion mass and electron temperature, since both ion polarisation current and the ability of electrons to establish a Boltzmann distribution play a role.

$$\rho_{\mathrm{s}} = \frac{\sqrt{m_i\, k_B T_e}}{Z\, e\, B} \ . \tag{1.19}$$

Additionally, $k \rho_{\mathrm{s}} = 1$ is a rough measure to localise the maximum in the turbulent spectrum, i.e. where the spectral power rolls over and starts to decay. This has already been demonstated in the early numerical simulations of drift-wave turbulence by Hasegawa and Wakatani [1983].

1.3.6 Brief history of theoretical modelling

Hasegawa and Mima [1978] derived equations to handle fluctuations in a magnetised plasma. They pointed out that there is nonlinear mode coupling due to the convective derivation of ion polarisation drifts. Wakatani and Hasegawa [1984] numerically solved model equations on a perpendicular 2D grid for tokamak plasma relevant parameter values and found a saturated turbulent state. The qualitative dependency of the energy spectrum on the wavenumber obtained by these authors has been verified both by measurements and by later more detailed simulations. The spectrum is characterised by a flat low wavenumber part, similar to white noise, a rollover at the specific wavenumber $k = \rho_{\mathrm{s}}^{-1}$ and a strong decay with increasing wavenumber. Furthermore power spectra of both k perpendicular to the magnetic field are similar. This means there is not only a turbulent mode structure in poloidal but also in radial direction, i.e. parallel to the density gradient.

When the location of the shoulder in the energy spectra was compared with measurements, however, the experiments reported a decay that started well below ρ_s^{-1}. Including additional dissipation effects, i.e. electron dynamics with friction in the dimension parallel to the magnetic field, Terry and Diamond [1984, 1985] analytically showed, that the width of the kinetic energy spectrum is reduced and that the decay should follow a $k^{-17/6}$ power law for medium wavenumbers. Further processes which transfer energy from short to long wavelengths and thus shrink the spectral width have been worked out by Similon and Diamond [1984]. A good overview of these early attempts is the review by Liewer [1985].

The details of the evolution till today shall be skipped here, but it was accompanied by significant progress in computer technology and thus allowed the efficient implementation of more and more detailed models. In the recent years advanced numerical studies have been carried out, including toroidal geometry in 3D. Exemplary the fluid model by Scott [1997] and the gyro-kinetic treatment by Jenko [1998] are mentioned. A detailed study in full stellarator geometry was done by Kendl et al. [2003]. The latter also supply two important pieces of information: First, there is a universal form in the turbulent energy spectra of both stellarator and more simple tokamak configurations. The shoulder of spectral power is always located between $0.1\,\rho_\mathrm{s}^{-1}$ and $0.2\,\rho_\mathrm{s}^{-1}$. Second, the time averaged turbulent particle fluxes down the density gradient display only marginal variation in parallel direction. This means that a local measurement of the turbulent flow should be representative for the flux tube and in this way for the magnetic surface.

1.4 Transport equations

There are several ways to deduce the equation for the energy transport. Very concisely it is possible by utilising the first law of thermodynamics in differential notation

$$\frac{3}{2}\,n\,k_B\,\frac{d}{dt}T = -\,p\,\operatorname{div}\boldsymbol{v} - \operatorname{div}\boldsymbol{q}\quad. \tag{1.20}$$

As defined in equation (1.12) d/dt is the advective derivative. On the left hand side is the change of thermal energy and on the right hand side the work released by the pressure forces and the divergence of the heat flow $\boldsymbol{q}$. The equation must be set up for electrons and ions separately and the sum of both yields the total transport of energy. Indeed an additional term H is lacking and will be introduced in the following. This term refers to the existence of an external source or sink of energy. Its origin is either a heating source H_E, which was electron cyclotron resonance heating (ECRH) in the experiments under investigation, or it is a sink connected to a non-zero particle source. For example, if the latter stems from the ionisation of cold neutral particles with source strength S_n, then there is need for the total ionisation work W_{ion} per neutral particle, and the resulting electrons and ions must be brought to the thermal energy. Since ionisation is achieved by collisions predominantly and

the complementary recombination process somewhere at the plasma edge is usually radiative, W_{ion} cannot be recovered. Altogether the H term to be inserted on the right hand side of equation (1.20) reads

$$H = H_E + H_{ion} + H_n = H_E - W_{ion}S_n - k_B(T_i + ZT_e)\,S_n \ .$$

Energy transfers between electrons and ions and vice versa need not be evaluated since they will cancel in the sum equation. General plasma radiation is also not accounted for and must be subtracted from the heating term H_E. This is a valid approximation because the plasma is transparent for electromagnetic radiation over a wide range of wavelengths (except for the narrow-band electron and ion cyclotron resonances of course).

In parallel to the energy there is the equation of continuity for the particles:

$$\frac{\partial}{\partial t}n + \mathrm{div}(n\,\boldsymbol{v}) = S_n \ , \tag{1.21}$$

where S_n is the particle source due to the impact ionisation of neutrals. Equation (1.21), too, must be evaluated for both electrons and ions. Source strengths are inherently balanced according to $S_{e,\,n} = ZS_{i,\,n}$.

If the formula (1.21) is multiplied with the thermal energy $k_B T_e$ and $k_B T_i$, respectively, then both may be added to the equation of the total energy transport. Now the partial derivatives on the left hand side combine to the partial derivative of the thermal energy density and both $\boldsymbol{v}\cdot\mathrm{grad}$ terms from the advective derivatives combine with $\mathrm{div}(n\boldsymbol{v})$ to a single divergence. On the right hand side H_n cancels the introduced products of particle source times thermal energy. Observing $n_e = n_0 = Zn_i$ the total transport of energy becomes

$$\frac{\partial}{\partial t}\left(\frac{3}{2}\,n_0\,k_B\left(T_e + \frac{T_i}{Z}\right)\right) \ + \ \mathrm{div}\left(\frac{3}{2}\,n_0\,k_B\left(T_e + \frac{T_i}{Z}\right)\,\boldsymbol{v}\right) \ + \ \mathrm{div}(\boldsymbol{q})$$

$$= -(p_i + p_e)\,\mathrm{div}\,\boldsymbol{v} \ + \ H_E \ - \ W_{ion}\,S_n \ . \tag{1.22}$$

This formula can be found in the comprehensive review by Braginskii [1965]. In principle, the electron and ion pressures p_e and p_i in the first term on the right hand side of equation (1.22) can be expressed by density and the temperatures. When only the radial transport by $E \times B$ drifts is evaluated, however, the multiplication factor $\mathrm{div}\,\boldsymbol{v}_{(\perp)}$ is nearly zero (to be explained in section 1.4.2) and thus the whole term can be neglected.

The advantages of the formulation (1.22) become clear when the equation is averaged in time and integrated over the plasma volume. In a stationary situation the partial derivative on the left hand side will vanish and the divergence can be transformed according to the divergence theorem. On the right hand side the volume integral of the external heating H_E is just the readily available total power that is absorbed by the plasma.

An alternative way to derive the formula (1.22) is to start with the Boltzmann transport or kinetic equation (e.g. see Golant et al. [1980]) for the velocity distribution. Assuming a Maxwellian with superimposed drift $\boldsymbol{v}$ and integrating over velocity space yields the particle continuity, the momentum conservation and the energy equation by evaluating successive velocity moments of the distribution function. Finally electric field and some inertia terms are eliminated from the $v^2 = \boldsymbol{v} \cdot \boldsymbol{v}$ moment by making use of the lower order moments. The conduction $\boldsymbol{q}$ is only achieved if the actual velocity distribution deviates from a Maxwellian. The source and sink terms S_n and H are to model the right hand side collision term in the Boltzmann equation. It turns out that equation (1.22) is a good approximation to the full treatment, at least as long as v^2 is small compared to the thermal velocity (1.2). If $\boldsymbol{v}$ is dominated by the turbulent $E \times B$ velocity then this condition is fulfilled for the typical plasma conditions found in toroidal magnetic confinement devices.

1.4.1 The role of temperature fluctuations

It is customary to denote the product $n\boldsymbol{v}$ as the particle flux $\boldsymbol{\Gamma}$. The continuity equation (1.21) therefore connects a change of density with the divergence of the particle flux and the particle source. In an analogous manner the energy flux from the first divergence term of equation (1.22) is referred to as $\boldsymbol{Q}$ and consists of the thermal energy times the particle flux

$$\boldsymbol{Q} = \frac{3}{2} k_B \left(T_e + \frac{T_i}{Z} \right) \boldsymbol{\Gamma} \ . \tag{1.23}$$

This way energy is transported together with particles and $\boldsymbol{Q}$ is called the *convective* energy flux. The heat flux $\boldsymbol{q}$ is complementary: It is an energy flux with $\boldsymbol{\Gamma}_q = 0$ at the same time. Thus $\boldsymbol{q}$ is termed *conductive*.

Since equation (1.22) is to be applied to a strongly magnetised and turbulent plasma, the dynamic evolution of the quantities n, T and $\boldsymbol{v}$ shall be examined. Most notably the radial direction, i.e. the direction perpendicular to the magnetic field lines and antiparallel to the plasma pressure, is of interest in the transport analysis of a magnetic confinement. Given the plasma is quiescent and collisionless, density and temperature are constant on magnetic surfaces and shall be written $\bar{n}$ and $\bar{T}$. The Lorentz force inhibits any perpendicular exchange, consequently both radial velocity and radial heat flux are zero on average,

$$
\begin{aligned}
< \boldsymbol{v}_\perp >_{t_S} &= \lim_{t_S \to \infty} \frac{1}{2 t_S} \int_{-t_S}^{t_S} \boldsymbol{v}_\perp \, dt = \bar{\boldsymbol{v}} = 0 \ , \\
< \boldsymbol{q}_\perp >_{t_S} &= 0 \ .
\end{aligned}
\tag{1.24}
$$

Now the turbulence comes into play: Following the drift wave picture as it was introduced in section 1.3.1, the only transport mechanism with a radial component

is ambipolar $E \times B$ convection, so that $\boldsymbol{v} \cdot \mathbf{e}_r = \tilde{\boldsymbol{v}}_{E \times B} \cdot \mathbf{e}_r = \tilde{v}_r$.

The temporal average of this radial velocity vanishes, because the generating electric field is a fluctuation. Radial convection in a background gradient of density and temperature immediately leads to fluctuations of n and T as well:

$$n = \bar{n} + \tilde{n} \ , \qquad \text{with} \quad < n >_{t_S} = \bar{n} \ ,$$
$$T = \bar{T} + \tilde{T} \ , \qquad \text{with} \quad < T >_{t_S} = \bar{T} \ .$$

The averaged products of $\tilde{v}_r$ with n or T can yield non-zero values, since these three quantities not necessarily fluctuate in phase. An example for a phase-shifting process has already been presented in the context of drift wave instability (section 1.3.2). Hence the averaged turbulent radial fluxes of particles and energy are:

$$\bar{\Gamma}_r = \quad < n\tilde{v}_r >_{t_S} \qquad\qquad = \qquad < \tilde{n}\tilde{v}_r >_{t_S} \tag{1.25}$$

$$\bar{Q}_r = \frac{3}{2} k_B < nT\tilde{v}_r >_{t_S} \quad = \frac{3}{2} k_B \left(\bar{T} < \tilde{n}\tilde{v}_r >_{t_S} + < \tilde{T}\left(\bar{n} + \tilde{n}\right)\tilde{v}_r >_{t_S} \right)$$

$$\qquad\qquad = \quad \frac{3}{2} k_B \bar{T}\, \bar{\Gamma}_r + \frac{3}{2} \bar{n}\, k_B < \tilde{T}^* \tilde{v}_r >_{t_S} \ , \tag{1.26}$$

$$\text{where} \quad \tilde{T}^* = \left(1 + \frac{\tilde{n}}{\bar{n}} \right) \tilde{T} \ .$$

The turbulent energy flux $\bar{Q}_r$ is split into a part following the particle flux and a second part proportional to the quantity $\tilde{T}^*$, which is proportional to the fluctuations of temperature. Note, however, that $\tilde{T}^*$ is not a true fluctuation, since its time average possibly contains a non-zero cross-term between the density and the temperature fluctuation. The physical meaning of $\tilde{T}^*$ is, that it describes pressure fluctuations which are not caused by density fluctuations

$$\tilde{p} = \bar{T}\,\tilde{n} + \bar{n}\,\tilde{T}^* \ .$$

This formalism has also been used by Liewer et al. [1986].

If the terms *convective* and *conductive* are strictly reinterpreted as the parts of the energy flux connected and not connected, respectively, with a particle flux, then it is self-evident to redefine them in the turbulence:

$$\boldsymbol{\Gamma}^* = \quad \langle \tilde{n}_0\, \tilde{\boldsymbol{v}}_{E \times B} \rangle_{t_S} \tag{1.27}$$

$$\boldsymbol{Q}^* = \quad \frac{3}{2} k_B \left(\bar{T}_e + Z^{-1}\bar{T}_i \right) \boldsymbol{\Gamma}^* \tag{1.28}$$

$$\boldsymbol{q}^* = \frac{3}{2} k_B \bar{n}_0 \, \langle \left(\tilde{T}_e^{\;*} + Z^{-1}\tilde{T}_i^{\;*} \right) \tilde{\boldsymbol{v}}_{E \times B} \rangle_{t_S} \tag{1.29}$$

$$\text{where} \quad \tilde{T}_{e,i}^{\;*} = \left(1 + \frac{\tilde{n}_0}{\bar{n}_0} \right) \tilde{T}_{e,i} \quad \text{and} \quad n_0 = n_e = Zn_i \ , \quad < \tilde{n}_0 >_{t_S} = 0 \ .$$

This formulation is also favoured by Ross [1992].

1.4.2 Flux measurement at the plasma edge

In this section the continuity equation for the energy (1.22) ought to be refined in order to make it applicable to the interpretation of measurement results. A few words should be spent on $\operatorname{div}\tilde{\boldsymbol{v}}_{E\times B}$ in advance. The divergence of the turbulent drift velocity scales with the inverse major radius of the plasma R_0^{-1} (see chapter 14 in Scott [2000]), i.e. the curvature of magnetic field lines. There is indeed an alternative formulation of the continuity equation for the energy with a factor 5/2 in the first divergence term and $\boldsymbol{v}\cdot\operatorname{grad}p$ replacing $-p\operatorname{div}\boldsymbol{v}$. The $\operatorname{grad}p$ term, however, scales with the inverse of the small plasma radius. Observing that a stellarator has a large aspect ratio, the correction by $\boldsymbol{v}\cdot\operatorname{grad}p$ to the 5/2 formulation would be much larger than the correction by $p\operatorname{div}\boldsymbol{v}$ in the used form (1.22). The divergence of the turbulent radial velocity is neglected in good approximation. This point was not discussed in the early derivation by Liewer et al. [1986] and it has been the object of some dispute [Düchs 1989; Ross 1989].

Now the remaining terms should be averaged in time, so that the partial derivative $\partial/\partial t$ vanishes in a stationary plasma. Finally the equation is integrated over the toroidal volume from the center until the radial position r_{eff}. For this the plasma will be divided into three different zones:

- *Core.* The plasma heating power is localised here. There are no particle sources and the exchange of particles is neglected ($\boldsymbol{v}\sim 0$). Transport is neoclassic.

- *Edge.* Transport in this region is dominated by $E\times B$ turbulence. At the same time recycling neutrals are ionised here, thus there is a net (plasma) particle source S_n. Since the magnetic surfaces are intact, only the radial transport has to be taken into account, whereupon $\operatorname{div}\tilde{\boldsymbol{v}}_{E\times B}=0$. The energy sink is connected with the ionisation of neutrals $-W_{ion}\,S_n$.

- *Scrape-Off Layer (SOL).* Radial transport is again caused by turbulent $E\times B$ convection. The particle source S_n is diminished and replaced by an effective source S_{eff} which includes the plasma loss to the limiters in parallel direction. A similar loss term H_{eff} is applied to the energy equation, where possibly non-zero contributions $\operatorname{div}\boldsymbol{q}_\parallel$ and $\operatorname{div}\boldsymbol{v}_\parallel$ occur.

The three zones are drawn schematically in figure 1.11. Altogether it can be concluded that a measurement of the turbulent flux profile allows one to determine the effective source profiles.

$$\operatorname{div}(\,\Gamma_r^*\,\mathbf{e}_r\,) \;=\; S_{\mathrm{eff}} \;=\; S_n \;-\; \begin{cases} 0 & , \quad \text{edge} \\ \operatorname{div}\boldsymbol{\Gamma}_\parallel & , \quad \text{SOL} \end{cases}$$

$$\operatorname{div}(\,(Q_r^*+q_r^*)\,\mathbf{e}_r\,) = H_{\mathrm{eff}} = H_E \;-\; W_{ion}\,S_n \;-$$
$$-\begin{cases} 0 & , \quad \text{edge} \\ \operatorname{div}(\mathbf{Q}_\parallel+\mathbf{q}_\parallel)-(p_i+p_e)\operatorname{div}\mathbf{v}_\parallel & , \quad \text{SOL} \end{cases}$$
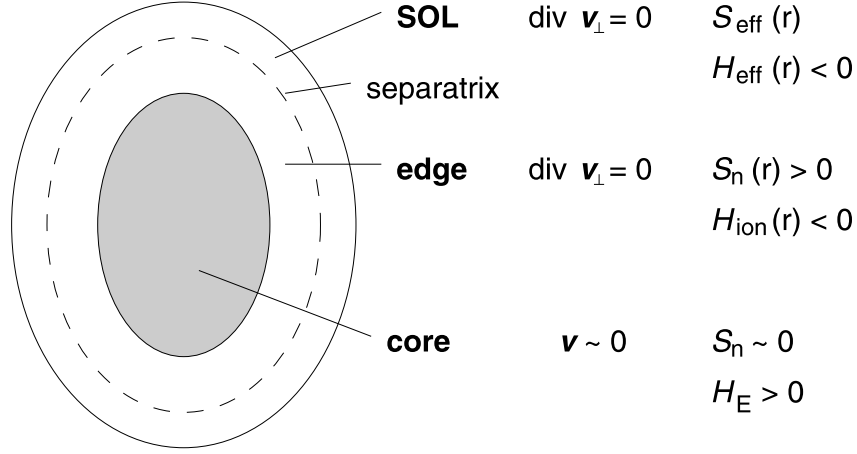
Figure 1.11: *Modelled arrangement of zones with different transport behaviour, visualised in the cross section of a magnetically confined plasma. Turbulence dominates the radial transport in both the edge and the scrape-off layer (SOL). The particle and energy source terms are modified in the SOL due to parallel losses.*

The divergence must be written in an appropriate coordinate system $\text{div} \approx \frac{1}{r} + \frac{\partial}{\partial r}$. Higher order corrections to this formula scale with the inverse of the major radius and are neglected with respect to the large aspect ratio of a stellarator. The divergence is the one of a cylindrical coordinate system.

If the measurement is located at the separatrix ($r_{\text{eff}} = r_{\text{sep}}$), then the total particle rate inside closed magnetic surfaces is obtained from the divergence theorem

$$\iiint_{r < r_{\text{sep}}} S_n \, dV = A(r_{\text{sep}}) \, \Gamma_r^*(r_{\text{sep}}) \,, \tag{1.30}$$

where $A(r_{\text{eff}})$ is the area of the magnetic surface with effective radius r_{eff}. For the energy this is similar:

$$\iiint_{r < r_{\text{sep}}} (H_E - W_{ion} S_n) \, dV = A(r_{\text{sep}}) \, (Q_r^*(r_{\text{sep}}) + q_r^*(r_{\text{sep}})) \,. \tag{1.31}$$

The volume integral over H_E on the left hand side is just the total heating power and the second addend is evaluated using (1.30). Finally, by comparing the measured flux through the separatrix to the plasma heating power in section 5.3 the question shall be answered, whether electrostatic $E \times B$ turbulence is able to explain the energy loss of a magnetised plasma.

Chapter 2

Experimental approach to turbulent transport

This chapter is titled an experimental approach although it contains also the theory that is needed to acquire and cope with fluctuation data. First some mathematical basics are introduced, then it is attempted to do a forecast of the expected fluctuation properties and finally the measuring method is selected.

2.1   Characterisation of turbulent fluctuations

Any statement about a quantity that undergoes turbulent fluctuations can barely be deduced from a single measurement, instead one must take into account spatial and temporal evolutions. Experimentally this is resolved by sampling, i.e. the fluctuating quantity A must be repeatedly measured at several locations. One should keep in mind, that the measurement result is provided on a discrete grid and that this is only an image of the underlying continuum.

$$A(t, y) \quad \rightarrow \quad A_{hi} \quad , \qquad h \quad \text{index of time sample,}$$
$$i \quad \text{channel index}$$
$$t = h \cdot dt$$
$$y = i \cdot dy$$

In this formulation the grid is regular, if dt and dy are constant and if h and i are integer numbers. The resolution that is defined by dt and dy must be fine enough with respect to the temporal and spatial scales of the variations in A. It is also essential to use a reasonable number of grid points, so that statistically significant amounts of data are available. The data can be reduced afterwards by the application of appropriate statistical methods, which are to be introduced in the following sections.

2.1.1 Probability density functions and derived quantities

If a fluctuating quantity is sampled, then the obtained values will differ for each measurement and the range of values can be described by a distribution function. The cumulative distribution function (CDF), also called the probability distribution function, returns for each value the probability that a single measurement will yield this particular or a lower value. If a limited number of samples is available, then an approximation [Theimer 1997] of the CDF is defined by

$$F(A) = \frac{1}{M\,N} \sum_{h=1}^{M} \sum_{i=1}^{N} H(\,A - A_{h\,i}\,) \;,$$

where $\quad H(x) \begin{cases} 0 & , \quad \text{if } \; x < 0 \\ 1 & , \quad \text{elsewhere} \end{cases}$ $\quad$ (Heaviside unit step) .

Starting from the CDF, the probability density function [1] (PDF) f is calculated by taking the first derivative

$$f(A) = \frac{d}{dA}\,F(A) \;, \quad \text{where} \quad \int_{-\infty}^{\infty} f(A)\,dA = 1 \quad \text{(normalisation condition)} \,.$$

Practically F and f are evaluated on a discrete grid in A, so that finite difference calculations can be applied. Often f is displayed in a histogram style. There are commercial packages available for the computer, e.g. IDL, developed by RSI [1997].

The expectation value $<A>$ is the mean value and can be deduced from f :

$$<A> = \int_{-\infty}^{\infty} A\,f(A)\,dA \approx \frac{1}{M}\sum_{h=1}^{M} A_h \;. \tag{2.1}$$

Here the spatial index i has been left out for simplicity. Note that the discrete approximation on the right hand side of equation (2.1), the so-called sample mean, usually converges rapidly towards $<A>$ with increasing M. A complementary formulation has also been used in the introduction, equation (1.24), section 1.4.1.

Once the mean value is determined, successive moments of the PDF can be evaluated. The expectation value of the rth moment is

$$m_r(A) = \int_{-\infty}^{\infty} (\,A - \,<A>\,)^r\,f(A)\,dA \;, \quad r \geq 2 \;.$$

Of particular interest is the variance m_2. When using measurements on a discrete and finite grid, an unbiased estimate for m_2 is only available via

$$m_2(A) \approx \frac{1}{M-1}\sum_{h=1}^{M} (\,A - \,<A>\,)^2 \;. \tag{2.2}$$

The form with M instead of $M-1$ in the denominator is called sample variance.

---

[1] sometimes simply called the probability or density function

A PDF supplies information about the spread of a fluctuating quantity but it cannot provide the relevant scales, since the chronology of the samples is not accounted for in the calculation. This gap can be bridged by the correlation function.

2.1.2   The correlation function

The correlation as a function of the lag is the covariance of two quantities, where the grid of the second one is shifted by the value of the lag. A discrete approximation to the correlation X_{AB} between two quantities A and B is in the time domain

$$X_{AB}(\Delta t) = \frac{1}{M} \sum_{h=1}^{M} (A_h - <A>)(B_{h+\Delta t/dt} - <B>) \; ,$$

where $\Delta t/dt := k$ must be an integer number. Thus X_{AB} is available on a discrete grid with spacing dt. The subtle distinction between unbiased and biased estimate has been dropped, which is a reasonable approximation whenever M is a large number. A more detailed background can be found in [Theimer 1997].

It is crucial that the sequence of individual samples is retained within each quantity. Note also that a convention has to be made about the treatment of the interval edges: For $k \neq 0$ the index range of B must not be exceeded. One possibility is to continuously shrink the sample range $(1 \ldots M)$ with increasing $|k|$ until all indices are within the available interval. Another possibility is to assume periodicity and to refill the overtraversed indices sequentially from the opposite end of the interval. This could speed up the computing time, because FFT [2] algorithms can be employed. The method is only a good approximation, however, if the correlation scales, i.e. the absolute value of Δt where the correlation value has dropped significantly, is small compared to the interval length $M \cdot dt$.

Now the correlation is to be extended into the spatial dimension. In various applications there are only a few spatial grid points, which are frequently called channels. Given a correlation length of the same order as the baseline that is spanned by the channels, the periodic continuation should be avoided. In the temporal dimension, however, the correlation time is easily exceeded by taking a large number of samples, so that the technique to use a temporal periodic continuation B^* of the signal B is a reasonable approximation. Hence, the spatio-temporal correlation function becomes

$$X_{AB}(\Delta t, \Delta y) \qquad \rightarrow \qquad X_{AB,\,kj}$$

$$= \frac{1}{N-|j|} \sum_{i=\max(1,\,1-j)}^{\min(N,\,N-j)} \frac{1}{M} \sum_{h=1}^{M} (A_{h\,i} - <A>)(B^*_{(h+k)\,(i+j)} - <B>)$$

$$\Delta t = k \cdot dt \; , \quad \Delta y = j \cdot dy \; , \quad \text{where} \quad j \in \{(-N+1) \ldots (N-1)\} \; . \qquad (2.3)$$

---
[2] Fast Fourier Transform

The first sum in equation (2.3), i.e. the sum over i, averages channel pairs with equal distance $|j|$. This procedure is justified, if the value of the correlation depends only on relative distances in space, in other words the region under investigation must be homogeneous. If in the measurement of plasma turbulence the driving mechanisms, i.e. the background gradients of density and temperature, are homogeneous along the probe array, and if the tips are carefully aligned within one magnetic surface, then this is a valid assumption. Averaging equivalent channel pairs effectively decreases noise.

Normalisation of the autocorrelation

The correlation function has been introduced using two different quantities. If both are identical, i.e. $B = A$ then $X_{AA}(\Delta t, 0)$ becomes a scaled autocorrelation function. At the point where the time lag is zero, the correlation value $X_{AA}(0,0)$ is equal to the sample variance. This is easily demonstrated by comparing equations (2.2) and (2.3), where for large M the distinction between $M - 1$ and M is neglected.

It is common to define the autocorrelation as $X_{AA, k0}$ normalised to the sample variance. In order to achieve this, any element is divided by $X_{AA, 00} \approx m_2(A)$. From this it follows that autocorrelation functions have got a central maximum with unity value. Towards large $|\Delta t|$ the envelope usually decays to zero. In the intermediate region negative values are possible, but they cannot go below -1.

One concluding remark about the visualisation of two-dimensional correlation functions: Throughout this work, contour plots are used. This technique is exemplified in appendix B.2.

2.1.3 Spectral analysis

In data analysis there are properties which can be investigated very conveniently in the spectral domain. The comparison between experimentally obtained and modelled fluctuation data, for instance, is preferably done in the wavenumber and frequency space. Since the correlation function has already been discussed, an important theorem should be introduced: The Cross-Correlation theorem and its special case for the autocorrelation, the so-called Wiener-Khinchin theorem. According to the former, the cross spectrum of two quantities A and B is equal to the Fourier transform of the cross-correlation [Weisstein 2005a]

$$C_{AB}(f, k) = \bar{\mathcal{F}}[A(t,y)] \, \mathcal{F}[B(t,y)] = \mathcal{F}[\, X_{AB}(\Delta t, \Delta y)\,]$$

$$= \iint\limits_{-\infty}^{\infty} X_{AB}(\Delta t, \Delta y) \, e^{-i\,(k\Delta y - 2\pi\,f\Delta t)} \, d(\Delta y)\, d(\Delta t) \ . \qquad (2.4)$$

Note that the spectrum $\mathcal{F}$ of a real signal is complex and hermitian :

$$\mathcal{F}(-f, -k) = \bar{\mathcal{F}}(f, k) \ ,$$

where $\bar{\mathcal{F}}$ is the complex conjugate. The backward transform is simply

$$X_{AB}(\Delta t, \Delta y) = \iint\limits_{-\infty}^{\infty} C_{AB}(f, k) \, e^{\, i\,(k\Delta y - 2\pi f \Delta t)} \, \frac{dk}{2\pi} \, df \ . \qquad (2.5)$$

The transformation (2.4), however, can only be approximated whenever it is applied to experimental data. Neither the infinite area in Δt and Δy , nor the continuum are accessible. Instead, fluctuating quantities are sampled and their time and space traces are truncated. After calculating X_{AB} with the help of equation (2.3), the discrete Fourier transform (see appendix A.2.2) can take over the transformation. But one must keep in mind two restrictions: aliasing and spectral leakage.

2.1.3.1 Insufficient sampling - aliasing

Data that contain fluctuations within a given bandwidth from 0 to $f_{\max}$ and $k_{\max}$ respectively, must be sampled at least with the Nyquist rates. In terms of grid spacing, this condition reads

$$dt \leq \frac{1}{2f_{\max}} \ , \quad dy \leq \frac{\pi}{k_{\max}} \ .$$

If there is spectral power above $f_{\max}$ or $k_{\max}$, then it will be mapped into the lower frequency (wavenumber) branch by the discrete transform. This effect is called aliasing. Existing power at low frequencies could not be distinguished thereof.

Aliasing must be suppressed before the acquisition. Since spectra of turbulent fluctuations usually decay towards high frequencies and wavenumbers, this can be achieved by refining the grid resolution. During data analysis one has a slight control of the success, if a monotonic and in the majority of cases even exponential spectral decay can be veryfied.

2.1.3.2 Truncation - spectral leakage

In a mathematical sense, truncation is corresponding to a multiplication of the infinite series with a rectangular window function. In Fourier space this is equivalent to the convolution of the true spectrum with the transform of the window function. Since the transform of any finite window function possesses so-called lobes on both sides of a central maximum, the spectral power of a truncated series, evaluated at a given frequency, will be composed from a broad spectral range. High power at low frequencies may leak through the lobes of the window's transform into distant spectral regions.

Truncation cannot be avoided, but the window function can be optimised in order to reduce the side-lobe level and thus minimise the spectral leakage. Generally a multiplication with the Hanning window w_H is a good choice [Brigham 1988]. In two dimensions the function reads

$$w_H(\Delta t, \Delta y) \;=\; \frac{1}{2} \;+\; \frac{1}{2}\cos\left(\pi\sqrt{\left(\frac{\Delta t}{\Delta t_H}\right)^2 + \left(\frac{\Delta y}{\Delta y_H}\right)^2}\right) \;, \tag{2.6}$$

$$\text{if}\quad \left(\tfrac{\Delta t}{\Delta t_H}\right)^2 + \left(\tfrac{\Delta y}{\Delta y_H}\right)^2 \le 1 \quad, \quad \text{elsewhere}\quad w_H(\Delta t, \Delta y) = 0 \;.$$

Note that using the Hanning window in combination with the correlation function is slightly different from the standard case, where w_H is applied to a series of samples. The correlation contains an amplitude product, therefore less power is attenuated by the window function. Only long range correlations are damped, that could otherwise generate power at high frequencies whenever the baseline in either direction of the $\Delta t - \Delta y$ domain is not an integer multiple of the correlation period. This can be understood by the property of the discrete Fourier transform to generate the spectrum of a dataset's periodic continuation.

Convenient widths for the window function Δt_H and Δy_H can be selected following these guidelines: If there is only a small number of channels N, then the largest available extent is to be used in spatial direction. Fine structures or steep slopes in the spectrum may nevertheless be smeared out, but the significance of these effects can only be estimated individually. Often it is worthwhile to test the resolvableness by a numerical sampling of a modelled and well-defined spectrum with N spatial grid points. In the temporal domain, where there is often an excess of samples available, a reasonable resolution of the order of several 100 bins should be chosen. Cast into formulas, the guidelines are

$$\Delta t_H \approx 100 \cdot dt \;, \qquad \Delta y_H = N \cdot dy \;.$$

Normally the temporal correlation can be evaluated with some $M \sim 10000$ samples. Hence, the application of a smaller Hanning window to the correlation function has actually the effect of smoothing the frequency spectrum: The real spectrum is folded with a broadened spectrum of the window function. Of course there are applications, where such procedure must be avoided, because fine structures of the spectrum would be smeared out, but in the investigation of turbulence with its inherently broad spectra, smoothing is rather an advantage for the visualisation.

2.1.3.3 Cross spectrum and the cross phase

The cross spectrum is obtained by transforming the cross-correlation X_{AB}, which has been shown in equation (2.4). There is also the valid picture to regard any transform $\mathcal{F}$ as a superposition of waves, see equations (2.4) and (2.5). Consequently, the complex spectrum contains amplitude and phase information. While for individual

signals the phases at different frequencies or wavenumbers depend on the absolute phase of the point, where the measurement started, this is different for the cross spectrum: The operation $\bar{\mathcal{F}}[A]\,\mathcal{F}[B]$ introduces for any frequency and wavenumber the difference of the absolute phases and the product of the amplitudes. The phase difference is called cross phase. If the cross spectrum is smoothed by a windowing technique as described in section 2.1.3.2, then the power will cancel out in spectral regions with random distributed phase differences and it will accumulate where the phase difference is stable.

To summarise, the cross spectrum between two quantities A and B can supply twofold information: First the spectral localisation of coherent power and second the spectrum of phase shift.

2.2   Experimental scales and resolution

Fluctuations have been measured in various plasma devices. In order to predict properties like the bandwidth in frequency and wavenumber space, one may review the measurements that have been carried out in similar machines. This has been done by Liewer [1985]:

- At the plasma edge, most of the spectral energy is in the region $k_\perp \rho_{\mathrm{s}} \leq 0.15$, which has been verified in the tokamaks Alcator A, PRETEXT, Caltech and TEXT. The symbol ρ_{s} denotes the dispersion scale and has been defined in equation (1.19).

- With respect to the localisation of fluctuation power in the frequency domain, there is the range $10\,\mathrm{kHz}$-$1\,\mathrm{MHz}$ in the Caltech tokamak and the range $10\,\mathrm{kHz}$-$500\,\mathrm{kHz}$ in the PRETEXT tokamak, where in both cases the power dominates in the region between $10\,\mathrm{kHz}$ and $50\,\mathrm{kHz}$.

Liewers conclusions could be confirmed in the W7-AS by separate measurements of the fluctuations of floating potential [Bleuel et al. 2002], density [Bruchhausen 2002; Holzhauer et al. 1996] and electron temperature [Bäumel 2002; Sattler et al. 1994]. With W7-AS edge electron temperatures of around $30\,\mathrm{eV}$, a main magnetic field strength around $2.5\,\mathrm{T}$, and hydrogen ions, the dispersion scale is $\rho_{\mathrm{s}} = 2.2 \cdot 10^{-4}\,\mathrm{m}$. Hence, the wavenumber perpendicular to the magnetic field $k_\perp$ at the estimated limit and the maximum grid size for adequate sampling are

$$k_{\mathrm{max}} = 6.7\,\mathrm{cm}^{-1}\ ,\qquad dy_{\mathrm{max}} = 4.7\,\mathrm{mm}\ .$$

Bandwidth in frequency and corresponding time grid at the Nyquist limit are

$$f_{\mathrm{max}} = 1\,\mathrm{MHz}\ ,\qquad dt_{\mathrm{max}} = 0.5\,\mu\mathrm{s}\ .$$

If absolute fluctuation amplitudes must be determined, only a few measuring systems are available. For instance beam emission spectroscopy [McCormick and AS-DEX Team 1985; Zoletnik et al. 1998] for density fluctuations and Heavy Ion Beam

Probes [Hallock et al. 1987] for density and potential fluctuations. A simultaneous measurement of potential, density and temperature in a magnetically confined plasma with the required resolution dt and dy, however, is yet only possible by Langmuir probes. Consequently, they are the measuring system that will be applied in the following experimental investigation.

The theory of Langmuir probes, which are also called electric probes, in plasmas is complex and will be outlined in the following sections. The main point concerning resolution should be anticipated: Spatial resolution is basically determined by the probe's extent. That could easily be made small enough to meet the requirement: a tip diameter of 0.9 mm is common. In order to measure wavenumbers perpendicular to the magnetic field, an aligned 15 tip array with tip spacing $dy = 2$ mm is utilised.

For the temporal resolution the argumentation is not so obvious. Actually, one electric characteristic is necessary in order to acquire one set of plasma quantities including density, electron temperature and electric potential. One electric characteristic can be provided by the current response to one sweep of the voltage. Since any period of a harmonic voltage contains two sweeps (the up and the down sweep), the rate of measured plasma quantities is two times the rate of the applied periodic voltage. With a design frequency of $f_{sweep} = 1$ MHz the time grid of plasma quantities is $dt = 0.5\,\mu$s.

The sweeping technique in the context of fluctuation measurements has been proposed earlier: Chen [1965] discussed the use of a pulsed voltage, which is applied to a Langmuir probe. On the toroidal gas discharge ZETA, Robinson and Rusbridge [1969] deduced plasma correlations from fluctuation levels that were measured with varying probe bias. Recent fast swept Langmuir probe measurements on fusion devices are reviewed in table 2.1.

measurement reported by	f_{sweep} [MHz]	# tips	comment
Liewer et al. [1986]	0.25	1	Caltech tokamak
Balbín et al. [1992]	0.3	1	TJ-1 tokamak
Giannone et al. [1994]	1	3	W7-AS
Pfeiffer et al. [1998]	2	4	W7-AS, $f_{sweep} = 3$ MHz tested
Boedo et al. [1999]	0.4	1	TEXTOR tokamak, harmonics technique
Meier et al. [2001]	0.25	2	TEXT-U tokamak, time domain triple-probe method

Table 2.1: *Fast swept Langmuir probe measurements on fusion devices. Due to technical improvements, the sweep frequency could gradually be increased. Note that the methods of Boedo and Meier are related approaches.*

2.3   Local variations of the turbulence

The Langmuir probe measurement will be local. Therefore a comment should be made on the question, whether there are toroidal and poloidal variations of the transport within one magnetic surface, or more general, whether the turbulence itself depends on the actual magnetic geometry. The topic has been addressed by several groups who work on the numerical simulation of plasma edge turbulence.

It is found, e.g. by [Scott 1997], that the radial transport depends strongly on the level of the magnetic shear $\hat{s}$, which specifies the variation of the rotational transform ι (equation 1.4) with the minor radius r :

$$\hat{s} = -\frac{r}{\iota}\,\frac{\partial \iota}{\partial r} \quad . \tag{2.7}$$

Since in a stellarator the inclination of magnetic field lines undergoes a local variation, ι must be replaced by the corresponding local quantity in equation (2.7) and thus $\hat{s}$ becomes also a local quantity. This effect was studied in detail by Kendl and Scott [2003]. They find the transport being nearly independent of localised peak values in $|\hat{s}|$ while keeping the averaged $|\hat{s}|$ constant along the extent of the simulation volume. Additionally, Kendl et al. [2003] studied the properties of the turbulence in a flux tube of the W7-X stellarator magnetic configuration. Their results display $\sim 15\%$ variation of the fluctuation amplitude along the line of the magnetic field within one field period. It will be assumed that the local variations in the W7-AS configuration are of the same order.

Until now the interchange instability, which is frequently called "ballooning" in the context of toroidal magnetic confinement, has been omitted. This mechanism would indeed introduce a strong inhomogeneity depending on the actual curvature of the magnetic field lines and, additionally, it would leave a different fingerprint in the cross phases of turbulent fluctuations. Lechte et al. [2002] did systematic simulations for the accessible parameter range of the TJ-K torsatron. They state that the signatures of ballooning, which they call MHD turbulence, are negligible compared to those from drift-wave turbulence. One point of their parameter space, namely $\hat{\nu} = 1$, $\hat{\beta} = 0.7$ comes close to the properties of the W7-AS edge plasma. But one has to keep in mind that the ratio between ρ_{s} and the machine size is large in the TJ-K, which is not the case in W7-AS. The dimensionless parameters are

$$\hat{\nu} = \frac{L_n}{t_{c,e}}\,\sqrt{\frac{m_i}{k_B T_e}} \qquad \text{and} \qquad \hat{\beta} = \frac{\mu_0\,n_0\,k_B\,T_e}{B^2}\,\left(\frac{R_0}{\iota\,L_n}\right)^2 \quad ,$$

where L_n is the gradient length of the electron density and $t_{c,e}$ the electron self-collision time. Using typical values from the boundary of the W7-AS, the parameters are

$$L_n = 2\,\text{cm} \ , \quad t_{c,e} = 0.8\,\mu\text{s} \ , \quad \hat{\nu}_{\mathrm{SOL}} \approx 0.5 \ , \quad \hat{\beta}_{\mathrm{SOL}} \approx 0.5 \ .$$

This result is taken as an indication, that the ballooning is of minor importance when discussing the W7-AS measurements.

If the detailed simulations by Zeiler et al. [1998] are considered then the picture is slightly different. The authors predict the main transport mechanism to be controlled by the parameters α_d and ϵ_n, which deviate from the above $\hat{\nu}$ and $\hat{\beta}$. In the W7-AS SOL, the parameters are $\alpha_d \approx 0.4$ and $\epsilon_n = 0.02$. According to Zeiler, this is closer to the area of resistive ballooning than to drift-wave turbulence, which the authors call "nonlinear instability". So far, the simulations have been carried out in the magnetic geometry of a tokamak only.

To summarise, poloidal and toroidal variations of plasma turbulence and transport were found in numerical simulations. The most detailed results in stellarator geometry [Kendl et al. 2003] predict small local deviations from the average of the order 15%. One should keep in mind, however, that this conclusion applies for the magnetic coordinates and does not affect the argumentation about flux expansion and the transport measured in the laboratory system. The latter will be discussed in section 3.1.1.

2.4   Measuring with Langmuir probes

Any Langmuir probe measurement is an invasive measurement. The probe must be immersed into the plasma, which results in a perturbation of the local equilibrium. Since plasma particles will recombine at the comparatively cold probe surface, the Langmuir probe acts as a particle sink. In order to work out the effect of this disturbance and infer the unperturbed plasma quantities from the measured characteristic, a detailed modelling must be exploited.

2.4.1   The plasma sheath

Macroscopically a plasma is quasi-neutral and positive and negative charges are balanced. The electrostatic potential within the bulk is defined by U_{plasma}. If a different electrostatic potential is introduced at some position, for instance with a biased probe, then it is screened from the bulk by the plasma itself. The extent of the screening, called the space charge or the sheath, is characterised by the Debye length [Chen 1974], which is a function of plasma density n_0 and temperature T

$$\lambda_D = \sqrt{\frac{\epsilon_0\, k_B T}{e^2 n_0}} \ .$$

(2.8)

Given that the temperature in the W7-AS edge plasma is equivalent to $30\,\mathrm{eV}$, and the plasma electron density is $n_0 = 5 \cdot 10^{18}\,\mathrm{m^{-3}}$, then $\lambda_D \approx 18\,\mu\mathrm{m}$. Typical probe dimensions are $\mathcal{o}(1\,\mathrm{mm})$, clearly larger than λ_D. This situation is called *thin sheath* [Chung et al. 1975].

The screening is obtained more precisely by solving the electrostatic Maxwell equation. Electrons with density n_0 and temperature T_e and several ion species k are distinguished. The ions have an independent ion temperature T_i, bulk densities

$n_{0,k}$ and charge numbers Z_k. Due to quasi-neutrality, the total electron charge equals the total ion charge in the unperturbed bulk.

$$\tau = \frac{T_e}{T_i} \ , \quad n_0 = \sum_k Z_k \, n_{0,k} \ .$$

Since $\boldsymbol{E} = - \operatorname{grad} U$ the Maxwell equation reads

$$\epsilon_0 \, \operatorname{div} \operatorname{grad} U = \ e \, (n_e - \sum Z_k n_k) \ , \qquad (2.9)$$

where $U = U_{plasma}$ is the zero-point of the potential scale. Assuming equilibrium within one species, the electrostatic potential energy can be included in the distribution function. This yields Maxwell-Boltzmann relations

$$n_e = n_0 \exp(\, e \, U \, / \, k_B \, T_e \,) \ , \quad n_k = n_{0,k} \exp(\, -e Z_k \, U \, / \, k_B \, T_i \,) \ .$$

If the potential energy is small compared to the kinetic energy, then it is sufficient to replace the exponential functions by first order Taylor series expansions. The approximated densities n_e and n_k are put into equation (2.9). Using quasi-neutrality the zero order terms cancel each other out. The remaining second order differential equation reveals the shielding length

$$\lambda_S = \sqrt{\frac{\epsilon_0 \, k_B T_e}{e^2 n_0 (1 + \tau Z_{eff})}} \ , \quad \text{with} \quad Z_{eff} = \frac{1}{n_0} \sum_k Z_k^2 \, n_{0,k} \ . \qquad (2.10)$$

Any spherically symmetric electrostatic potential U_0 at sphere radius r_0 has got a modified Coulomb potential of finite range in a plasma

$$U(r) = U_{plasma} \ + \ U_0 \, \frac{r_0}{r} \, \exp\left(-\frac{r}{\lambda_S}\right)$$

where r is the distance from the center of the sphere.

2.4.2 Interconnection between sheath and bulk plasma

Depending on the application the spatial evolution of electrostatic potential and charged particle densities near a sheath must be refined. Probes used for measuring fluctuations in a magnetised plasma are usually biased negative with respect to the bulk potential. Thus, the probe will repel electrons and collect ions. Close to the probe a monotonic increment of the electric field strength is expected. It has been shown by Bohm [1949] that a monotonic potential drop towards the probe is only possible, if the ions enter the sheath with a minimum critical velocity $v_{i,\,crit}$:

$$\frac{m_i \, v_{i,\,crit}^2}{2 \, Z} = \ - \, e \, U_{crit} \ \geq \ \frac{1}{2} \, k_B \, T_e \ , \qquad (2.11)$$

where $U_{crit}(< 0)$ is the electrostatic potential difference between the so-called *sheath edge*, which is the boundary between sheath and plasma, and the unperturbed plasma potential. Equation (2.11) is called *Bohm's criterion*. It was deduced for monoenergetic ions and it can be extended to a mixture of different ion species [Riemann 1991].

For an arbitrary distribution function f_i of single charged ions, evaluated at the sheath edge, a kinetic Bohm criterion was deduced by Harrison and Thompson [1959] and extended for a multicomponent plasma by Riemann [1995]. The generalised equations have this form:

$$\int_{-\infty}^{\infty} dv_i \, \frac{f_i(v_i)}{v_i^2} \; \leq \; \frac{m_i}{k_B \, Z \, T_e} \; ,$$

which is adapted from [Bissel and Johnson 1989] for arbitrary Z. Obviously, the precise shape of f_i is important, since a singularity may appear for small v_i. Note also that v_i is the component of the ion velocity parallel to the gradient of the electrostatic potential.

There is this serious consequence of the Bohm criterion: The picture of a shielded potential with a decay length λ_S, as defined in equation (2.10), is only valid when the local potential is already below U_{crit}:

$$U_{crit} = U_{plasma} - g \cdot \frac{k_B T_e}{2 \, e} \; .$$

Here g is a correction factor of the order $\mathcal{O}(1)$ that is attributed to the precise shape of the ion distribution function at the sheath edge. An additional interface, the *presheath*, is necessary to connect the sheath edge and the bulk plasma. Its extent is usually much larger than λ_S. The presheath will be discussed in section 2.4.4 after taking into account the effects of a magnetic field.

2.4.3   Basic considerations in a magnetic field

The magnetic field forces the particles to move on helical trajectories, whereupon the extent of the helix radius, i.e. the gyro radius, is the characteristic length scale. In the boundary plasma of the W7-AS with an average temperature of $30\,\text{eV}$, an unperturbed electron density of $n_0 = 5 \cdot 10^{18}\,\text{m}^{-3}$ and a local magnetic field strength of $2.3\,\text{T}$ the average gyro radii of electrons and hydrogen ions can be calculated from the equations (1.1) and (1.2) and amount to

$$\bar{r}_{L,\,e} = 7\,\mu\text{m} \; , \quad \bar{r}_{L,\,i} = 0.3\,\text{mm} \; .$$

There are three other scales which are important in probe theory: the mean free path, the probe radius and the Debye length. The latter has already been introduced, and for the W7-AS edge plasma with $\lambda_D \approx 18\,\mu\text{m}$ it is more than two times larger than the electron gyro radius, however small compared to all other lengths.

Probe size and mean free path

The ratio of the mean free path to the probe dimension is called the Knudsen number. If this number is large, then the electric probe is a so-called classical Langmuir probe [Chung et al. 1975]. The radius of a cylindrical probe r_p at the W7-AS and the mean free path λ_{mfp} are

$$r_p = 0.45 \, \text{mm} \; , \quad \lambda_{mfp} = 2.9 \, \text{m} \; ,$$

where λ_{mfp} is the product of the average thermal velocity $\sqrt{8 \, k_B T \, / \, \pi \, m}$ and the self-collision time t_c from appendix A.1.2, both evaluated in the W7-AS edge plasma. Note that λ_{mfp} is equal for electrons and ions, since the particle mass cancels out. Altogether the W7-AS edge plasma can be regarded as collisionless.

Effective collection area

Before the modifications to the probe current by the magnetic field are evaluated, the necessary assumptions are summarised: Keeping in mind that the probe is operated with strong negative bias relative to the plasma potential, it is regarded as a perfect absorber for all attracted ions, since they will recombine on the comparatively cold probe surface. Due to the small Debye length with respect to the ion gyro radius, the influence of the sheath on the ion current is neglected in good approximation.

In general, the electric current of a biased probe is reduced in a magnetic field. Particles can move freely only parallel to the field lines, so that the collection area is defined by the projection of the probe to the plane perpendicular to $\boldsymbol{B}$. For instance, the effective area for electrons ($\bar{r}_{L,\,e} \ll r_p$) of a cylindrical probe with its axis perpendicular to the field, is

$$A_\perp = 4 \, r_p \, l_p \; ,$$

where $2 \, r_p$ is the probe diameter, l_p is the cylinder length and the additional factor 2 comes from the two opposite exposed sides.

If the average gyro radius is not small compared to the probe dimensions, as it is the case for the ions, then the effective collection area is slightly modified. For cylindrical probes the transition from large to small gyro radii and its effect on the collection of charged particles were numerically studied by Laframboise and Rubinstein [1976]. They calculate currents in the adiabatic limit $\bar{r}_L \ll L_\varphi$, where L_φ is the characteristic scale length of the probe potential. This adiabatic limit is fulfilled for the electrons. For the ions in the presheath it is approximately valid from the bulk up to the sheath edge. Results for the effective collection area $A_{\perp \, \text{eff}}$, normalised to the case without magnetic field, are shown in table 2.2. The ratio decreases from 1 to $2/\pi$ with increasing ratio $r_p/\bar{r}_L$, i.e. with increasing magnetic field strength B. Towards small $\bar{r}_L$ it converges to the function $(1 + \bar{r}_L/r_p) \cdot 2/\pi$.

$r_p \, / \, \bar{r}_L$	0	0.1	0.2	0.5	1	2	5	10	∞
$A_{\perp \, \text{eff}} \, / \, 2\pi \, r_p \, l_p$	1	0.978	0.958	0.914	0.863	0.801	0.727	0.692	$2/\pi$

Table 2.2: *Current collection of a cylinder with radius r_p and length l_p ($\gg r_p$) for various magnetic field strengths ($\bar{r}_L \sim B^{-1}$). The alignment of the cylinder axis is perpendicular to the magnetic field vector. Taken from Laframboise and Rubinstein [1976].*

2.4.4 Model for the presheath

In section 2.4.2 it was pointed out, that the presheath is necessary in order to create a link between the sheath edge and the bulk plasma. Emmert et al. [1980] proposed a kinetic model that assumes a particle source in the presheath and solved the equations for the evolution of the plasma potential Φ analytically. This model includes warm ions, neglects collisions and evaluates the dimension parallel to B only. The characteristic of the potential is shown in figure 2.1. Of particular importance is the fact, that regions of arbitrary length can be inserted into the characteristic at any x, if they contain neither source nor a change of the potential. Thus the origin ($x = 0$) represents the unperturbed bulk plasma.

The distribution function of the particle source is chosen in a way, that the ion distribution function is Maxwellian for the case of zero gradient of the electrostatic potential in the plasma. According to Bissel and Johnson [1989], Emmert's ion source is

$$S(x, v_x) \quad \sim \quad v_x(x) \, \exp\left(-\frac{v_x(x)^2}{v_{th}^2} \right) \, , \tag{2.12}$$

$$v_x(x) \quad = \quad \sqrt{\frac{2}{m}\left(E_\parallel - Ze\,\Phi(x) \right)} \quad , \tag{2.13}$$

and replenishes those particles that are lost to the wall or probe. $E_\parallel$ is the kinetic energy of the ions parallel to the lines of the magnetic field, before they are born in the presheath. Electrons are assumed to follow a Maxwell-Boltzmann distribution. When applied to a probe measurement, these assumptions comply with a situation, where the perpendicular transport, e.g. by turbulent fluctuations, balances the wall loss by continuously refilling the velocity space.

The Bohm criterion is fulfilled in the Emmert model [Bissel 1987]. There is, however, one pecularity in the choice of the source function: The faster ions are refilled more rapidly. In the limit of high ion temperatures, i.e. $\tau = T_e \, / \, T_i \; \rightarrow \; 0 \,$, this would lead to an ion outflow of twice the Maxwellian flow into one half space [Lipschultz et al. 1986]. This case, however, is not considered to be a serious restriction for the probe data evaluation, since $T_e \sim T_i$ in the boundary of W7-AS.
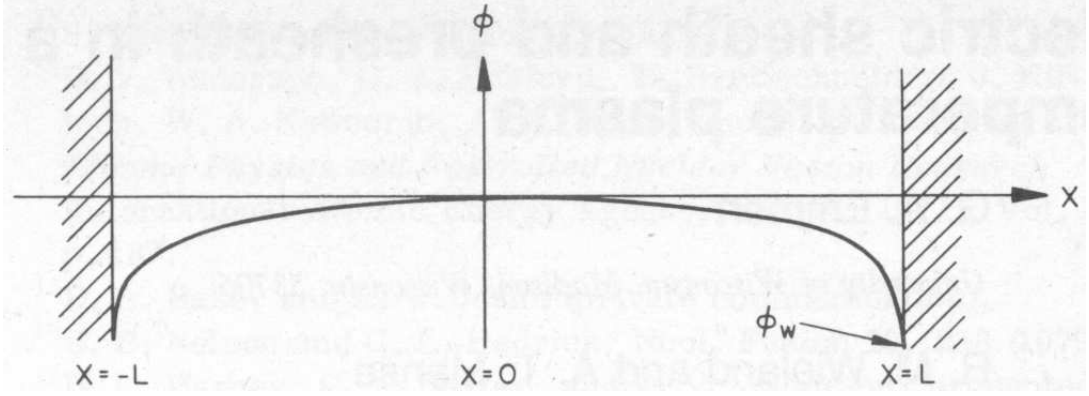
Figure 2.1: *Shape of the potential Φ in a plasma bounded by floating walls at $x = \pm L$ according to the collisionless model by Emmert et al. [1980] with a uniform source along x.*

Following Emmert, several equations characterise the physics in the presheath. Firstly, the balance of ion and electron current for a floating wall or probe,

$$Z \int_x dx \int_{v_x} dv_x \, S(x, v_x) = \frac{1}{4} \, n_0 \, (1 - \gamma_e) \, \sqrt{\frac{8 \, k_B T_e}{\pi \, m_e}} \, \exp \left(\frac{e \, \Phi_W}{k_B T_e} \right) . \tag{2.14}$$

Here Z is the ion charge, γ_e is the coefficient for the emission of secondary electrons (see below), n_0 is the unperturbed electron density at $x = 0$, and Φ_W is the floating potential.

Secondly, the normalised overall voltage drop ψ within the presheath up to the sheath edge is defined by a transcendental equation,

$$\frac{2}{\sqrt{\pi \tau Z}} \, \hat{D}(\sqrt{\psi}) \, \exp(-\psi \tau Z) \; = \; 1 - \mathrm{erf} \left(\sqrt{\psi \tau Z} \right) . \tag{2.15}$$

In this formula $\hat{D}(y) = \exp(-y^2) \int_0^y \exp(t^2) \, dt$ is the Dawson integral (see Rybicki [1989] for the computation), the symbol $\mathrm{erf}(y)$ denotes the error function, τ is the ratio of electron temperature versus ion temperature, and $\psi = - e \, \Phi_1 / k_B T_e$, where Φ_1 is the potential at the sheath edge with respect to the potential of the unperturbed plasma. A particular important fact is, that the total presheath potential drop does not depend on spatial variations in the particle source $S(x, v_x)$.

Finally, the ionic charge flux as a function of the density $n_0(x = 0)$ and the floating potential $\Phi_W = -(U_{plasma} - U_{float})$ can be evaluated:

$$j_{i, \, sat} \;\; = \;\; e \, n_0 \, \frac{\sqrt{8} \, \hat{D}(\sqrt{\psi}) \, (1 + \frac{1}{\tau Z})}{\pi} \, \sqrt{\frac{Z \, k_B T_e}{m_i}} \;\; , \tag{2.16}$$

$$\Phi_W \;\; = \;\; - \frac{k_B T_e}{e} \, \ln \left(\frac{(1 - \gamma_e)}{4 \, \hat{D}(\sqrt{\psi}) \, (1 + \frac{1}{\tau Z})} \, \sqrt{\frac{\pi \, m_i}{Z \, m_e}} \right) . \tag{2.17}$$

The coefficient for the emission of secondary electrons γ_e should be commented. This coefficient enters the evaluation of the correct plasma potential U_{plasma} from the measured U_{float} via equation (2.17). Secondary electron emission depends on the material of the probe tip, additionally on the condition of the surface and on the angle of incidence of the incoming, i.e. primary electrons. For fusion related materials a detailed study was done by Pedgley et al. [1992]. If the wall or probe is made of pure graphite, and if the primary electrons have an energy corresponding to a plasma temperature of 30 eV, Pedgley et al supply a value $\gamma_e = 0.4$ at normal incidence. The number increases considerably with the amount of implanted hydrogen ions and with the angle. Since implantation cannot be excluded during operation in a hydrogen plasma and since the angle of incidence varies over the surface of a perpendicular cylindrical probe, the values 0.4, 0.5 and 0.6 will be used for data evaluation and the impact on the results is to be discussed.

The detailed Emmert model and its subtle but indeed strictly arithmetic dependencies are often neglected in favour of the more convenient probe evaluation following Stangeby [1986]. If the ion temperature is comparable to the electron temperature, as it is the case in the boundary of a fusion experiment, then the model by Stangeby displays significant deviations. A quantitative comparison is carried out in appendix B.1. In the following, Emmert will be used for probe data evaluation, and Stangeby, whenever only the order of a quantity's magnitude is to be estimated.

2.4.5   Length of the presheath

To round off the treatment of the presheath, its spatial extent along the lines of the magnetic field should be estimated. The resulting length is frequently called collection length L. Basically the parallel particle flux absorbed by the probe is balanced by a perpendicular transport into the presheath. If the mechanism underlying the perpendicular transport is a diffusion, then the collection length can be estimated with

$$L \;=\; f_{\mathrm{geo}} \, \frac{c_s \, d_p^2}{D_\perp^{\mathrm{eff}}} \qquad [\text{Stangeby 1986}]\,, \tag{2.18}$$

where c_s is the sound velocity (appendix B.1), d_p is a characteristic length of the probe, $D_\perp^{\mathrm{eff}}$ is an effective diffusion coefficient, and f_{geo} a geometrical factor. For a quadratic probe with side length d_p Stangeby supplies $f_{\mathrm{geo}} = 1/8$. Note that it is a simplification to use $D_\perp^{\mathrm{eff}}$. Probably the perpendicular transport is caused by turbulence, i.e. anomalous and thus not diffusive at all.

Using numerical values of a hydrogen plasma at the boundary of the W7-AS ($T = 30\,\mathrm{eV}$) the sound velocity is $8 \cdot 10^4\,\mathrm{m\,s^{-1}}$, the diffusion coefficient is of the order $1\,\mathrm{m^2\,s^{-1}}$, and with a probe diameter of $1\,\mathrm{mm}$ the collection length becomes

$$L = 8\,\mathrm{cm} \quad (f_{\mathrm{geo}} = 1) \;.$$

This means even the transit time of the ions at c_s is only $1\,\mu s$, smaller than typical lifetimes of the fluctuations.

Since the probe tips cannot be inserted into the plasma without a solid mounting, called the probe head in the following, it has been proposed [Stangeby 1986] to use the diameter of the probe head instead of the tip, in order to define the scale length of the plasma disturbance. The probe head at the W7-AS has a diameter of 5 cm, which would enlarge the collection length up to the order of 100 m depending on f_{geo}. This exceeds typical connection lengths in the scrape-off layer and would, therefore, basically change the properties of the transport in the edge plasma.

What is neglected in this estimation of the perturbation length is the poloidal convection of the plasma due to the background radial electric field. The convection continuously shuffles unperturbed plasma into the presheath and thus contributes to the replenishment of the probe shadow. Particularly farther away from the probe, where the density gradients from the surroundings into the presheath are flat, convection becomes important. Considering a cylindrical probe (length l_p, radius r_p), aligned perpendicular to the magnetic field, and a background poloidal flow with a realistic velocity of $v_\theta \approx 10^3 \, \text{m s}^{-1}$, the balance of poloidal and absorbed flow yields for one side

$$2 \, r_p \, l_p \cdot \frac{n_0}{2} \, c_s = L \, l_p \, n_0 \, v_\theta \qquad \rightarrow \qquad L = \frac{c_s}{v_\theta} \, r_p \ .$$

Although this is a very strict simplification, for it disregards the processes that could change the direction of the poloidal flow towards the probe and thus introduce a flux divergence, it nevertheless suggests, that the presheath length grows only linear with the probe head radius r_p. Using numerical values from the W7-AS, the result for the disturbance length of the probe head is $L_{\text{head}} = 2 \, \text{m}$, clearly shorter than typical connection lengths, which are of the order $\mathcal{o}(10 \, \text{m})$.

The conclusions concerning the presheath and the disturbance length of a probe in the W7-AS edge plasma are: The effect of the probe tip is negligible, since its presheath length is small compared to the connection legth. Tip presheath transit times of any particle species are small compared to the lifetime of fluctuations. In a situation with purely diffusive replenishment of the presheath, the disturbance by the probe head can be significant and may establish a radial transport, which is not simply related to the unperturbed case [LaBombard 2002]. The corresponding models, however, neglect the experimentally observed poloidal convection. That can reduce the calculated disturbance length to values below the connection length. Hence the fluctuation induced transport measured by the probe should still be dominated by the unperturbed region beyond the presheath. Particularly the measurement of the electron temperature is affected least, because the highly mobile electrons cover distances much longer than the presheath length. A proper kinetic modelling must be two-dimensional and include both the parallel and the perpendicular direction. This is, however, beyond the scope of this thesis.

2.5 Fluctuation measurements with probes

Summing up the results of the previous sections, the current voltage characteristic of an electric probe in a magnetised plasma, based on the given assumptions, obeys

$$I(U) = -I_{sat} \left(1 - \exp \left(\frac{e}{k_B T_e} (U - U_{float}) \right) \right) \ , \quad |U - U_{float}| \lesssim k_B T_e / e \ .$$
$$(2.19)$$

In this formula, the ion current

$$I_{sat} = A_{\perp \text{ eff}} \cdot j_{i, sat}$$

is constant, since the probe is kept at large negative voltages with respect to the plasma potential, i.e. below or close to the floating potential U_{float}. This means that variations of U are compensated by the Debye sheath alone. Changes of the measured current I with the probe voltage U are only an effect of the electrons, being repelled to a greater or lesser extent. The derivative at $U = U_{float}$ is simply

$$\left. \frac{dI}{dU} \right|_{U=U_{float}} = \frac{e \, I_{sat}}{k_B T_e} \ . \tag{2.20}$$

Hence, the small signal impedance of a Langmuir probe at floating potential is $k_B T_e / e \, I_{sat}$. From a recorded $I - U$ characteristic, the unperturbed electron density n_0 can be calculated by using I_{sat} and T_e, and the plasma potential U_{plasma} by using U_{float} and T_e. Thereby an assumption on the ion temperature is necessary.

If the plasma parameters I_{sat}, U_{float}, and T_e are fluctuating due to turbulence, then the time to take one characteristic should be sufficiently short, i.e. the frequency of the voltage sweeps should be higher than the bandwidth of the fluctuations. This poses the question, whether the bandwidth of the actively applied U must be limited in order to retain the validity of equation (2.19).

2.5.1 Limiting frequency for the Debye sheath

An estimate of parasitic high frequency currents is possible by modelling the sheath as a plate capacitor with an area equal to the current collection area $A_{\perp \text{ eff}}$ and a plate distance equal to the shielding length λ_S (equation 2.10). Given the probe is operated in the vicinity of the floating potential, the critical angular frequency, where the ohmic current balances the amplitude of the capacitive current, is the inverse of the RC time constant. In this case C is equal to the sheath capacitance and R is equal to the real sheath impedance from equation (2.20).

$$\tau_{RC, \text{Debye}} = \frac{\epsilon_0 \, A_{\perp \text{ eff}}}{\lambda_S} \frac{k_B T_e}{e \, I_{sat}}$$

Using the Stangeby model, one obtains with a single ion species and $T_e = T_i$

$$\omega_{\text{Debye}} = \tau_{RC,\,\text{Debye}}^{-1} = \sqrt{\frac{e^2 \, n_0}{4 \, \epsilon_0 \, m_i}} = \frac{\omega_{p,\,i}}{2 \, \sqrt{Z}} \ . \tag{2.21}$$

The ion plasma frequency $\omega_{p,\,i}$ is $\mathcal{O}(3\,\text{GHz})$ in the boundary of the W7-AS. Thus, for hydrogen and sweep frequencies $\mathcal{O}(1\,\text{MHz})$ the sheath is stationary ($\omega \ll \omega_{p,\,i}$) and there is no objection against equation (2.19) from that side.

Non-saturation and hysteresis of flush mounted probes

With plane flush mounted probes and small angles of inclination between the probe surface and the lines of the magnetic field, the area for ion collection depends significantly on the probe voltage [Weinlich 1995]. This is an effect of the so-called magnetic presheath. Additionally, capacitive hysteresis loops at voltage sweep frequencies far below $\omega_{p,\,i}$ were reported in this situation by Verplancke [1996]. The complications can be avoided, if the angle of incidence of the magnetic field to the probe surface is sufficiently large. This is the case for most of the effective area of cylindrical probes aligned perpendicular to $\boldsymbol{B}$.

2.5.2 Dynamics of the voltage drop in the presheath

The electric current drawn by the probe will predominantly flow in parallel with the lines of the magnetic field. If the potential of this particular field line varies with a high frequency relative to the surrounding plasma, then according to equation (1.11) ion polarisation currents flow in perpendicular direction. Such thing could happen in the far-ranging presheath of a probe. Nedospasov and Uzdensky [1994] proposed an appropriate model for measurements with swept probes and it was shown, that the polarisation current acts as a perpendicular capacitance. Written as a capacity per unit length the formula in cylindrical geometry is

$$c_{pol} = \frac{C}{L} = \frac{2\pi \, n_0 \, m_i}{\ln \frac{r_a}{r_i} \, Z \, B^2} \ , \tag{2.22}$$

which is the one of a long cylindric capacitor with inner and outer diameters r_i and r_a, respectively, and $n_0 m_i / Z B^2$ replacing the electric constant $\epsilon_r \epsilon_0$. Note that the electron density n_0 over Z is the ion density. Approximating the natural logarithm with 1, the expression (2.22) was used by Geier [1997] in order to model Langmuir probe characteristics in the edge plasma of the W7-AS. There, with hydrogen ions the capacitive coating has an electric constant of $1.3 \cdot 10^{-9}\,\text{As}\,\text{V}^{-1}\text{m}^{-1}$, which is more than two orders of magnitude higher than in the vacuum case.

Geier could demonstrate experimentally, that using c_{pol} only is not sufficient to characterise high frequency phenomena with large electron currents. Therefore the model was extended by longitudinal inductance and resistivity, and a perpendicular

conductivity [Niedermeyer et al. 1996]. Altogether this led to reasonable agreement with the experiment. The inductance is simply the vacuum value [Verplancke 1996], i.e. in cylindrical geometry

$$l_{vac} = \frac{L_{ind}}{L} = \frac{\mu_0}{2\pi} \ln \frac{r_a}{r_i} \ .$$ (2.23)

In order to calculate the parallel resistance per unit length $r_\parallel$, there is the Spitzer value for the resistivity η (see appendix A.1.3), so that $r_\parallel = \eta / \pi r_i^2$. The perpendicular conductance $g_\perp$, however, is not yet fully understood. Theoretical predictions by Spitzer yield $g_\perp^{-1} \sim \eta_\perp \approx 3.3\,\eta$ [Chen 1974], whereas experimental values are by far too large [Weinlich 1995]. Utilising an effective perpendicular resistivity $\eta_\perp^{\mathrm{eff}}$ the conductance per unit length becomes

$$g_\perp = \frac{G}{L} = \frac{2\pi}{\eta_\perp^{\mathrm{eff}} \ln \frac{r_a}{r_i}} \ .$$ (2.24)

Weinlich [1995] estimated the ratio $\eta_\perp^{\mathrm{eff}} / \eta$ in the scrape-off layer of the ASDEX Upgrade Tokamak from both a model with ion-neutral friction and from the anomalous Bohm diffusion. His results were $8 \cdot 10^6$ and $3 \cdot 10^7$, respectively.

Summing up, the complex high frequency impedance of the presheath W is the one of a coaxial transmission line with losses

$$W = \sqrt{\frac{r_\parallel + i\omega\,l_{vac}}{g_\perp + i\omega\,c_{pol}}} \ .$$ (2.25)

Since the phase velocity in such a line $(l_{vac}\,c_{pol})^{-0.5}$ is equal to the Alfvén velocity, the model is referred to as the Alfvén wave cable model. If one wants to include W when evaluating probe characteristics, particular attention must be paid to the fact, that in a fluctuating environment neither density nor temperature are constant and, consequently, the straightforward application of equation (2.25) with constant coefficients $r_\parallel$ and c_{pol} in Fourier space is not possible. Furthermore the anomalous and averaged value of $g_\perp$ should be called into question and it is worthwhile to check, whether a strongly fluctuating c_{pol} (density fluctuations) can take over this contribution.

The impedance of the return sheath will be considered briefly. It is part of the return circuit, but because of its larger area, it won't contribute significantly to the probe characteristic unless the probe draws an electron current [Niedermeyer et al. 1996]. Only in the latter case there is a low specific probe impedance and a high specific return sheath impedance. The Alfvén wave cable model and the return circuit are displayed schematically in figure 2.2.
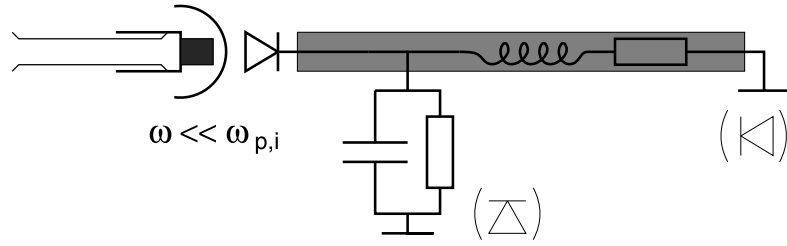
Figure 2.2: *Equivalent circuit for the presheath (shaded region). It is connected to the probe tip on the left via the Debye sheath, modelled as a diode with a real impedance ($\omega \ll \omega_{p,i}$). The capacitance, inductance, and conductances shown are intended to be infinitesimal and their arrangement must be repeated several times along the extent of the presheath in order to provide a realistic numerical modelling. Contacts to the wall by additional sheaths (slim diodes) can be neglected, if the probe does not draw significant electron current.*

Chapter 3

Experimental and technical concepts

Several technical challenges have to be overcome in order to set up a Langmuir probe diagnostic with the specified resolution at the Wendelstein 7-AS. In particular the electronic transmission and acquisition system turned out as the most complex part. This will now be discussed after giving a short introduction into the experimental boundary conditions and the magnetic configuration.

3.1 The Wendelstein 7-AS

The Wendelstein 7-AS is a stellarator with a five-fold symmetry (section 1.1.3). Its main components are a toroidally closed vacuum chamber, three coil systems, and various auxiliary devices for plasma heating and plasma diagnostics to modify and detect, respectively, the properties of the plasma.

The independent coil systems (see figure 1.3) can be used to produce various configurations of the magnetic field by superposition. There is a modular system, a planar one, and one to produce a vertical field. Hence, to characterise the magnetic configuration three parameters are necessary. Naturally it is the three currents that flow in the different systems, but for convenience the derived parameters t, B_0 and B_z are frequently used, where t is the edge rotational transform, B_0 is main magnetic field strength on the torus axis, and B_z is the strength of the vertical magnetic field.

In addition to the magnetic configuration, working gas, plasma density, heating power, and the heating method have to be specified. Hydrogen is used in the case of the probe measurements, released as neutral gas from a valve into the chamber. During plasma operation the valve is controlled by a real-time measurement of the plasma density in a feedback loop in order to hold the density stationary. Electron cyclotron resonance heating (ECRH) with $\sim 0.5\,\mathrm{MW}$ is utilised as a power source. This heating scheme produces plasmas which are highly reproducible and stationary.

3.1.1 Details on the magnetic configuration

When finally the measurements of turbulent fluxes are compared to the total turnover of particles and energy, the magnetic geometry at the position of the measurement plays a role. There are tools available to investigate this geometry, mainly the TRANS code [Sardei and Richter-Glötzl 1988] to map the coordinates of the probe tips to magnetic surfaces, and the GOURDON code [Gourdon and Lotz 1970] to do a field line tracing. The GOURDON code is also useful to calculate intersection points with in-vessel components and thus determine so-called connection lengths along the lines of the magnetic field.

Magnetic surface area of the W7-AS

The concept of an effective radius r_{eff} has already been introduced in equation (1.6). The average cross section is characterised by $A = \pi r_{\text{eff}}^2$ and the volume of an equivalent circular torus is in good approximation $V = 2\pi^2 R_0 \, r_{\text{eff}}^2$, where the major radius R_0 of W7-AS is 2 m.

For the surface area the evaluation is more difficult. If a torus with an elliptical cross section is considered, then its volume is $V_\kappa = 2\pi^2 R_0 \, a^2 \kappa$, where κ is the elongation b/a, and a and b are the semiminor and semimajor axis of the ellipse, respectively. Calculating the surface area A_κ by multiplying the ellipse perimeter [1] U_κ with the circumference along the torus major axis yields

$$A_\kappa = 2\pi^2 R_0 \, a \, (1 + \kappa) \cdot f(\kappa) \ .$$

If the elongation is not too large, the correction $f(\kappa)$ is of the order one:

$$\kappa = 2 \quad \rightarrow \quad f = 1.03 \quad \text{(precision is at least 1\%)}.$$

The average elongation in the W7-AS is $\kappa \approx 2$ [Geiger et al. 2004]. From the comparison of V and V_κ the average semiminor axis $a = \kappa^{-0.5} \, r_{\text{eff}}$ can be deduced. Hence, the area of the last closed magnetic surface with $r_{\text{eff}} = r_{\text{sep}} \approx 17.5 \, \text{cm}$ is

$$A_\kappa(r_{\text{sep}}) = 15.1 \, \text{m}^2 \ .$$

Importance of the local flux expansion

There is experimental evidence, that both fluctuation amplitude and phase are constant and far extended along the magnetic field lines for connection lengths of several meters [Bleuel 1998]. The local magnetic geometry determines the transport relevant poloidal electric field and thereby the magnitude of the fluxes that are measured in the laboratory system. In particular, the measured fluxes are proportional to the

---

[1] $\quad U_\kappa = \pi a \, (1 + \kappa) \cdot f(\kappa) \ , \quad f(\kappa) = 1 + \frac{1}{4} \left(\frac{\kappa-1}{\kappa+1} \right)^2 + \frac{1}{64} \left(\frac{\kappa-1}{\kappa+1} \right)^4 + \mathcal{O}\left(\left(\frac{\kappa-1}{\kappa+1} \right)^6 \right)$

[Weisstein 2005b]
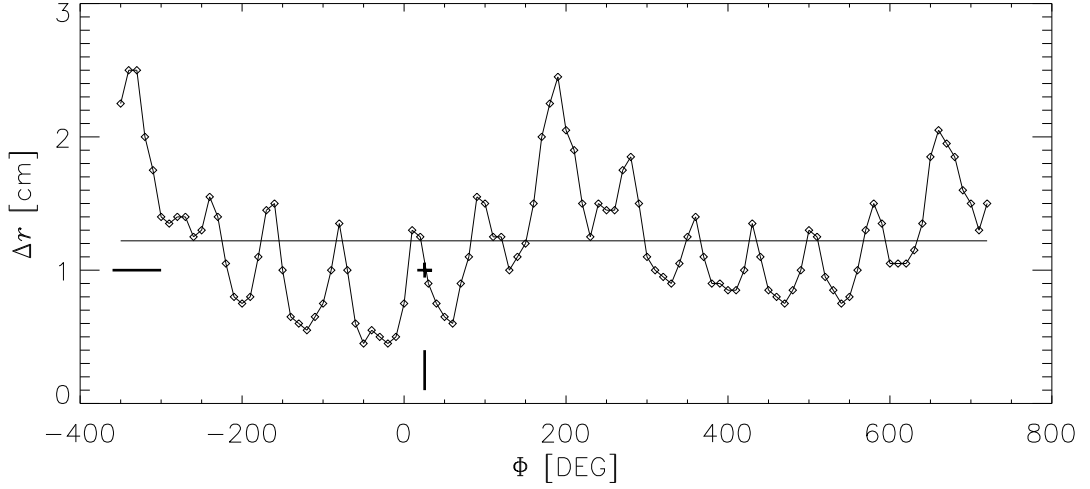
Figure 3.1: *Radial separation of two magnetic field lines versus toroidal angle Φ in the edge (r_{eff}=17.5 cm) of W7-AS according to field line tracing calculations at $t = 0.3497$, $B_0 = 2.553\,\mathrm{T}$ and $B_z = 10.13\,\mathrm{mT}$. Individual values are plotted with small diamonds as a function of the toroidal angle. The horizontal line denotes the average. At the probe position ($25.4°$, starting point of the calculation, indicated by the solid cross) the separation is 1 cm.*

actual distance between adjacent magnetic field lines in radial direction [Endler 1999].

Exemplarily two adjacent field lines should now be considered. Their spacing depends on both the poloidal (θ) and the toroidal (Φ) coordinate in the W7-AS. The two field lines are selected such, that they both intersect the reciprocation axis of the probe, but with a radial distance of 1 cm. Since the rotational transform t is close to 1/3 in the magnetic configuration of the measurement, the lines have been traced three times along the toroidal circumference (in total 38 m), which corresponds to a poloidal rotation of $\theta = 360°$. Every $\Delta\Phi = 10°$ the magnetic surface cross section and the field line position were overplotted and the radial distance was evaluated geometrically. In figure 3.1 the results are shown. Following considerations from above, the ratio between the spacing at the probe position and the average radial spacing should be equal to the ratio between the flux measured by the probe and the average flux. The average fluxes $\mathbf{\Gamma}^*$, $\mathbf{Q}^*$, and $\mathbf{q}^*$ (equations 1.27-1.29) are increased by a factor of 1.22 above the local fluxes at the probe position. The relative error of this value deduced from the standard deviation is 4%.

3.2 The probe diagnostic

Since the plasma performance of the W7-AS depends on the quality of the vacuum in the main chamber and on the condition of the walls, the vessel is usually kept closed and evacuated. If a Langmuir probe measurement system is to be installed, it must

be connected vacuum tight to the outboard side of a gate valve that terminates a port of the main vessel. After several weeks of pumping, when vacuum pressures are comparable on both sides of the valve, the shutter can be opened and the probe is advanced into the port by a remotely controlled manipulating system. Schematically this is displayed in figure 3.2.
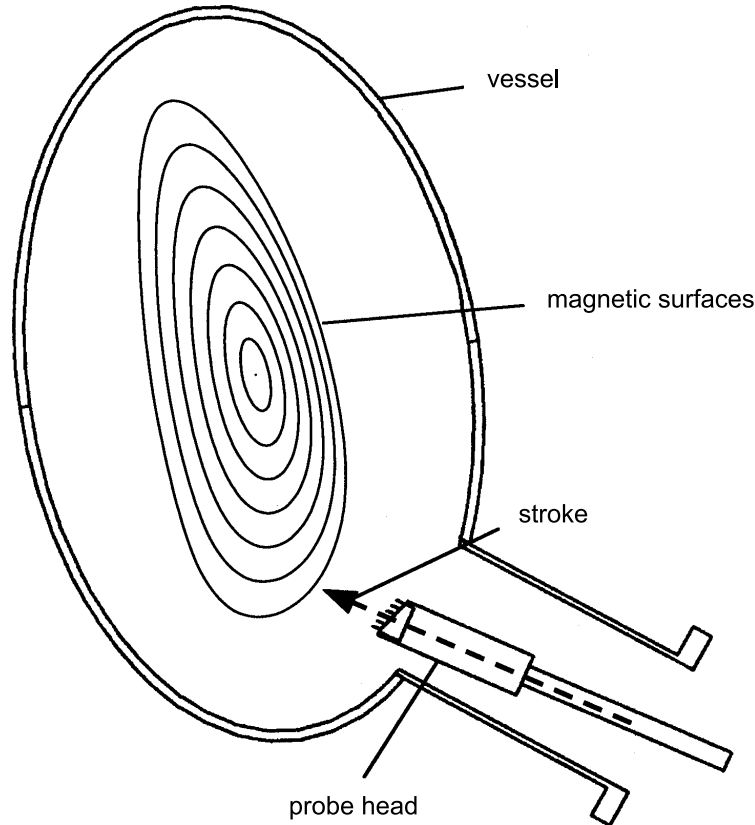

Figure 3.2: *Set-up of the probe system at the W7-AS. A cross section of magnetic surfaces and of the vacuum vessel is shown. From the lower right the probe is advanced into the vessel by a manipulator system over a distance of ∼ 70 cm. During plasma operation the probe head, which carries an array of 15 tips, can be brought into plasma contact by a fast reciprocation. The direction of the stroke of this reciprocation is indicated and it amounts to ∼ 10 cm.*

Probe tip geometry

At Wendelstein 7-AS good expertise exists with the usage of small graphite cylinders used as electrical probes for fluctuation measurements [Bleuel 1998]. Graphite as the plasma facing component has sufficient electrical conductivity and can withstand the high heat fluxes in the edge plasma. For the measurements described in this work, an array of graphite tips has been used, where the individual tips are stacked

vertically and the envelope of the tip front is tangent to the magnetic surfaces, thus the arrangement is called a poloidal array. Since the inclination of field lines is small $\mathcal{O}(2°)$ at the position of the probe, the poloidal array can be regarded as aligned perpendicular to the lines of the magnetic field in good approximation.

Any tip and its eletrical connection are built coaxially and they are shielded in order to suppress cross-talk and to ensure adequate high frequency properties. The graphite cylinder is insulated by ceramics, leaving a length of 2 mm exposed on the plasma facing side (figure 3.3). At the opposite end it is connected to the inner conductor of a coaxial cable, whereas the shield of that cable is connected to the steel tube that covers the tip insulation.
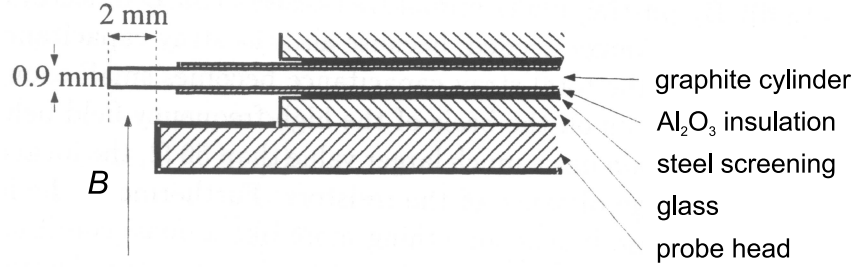

Figure 3.3: *Detail of the tip mounting within the probe head. To produce the 15 tip array the tip structure including insulation and screening is stacked in the direction perpendicular to the plane of this view.*

Individual tips are supported by a block made of glass ceramics, which is attached to the vacuum feedthrough (see figure 3.4). Block, glass support and cables are covered by the probe head, made of the insulating material boron nitride. At the leading edge the probe head is flush mounted with the tip insulation.

Behind the vacuum feedthrough there is a small cylindrical cell, that is air-vented and connected to the outside by a long tube. This cell provides space for the high frequency differential amplifiers (to be discussed in the following section), whereas the tube is needed as a duct for the data cables and also for the mechanical support. The whole system can fulfill a reciprocating stroke of ~ 10 cm within ~ 300 ms by means of a pneumatical drive, which is located outside the vessel port. Hence, it is possible to minimise the exposure time of the probe head and the tips. Additionally the reciprocation is useful to record a radial profile.

3.3 Design of the measurement electronics

The tip voltage should stay below the floating potential in order to retain the validity of the Emmert model for the presheath (section 2.4.4), and the voltage should be actively swept with an amplitude $\mathcal{O}(\frac{1}{2} k_B T_e)$ to resolve the nonlinearity of the
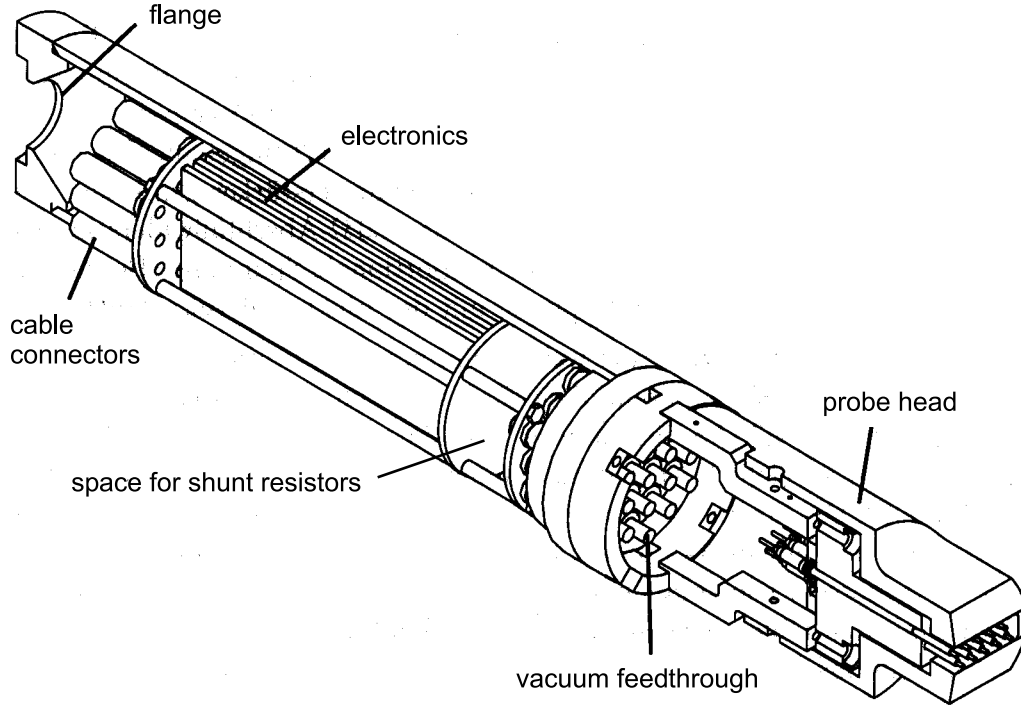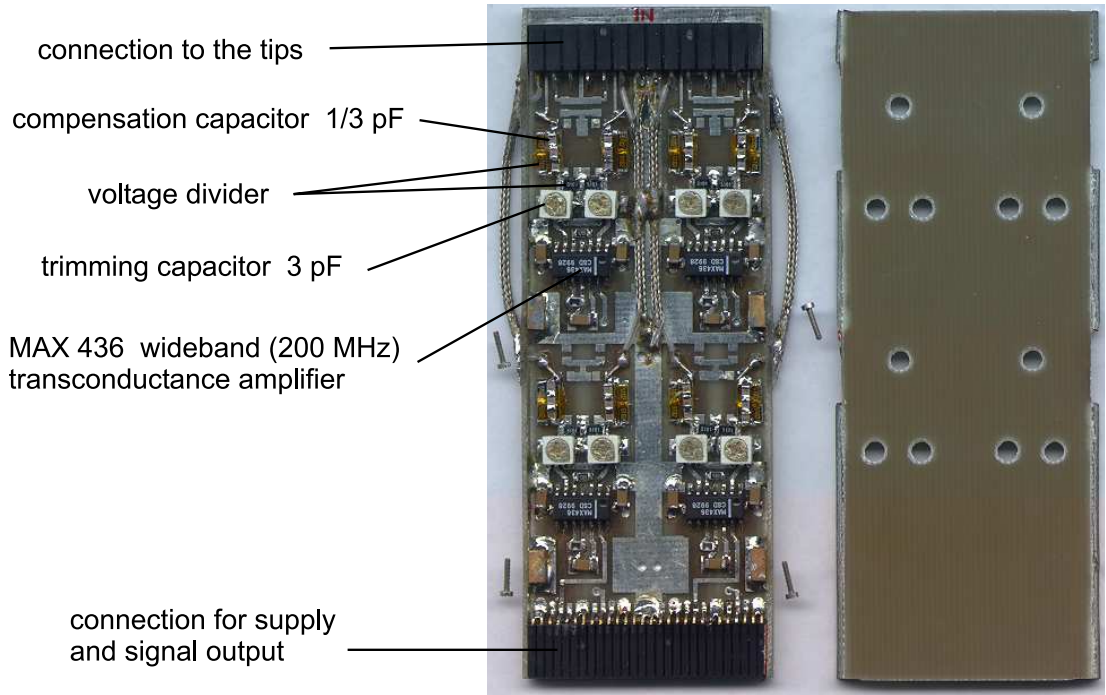
Figure 3.4: *Front end of the probe system. To the right is the plasma facing side with the graphite tips and the probe head covering. The probe tips are connected to the vacuum feedthrough by coaxial cables. The cylindrical cell behind the feedthrough is used for the measuring electronics, including shunt resistors and several amplifier boards.*

characteristic. In the edge plasma of the W7-AS, $\frac{1}{2} k_B T_e$ is equivalent to $\sim 15 \, \mathrm{V}$. Since the floating potential is close to the reference potential of the vessel $(0 \, \mathrm{V})$, a bias equal to the sweep amplitude is necessary.

The required time resolution was specified (see section 2.2) and defines a design value for the frequency of the voltage sweep $1 \, \mathrm{MHz}$. In principle the waveform of the voltage can be harmonic, i.e. sinusoidal. A proper impedance matching, however, is not possible, because the tip impedance is nonlinear and fluctuating. Therefore reflections will be present in the transmission system, distorting the sinusoidal sweep. Altogether an extended bandwidth of the voltage measurement is required, the design value is $10 \, \mathrm{MHz}$.

There are similar requirements for the current measurement on individual tips. Even if the tip voltage is sinusoidal, the sheath current depends nonlinearly on it, which generates higher harmonics. Hence, the bandwidth of the current measurement must also be $> 1 \, \mathrm{MHz}$, the design value is $10 \, \mathrm{MHz}$.

Since the phase of the current must be measured precisely relative to the phase of the voltage, cable lengths must be critically discussed in such high frequency circuits. If the cable connected to one tip passes through the probe head, the cable duct and finally through the vessel port, then cable lengths of $3 \, \mathrm{m}$ cannot be avoided at the W7-AS before any measuring device outside the vacuum vessel is

connection to the tips

compensation capacitor 1/3 pF

voltage divider

trimming capacitor 3 pF

MAX 436 wideband (200 MHz)
transconductance amplifier

connection for supply
and signal output

Figure 3.5: *An amplifier board containing 4 channels for the current measurement. SMD devices are utilised to build the miniaturised circuits. The overall board dimensions are $100 \times 40 \times 4\,\mathrm{mm}$. On the right hand side is the top cover, which has got a grounded inlay in order to prevent the pick-up of HF from the surrounding. Circular gaps in the cover provide access to the trimming capacitors after closing the board.*

reached. Tip impedance is usually far above the $50\,\Omega$ impedance of a coaxial cable and thus the cable behaves as a parasitic capacitive load, giving rise to displacement currents which must be compensated. These currents have been observed to limit the achievable bandwidth in earlier measurements by Giannone et al. [1994], who used high bandwidth clamp-on ammeters. The conclusion is to reduce the cable length between the tip and the measuring device.

A practicable solution was proposed by Pfeiffer [1997], who also built the prototypes: Miniaturised amplifier boards are placed within the cylindrical cell directly behind the tips (see figure 3.4), allowing for a short cable connection $o(0.1\,\mathrm{m})$. Such board is displayed in figure 3.5, it contains 4 channels to measure tip currents. Altogether four boards are stacked, providing measurement channels for all 15 tips. Basically the amplifiers do an impedance transform and drive a correctly terminated $50\,\Omega$ transmission line, which can be sufficiently long $o(10\,\mathrm{m})$ to reach the analog to digital converters (ADCs) of a fast sampling data acquisition system. For a detailed description of the amplifiers, see appendix C.

3.3.1   Signal flow overview

Additional components are necessary in order to set the bias and the sweep voltage. For the DC bias, a remotely controlled voltage supply (F.u.G. NTN, $0 - 125\,V$, $0 - 10\,A$) is used, capable of delivering I_{sat} for any tip up to the density $n_0 = 3 \cdot 10^{19}\,\mathrm{m^{-3}}$ ($T_e = T_i = 30\,\mathrm{eV}$), which is considered to be sufficient.

The sweeping voltage is generated by a radio frequency (RF) amplifier (BONN BTA 0110-1000) with a maximum output power of $1\,\mathrm{kW}$ into $50\,\Omega$. The total high frequency impedance of all tips including the shunt resistors can be estimated to $\sim 20\,\Omega$ in the edge plasma. Even though the transmission line from the amplifier to the probe head is thus not terminated correctly, there is abundant RF power to produce the required amplitude of the sweep voltage.

The RF amplifier has got a gain of $60\,\mathrm{dB}$ and is driven by a remotely controlled function generator. Since the sweep voltage is only to be generated during the acquisition time of $\sim 0.17\,\mathrm{s}$, the function generator output is gated, while the RF amplifier will run continuously.

Both DC and RF supply are brought to the probe system by independent transmission lines over a distance of approximately $10\,\mathrm{m}$. Before the signals are fed into the probe voltage line, they run through a mixing network (figure 3.6). Note that close to the output of the mixing network the voltage line is tapped by the inverting amplifier, which is necessary to provide the active common mode rejection (see appendix C.2).
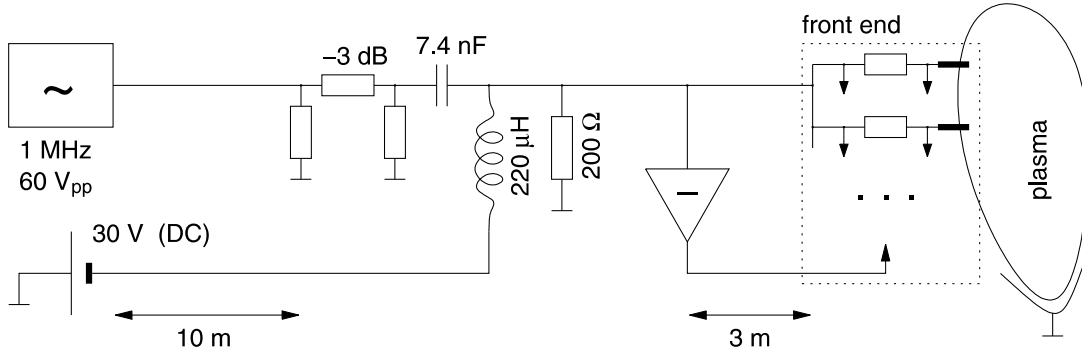
Figure 3.6: *Mixing network for the DC and the RF part of the probe voltage. It consists of a $-3\,\mathrm{dB}$ attenuator to improve impedance matching and damp reflections, furthermore of a capacitor for the RF coupling and a coil to connect the DC line. Towards the probe, an ohmic load is provided ($200\,\Omega$). This introduces a finite impedance to fluctuations with intermediate frequencies and, thus, prevents the voltage line between mixing network and front end from large excursions. On the right the hybrid inverting module (see appendix C.2) and the shunt resistors for the current measurement are indicated.*
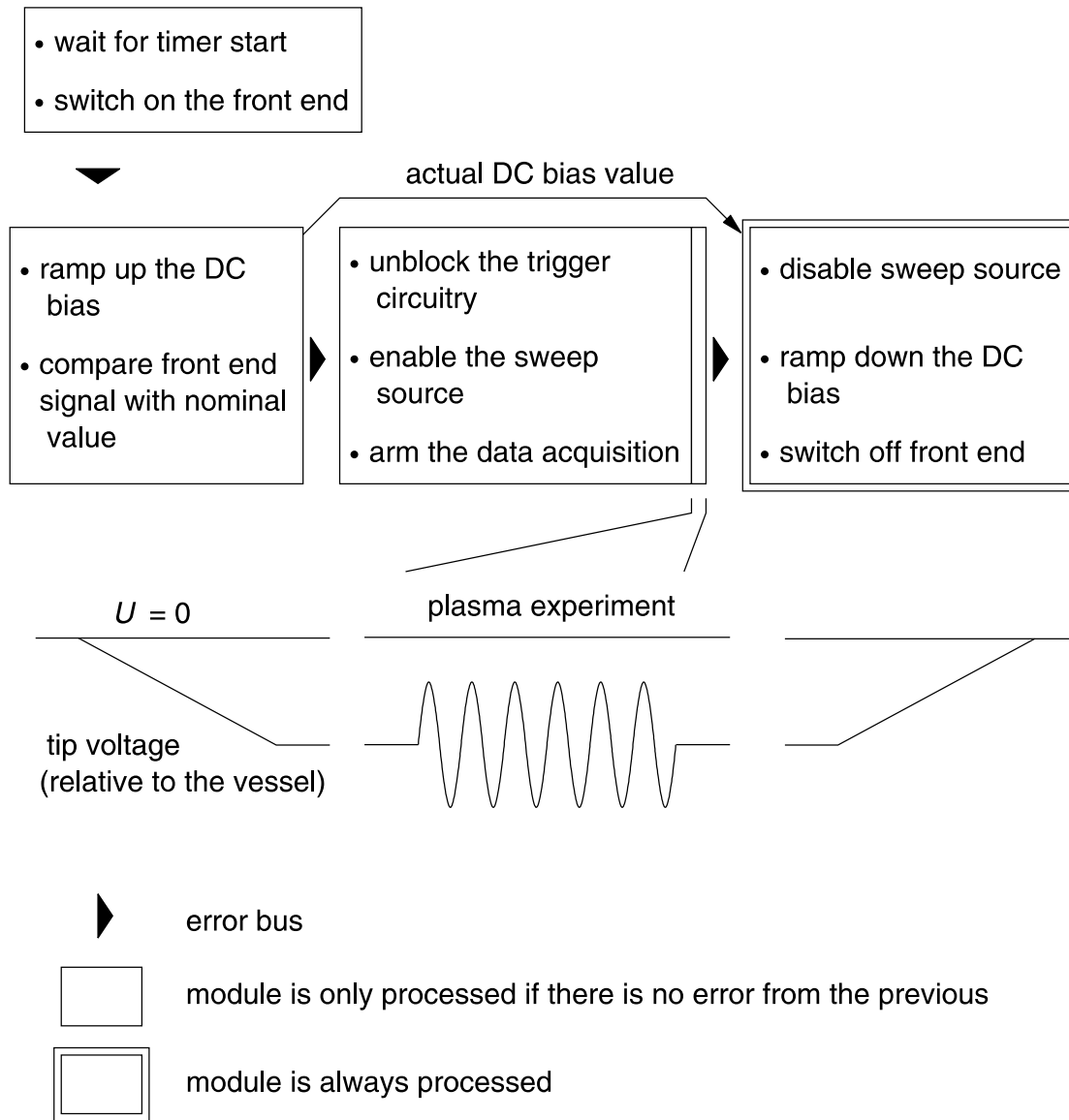
3.3.2 System control, monitoring and safety

On one hand there are high voltages in the signal source system: Peak values of $\mathcal{O}(100\,\text{V})$ are possible, depending on the phase of the sweep voltage and on plasma induced voltage fluctuations. On the other hand a delicate data acquisition system [Sig 1997; FAS 2001] with a sampling rate of 50 MHz is used, which can be damaged by input voltages that exceed $\pm 4\,\text{V}$. The source and the acquisition system are separated by voltage dividers and by the current amplifiers. Nevertheless one can construct a scenario with a fail of one or more electronic components, that can lead to an overvoltage at the ADC input. Two independent safety measures are taken to prevent such an accident: First, a regular and automatic self-test, and second, an electronic common mode monitoring within the probe head, connected to an interlock which blocks both the RF and the DC source.

The self-test is compliant with a pulsed operation, it can be carried out before the measurement. Generally all signal sources, DC, RF, and also the measuring circuits are switched off in order to prevent the densely packed current amplifiers in the front end from overheating. After switching on, the DC bias is ramped up in two steps, each time comparing the nominal bias with the output of the tip voltage measurement. Only if the nominal and real values of both steps are in accordance within a given tolerance, then the sweep signal source is enabled. This procedure is written in LabVIEW [Nat 2000] and uses a multi I/O card (AT-MIO-16XE-50) as interface to the hardware. Schematically the program is displayed in figure 3.7. Since the status of the self-test is available before the start of the plasma operation, it is possible to block the probe reciprocation in case an error occurs.

The common mode monitor and interlock system basically controls the operation of the inverting amplifier that is necessary for the active common mode compensation. Since the level of the common mode is measured continuously by a special channel in the probe head (see appendix C), any fail of the inverting amplifier can be detected. This is done by a fast comparator, which finally triggers the interlock of the entire system. The sequence of interlock effects and corresponding time constants are:

- Blocking the gate of the function generator within $\approx 2\,\mu\text{s}$. This is the fastest measure and will remove the sweep signal from the input of the RF power amplifier.

- Deactivation of the power amplifier by a relais circuit. Response time of the relais $\approx 0.1\,\text{ms}$, amplifier power off within several ms .

- Removal of the DC bias after $\approx 100\,\text{ms}$, i.e. within the duration of the probe reciprocation. That could be made faster, but if the probe still has contact with the plasma, then tip currents are minimised with the bias, because the floating potential is usually negative when crossing the separatrix. The bias alone is unlikely to produce an overvoltage at the ADC input.

- wait for timer start

- switch on the front end

actual DC bias value

- ramp up the DC bias

- compare front end signal with nominal value

- unblock the trigger circuitry

- enable the sweep source

- arm the data acquisition

- disable sweep source

- ramp down the DC bias

- switch off front end

$U = 0$

plasma experiment

tip voltage
(relative to the vessel)

▶ error bus

☐ module is only processed if there is no error from the previous

▣ module is always processed

Figure 3.7: *Automatic test and measurement procedure, implemented in LabVIEW software. Below the program modules the corresponding evolution of the tip voltage is displayed schematically. Note that two analog signals come from the W7-AS environment in order to trigger the preparation ("timer start") and the acquisition ("plasma experiment") phase.*

Chapter 4

Data evaluation

In this chapter the procedure is specified that allows one to generate spatio-temporal data of plasma quantities from the raw data. Starting with the recorded time series of tip currents and the common applied voltage, the critical point of addressing individual characteristics is discussed. The measured turbulent fluctuations have a rather high bandwidth in the frequency domain, therefore a fit model with continuous evolution of parameters in the time domain must be introduced. Analysing the statistical properties of the fit result, it is found that the parameters become covariant whenever the interrelation between tip current and tip voltage deviates from the ideal exponential law. In correlation functions, the covariance of parameters leaves a characteristic fingerprint, which will be referred to as noise, to be distinguished from plasma fluctuations. Eventually a workaround is presented in order to mask the noise and recover the information relevant for plasma turbulence. With a final note on channel equilibration this chapter shall close.

4.1   Raw data and addressing of characteristics

When the multi-tip probe is operated with the fast voltage sweep in a W7-AS plasma, a proper timing is essential. The duration of the stationary plasma state is typically $1\,\mathrm{s}$ and the pneumatic probe reciprocation takes roughly two times $150\,\mathrm{ms}$, once for the forward and once for the backward movement. Since the stroke is large compared to the gradient lengths of the plasma quantities at the edge, only the central part of the reciprocation around the point where the probe extends furthermost into the plasma, is useful to acquire data. The memory of the high speed multi channel acquisition system is limited to $168\,\mathrm{ms}$ and it is not fully synchronised. Hence, in order to identify equivalent sweeps in the recorded voltage and in the recorded tip currents, both the start and the termination of the active voltage sweep are to be recorded.

Altogether the timing is like this:

- Self-test of the sweep system (see section 3.3.2), preparation of the W7-AS plasma operation.

- Main timer signal indicates begin of plasma discharge, the reciprocation is triggered with a delay of several $100 \, \text{ms}$.

- Typically $100 \ldots 200 \, \text{ms}$ after the start of the reciprocation, the $50 \, \text{MHz}$ acquisition system is triggered and with an additional delay of some μs also the HF voltage sweep.

- The sweep is terminated before the acquisition runs out of memory.

The procedure is illustrated for a W7-AS plasma experiment in figure 4.1. General timing, trigger and reciprocation signals are recorded by slowly sampling ($5 \, \text{kHz}$)
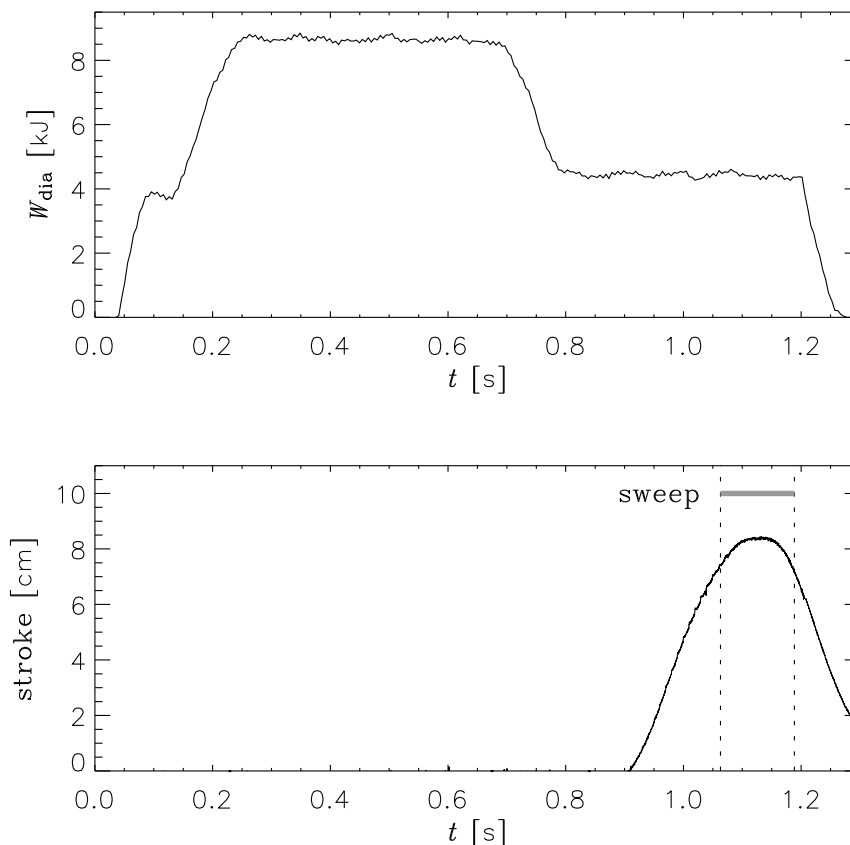
Figure 4.1: *Timing of the W7-AS plasma discharge #55760. On top the total kinetic energy content of the plasma, measured by a diamagnetic loop. From $t = 0.7 \, \text{s}$ on a plasma current was induced artificially, which changed the confinement. The probe is driven into the second stationary phase. At the bottom, the reciprocation signal is displayed together with the interval of the fast voltage sweep.*
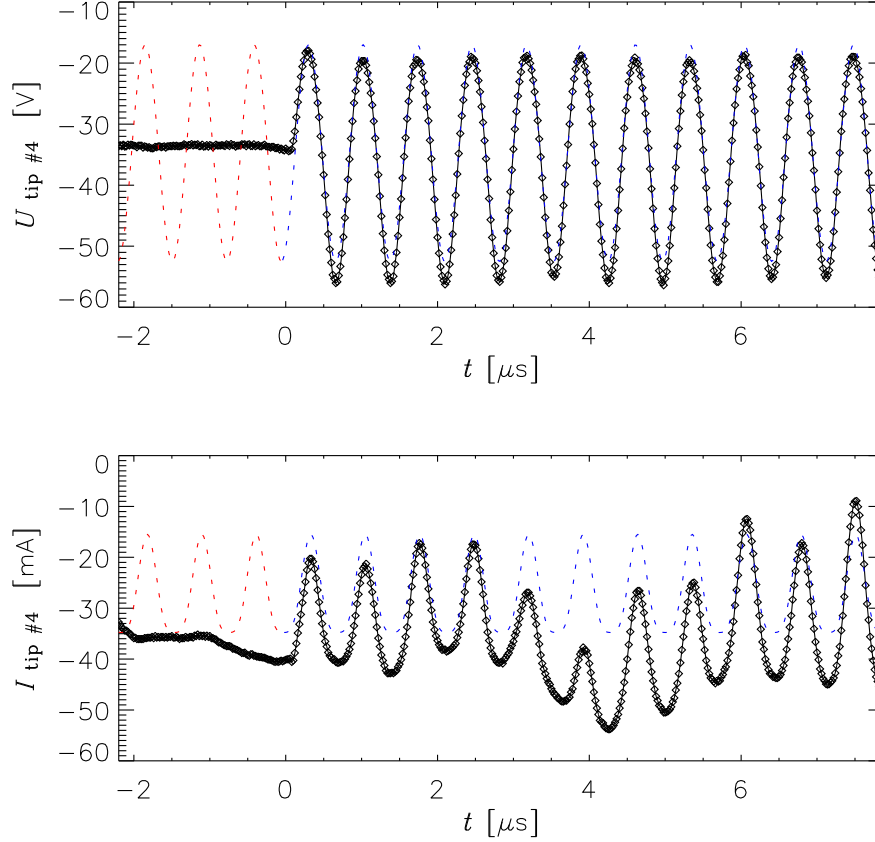
Figure 4.2: *Start of the active sweep on one probe tip. On top the tip voltage and at the bottom the tip current as a function of time. Sampled data are displayed using diamonds and an interconnecting line. The "global fit" which is used to address individual characteristics is overplotted with a dotted line.*

ADCs, so that the time window of the fast swept probe measurements can be mapped to the actual probe position and to the W7-AS experiment time.

Start and termination of the voltage sweep on one of the fifteen probe tips is displayed in the figures 4.2 and 4.4. Clearly the sinusoidal signal source generates a dominating first harmonic in both the tip voltage and the tip current. Due to the nonlinear response, each half period of the tip current together with the corresponding half period of the voltage forms one characteristic. In order to map the half periods correctly between unsynchronised channels the "global fit" must be introduced.

4.1.1 The "global fit" synchronisation

The task to isolate single characteristics is somehow equivalent to the localisation of minima and maxima in the current and voltage data. If there are large fluctuations in the plasma quantities (see figure 4.3), then the minima and maxima are smeared out and become difficult to localise. If one additionally takes into account the
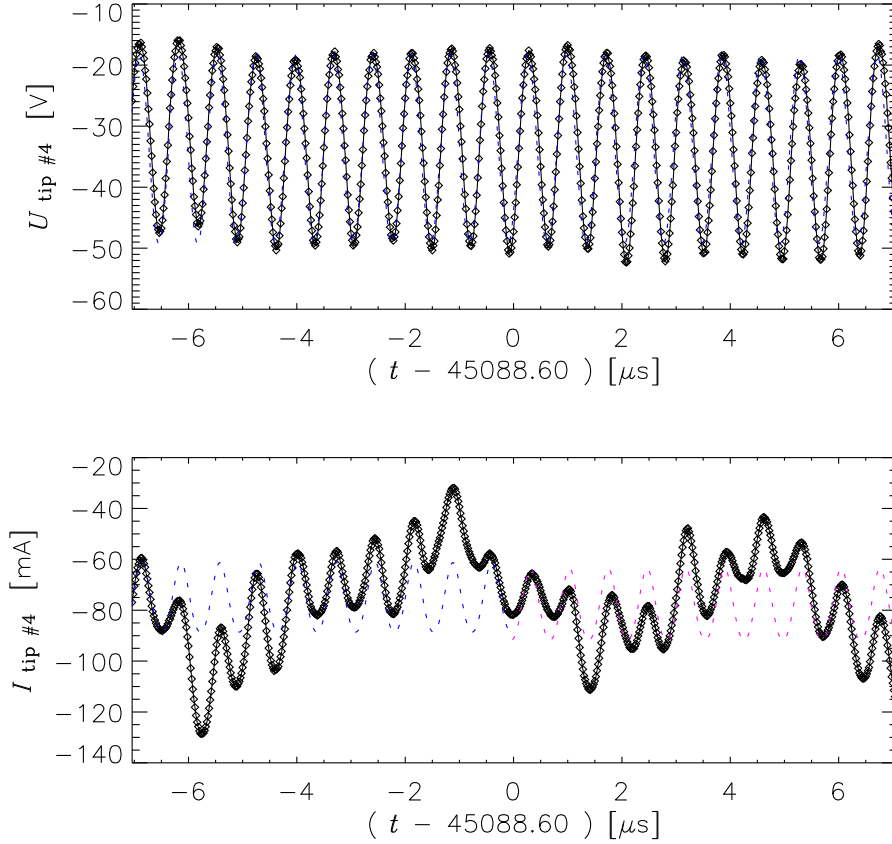
Figure 4.3: *Active voltage sweep (top) and tip response (bottom) for maximum stroke of the probe. The time axis has been shifted relative to the sweep start. A joint of two global fit segments is shown with dotted lines in blue and magenta.*

amount of the order of 10^5 recorded characteristics per channel, then it is obvious that a manual separation is not possible at all.

Hence, a harmonic model function is to be adapted to the data by a numerical fit procedure (routine E04FYF from [Num 1999]). Phase, angular frequency, offset and two amplitudes corresponding to two harmonics are free parameters. Since either source or sampling frequency (which of the two could not be figured out) were observed to vary slightly within the acquired interval, the fitting is done in segments, each segment containing typically $5 \cdot 10^4$ samples or 1000 sweep periods. When all of the data is eventually modelled, individual sweep periods can be addressed via the phase of the model function. Note that the global fit sets up a new time base, which is defined by the sweep frequency and independent of the sampling rate.

Fit algorithms try to establish an optimum, i.e. minimum deviation between data and model function. Not necessarily this procedure converges and additionally it may run into a local instead of the global minimum of the deviation. In the case of the global fit, two measures are taken to control these effects: First, the minimisation routine's output flags are checked. If there were too many iterations without convergence or if the mathematical conditions for a minimum are not met,
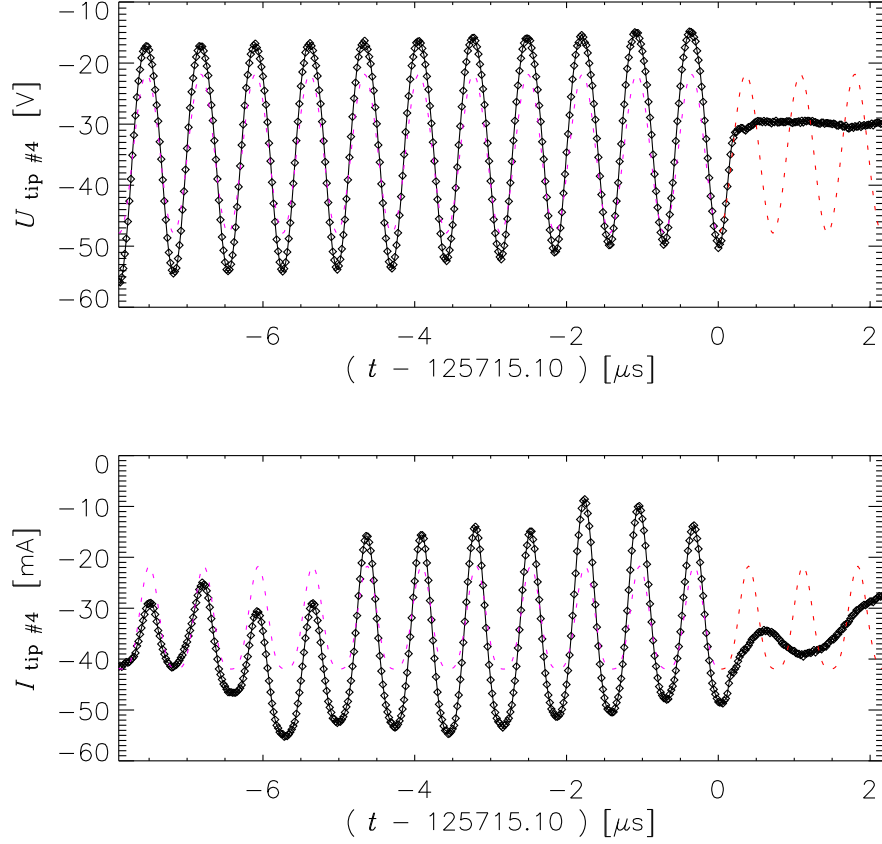
Figure 4.4: *Termination of the active voltage sweep. On top the tip voltage and at the bottom the tip current, where the time axis was shifted relative to the sweep start corresponding to the duration of the sweep interval. The "global fit" is overplotted with a dotted line in magenta during the sweep and in red after the termination.*

then the routine terminates with an error value. Second, the boundaries between the segments are examined. From both sides, i.e. using the previous and the following model function, the temporal localisation of the minimum closest to the boundary is calculated. Only if these two calculated positions coincide within a given tolerance (± 80 ns typically) then both fits are accepted. An example showing such a junction is displayed in figure 4.3.

In the partly synchronised system, it is in principle sufficient to generate the global fit once for each different timebase. Nevertheless it proved to be a benefit, if the procedure is applied to each channel for two reasons: One is the trigger uncertainty of individual ADC boards, which was observed to be several samples. The other is the need to allow for an artificial and individual even though small phase shift between voltage and current. This leads to the next section.

4.1.2 Artificial phase shift

If current channels are synchronised with the voltage by means of the global fit, then usually the data samples of different channels won't lie exactly at the same phase of the model function. Thus, in order to bring the samples together, the current signals are interpolated using a cubic spline (routines E01BAF and E02BBF from [Num 1999]). Since the sample noise is small compared to the sweep signals, the interpolation is not considered to be a significant source of error.

By a straightforward cutting of the signals at the maxima and minima of the model function and eventually fitting single up and down sweeps with the exponential formula from equation (2.19), time series of the fit parameters are obtained. If the fits from the upward sweeps are compared to those of the downward sweeps, then a systematic deviation is often observed, e.g. see figure 4.5.

Such deviation can be explained, if the phase of the current signal is shifted relative to the voltage signal. But, since the signals were actually synchronised to the local minima and maxima of the dominating first harmonic oscillation, the
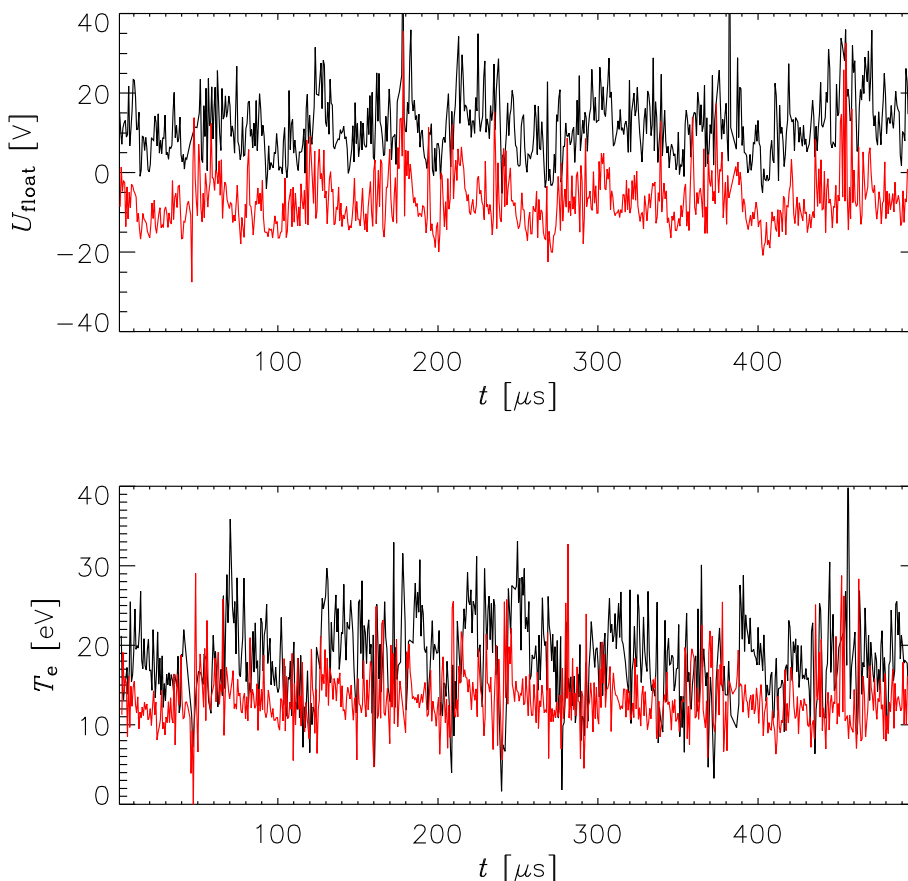

Figure 4.5: *Time series of fit parameters U_{float} and T_e from upward sweeps only (black), compared to the corresponding series of the downward sweeps (red). Clearly there is a systematic deviation between the two time traces.*

problem must be more subtle. If higher harmonics are shifted, then also the shape of the up sweep will be different from the down sweep. Reasons can be either the transmission line between the tip and the shunt resistor, where actually the tip impedance does not match the characteristic impedance of the line, or the complex impedance of the tip's presheath. The former can be quantified, which will be done in the next section, but it can explain the phase shift only partly. Hence, the phase shift is most probably caused by a mixture of both effects. Note that the real impedance of the sheath ($\omega_{\mathrm{sweep}} \ll \omega_{p,i}$) cannot be responsible.

Introducing an artificial and uniform phase shift turned out to be a satisfactory countermeasure. Therefore the phase of the tip current was varied in order to minimise the up-down assymetry of the most sensitive fit parameter U_{float}. For the given example, the result is displayed in figure 4.6, where the up and down series of U_{float} and of T_e are nearly congruent after the phase correction.

In a spectral analysis, the up-down assymetry corresponds to a sharp peak at the Nyquist frequency. If such a peak appears then it is to be nulled, which is a complementary approach to remove up-down asymmetries.
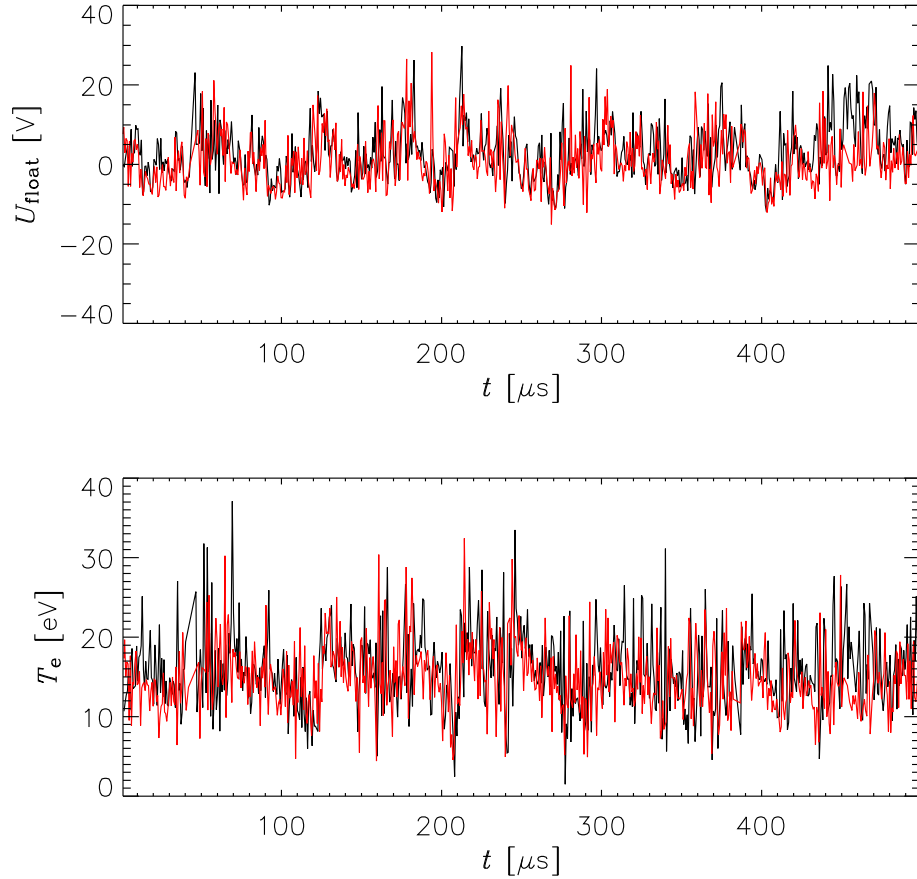
Figure 4.6: *Time series of U_{float} and T_e, separately for the up sweep (black) and for the down sweep (red). The raw current signal was shifted artificially by $-40\,\mathrm{ns}$.*

Transmission line transformation

There is a short transmission line in between the probe tip and the shunt resistor, where the tip current and the common voltage are actually measured. Although the length has been kept to a minimum, it can cause observable phase shift between current and voltage.

The plasma sheath at the tip does not terminate the transmission line properly, additionally the strong nonlinearity of the sheath generates higher harmonics. In a transmission line, however, voltage and current are coupled uniquely for a wave travelling into one direction. Hence, if both voltage and current are known, then the waves propagating in both directions can be calculated. This allows one to transform the measured values from the position of the shunt resistor to the location of the tip. Equations for the transform are [Russer 1993] :

$$
\begin{aligned}
U^{(\omega)} &= U_m^{(\omega)} \cos(\omega\,\tau_W) \;-\; i\,Z_W\,I_m^{(\omega)} \sin(\omega\,\tau_W) \\
I^{(\omega)} &= I_m^{(\omega)} \cos(\omega\,\tau_W) \;-\; i\,Z_W^{-1}\,U_m^{(\omega)} \sin(\omega\,\tau_W) \;,
\end{aligned}
$$

where $U_m^{(\omega)}$ and $I_m^{(\omega)}$ denote the complex Fourier spectra at the position of the measurement, while $U^{(\omega)}$ and $I^{(\omega)}$ are the corresponding spectra at the location of the tip. The characteristic impedance of the transmission line is $Z_W = 50\,\Omega$, ω is the angular frequency, and the length of the line is included in $\tau_W = l_W\,/\,c_W$ with the phase velocity being a fraction of the vacuum speed of light $c_W \approx \frac{2}{3}\,c_0$.

Realistic numerical values are

cable length between tip and shunt	l_W	$= \quad 0.15\,\mathrm{m}$
angular frequency of first harmonic	ω_1	$= \quad 8.75 \cdot 10^6\,\mathrm{s}^{-1}$
first harmonic voltage amplitude	$U_m^{(1)}$	$= \quad 20\,\mathrm{V}$
second harmonic voltage amplitude	$U_m^{(2)}$	$= \quad -1\,\mathrm{V}$
first harmonic current amplitude	$I_m^{(1)}$	$= \quad 12\,\mathrm{mA}$
second harmonic current amplitude	$I_m^{(2)}$	$= \quad 2\,\mathrm{mA}$

The amplitudes are a typical global fit result. Note that the second harmonic voltage is in antiphase to the first harmonic and therefore written with a minus sign. From these figures follow the time lags of both harmonic currents relative to the voltage at the location of the tip. While the first harmonic is delayed by 25 ns, the second harmonic comes more early by 7.5 ns .

4.2   Evaluation of characteristics

The details of how to actually fit the nonlinear $I(U)$ characteristic in a turbulent plasma should now be specified. It is necessary to account for fluctuations which are nearly as fast as the voltage sweep. Already the raw data displayed in figure 4.3

suggests that such thing can happen and this means that the fit parameters I_{sat}, U_{float} and T_e in the exponential formula (2.19) cannot be regarded as constant during one sweep. The solution to this problem is simply to allow a temporal evolution of the fit parameters, which is valid since the sheath impedance is real, i.e. it does not introduce a time lag. In order to implement an appropriate fit function, the raw signal must be processed in packets containing several sweeps, and, therefore, different timebases must be distinguished. The fit method together with the result of its application are presented afterwards. It is observed that strongly localised overshoots can appear in the parameters, whenever the fit problem is not well posed. This perturbs the calculation of U_{plasma} and n_0, and, since fit parameters can become covariant, it has also an influence on the cross phase between different quantities. Hence, in order to supress overshoots a smoothing technique is built into the fitting routine.

4.2.1 The different time bases

Basically there will be three time bases:

First, the sampling of the data acquisition defines the grid with the highest available resolution. It is equal to the time points of the common tip voltage. Current signals that were not synchronised are mapped to this grid by an interpolation. Also the fit function will be calculated with the same resolution.

Second, the sweep frequency which defines the "natural" time base of $I - U$ characteristics. Typically it is slower than the sampling by the ratio $\mathcal{O}(1/50)$, but since the signal source for the sweep and the acquisition clock are not synchronised, this is neither a rational fraction nor constant throughout the entire acquisition interval. Using two times the sweep frequency as the time base for the fit parameters is a favourable choice, because the parameters are well defined by either up or down sweep. The plasma quantities U_{plasma} and n_0 will be calculated from the fit parameters, thus two times the sweep frequency is the effective sampling frequency with respect to the measurement of the plasma turbulence.

Third, the length of the fit packet. On one hand the packet is necessary in order to incorporate the temporal evolution of the fit parameters and it must consist of at least two sweeps. On the other hand discontinuities remain at the packet boundaries, and the number of the latter can only be reduced by making the packets large. In reality one has to restrict the packet length to keep the computing time small, so it turned out that a length of 6 sweep periods, i.e. 12 time points for the fit parameters, is a convenient choice. The discontinuities at packet boundaries are removed efficiently by doing several cycles, each time using the result of the previous cycle to predict the temporal dependency at and beyond the end of the actual packet. After 5 cycles including the initial one, no significant change of the result has been observed.

4.2.2 Fit function

In principle when evaluating probe characteristics the method is similar to the one for setting up the global fit (section 4.1.1). A model function depending on the measured tip voltage and on several parameters is evaluated on the grid of the current signal and subtracted. The square deviation is minimised by varying the parameters (routine E04FYF). If this numerical process has converged, the parameters are "fitted", they hold most probable values. Additionally estimations for their uncertainties can be extracted from the variance-covariance matrix, which is set during the fit procedure (routine E04YCF from [Num 1999]).

Measured data are processed in packets, where each packet consists of 6 sweep periods, and two sets of the fit parameters I_{sat}, U_{float} and T_e are assigned to any period. The points in time for the parameters are the center of the up and of the down sweep, respectively. When calculating the model current, the parameter values are mapped to the fine grid of the measurement by a linear interpolation. At the boundary to the following packet the parameter values of the previous fit cycle are utilised. Altogether the temporal evolution of the fit parameters is continuous but the first derivative is not.

In order to test whether the Alfvén wave cable model (section 2.5.2) for the presheath can improve the quality of the fit, the equation (2.25) of the lossy transmission line was applied once per packet. This modifies the spectrum of the measured tip voltage

$$U_{mod}^{(\omega)} \;=\; U^{(\omega)} \;-\; W(\omega, r_\parallel, c_{pol})\, I^{(\omega)} \quad .$$

The parameters $r_\parallel$ and c_{pol} can be calculated from the fit result of the previous cycle, but they must be kept constant along the packet, otherwise the calculation in Fourier space is not possible. Concerning the scaling of the perpendicular conductivity, the value from Bohm diffusion was used $\eta_\perp^{\text{eff}}\,/\,\eta = 3 \cdot 10^7$, and for the cable diameter ratio $\ln\frac{r_a}{r_i} = 1$.

To anticipate the result: This kind of approximation to the Alfvén wave cable model was not successful, i.e. the deviation between measured and modelled current was slightly increased. Two reasons are assumed to be responsible for that. On one hand there is no self consistency in the fit of both sheath and presheath, because the presheath parameters were calculated from the previous cycle. On the other hand fluctuations of $r_\parallel$ and c_{pol} within one packet were neglected. The first problem could be solved if the dependence of $r_\parallel$ and c_{pol} on the fit parameters is included in the fit algorithm. Since several Fourier transforms are necessary, this is at the expense of computation time. The second problem required proper treatment of a transmission line with fluctuating impedance, but the correct implementation is beyond the scope of this thesis. As a matter of fact the modification of U by $r_\parallel$ and c_{pol} is neglected in all results that are presented in the following.

Assessment of the fit model

Once the parameters I_{sat}, U_{float} and T_e are fitted, any probe tip's current can be reconstructed. The result was to be compared with the measured current on the fast sampling timebase. Exemplary this is done in figure 4.7. The reconstructed tip current shows excellent agreement with the recorded one. A dynamic evolution of T_e, U_{float} and I_{sat} is clearly observed even in this narrow time window of $9\,\mu$s. This indicates fast events in the plasma that significantly change temperature and density. Note that $-I_{sat}$ is proportional to the density n_0, therefore the "event" at $t = -2\,\mu$s is nearly simultaneous and carries the same sign in both n_0 and T_e.

Sometimes slight up-down assymetries are visible as systematic oscillations of parameters, e.g. for T_e and U_{float} at $t \sim 0\,\mu$s, or for I_{sat} at $t \sim 2.5\,\mu$s. The fit routine obviously minimised the deviation between measured and modelled data by shifting the value of adjacent parameters in opposite directions. This effect and its consequences were discussed (section 4.1.2).
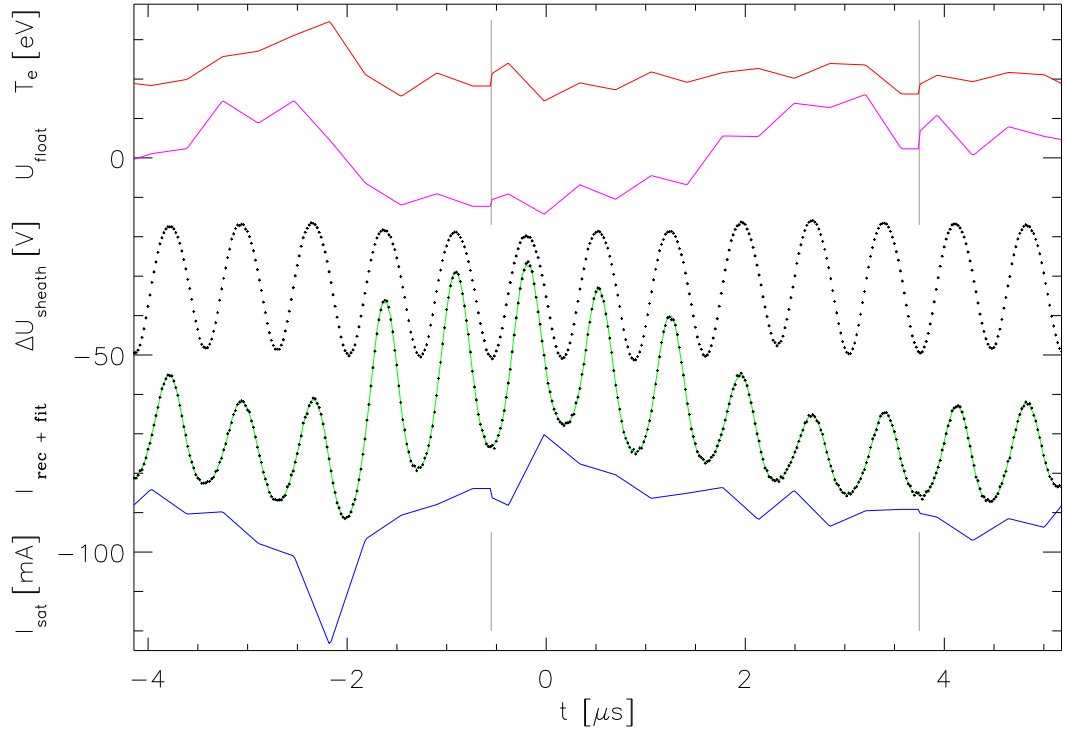
Figure 4.7: *Time traces of measured voltage and current data from tip #8 together with the continuous evolution of fit parameters. Voltage ($\Delta U_{\mathrm{sheath}}$) and current ($I_{\mathrm{rec}}$) are plotted with small crosses (black). First line: fit parameter T_e (red), second line U_{float} (magenta). Last line I_{sat} (blue). The modelled tip current is overplotted with a solid line (green). Note that the unit of the vertical axis depends on the signal type, i.e. current in mA, voltage in V, temperature in eV. Packet boundaries are indicated by vertical lines and discontinuities are still visible since this is the result of the first fit cycle.*

71
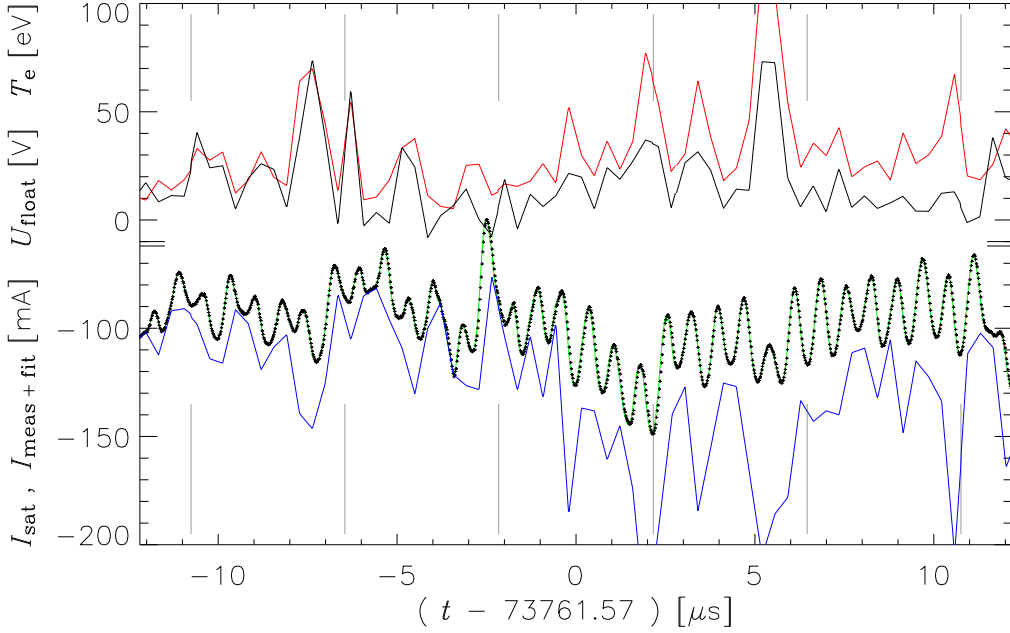
Figure 4.8: *Evolution of fit parameters in a measurement of strong fluctuations. Probe position is close to the separatrix, data is from tip #8 . The solid lines represent T_e (red), U_{float} (black), and I_{sat} (blue). Measured and modelled tip current are overplotted for comparison (small crosses and green line). Note that the unit on the vertical axis is different for each curve. Additionally the vertical scale has been compressed in the range between -60 and -10 . Packet boundaries are indicated by vertical lines.*

A qualitative validation of non-systematic oscillations is possible "by eye". If one compares the shape of the raw current and voltage signals and the plasma induced fluctuations of the parameters, then there are the following correlations:

- According to the exponential $I(U)$ characteristic I_{sat} is proportional to the lower envelope of the oscillating current everywhere.

- Any drop in U_{float}, for instance the one at $t = -2\,\mu$s, displaces the current level (signal $I_{rec+fit}$ in figure 4.7) in positive direction.

- A drop in T_e (e.g. also at $t = -2\,\mu$s) is accompanied by an increase of the current amplitude. This is due to the fact that the $I(U)$ characteristic is the steeper the lower the temperature.

4.2.3   Inherent smoothing of the fit function

If the fluctuation bandwidth is very large, as it is the case for a probe located close to the separatrix, then the fit parameters display a rather erratic behaviour (figure 4.8). Additionally the strict minimisation of the square deviation between data and fit generates a tendency for temporary overshoots in I_{sat}, U_{float} and T_e simultaneously.
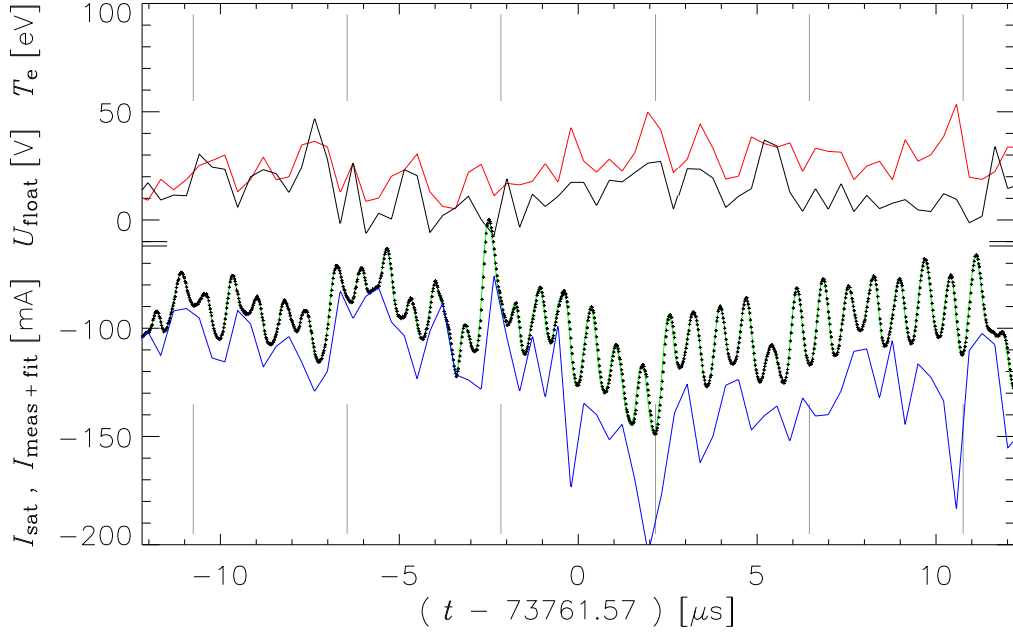
Figure 4.9: *The effect of smoothed fitting on the evolution of fit parameters. Raw data, axis range and color coding is exactly identical to figure 4.8. Smoothing parameter $k_{\mathrm{sm}} = 10^{-5}$ for both U_{float} and T_e. Note that there are no discontinuities at the packet boundaries, since this is the result of the fifth fit cycle.*

A damping of these overshoots like in figure 4.9 is desired in order to provide smooth time traces, which are necessary for the reliable calculation of average values. But at the same time smoothing restricts the bandwidth of the measurement, leading to a loss of information on high frequency fluctuations. This dilemma must be solved individually, i.e. the impact on a particular result is to be discussed.

Smoothing can be achieved methodically by making use of two peculiarities in the data evaluation. On one hand the length of the fit packet provides a convenient width for the averaging window. On the other hand the scatter of one fit parameter around its average within one packet can be made an additional minimisation criterion. The weight of the scatter relative to the deviation between measured and model current is controlled by a smoothing parameter k_{sm}. Hence the expression to be minimised in each packet is of the form:

$$\sum_h \left(I_{h\,\mathrm{mod}}(p_{qr}) - I_{h\,\mathrm{meas}} \right)^2 \quad + \quad \sum_q k_{q\,\mathrm{sm}} \cdot \frac{1}{n_r} \left(\sum_r (p_{qr} - \bar{p}_q)^2 \right) \quad \overset{!}{=} \quad \min \quad ,$$

where I_{meas} and I_{mod} are measured and modelled current, respectively, h is the sample index on the fast time base, r is the index on the "natural" time base of the sweep, n_r is the count of r within the packet, and q is an index to distinguish I_{sat}, U_{float} or T_e. The value of $\bar{p}_q$ is the packet average over r of the corresponding fit parameter p_{qr}.

In figure 4.9 the result of smoothed fitting is displayed. Actually this is the

counterpart to the time traces without smoothing in figure 4.8. The smoothing parameter value was $k_{\mathrm{sm}} = 10^{-5}$ for both U_{float} and T_e, while for I_{sat} it was 0.

How much smoothing is necessary ?

It has been pointed out, that a good compromise has to be found when the magnitude of the smoothing parameter is set. The appearance of overshoots in the time traces of the fit parameters is one hint which indicates the necessity for increased smoothing. More accurately that can be quantified by monitoring the power weighted cross phase between fit parameters. This cross phase describes the lag between fluctuations that are coherent in different quantities and its exact definition is given in section 5.2.3.3.

Since the fit parameters of one characteristic are covariant to some extent (to be discussed in section 4.3), any overshoot in one parameter also yields an in-phase overshoot of the remaining parameters (see the time traces of figure 4.8). This is equivalent to an in-phase correlation. Given the overshoots are triggered by deformations of the characteristic due to plasma fluctuations, then they can also be coherent in different channels and, therefore, a parasitic cross-correlation superposes to the cross-correlation of plasma fluctuations. Smoothing damps the overshoots and thus damps also the amplitude of methodic in-phase correlations, so that ideally only the correlations due to plasma fluctuations remain.

The smoothing parameter has been varied and its effect on the cross phase is displayed in figure 4.10. There is a transition between the points $k_{\mathrm{sm}} = 2 \cdot 10^{-6}$ and $k_{\mathrm{sm}} = 10^{-5}$, which coincides with the disappearance of the overshoots in the time traces (figures 4.8 and 4.9). This transition is largest when the probe is located near the separatrix and it is much less pronounced in the SOL. What happens at this
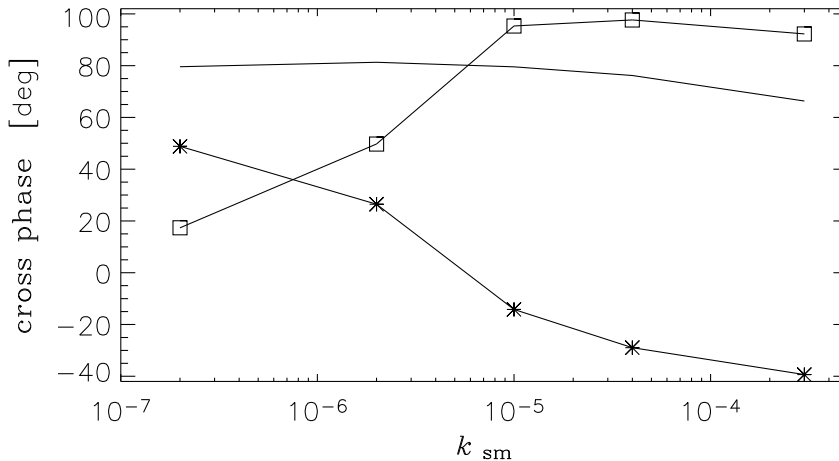
Figure 4.10: *The effect of the smoothing parameter k_{sm} on the power weighted (2D) cross phase (section 5.2.3.3) of the fit parameters. The probe is located close to the separatrix and the smoothing was applied to both U_{float} and T_e. The solid line without symbols represents the pair U_{float}-I_{sat}, squares denote U_{float}-T_e and asterisks T_e-I_{sat}.*

transition can be discussed qualitatively:

Firstly, the fit parameter with the largest uncertainty is T_e , whereas U_{float} and I_{sat} are determined more accurately. Hence, the cross phase between U_{float} and I_{sat} is robust and does not depend on the smoothing parameter.

Secondly, the covariance between T_e and U_{float} is larger than between T_e and I_{sat} , which is due to the fact that the real floating potential, i.e. the current free probe, is hardly approached during the voltage sweep. Thus, fitting the point with zero current of the characteristic is an extrapolation which depends on both parameters T_e and U_{float}. In contrast, since the probes are operated near the true ion saturation current, I_{sat} is usually well determined. If now the smoothing is too small, i.e. $k_{sm} < 10^{-5}$ and overshoots are clearly visible, then the covariantly high amplitudes of the parameters T_e and U_{float} dominate the power weighted cross phase and, consequently, the latter tends to zero. Naturally the cross phase between T_e and I_{sat} reacts to these different boundary conditions.

4.2.4   Post processing

If the fitting procedure does not converge or if the quality of the fit is very poor then a discontinuity appears in the time series of the fitted quantities. A fail of convergence can be identified by the fitting routine's output flags, while a poor fit results in a large uncertainty of fit parameters, which is detectable in the variance-covariance matrix. In order to remove such a discontinuity, the data point in question is replaced by a linear interpolation of two adjacent points (one to the left and to the right) that displayed regular convergence and small uncertainty.

The detection limit for poor fits is set up in the following way: For $|I_{sat}|$ and T_e a relative uncertainty limit of 50% of the actual value is defined. All data points that exceed this limit are replaced by the interpolation procedure. In the case of U_{float} the definition of the relative uncertainty must be changed, because U_{float} can carry both signs and its absolute can be close to zero. Eventually U_{plasma} is of interest, which is U_{float} plus some factor times T_e. Therefore the "relative uncertainty" of U_{float} is calculated by normalising the absolute uncertainty of U_{float} to the sum of U_{float} and T_e.

Figure 4.11 exemplarily displays normalised PDFs of the fit parameters and their relative uncertainties when the probe is located close to the separatrix. Clearly the distribution of the parameter values is not Gaussian but has got a tail towards positive values in U_{float}, T_e and $|I_{sat}|$. This means that the average values are higher than the most probable values, for instance in the case of T_e these two are 40 eV and 20 eV, respectively. For I_{sat} this shape of the PDF is known [Endler 1994], while for T_e this could not be measured before. Stationary measurements of U_{float} usually display a Gaussian PDF [Bleuel 1998]. The reason for the deviation between the stationary measurements by Bleuel and the actual PDF is the covariance of the fit parameters T_e and U_{float}, which will be discussed in the next section.

In the PDFs of the relative uncertainty (bottom of figure 4.11) different levels
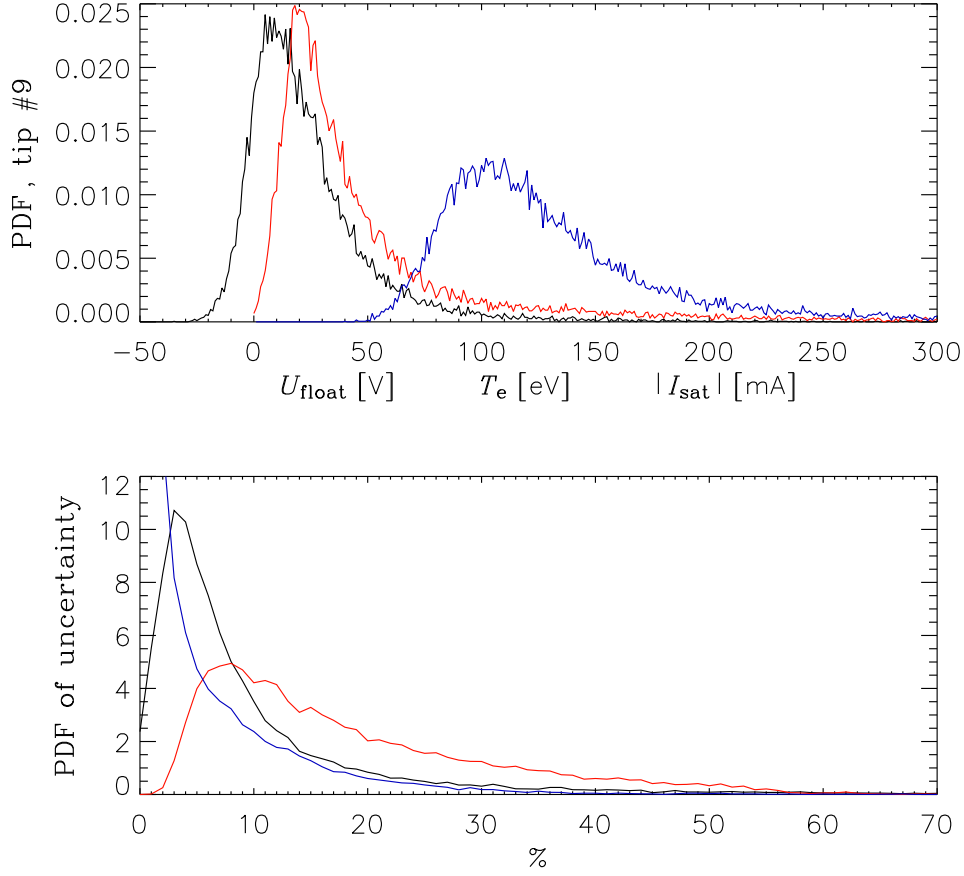
Figure 4.11: *Top: Normalised PDFs of fit parameters U_{float} (black), T_e (red), and I_{sat} (blue), for a probe position close to the separatrix. Note that the unit on the x-axis depends on the parameter. Bottom: PDFs of the relative uncertainties of these fit parameters.*

are observed for the three parameters. While I_{sat} is fitted very accurately, i.e. its average level of uncertainty is rather low (6%), the uncertainty of the parameter U_{float} relative to the sum of U_{float} and T_e is increased (10% on average), and the parameter T_e has got the largest uncertainties (17% on average) together with a very broad distribution. During post processing it is observed, that typically 10% of the fitted T_e data exceeds the uncertainty limit and, therefore, must be replaced by the interpolation. The percentage of interpolations in I_{sat} and U_{float} data is considerably smaller.

4.3 Covariance of the fit parameters

4.3.1 Phenomenology

In the fit model for the $I(U)$ characteristic, the parameters can become covariant whenever the samples deviate from the ideal exponential curve. Reasons for a deviation can be either electronic noise or a change of plasma quantities during one sweep. The latter is relevant if frequency components of the fluctuating quantities not much below the sweep frequency still contain significant power in the probe tip frame of reference, e.g. due to fast poloidal $E \times B$ rotation. This is the case when the probe approaches the shear layer and the separatrix and, therefore, the level of covariance increases with the stroke of the probe.

The fingerprint of parameter covariance in a single fit is, that the statistical errors of I_{sat}, U_{float} and T_e depend on each other. For instance, if the value of T_e is fitted too high, though still within the statistical error margin, then also the values of U_{float} and I_{sat} are affected in a particular direction. This situation is illustrated in figure 4.12, where two sets of fit parameters actually yield comparable least square deviations from an artificial characteristic. Only if the parameters are changed covariantly then this proper matching is retained. If one or two parameters are changed by the same amount without adjusting the third then the deviation would be clearly visible.

The covariance in any pair $A\,B$ out of I_{sat}, U_{float} and T_e is positive. Given the
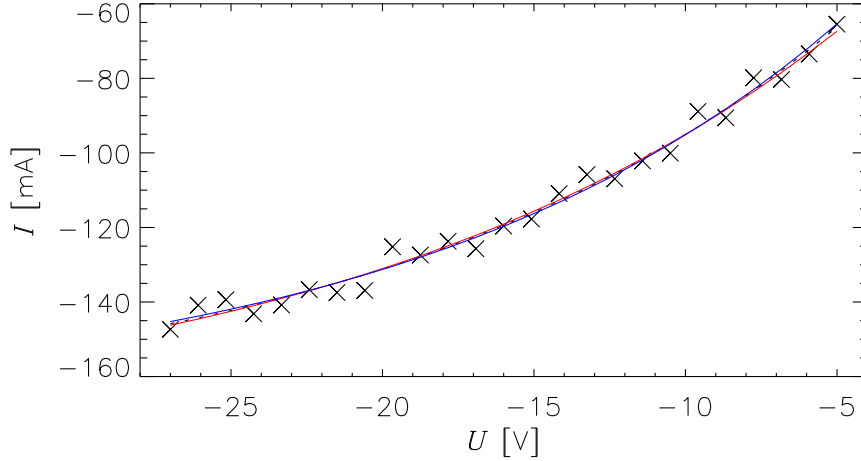
Figure 4.12: *An artificial $I(U)$ characteristic containing noise is plotted using crosses. The data were generated with $I_{sat} = -170\,\mathrm{mA}$, $U_{float} = 2\,\mathrm{V}$, $T_e = 15\,\mathrm{eV}$, plus uniformly distributed current noise with amplitude $5\,\mathrm{mA}$. An exponential least square fit yielded the fit parameters $I_{sat}{}^* = -172 \pm 8\,\mathrm{mA}$, $U_{float}{}^* = 2.7 \pm 1.4\,\mathrm{V}$, $T_e{}^* = 15.8 \pm 2.1\,\mathrm{eV}$, where all uncertainties contain positive covariance. Overplotted with a red and a blue line are the characteristics $(I_{sat}\,[\mathrm{mA}], U_{float}\,[\mathrm{V}], T_e\,[\mathrm{eV}]) = (-176, 3.2, 17)$ and $(-168, 2.2, 14.6)$, respectively. Note that the fit, which was overplotted using dots can hardly be distinguished from these two.*

definition of the correlation function from equation (2.3), this can be put into the following expression

$$X_{AB}^{(\text{cov})}(\Delta t, \Delta y) = \left\{ \begin{array}{ll} > 0 & , \quad |\Delta t| < \text{ packet length }, \quad \Delta y = 0 \\ = 0 & , \qquad\qquad\quad \text{elsewhere }. \end{array} \right. \tag{4.1}$$

Strictly speaking the covariance is equal to $X_{AB}^{(\text{cov})}(0,0)$, but since the data is fitted in packets and since fit parameters are interpolated between adjacent time points, there is a correlation along the temporal extent of the packet. Note that the covariance disappears for $\Delta y \neq 0$, if it has a random occurrence. Overshoots, which are triggered by plasma fluctuations can be correlated for $\Delta y \neq 0$ (section 4.2.3).

Impact on the spectral representation

When the complete two-dimensional cross-correlation function is evaluated, it will contain contributions from the plasma fluctuations and from the covariance of the fit parameters

$$X_{AB}(\Delta t, \Delta y) = X_{AB}^{(\text{plasma})}(\Delta t, \Delta y) + X_{AB}^{(\text{cov})}(\Delta t, \Delta y) \quad .$$

It has been shown in equation (4.1) that the covariance of the fit parameters produces a highly localised structure, whereas the plasma fluctuations are comparatively long-range correlated.

The Fourier transform of X_{AB} is the superposition of the Fourier transform of both addends. Due to the high localisation of $X_{AB}^{(\text{cov})}$, its Fourier transform will be rather broad. Hence, the total power spectrum will be flat towards high wavenumbers or frequencies and the power spectrum of plasma fluctuations is masked. The impact is similar in the cross phase spectrum: Since the covariance is positive, the cross phase of its Fourier transform is zero. Consequently, the entire cross phase spectrum deduced from X_{AB} will always tend to zero towards high wavenumbers or frequencies.

To conclude, a reliable cross spectrum of plasma fluctuations can only be obtained, if one is able to separate the constituents $X_{AB}^{(\text{plasma})}$ and $X_{AB}^{(\text{cov})}$ before the transform.

4.3.2 Correction in the data analysis

When two-dimensional cross-correlation functions are evaluated using fitted data from fast swept probe measurements, the precise localisation of the covariance peak is clearly observed. Thus, this peak can be masked, but the missing values must be replaced. A convenient way in order to achieve this is to do a two-dimensional interpolation. Two options were investigated: To use the values of a minimum curvature surface, and to fit a two-dimensional model function. In principle both methods are appropriate, whereupon the fit yields slightly better results and should

be preferred, provided there is an adequate model. In the case of plasma fluctuations, model functions are supplied in appendix A.3.

Exemplarily the two-dimensional interpolation is demonstrated using the minimum curvature method to correct the cross-correlation between the fit parameters U_{float} and T_e. The primary two-dimensional function is displayed in figure 4.13. First, the base area in Δt and Δy is selected, which has usually the same size as the cutout shown in the figure. Second, at $\Delta y = 0$ the peak and its extent in temporal direction are masked. A numerical procedure (min_curve_surf, [RSI 1997]) eventually calculates the minimum curvature surface using all data of the base area except the masked values, and finally the values in the gap are replaced by the values on the surface. The resulting cross-correlation without the covariance peak is also displayed in figure 4.13. In this case it can be observed, that the ridge of the underlying correlation structure, which stems from plasma fluctuations, does not pass through $\Delta y = 0$ and $\Delta t = 0$. Hence, there is a non-zero phase shift between U_{float} and T_e fluctuations.
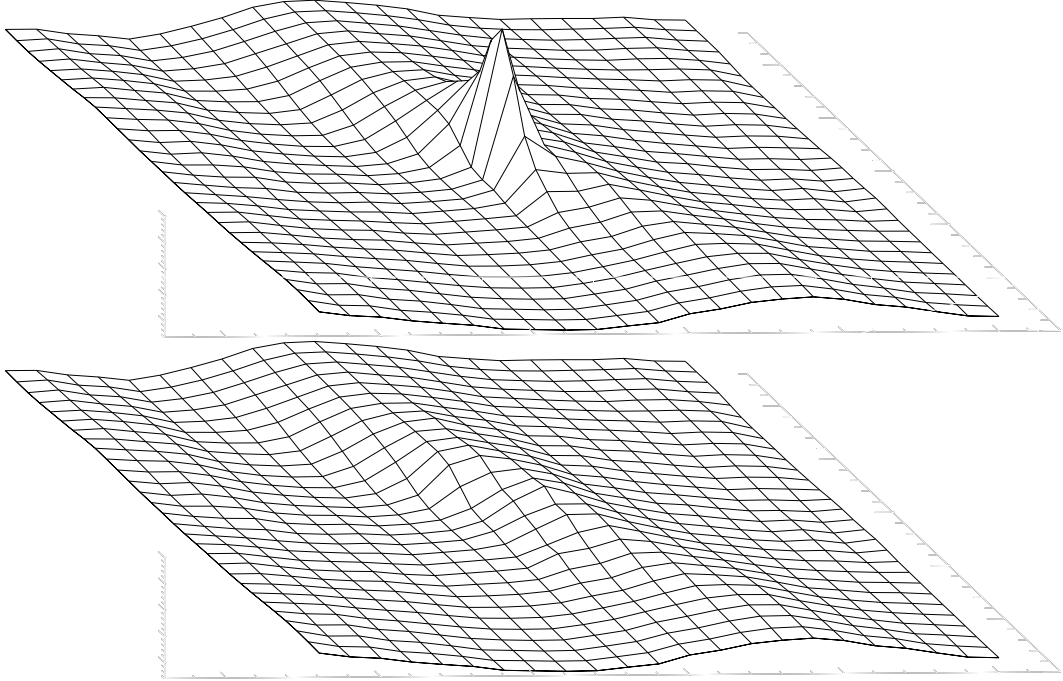
Figure 4.13: *Replacing the covariance peak by a two-dimensional interpolation. On top is the cross-correlation function between the fit parameters U_{float} and T_e, shown as a surface with the function value in the vertical coordinate and the independent variables Δy and Δt forming the two-dimensional grid. The ranges are $\Delta t = \pm 5\,\mu s$ (front to back) and $\Delta y = \pm 2.2\,cm$ (right to left), with a spacing of $0.35\,\mu s$ and $0.2\,cm$, respectively. Connected to the peak is a small ridge (± 5 samples or $|\Delta t| < 1.8\,\mu s$) extending in temporal direction at $\Delta y = 0$. At the bottom the result of a two-dimensional interpolation is displayed, where the peak and the ridge have been replaced.*

Note that the technique to mask the central peak can also be applied to the autocorrelation function. In this case the variance instead of the covariance is the source of the peak. Masked values can be replaced using the fit function from appendix A.3.1. After the correction, the autocorrelation should be renormalised to the interpolated value at $\Delta y = 0$ and $\Delta t = 0$.

A separation of signal and methodic or experimental noise in the domain of the correlation function is a common technique. For instance it has been applied successfully by Sattler and Hartfuss [1993] and Bäumel [2002] in order to measure temperature fluctuations in the plasma core by highly resolved electron cyclotron emission radiometry.

No correction in single channel analysis

One must not forget that despite the feasible correction of the correlation function, recovering the time traces of I_{sat}, U_{float} and T_e without the covariance induced noise is not possible. Consequently the cross spectrum between two quantities on the same tip is in error, at least as long as the fluctuation amplitudes are smaller than the influence of the covariance. An arithmetic effect can lead to an apparently defined phase between n_0 and T_e: Since n_0 is calculated from fitted I_{sat} and T_e by the operation

$$n_0 \sim \frac{I_{sat}}{\sqrt{T_i + T_e}} \ ,$$

the assumption $T_i = T_e$ together with the fact that the relative fit error of I_{sat} is much smaller than the one of T_e leads to an anticorrelation of n_0 and T_e. Indeed using swept Langmuir probes a phase shift of π between n_0 and T_e has been reported in the past [Hidalgo et al. 1992], but the influence of the fit parameter covariance was not discussed.

4.4 Channel Equilibration

If wavenumber spectra are to be generated, it is necessary to do a multichannel analysis. Here, individual channels correspond to probe tips, which are connected to separate amplifiers, transmission lines and data acquisition channels. In order to deduce the correct spatial fluctuation patterns one requires equal sensitivites for all channels. Such state is hardly feasible in the experiment. For instance the Langmuir probe tips themselves are a common source of deviation between different channels: The contact resistance between the graphite tip and the copper cable cannot be reproduced with arbitrary precision. Additionally, the exposed part of the tip will suffer from thermomechanical stresses that possibly lead to micro cracks or defects in the graphite, which finally affect the electric resistance, too. Thus, even an initial state with nearly homogeneous sensitivites may deteriorate after several cycles of operation in a plasma.

It is possible to compensate for different channel sensitivities in the later ana-lysis by redistributing the measured signal power evenly among the channels. A common way to achieve this is to introduce weighting factors for each channel's amplitude. The process to deduce these weighting factors by statistical methods is called equilibration and will be specified in the following sections.

4.4.1 Basics

Since the analysis is to be carried out with fluctuation data, the first important step is to remove the offset value and low frequency components. Therefore, a second order regression was subtracted from the time trace of every quantity and the residuum was filtered by a second order highpass with Bessel characteristic [Tietze and Schenk 1980]. A threshold frequency of $1\,\mathrm{kHz}$ turned out to be appropriate for this application.

The simplest form of equilibration is to conserve the total measured fluctuation power P_t and to distribute it uniformly. This is called the power weighted equilibra-tion and, given the power, or more accurately *autopower*, P_i is measured at channel i $(i = 1 \ldots N)$, this yields

$$w_i^2\, P_i \;=\; \frac{1}{N}\, P_t \;=\; \frac{1}{N} \sum_{i=1}^{N} P_i \;,$$

where w_i are the individual channel weights that are multiplied with the amplitude. Dividing this equation by w_i^2 and adding up all channels, it is obvious that the weigths obey

$$\sum_{i=1}^{N} \frac{1}{w_i^2} \;=\; N \;. \tag{4.2}$$

The method is robust but naturally it does not distinguish between signal and noise. In a situation where the signal to noise ratio varies between different channels, this can lead to unsatisfying results. An example (table 4.1) should illustrate this: Consider four channels A-D, where A and B have the same properties, C is noisy and D has got a reduced sensitivity, i.e. a lower amplitude. Ideally the channels

channel	A	B	C	D
ratio of noise power	0	0	$\frac{1}{2}$	0
relative sensitivity	1	1	1	$\frac{1}{2}\sqrt{2}$
w_i^2 from simple equilibration	1	1	$\frac{2}{3}$	2

Table 4.1: *Equilibration of channels A-D with different sensitivities and different signal to noise ratios, and corresponding weights w_i according to equation (4.2).*

A-C should receive equal weights and the fourth channel should be rescaled, but if the power weighted equilibration is applied straightforward, this is not the case, as shown in the table. To improve the power weighted equilibration, one must distinguish between signal and noise during the equilibration procedure.

4.4.2 Equilibration of Correlated Power

It is helpful to consider the measured power per channel as sum of signal power and power due to noise,

$$P_i \; = \; P_{i,\,signal} \; + \; P_{i,\,noise} \quad .$$

Usually, noise and signal cannot be disentangled in a single channel measurement. In particular, the noise amplitude as a function of time is not available.

If there exist several channels and if the signals are correlated between these channels, it is possible to evaluate the non-zero cross-power $P_{(i)\,(i+j)}^{(X)}$, which is the covariance of the channel i amplitude and the channel $i+j$ amplitude. Note that the second channel is denoted by the relative channel distance j, which can be both negative and positive. Additionally, the cross-power should be evaluated at a particular time lag $\hat{\tau}$ between channels i and $i+j$, where the signals are not orthogonal. For a more detailed definition of orthogonal and uncorrelated fluctuations, see [Müller and Heywang 1990]. The result of the cross-power calculations will be similar to the unnormalised cross-correlation (2.3), but without an averaging over equivalent channel pairs. Uncorrelated noise will be strongly damped. Rescaling the channels by weighting factors modifies the cross-power according to

$$P_{(i)\,(i+j)}^{(X)}(\hat{\tau}) \quad \rightarrow \quad w_i\,w_{i+j}\,P_{(i)\,(i+j)}^{(X)}(\hat{\tau}) \quad . \tag{4.3}$$

Hence, the weights should be adjusted in such a way, that the rescaled cross-power on the right hand side of formula (4.3) does not depend on i when j and $\hat{\tau}$ are fixed. Conservation of total power, however, is not guaranteed by this procedure and must be included separately as a constraint. The equilibration becomes a numerical nonlinear optimisation problem, where the following expression has to be minimised:

$$\sum_{\hat{\tau},\,j} \sum_{i=\max(1,\,1-j)}^{\min(N,N-j)} \left(w_i\,w_{i+j}\,P_{(i)\,(i+j)}^{(X)}(\hat{\tau}) - \frac{1}{N-|j|} \sum_{i=\max(1,\,1-j)}^{\min(N,N-j)} w_i\,w_{i+j}\,P_{(i)\,(i+j)}^{(X)}(\hat{\tau}) \right)^2$$

$$+ \; \lambda \left(N - \sum_i \frac{1}{w_i^2} \right)^2 \quad \overset{!}{=} \quad \min \quad . \tag{4.4}$$

There are three terms on the left hand side of equation (4.4): The first addend within the double sum is the actual cross-power and the second is the actual average of channel pairs with distance j. By taking the difference between both addends squared, deviations of individual cross-power are minimised. Outside the double

sum there is the formulation of power conservation like in equation (4.2), only it is weighted relative to the cross-power by the constraint parameter λ .

The sum over $\hat{\tau}$ and j is important for two reasons: Firstly, oscillatory solutions of adjacent w_i could result, if only one sort of channel distances, even or odd j are accounted for exclusively. Therefore a mix of even and odd j is recommended, and their count must be at least equal to N being the number of free parameters. Secondly, one must select particular values of $\hat{\tau}$, where the signal fluctuations are not orthogonal, i.e. where the covariance is non-zero. Furthermore, the statistics can be improved, if a set of different $\hat{\tau}$ is used simultaneously.

Equation (4.4) was implemented in a computer code using the module E04JYF from the numerical library [Num 1999] for minimisation. By testing different values of the constraint parameter, it has been observed that one should select a small value in the beginning, and repeat the calculation with increasing magnitudes of λ . Meanwhile, the optimisation success and the quality of power conservation must be carefully monitored. Finally, the iteration can be stopped, if the deviation of the total power is below an appropriate threshold. For the analysis of the Langmuir probe data the threshold was set in such a way, that equation (4.2) must be fulfilled within 1% relative deviation.

To illustrate the capability of the numerical method, the sample data of the previous example (table 4.1) can be used. An assumption about the cross-power must be made in advance: It will be set exemplarily to 0.5 at one channel distance, and to 0.2 at two channel distance. If routed through the previously defined sensitivities, that would yield "measured" cross-powers of 0.5 for the combinations AB or BC, $\frac{1}{4}\sqrt{2}$ for CD, 0.2 for AC, and $\frac{1}{10}\sqrt{2}$ for BD. The result of the numerical equilibration is shown in table 4.2 with two different values of the constraint parameter. If λ vanishes, N and $\sum w_i^{-2}$ deviate, but as soon as the influence is significant, the "ideal" weighting is obtained within numerical precision.

channel	A	B	C	D
ideal weighting w_i	0.9354	0.9354	0.9354	1.3229
numerical equilibration				
w_i ($\lambda = 10^{-12}$)	0.9056	0.9056	0.9056	1.2807
w_i ($\lambda = 10^{-6}$)	0.9354	0.9354	0.9354	1.3229

Table 4.2: *Numerical equilibration with the correlated power method. Sensitivities were taken from table 4.1 . The nominal cross-power was set to 0.5 for the one-channel distance and to 0.2 for the two-channel distance.*
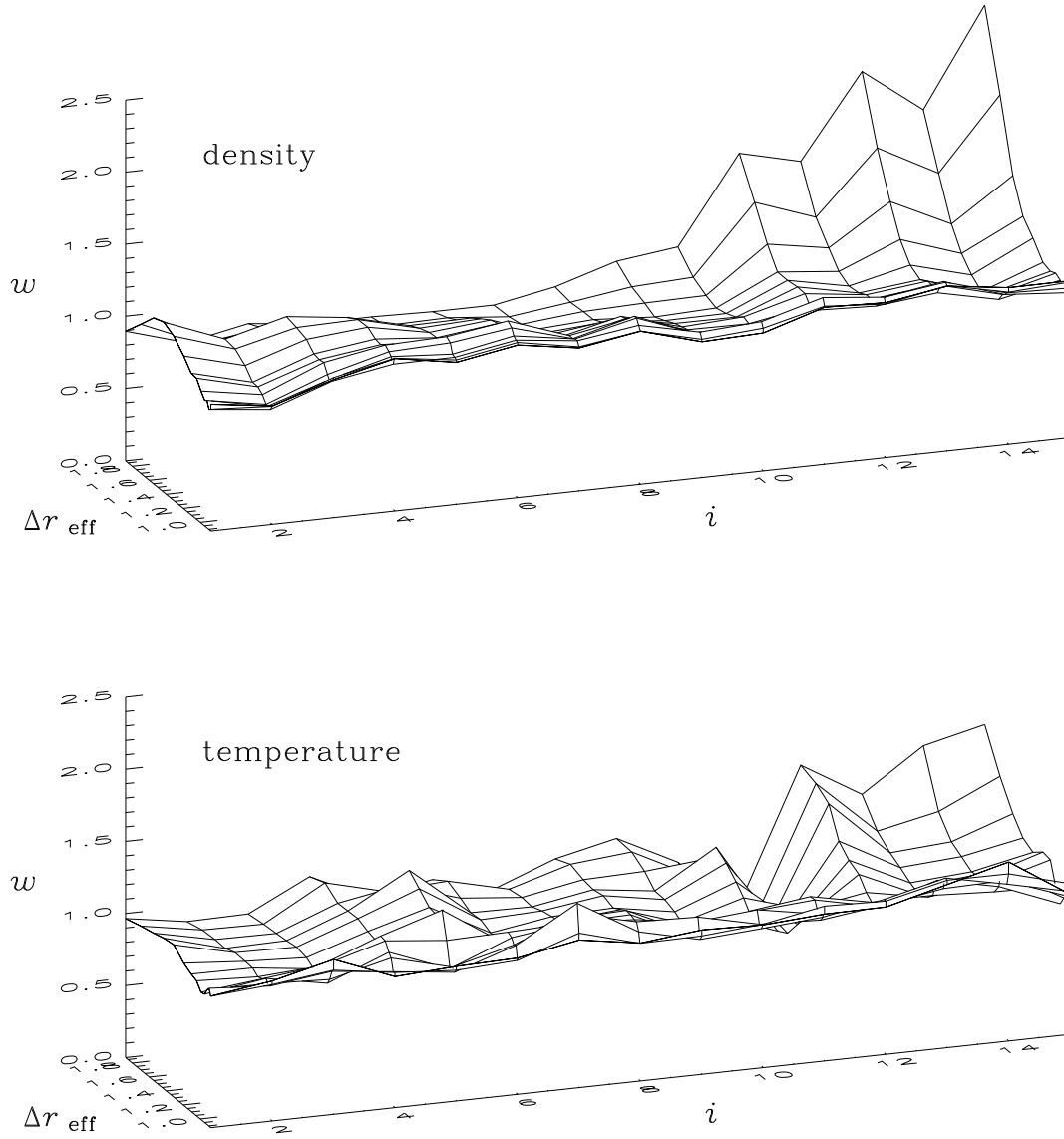
Figure 4.14: *Weights of density and temperature fluctuation data as a function of both the channel number i and the probe position r_{eff} . The weights were estimated by minimising the expression from equation (4.4).*

4.4.3 Weighting of the Langmuir Probe Data

Now the 15 tip Langmuir probe array should be considered. The weighting factors have been determined by the correlated power method, separately for each fluctuating quantity and for each radial position of the probe. Channel distances j from 1 through 5, and 10 different values of $\hat{\tau}$ were used. In figure 4.14 the results are presented for the fluctuations of electron temperature and density during the probe's outward movement.

When looking at the data for small Δr_{eff} , i.e. close to the bulk plasma, the

weighting is nearly homogeneous with values close to unity. This means that both proper reproduction of measurement channels and probe tip alignment were successful. For large Δr_{eff} a trend is visible in temperature and density, which assigns larger weights to the higher channel numbers i. Probably the alignment of the tip array to the magnetic surface is not at its optimum there.

Note, that the fine structure of the weighting is different for density and temperature. This is, however, not necessarily a contradiction, since on one hand the radial scale length of the two quantities may well be different. On the other hand at fixed radial position separate weighting profiles along the channel index i are also possible. For instance, if the tip areas are slightly different, then mainly the evaluated density is affected but not the temperature. If there are parasitic currents that shift the phase in the current voltage characteristic, then it is vice versa. The latter effect will preferably appear for small current signals, i.e. for large Δr_{eff}, and it is most likely the cause of the weight dropout in the temperature of the channel with the index $i = 11$.

4.5 On the use of correlation functions

4.5.1 Correlation of the poloidal electric field

The poloidal electric field will be obtained from $\boldsymbol{E} = -\operatorname{grad} U_{plasma}$, where U_{plasma} is calculated from the fit parameters U_{float} and T_e according to the Emmert model (equation 2.17). In the following only the gradient perpendicular to the magnetic field and tangent to the magnetic surface is of interest and this is approximated by taking finite differences of U_{plasma} on adjacent probe tips

$$E_{pol} = -\frac{1}{d} \left(U_{i+1} - U_i \right) \ ,$$

where d is the tip spacing. Individual U_i are the sum of the scaled local T_e and U_{float}, and both are covariant fit parameters, i.e. they contain correlated noise. Thus, the deduced electric field is erroneous, but its correlation function can be recovered:

Firstly, the noise is identified with the central peak (typically $|\Delta t| < 7\,\mu\text{s}$, $\Delta y = 0$) in the correlation function of the plasma potential. This has been discussed in section 4.3.2. The peak is masked and the missing values are replaced by model values, which are obtained from the fitted model function (appendix A.3.1). The new correlation function without the noise peak is referred to as the *corrected* correlation.

Secondly, the Wiener-Khinchin Theorem [Weisstein 2005c] says, that the backward transform of the absolute square of the $U := \tilde{U}_{plasma}(t, y)$ Fourier transform yields the two-dimensional correlation function.

$$X_{UU}(\Delta t, \Delta y) = \mathcal{F}^{-1}\big[\ |\ \mathcal{F}[U(t, y)]\ |^2\ \big] \qquad (4.5)$$

In this formula $\mathcal{F}^{-1}$ denotes the backward transform. If the spectrum $\mathcal{F}[U(t,y)]$ is multiplied with the wavenumber k in Fourier space, it corresponds to the first derivative in real space, i.e. the electric field. The absolute square is the spectrum of the electric field's correlation function. Since it contains k^2, this is equal to the second spatial derivative applied to the $\tilde{U}_{plasma}$ correlation function.

In order to approximate the second spatial derivative, a finite difference formula is used, which can easily be derived from the following consideration: Assume that U is known in between two tips, so that

$$E_{pol,\,i} = \frac{1}{d} \left(U_{i-\frac{1}{2}} - U_{i+\frac{1}{2}} \right) \;.$$

By making use of the linearity in the correlation integral, the (unnormalised) correlation value between arbitrary tips i and j becomes

$$E_{pol,\,i} \star E_{pol,\,j} =$$
$$\frac{1}{d^2} \left(U_{i-\frac{1}{2}} \star U_{j-\frac{1}{2}} + U_{i+\frac{1}{2}} \star U_{j+\frac{1}{2}} - U_{i-\frac{1}{2}} \star U_{j+\frac{1}{2}} - U_{i+\frac{1}{2}} \star U_{j-\frac{1}{2}} \right)$$

Both the first and the second term on the right hand side correspond to the value of the correlation function of U at space lag $\Delta y = (j-i) \cdot d$. The third term denotes the space lag $\Delta y = (j-i+1) \cdot d$ and the last term $\Delta y = (j-i-1) \cdot d$. It is obvious that a noise peak in the correlation function of U would appear in the one of E_{pol} three times, namely for $(j-i) \in \{-1, 0, 1\}$.

To summarise, the correlation function of the poloidal electric field is

$$X_{EE}(\Delta y) = \frac{1}{d^2} \left(2X_{UU}(\Delta y) - X_{UU}(\Delta y + d) - X_{UU}(\Delta y - d) \right) , \qquad (4.6)$$

where the additional dependency on the time lag Δt has been omitted, since it is common to all terms. Formula (4.6) represents the negative spatial curvature of the corrected correlation X_{UU} in finite difference approximation.

4.5.2 Cross-correlation and the calculation of transport

Turbulent radial fluxes Γ_r^*, Q_r^* and q_r^* (see section 1.4.1) are calculated by multiplying the radial velocity $\tilde{v}_r$ with fluctuations of density and temperature, respectively. The radial velocity is an $E \times B$ drift velocity and it is generated by that part of the electric field which is perpendicular to the magnetic field and tangent to the magnetic surfaces.

$$\tilde{v}_r = B^{-1} \tilde{E}_{\text{e dia}}$$

If outward fluxes are counted positive, then the electric field vector must point in the direction of the electron diamagnetic drift, where the latter is defined by the nonfluctuating gradient of the plasma pressure and $\boldsymbol{B}$. This convention is illustrated in figure 4.15, and in the following the symbol $\tilde{E}_{\text{e dia}}$ is used to indicate fluctuations of the electric field relevant for radial transport.
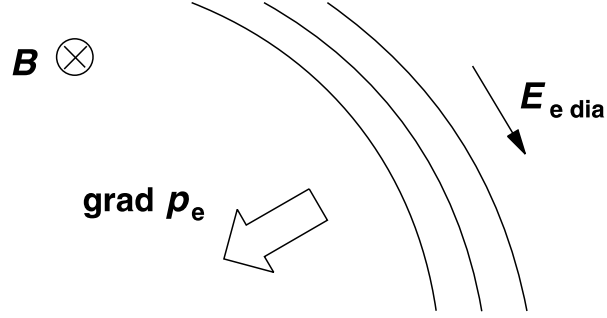
Figure 4.15: *Definition of the transport relevant electric field, pointing into the electron diamagnetic direction. Schematically a sector of the cross section in a toroidal magnetic configuration is shown. The plasma center is to the left and the plasma edge is on the right. The lines denote magnetic surfaces.*

Since only the stationary flow is examined, the product of $\tilde{n}_0$ (or $\tilde{T}_e$) and $\tilde{v}_r$ must be averaged in time and space. One should remember that the cross-correlation already provides the required average, when evaluated at $\Delta t = 0$, $\Delta y = 0$:

$$< \tilde{n}_0 \, \tilde{v}_r >_{t_S, \, y_S} \; = \; \lim_{t_S, y_S \to \infty} \; \frac{1}{(2 \, t_S) \, (2 \, y_S)} \int_{-t_S}^{t_S} \int_{-y_S}^{y_S} dy \, dt \; \tilde{v}_r(t, y) \, \tilde{n}_0(t, y) \; . \qquad (4.7)$$

In order to obtain the correct flux, one has to take care that this correlation function is not normalised to any variance of the fluctuating variables but only to the lengths of the integration intervals. For discrete and finite data the correct form has been supplied in equation (2.3).

The poloidal electric field $\tilde{E}_{e \, dia}$ is eventually calculated by taking finite differences of the plasma potential on neighbouring probe tips. Denoting the channel or probe tip by the subscript i and considering the tip arrangement from bottom to top at the outward side of the W7-AS plasma, the transport relevant electric field is

$$(\tilde{E}_i)_{e \, dia} \; = \; \frac{1}{2d} \left(\tilde{U}_{i+1} \; - \; \tilde{U}_{i-1} \right) \; , \quad \text{where} \quad \tilde{U} = \tilde{U}_{plasma} \qquad (4.8)$$

and d is the distance between adjacent tips. The electric field at position i is deduced from the potential difference of both neighbouring tips $i+1$ and $i-1$, therefore the denominator in the formula is $2d$. Formula (4.8) yields a positive $\tilde{E}_{e \, dia}$ if the main magnetic field in the W7-AS carries a positive sign.

Since the transport relevant flux in equation (4.7) is linear in the plasma potential, it is possible to interchange the integral with the finite-difference evaluation of the electric field. Writing $X_{Un}(\Delta t, \Delta y)$ for the discrete correlation function between

plasma potential and density, the average particle flux can be expressed as

$$
\begin{aligned}
< \tilde{n}_0 \, \tilde{v}_r >_{t_S} \quad &= \quad (B \, 2d)^{-1} \left(< (\tilde{n}_0)_i \, \tilde{U}_{i+1} >_{t_S} - < (\tilde{n}_0)_i \, \tilde{U}_{i-1} >_{t_S} \right) \\
&= \quad \frac{1}{B \, 2d} \left(X_{nU}(0, d) - X_{nU}(0, -d) \right) \\
&= \quad \frac{1}{B \, 2d} \left(X_{Un}(0, -d) - X_{Un}(0, d) \right) \; .
\end{aligned}
\tag{4.9}
$$

Note, that at this point the result is not affected by a noise peak at $\Delta y = 0$ in the correlation function X_{Un}.

In order to estimate the wavenumber spectrum of the flux, the cross-correlation X_{Un} has to be corrected for the central noise peak. To achieve this, the noise peak should be replaced by the values of the fitted model function from appendix A.3.2. The corrected function is used in the calculation of the cross-correlation between electric field and density X_{En} following the finite difference approximation of the equations (4.8) and (4.9). Thereby the full range of Δt and the available range of Δy is retained.

Investigating the formula for the backward transform of the cross spectrum from equation (2.5), it becomes obvious that the origin of the independent variables $\Delta t = 0$ and $\Delta y = 0$ is the relevant point for the mean transport. This has been set up explicitly in equation 4.7. The mean transport is equivalent to the total and complex sum of the cross spectrum with constant phase factor equal to unity (see equation 2.5). During the summation all imaginary parts cancel due to the hermitian symmetry and only the real parts remain. The latter are the Fourier image of even waveforms, i.e. only even patterns in the cross-correlation between electric field and density contribute to the transport.

A different approach to the spectrum of the transport is also possible, if one argues that transport is the convolution of potential and density in Fourier space [Theimer 1990].

Chapter 5

Results on Wendelstein 7-AS plasma

The main results are presented and discussed. Based on measurements with the multi-tip fast swept Langmuir probe array in the edge plasma of the Wendelstein 7-AS, the following contains several aspects of the observed turbulent fluctuations. The behaviour of floating potential U_{float} and ion saturation current I_{sat} data are known from other machines (e.g. Zweben and Gould [1985]) and also from former W7-AS measurements (Bleuel et al. [2002]). With the present campaign the electron temperature T_e is available simultaneously to U_{float} and I_{sat} and with good resolution. Thus, some of the figures are the first of their kind.

In the beginning a basic comparison with independent diagnostics is done. By plotting average values of the highly resolved probe data, fair agreement is found. For the second part average values are subtracted and only the turbulent fluctuations are discussed. Spatio-temporal as well as wave properties are exposed using correlation and Fourier transform techniques, respectively. A relationship between different plasma quantities is established. In the third and final part the fluctuation induced transport is calculated and compared to global plasma confinement.

Constraints

The Wendelstein 7-AS target plasma was generated by electron cyclotron resonance heating (ECRH). For the machine configuration several constraints had to be fulfilled:

- Magnetic surfaces must be smooth at the position of the probe tips and no magnetic islands should be present. The shape of the tip array must be correct for this specific configuration as well. For such conditions correct alignment within one magnetic surface is possible and one can assume both average values and fluctuation properties to be homogeneous along the tip array. The geometry of magnetic surfaces in the W7-AS is determined by the rotational transform t (equation 1.4), which depends on the current ratio in the external

coil systems. In our case, the tip alignment was optimised for values of $\iota \approx 0.35$. The calculation of magnetic surfaces and mapping of the probe tips was done with the TRANS code [Sardei and Richter-Glötzl 1988].

- The power flux should be small to reduce the heat load on the tips. This will allow for either maximal intrusion of the probe into the plasma or maximal lifetime of the graphite tips. Therefore, only one gyrotron was used for plasma heating. The nominal field strength in this mode of operation is $B = 2.5\,\text{T}$ (on axis).

When the probe is reciprocating in the stationary phase of a W7-AS plasma, data from the inward going probe can be compared to data from the outward going probe in order to analyse, whether a hysteresis exists in the radial profile of average (i.e. non-fluctuating) values. To summarise the experimental findings, such a hysteresis was not found, at least as long as the probe did not reach the last closed magnetic surface (LCMS). For such case, i.e. the probe crossed the separatrix and intruded into the bulk plasma, usually global signals like plasma energy content, bulk temperature profiles or line averaged density changed. The plasma could not be regarded as stationary any more and the data was disregarded.

In principle, the interpretation of the measurement is easiest, if the probe is located exactly at the separatrix (see section 1.4.2). Due to the high fluctuation levels, however, the evaluation of the recorded probe characteristics becomes unreliable at this position. Hence, the presented data covers only the range from the SOL until several mm outside the LCMS.

5.1 Validation of average values

Radial profiles of the electron temperature T_e and density n_0 are measured in the bulk plasma by the W7-AS Thomson scattering system. T_e is additionally measured by electron cyclotron emission (ECE). Both systems are located at different toroidal positions, therefore they must be mapped onto the r_{eff} coordinate. Since their temporal resolution is much smaller than that of the fast swept Langmuir probe, only a temporally averaged value of the Langmuir probe data can be compared.

T_e and n_0 values from the Langmuir probe data are averaged in several time windows that correspond to different radial positions. The reciprocation of the probe within the scrape-off layer (SOL) is mapped to the r_{eff} coordinate. But there is a restriction: Outside the LCMS, i.e. outside the separatrix, the radial decay length of the plasma depends on the local connection length to the next limiter in the direction parallel to the lines of the magnetic field. The connection length may vary significantly for different toroidal and poloidal positions. Hence, outside the separatrix the mapping via r_{eff} is not possible. If the profile is extrapolated towards the separatrix, however, one would expect a smooth junction with the profiles from the bulk measurement systems. Additionally there must be a monotonic decrement
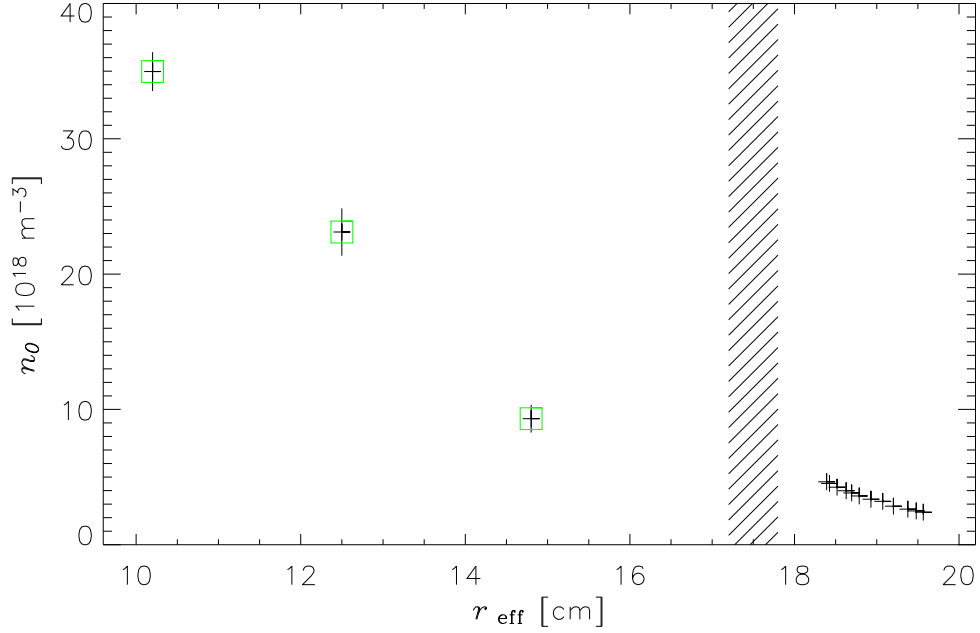
Figure 5.1: *W7-AS discharge #55760 at $t = 1.1\,$s. Plasma electron density measured by YAG Laser Thomson Scattering (crosses with squares) as a function of r_{eff}. Vertical lines are error bars obtained from the standard deviation of several time points within the stationary plasma phase. The crosses for r_{eff} larger than $18\,$cm are Langmuir probe measurements with vertical error bars from the standard deviation of the 15 tips. The grey shaded region indicates the position of the separatrix.*

of T_e in radial direction, since the only heat source is located in the center of the plasma at $r_{\mathrm{eff}} = 0$ (on-axis ECRH).

In figure 5.1 it is shown that the density is decreasing monotonically and that the YAG System and the probe don't yield contradictory results. When extrapolating the YAG and the probe profile linearly to the separatrix, it seems that the probe slightly overestimates the density. This could be explained with an underestimated ion temperature T_i, for the density is calculated from the ratio of the measured saturation current I_{sat} and the sound velocity. If T_i is actually higher, then the sound velocity increases and the calculated density value decreases.

The calibration of the horizontal axis must be commented. In this case, the probe alignment relative to the W7-AS vacuum vessel in conjunction with a TRANS code calculation were used to determine the abolute position in terms of the magnetic surface label r_{eff}. In order to estimate the separatrix position r_{sep} experimentally, the fingerprint of structures with opposite propagation directions in the correlation function of U_{float} fluctuations was utilised. The radial electric field changes sign close to the separatrix, producing a so-called velocity shear layer, e.g. see [Ritz et al. 1984]. On W7-AS Bleuel [1998] showed, that the radial width of the velocity shear layer is typically 1 cm and that both poloidal propagation directions are visible in this region. If it is assumed, that the separatrix is reached after having penetrated the shear
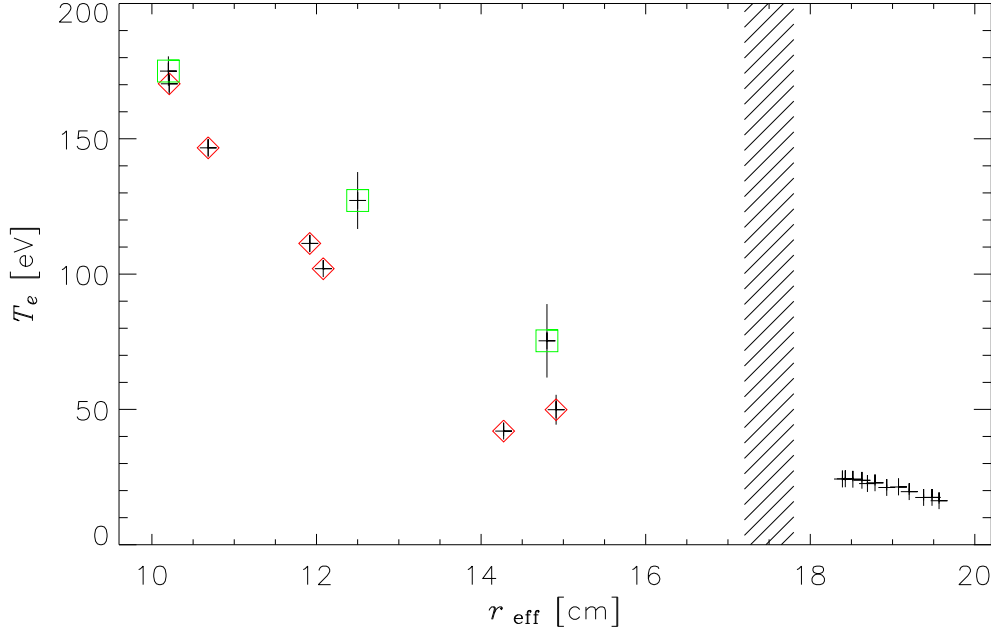
Figure 5.2: *Plasma electron temperature as a function of r_{eff}. Crosses with squares from the YAG system and with diamonds from ECE measurements. Vertical lines are error bars and obtained from standard deviation of several time points within the stationary phase. The crosses for r_{eff} larger than 18 cm are T_e values from the Langmuir probe.*

layer from outside, the separatrix position in terms of the magnetic surface label is $r_{\mathrm{sep}} = 17.5$ cm. The uncertainty of the beginning of the shear layer is estimated to 0.5 cm, based on the comparison of several two-dimensional U_{float} correlation functions to data obtained by Bleuel. The accuracy of the probe's geometrical alignment relative to the W7-AS vacuum vessel is estimated to 0.2 cm.

For T_e (figure 5.2) the profile comparison is similar to n_0. This time there is no indication of an over- or underestimation. But there is also a deviation between YAG and ECE values, which is larger than the error bar, and which is probably due to mapping uncertainties, i.e. the r_{eff} coordinate is in error. There are attempts to find a formulation of mapping uncertainties and their effects and thus bring together several diagnostics from different locations by application of probability theory [Svensson et al. 2004], however this will not be discussed here.

5.2   Characterisation of W7-AS edge turbulence

The simplest way to give an impression of the plasma fluctuations as measured by the probe array is to show a two-dimensional contour plot, where the gray scale denotes the fluctuation amplitude. Temporally and spatially resolved saturation current I_{sat} (figure 5.3) and electron temperature T_e (figure 5.4) are compared. The data were recorded in the scrape-off layer plasma of the W7-AS discharge number

55760. For I_{sat} such visualisation already exists [Bleuel 1998], whereas for T_e such representation was not available before.
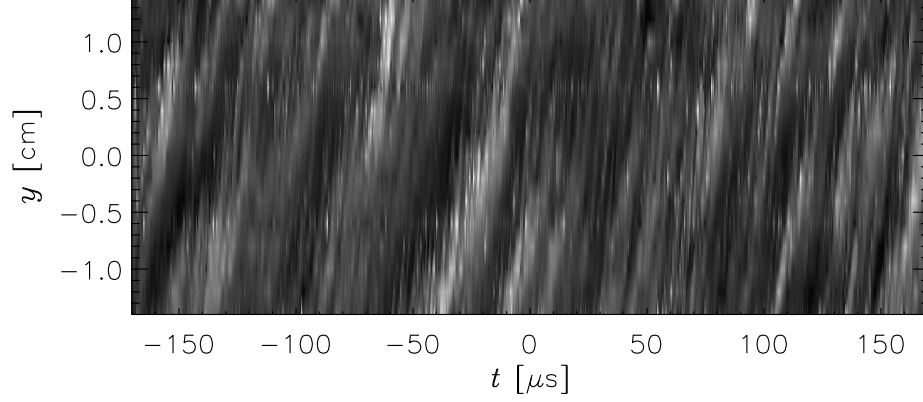
Figure 5.3: *A finite time window extending along the horizontal axis for all 15 channels, which are assigned to the vertical axis, displaying the spatio-temporal evolution of $|I_{sat}|$ fluctuations. The amplitude is encoded using different shades of grey, where lighter shades correspond to higher amplitudes. By suppressing the average value the colour range is used most effectively. The structures reflect mainly fluctuations of the plasma density n_0.*
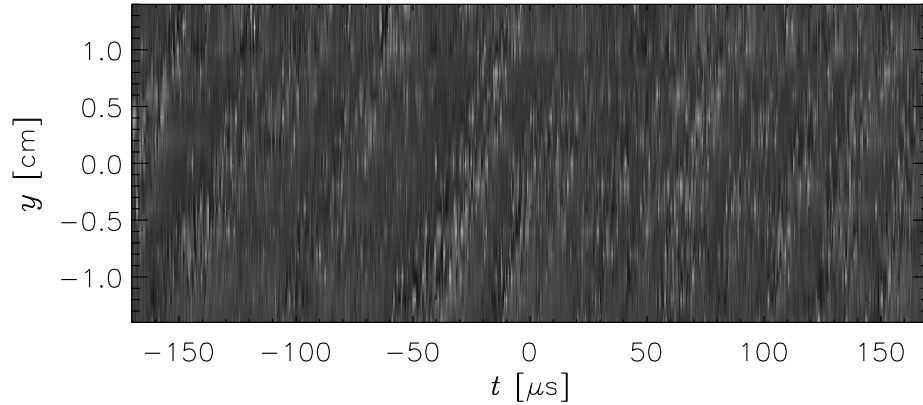
Figure 5.4: *The same window with the spatio-temporal evolution of T_e. Again the shade of grey corresponds to the fluctuation amplitude and the mean value is suppressed.*

Since the channels are arranged poloidally and since the inclination of the magnetic field lines is small, the vertical direction in the picture corresponds in good approximation to the coordinate, which is perpendicular to the field lines and tangent to one magnetic surface. To compensate for different channel sensitivities, all channels have been normalised to equal standard deviation.

Please note, that the vertical resolution in the figures 5.3 and 5.4 is 15 points. The continuous evolution of the colour chart along the y-axis is only generated by

an interpolating algorithm of the visualisation routine CONTOUR [RSI 1997].

Stripe patterns with varying lengths and sizes are observed in both figures. The patterns are inclined, indicating a nearly uniform motion of the structures in the upper direction. In other words: There is an average poloidal velocity. Since the magnetic field is pointing left to right and since the pressure gradient is directed radially inward (i.e. into the image plane), the upward movement is in direction of the ion diamagnetic drift. Within $30\,\mu$s the structures propagate $2\,$cm on average, thus the magnitude of the poloidal velocity is roughly $7 \cdot 10^2\,\mathrm{m\,s^{-1}}$. Considering the local magnetic field strength of $2.3\,$T, and assuming that the poloidal velocity arises from $E \times B$ drift (equation 1.5), then there must exist an electric field, which points radially outward and has a strength of $+1.6 \cdot 10^3\,\mathrm{V\,m^{-1}}$.

Various structure sizes are typical for turbulent phenomena. Additionally, such fluctuation structures exist only for a limited amount of time. That can be recognised in the figures, for instance the large stripe at $t = -30\,\mu$s corresponds to a fluctuation that enters from below at $y = -1.4\,$cm and starts to decay at $t = -10\,\mu$s and $y \approx 0.5\,$cm. Other structures are "born" and grow within the spatial extent observed by the probe array like the one at $t \approx -75\,\mu$s and $y \approx 0.5\,$cm (figure 5.3).

Comparing pictures 5.3 and 5.4, two things are remarkable: First, a resemblance at least of the major structures is visible. Given I_{sat} reflects mainly the density, this means that fluctuations in plasma density and temperature are similar. Second, the picture of T_e, which is actually a fit parameter, is much more noisy. In order to extract those structures coherent in I_{sat} and T_e, refined statistical methods are to be employed.

### 5.2.1 Lifetime and poloidal size

Spatio-temporal correlation functions (see section 2.1.2) are evaluated now. This function works out average shape and lifetime of the fluctuation structures. Coherent oscillations would show up as an undamped oscillation, but that is not observed in the probe data and, therefore, the finite lifetime is accounted as another indication of the turbulent origin of the fluctuations.

At $\Delta t = 0$ there is a characteristic width of the correlation function in the spatial direction (figures 5.5 and 5.6). This width is referred to as the poloidal size d_{pol}. It is defined as twice the distance from the central maximum up to the point, where the maximum correlation value has dropped to the fraction $e^{-1} \sim 0.37$.

The correlation function is tilted due to the poloidal propagation. Hence lifetimes τ_L must be measured in the comoving frame of the fluctuations. This can be approximated by taking the extent along the principal axis. More accurately it is defined in [Endler 1994]. It has been demonstrated by Theimer [1997], that the velocity of a uniform poloidal propagation can be deduced from the inclination of the central correlation structure. For small $|\Delta t|$ the ridge defined by subsequent slices $\Delta t = const$ yields the propagation velocity. Similar to the definition of the poloidal size, the lifetime is twice the distance from the origin up to the e^{-1} drop-off.
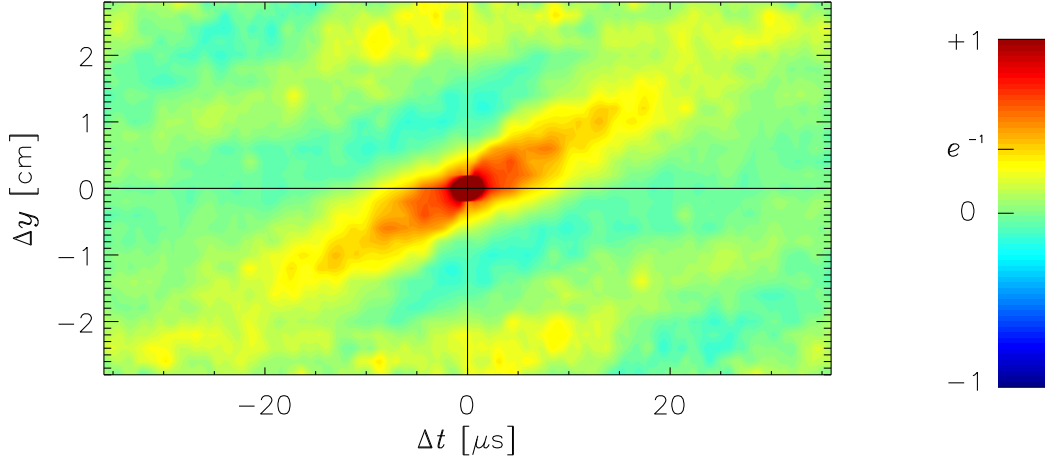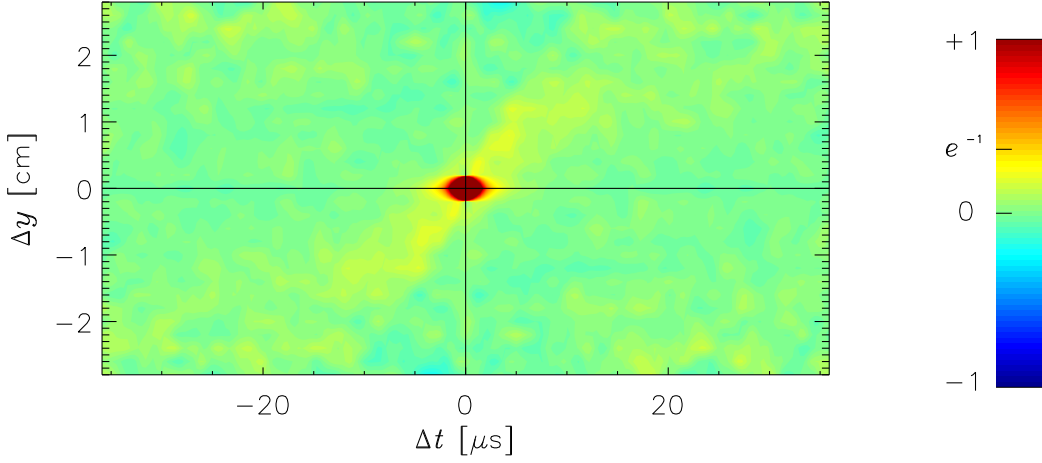
Figure 5.5: *Spatio-temporal correlation function of the electron temperature T_e as a function of time and space lag. The tilt reflects the poloidal propagation. Probe position is in the SOL, about $2\,\text{cm}$ outside the separatrix. A time window of $7\,\text{ms}$ in length was used, corresponding to roughly 20000 samples.*
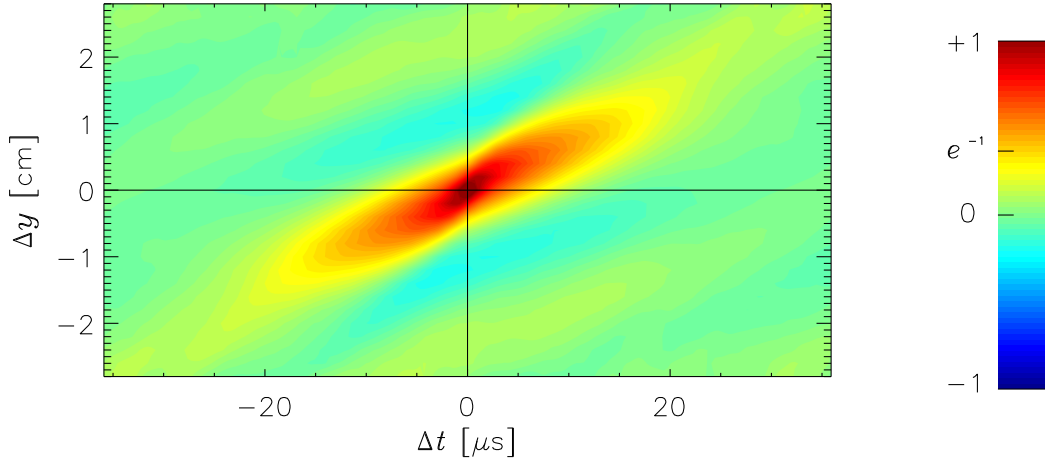
Figure 5.6: *Spatio-temporal correlation function of the electron density n_0 . Same probe and evaluation parameters as in figure 5.5 .*

Figures 5.5 and 5.6 display the two-dimensional correlation functions of electron temperature and electron density fluctuations. In this case the density has been calculated from I_{sat} and T_e according to the Emmert model (section 2.4.4), assuming a constant ion temperature $T_i = \bar{T}_e$. The similarity between $\tilde{n}_0$ and $\tilde{T}_e$ that has been supposed in the previous section is confirmed. Lifetime and poloidal size are basically the same, namely $d_{pol} \approx 28\,\mu\text{s}$ and $\tau_L \approx 1\,\text{cm}$.

When the probe approaches the separatrix and the LCMS (figures 5.7, 5.8, 5.9), the poloidal propagation of the fluctuation structures becomes faster. In this so-called velocity shear region [Bleuel et al. 2002], the measured speed-up is assumed

Figure 5.7: *Spatio-temporal correlation function of T_e when the probe is located close to the separatrix between bulk plasma and SOL. The underlying correlation structure covers only a small range of the color scale, since the latter is normalised to the central noise peak at $\Delta y = 0$ and $\Delta t = 0$.*

to be an effect of an increased radial electric field. The speed-up, however, involves a drawback: The higher the poloidal velocity, the higher are the fluctuation frequencies that are seen by the probe tips. Since the fluctuation frequencies come close to the sweeping frequency, the quality of individual probe characteristics degrades. The reliability of the fitting decreases and the noise of the evaluated parameters increases. It is observed that the electron temperature is affected primarily (figure 5.7).

In order to visualise the underlying structure of correlations due to T_e fluctuations, the colorbar has been compressed in figure 5.8. A structure appears which is similar to the SOL measurement in both d_{pol} and τ_L. Additionally a short living anticorrelation of $\tilde{T}_e$ is observed on adjacent tips ($\Delta y = \pm 2\,\mathrm{mm}$) and with zero time lag. The width in Δt is approximately $1\,\mu\mathrm{s}$. Although this is a small detail in figure 5.8, its impact on the fluctuation spectra is significant (see section 5.2.2). The origin of this structure could not be identified. In further steps of the data analysis, however, it is not considered to be the result of turbulent plasma fluctuations. It is imaginable that in the strongly fluctuating plasma close to the separatrix, the presheaths of neighbouring probe tips are coupled via polarisation currents. This coupling would be capacitive (see the Alfvén wave cable model in section 2.5.2) and it would influence the current in the steep part of the characteristic, and thereby the fitted T_e. Due to the reported problems (see section 4.2.2), when trying to include the Alfvén wave cable model in the evaluation of the characteristics, further investigation has been omitted.

For comparison with the T_e correlation in figure 5.8 the correlation function of the plasma density at the same probe position is shown in figure 5.9. This quantity is significantly less affected by the noise and a rescaling is not necessary.

To conclude, the similarity between the fluctuations of electron temperature and
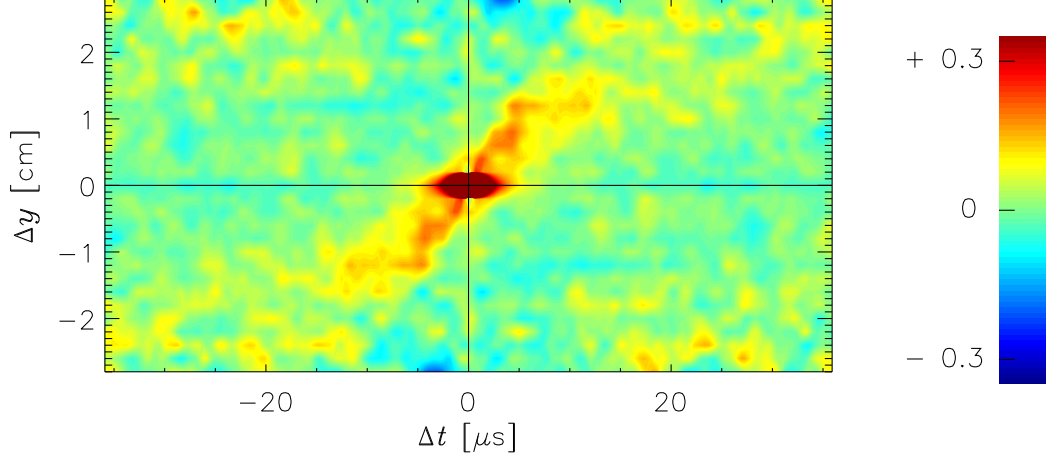
Figure 5.8: *Correlation function of electron temperature, figure 5.7 rescaled.*
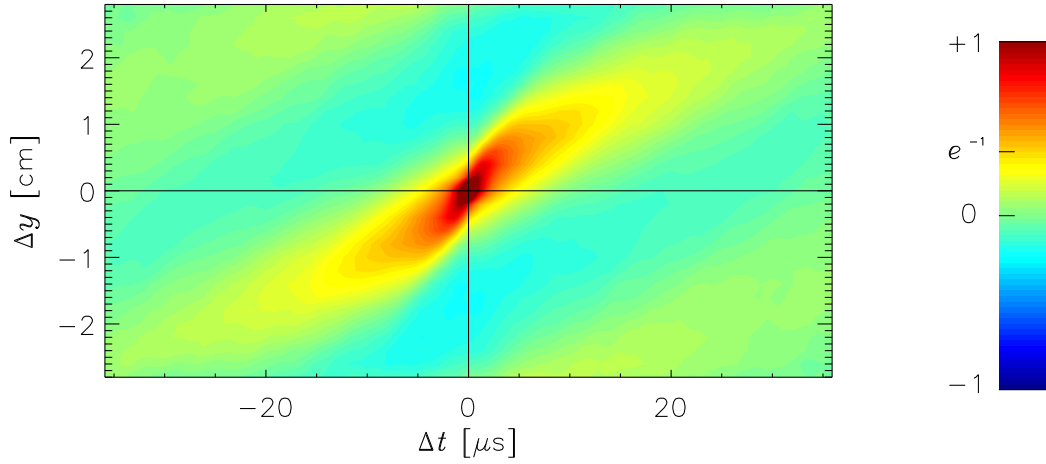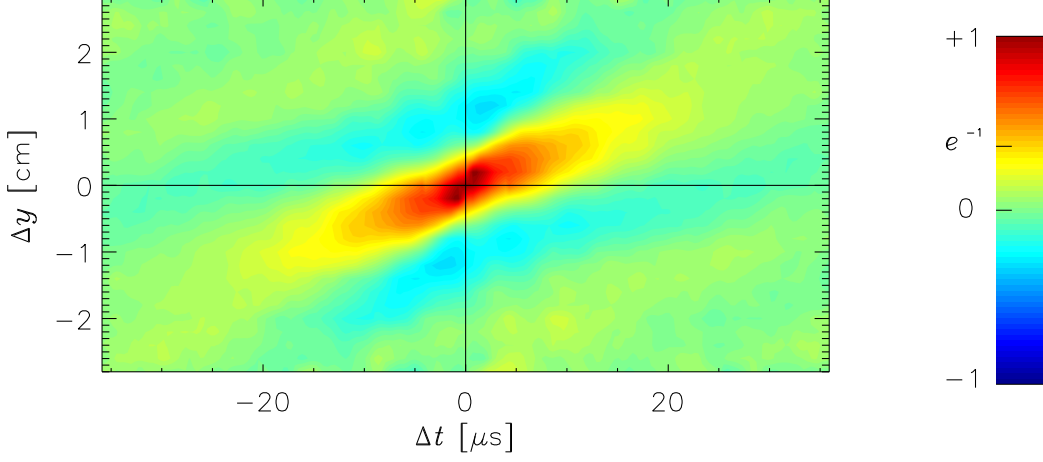

Figure 5.9: *Correlation function of density, probe parameters as in figure 5.7.*

density does not change for the whole range of radial probe positions. When the probe is located close to the separatrix, the fluctuation lifetime is slightly smaller than in the SOL and amounts to $22\,\mu$s, whereas the poloidal size is basically the same as in the SOL. Close to the separatrix a propagation velocity of $2.5 \cdot 10^3\,\mathrm{m\,s^{-1}}$ can be estimated from the inclination of the correlation function in the region $|\Delta t| < 5\,\mu$s. Taking into account the local strength of the magnetic field this corresponds to a radial electric field of $+5.8 \cdot 10^3\,\mathrm{V\,m^{-1}}$.

Correlation functions of plasma potential and electric field

In order to extend the experimental picture of plasma fluctuations further, the correlation functions of the plasma potential and of the poloidal electric field are discussed. For the probe positioned in the SOL, the two-dimensional correlation func-
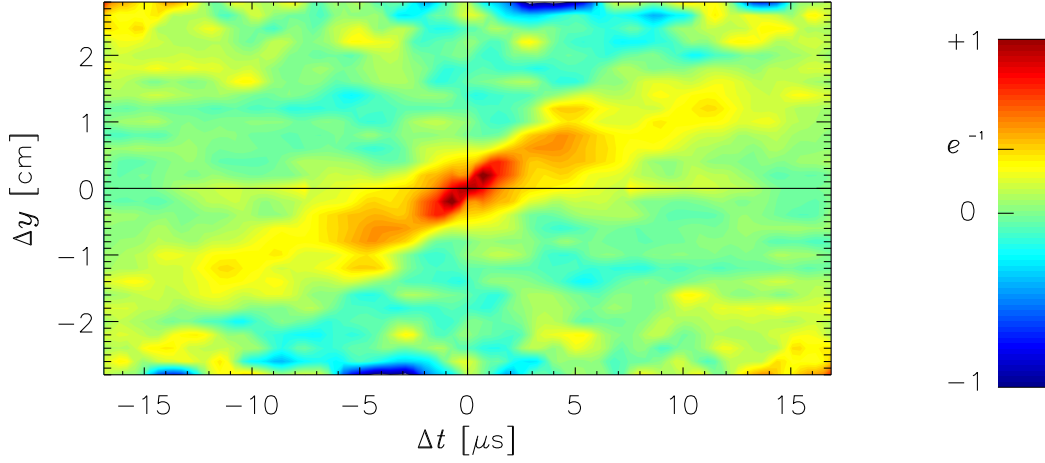
Figure 5.10: *Corrected spatio-temporal correlation function of U_{plasma} fluctuations. The probe is located in the scrape-off layer.*
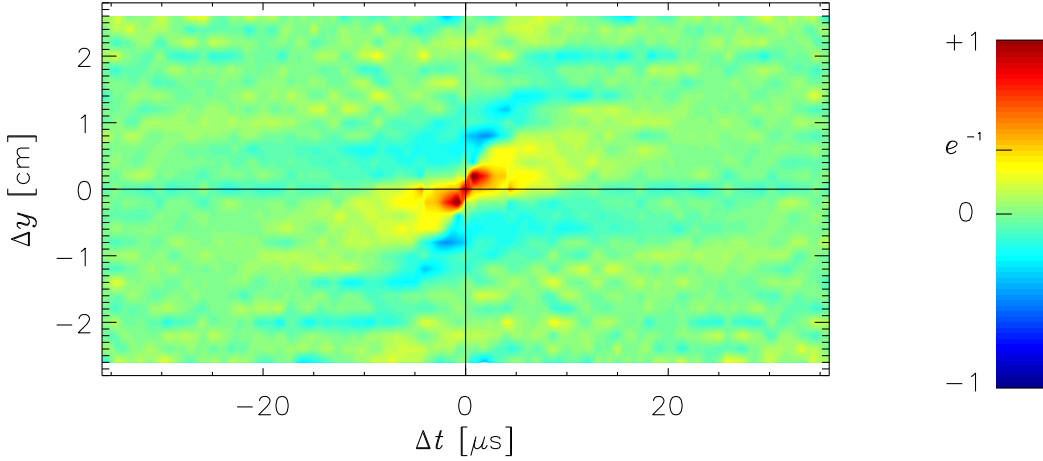
Figure 5.11: *Correlation function of the poloidal electric field, deduced from the U_{plasma} data by evaluating the second spatial derivative. The baseline in Δy direction is smaller than in the previous figure, since finite differences were utilised.*

tions are shown in the figures 5.10 and 5.11, where the latter was generated from the U_{plasma} correlation function utilising the second spatial derivative in finite difference approximation (see section 4.5.1). Note that the U_{plasma} correlation function in figure 5.10 is a corrected one.

It is obvious, that poloidal size, lifetime and propagation speed of the plasma potential fluctuations are essentially the same as for the temperature and density fluctuations. For the fluctuations of the poloidal electric field (figure 5.11) it is different: Poloidal size and lifetime are significantly smaller. This could be expected for the space domain, since the spatial derivative increases the weight of high wavenumbers, but for the time domain it is an interesting feature. The values are:

Figure 5.12: *Corrected spatio-temporal autocorrelation function of U_{plasma} fluctuations. Probe is located near the separatrix.*

$d_{pol} = 0.4 \, \mathrm{cm}$ and $\tau_L \approx 10 \, \mu\mathrm{s}$.

When the probe approaches the separatrix, the correlation of U_{plasma} in figure 5.12 displays an additional structure if compared to the correlation of density or temperature: An oblique stripe appears, passing from the top at $\Delta t = -5 \, \mu\mathrm{s}$ through the origin to the bottom at $\Delta t = 5 \, \mu\mathrm{s}$, and indicating fluctuations that move in the opposite direction. The corresponding speed is higher than for the main structure: $-5 \cdot 10^3 \, \mathrm{m \, s^{-1}}$ or equivalent to a radial electric field of roughly $-12 \cdot 10^3 \, \mathrm{V \, m^{-1}}$. This phenomenon is attributed to the velocity shear layer at the separatrix. Both propagation directions are visible within this layer, whose thickness was often found to be the order of $1 \, \mathrm{cm}$ in radial direction [Bleuel 1998]. This information is valuable to calibrate the actual radial position of the probe.

Please note, that the high amplitudes at the lower and the upper edge of figure 5.12 have no physical meaning. They are caused by poor statistics, since only one pair of probe tips is available to sample the highest spatial distance. For small spatial distances more pairs of tips are available and the statistics get better.

In figure 5.13 it is easy to see that the noise is strongly amplified, if the correlation function of poloidal electric field fluctuations is calculated straightforward from the U_{plasma} correlation function, when the probe is close to the separatrix. To work out the significant structure, the model function defined in appendix A.3.1 was fitted to the U_{plasma} correlation function and the E_{pol} correlation function was calculated alternatively from the model. This result is displayed in figure 5.14. Although the structure sizes now come close to the limits of the available resolution (tip spacing $0.2 \, \mathrm{cm}$, temporal resolution $0.35 \, \mu\mathrm{s}$), a poloidal size of $0.4 \, \mathrm{cm}$ and a lifetime of $4 \, \mu\mathrm{s}$ can be estimated.

To summarise: While the fluctuations of plasma potential still bear resemblance to the fluctuations of density and temperature, the electric field has much smaller structure sizes. This is expected for the spatial scale, but it is also observed in the
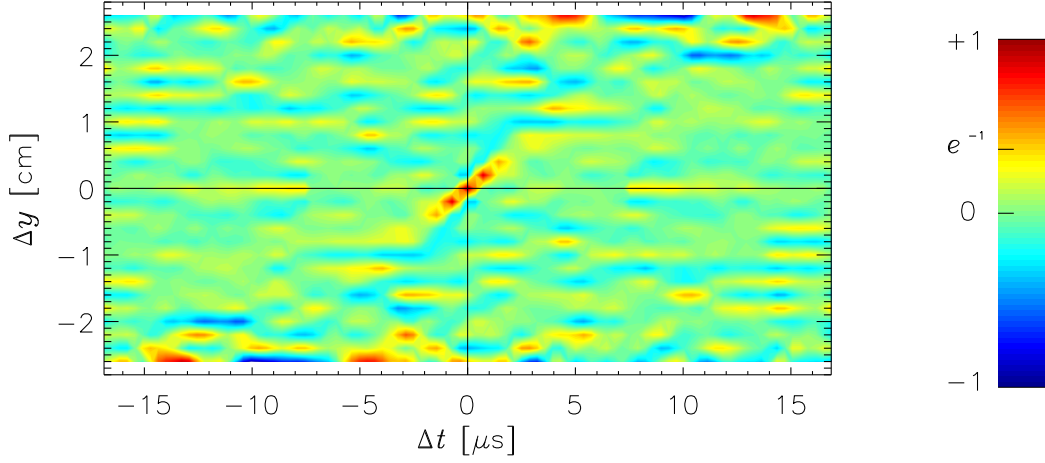
Figure 5.13: *Two-dimensional correlation function of the poloidal electric field E_{pol} fluctuations, calculated as the negative second spatial derivative of the data from figure 5.12.*
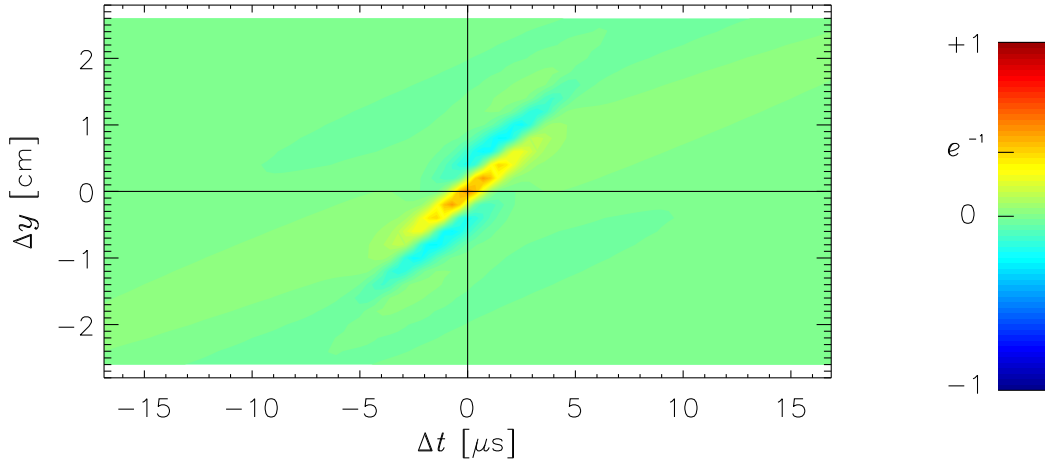
Figure 5.14: *Correlation of E_{pol}, calculated from the model function of the U_{plasma} correlation. The latter had been fitted to the data from figure 5.12.*

time domain. When the probe is located close to the separatrix, counter-propagation of potential structures is visible, which indicates the vicinity of the shear layer.

5.2.2 Power spectra

It is possible to estimate power spectra P of the fluctuations in density and temperature by transforming the correlation into Fourier space

$$ P = |\,\mathcal{F}[U(t,y)]\,|^2 = \mathcal{F}\big[\,X_{UU}(\Delta t, \Delta y)\,\big]\ , $$

according to equation (4.5) from section 4.5.1. Since there is the effect of the fit parameter covariance (section 4.3), also the variance is comparatively high, which
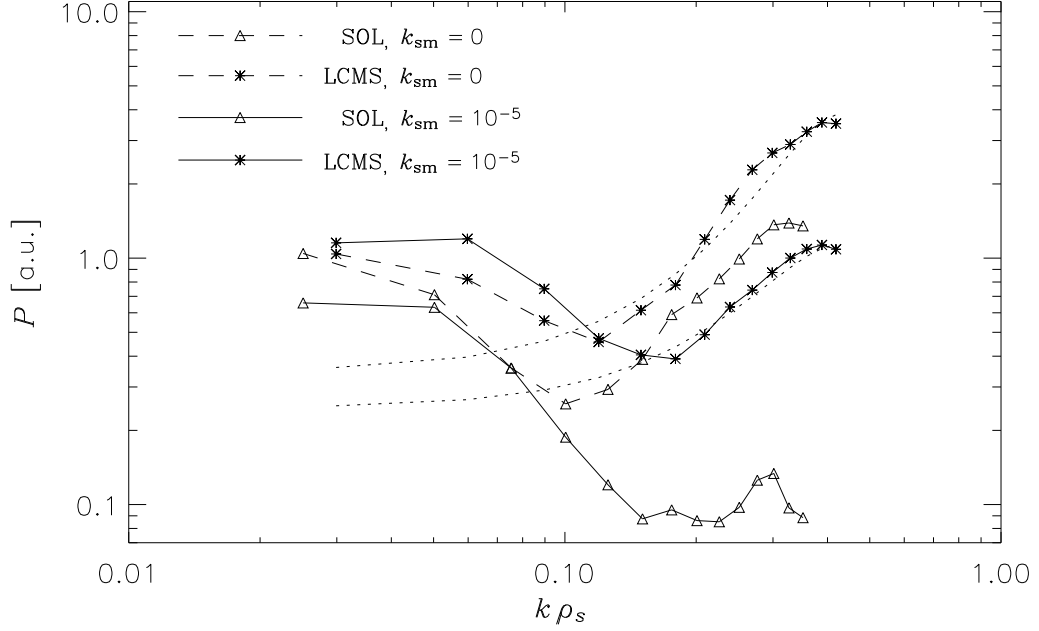
Figure 5.15: *Fourier transform of electron temperature fluctuations. Two probe positions are displayed: triangle symbols for SOL, asterisk for the separatrix. Solid lines represent the evaluation with limited bandwidth in the frequency domain (smoothed fitting) and the dashed lines full bandwidth. The effect of the anticorrelation between adjacent tips is indicated by the dotted lines that correspond to both separatrix positions.*

produces a large noise peak at the origin of the two-dimensional correlation. Therefore, power spectra should be deduced after the noise correction (section 4.3.2), where the central peak is replaced by function values from the model function (appendix A.3.1). After the two-dimensional transform summing up all frequencies finally yields the k-spectrum.

One must keep in mind the arbitrariness introduced to some degree by this method: The height of the fitted central peak significantly changes the width and the power level of the calculated spectrum. Hence, the shape of the result spectrum depends on the choice of the fit function.

Figure 5.15 displays the Fourier transform of the corrected T_e correlation function. The independent variable is the wavenumber normalised to the inverse of the dispersion scale ρ_s from equation (1.19). Only the values below $k\rho_s = 0.1$ are considered to reflect the power spectrum of real temperature fluctuations. For higher wavenumbers, the spectral power strongly increases, which is caused by the strong anticorrelation on neighbouring tips $\Delta y = \pm 2\,\mathrm{mm}$ at time lag $\Delta t = 0$ (see figure 5.8). When fitting the model function, this anticorrelation is modelled by the third addend in the fit formula (appendix A.3.1) and its contribution to the power spectrum can be visualised by a separate transform (dotted lines in figure 5.15). The spectra are calculated for the two extreme probe positions and for two different bandwidths during the fitting of the probe characteristics. These bandwidths are
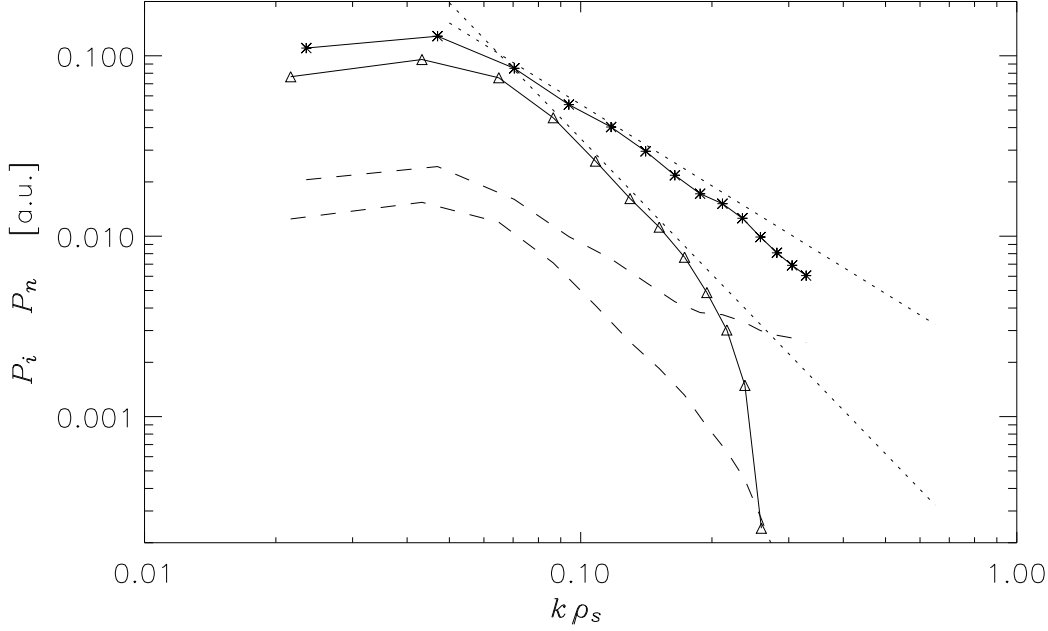
Figure 5.16: *Power spectra of $\tilde{n}_0$ and $\tilde{I}_{sat}$ as a function of the wavenumber. Triangles denote $\tilde{n}_0$ and a probe position in the SOL and asterisks $\tilde{n}_0$ close to the separatrix. Dashed lines belong to the corresponding spectra of $\tilde{I}_{sat}$. The dotted lines are plotted in order to indicate the power law $P \sim k^x$ with $x = -2.5$ (SOL) and $x = -1.5$ (separatrix).*

determined by the magnitude of the smoothing parameter within one packet, and, since the packet length is $4.3\,\mu$s, strong smoothing is comparable to a $230\,$kHz low pass in the frequency domain.

Obviously, the smoothing damps the short range anticorrelation and consequently it damps also the enhancement of the power at high wavenumbers. But at the same time the slope at the steepest part of the spectrum ($k\rho_s \approx 0.08$) is changed. While a power law $P \sim k^x$ with an exponent $x = -2$ for the wavenumber can be estimated from the spectra with smoothed fitting, the evaluation without smoothing suggests $x = -1.5 \ldots -1$. It must be concluded that the smoothed fitting also attenuates turbulent plasma fluctuations with wavenumbers $k\rho_s \lesssim 0.1$.

Power spectra of density fluctuations do not suffer from the effect of anticorrelation. In figure 5.16 there is no enhancement of the power at high k values. This time the spectra indicate a characteristic exponent for the wavenumber of $x = -2.5$ in the SOL and of $x \approx -1.5$ close to the separatrix. The latter value is similar to the exponent from the $\tilde{T}_e$ spectrum.

There is a steepening of the $\tilde{n}_0$ curve around $k\rho_s \approx 0.2$ when the probe is in the SOL. Such steepening is not observed when the probe is close to the separatrix. Comparing the spectra of $\tilde{n}_0$ and $\tilde{I}_{sat}$ one observes that the spectral decay of $\tilde{I}_{sat}$, being a compound of both $\tilde{T}_e$ and $\tilde{n}_0$, is much slower. This finding is consistent with enhanced $\tilde{T}_e$ spectra.

In the strict sense, n_0 is calculated from I_{sat}, T_e and T_i, and therefore the
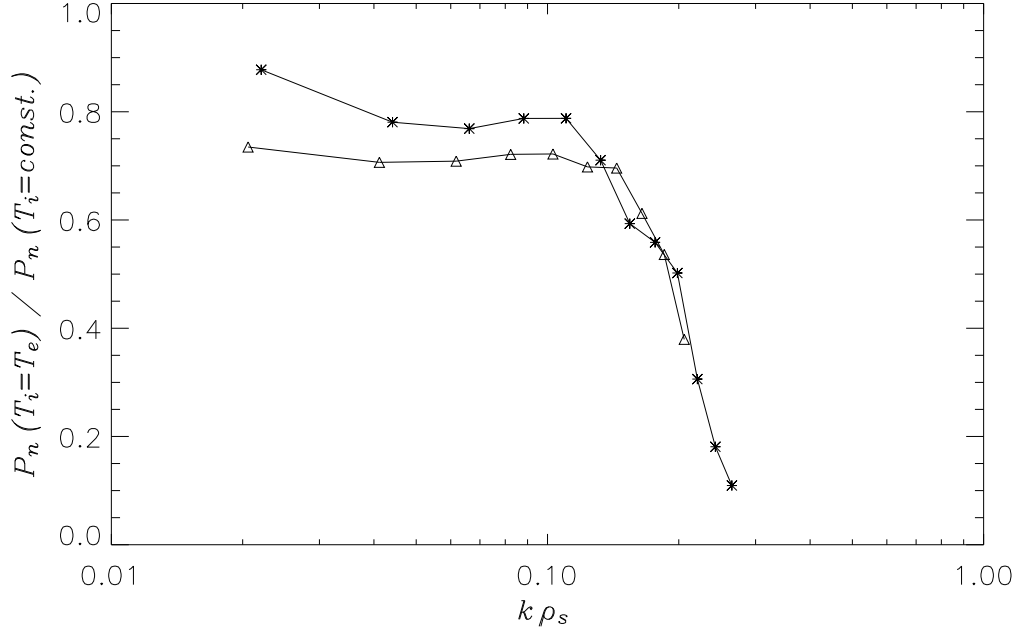
Figure 5.17: *Ratio of density fluctuation power for the assumption $T_i = T_e$ relative to the model $T_i = \bar{T}_e = const$. Two probe positions SOL (triangle) and separatrix (asterisk) are shown.*

assumption on the ion temperature also affects the result. The model $T_i = \bar{T}_e = const$ was used to evaluate $\tilde{n}_0$ in figure 5.16. In order to study the impact of a different ion temperature model, a second calculation with the assumption $T_i = T_e$ even for the fluctuations has been made. The obtained power spectra are similar, but the magnitude of the n_0 fluctuations is considerably decreased. This is due to the fact that $T_e = T_i$ fluctuations generate a larger fraction of the measured I_{sat} fluctuations than T_e fluctuations alone.

In figure 5.17 the ratio of the power spectra calculated with the two different models is displayed for both probe positions. Up to $k\rho_s \approx 0.1$ the model with $T_i = T_e$ yields $\sim 80\%$ of the fluctuation power when compared to the $T_i = const$ model. The ratio is nearly independent of k, which indicates that this part of the $\tilde{n}_0$ spectrum is reliable. For higher wavenumbers $k\rho_s > 0.1$ the $\tilde{T}_e$ power anomaly due to short range anticorrelation, together with $T_i = T_e$ expectedly affects the shape of the spectrum.

5.2.3   Mutual relations between different quantities

The analysis is extended towards compound properties of fluctuations in different quantities. With respect to fluctuation induced transport the main focus is on the cross phases, which are prepared by analysing the Fourier transform of corrected cross-correlation functions (see section 2.1.3). In detail this is exemplarily demonstrated with the pairs U_{float}-T_e and T_e-n_0, where the notation (e.g.) U_{float}-T_e actually

denotes the cross relation between the fluctuations of U_{float} and T_e.
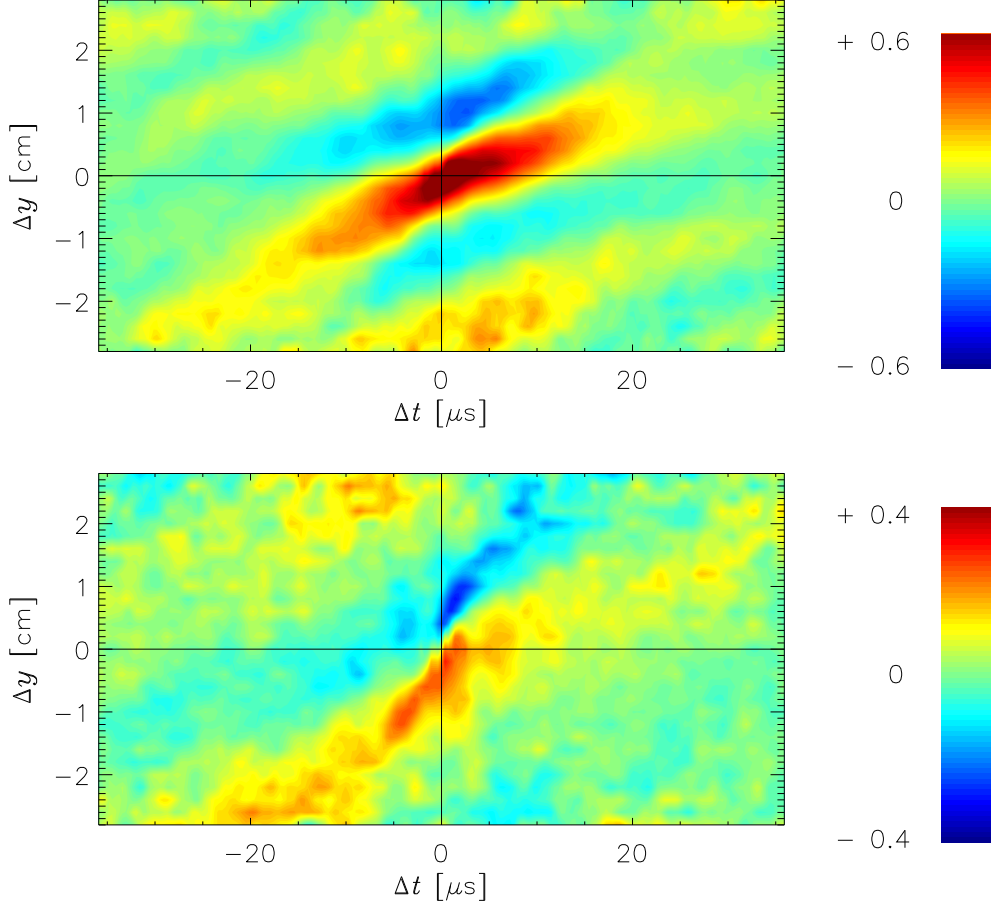
Figure 5.18: *Corrected cross-correlation functions between $\tilde{U}_{float}$ and $\tilde{T}_e$, on top for a probe position in the SOL, bottom for a probe position close to the separatrix. The time lag is displayed on the horizontal axis and on the vertical axis the tip separation. The value of the cross-correlation is colour-coded and normalised to the absolute maximum found within that region.*

5.2.3.1 Cross-correlation

The spatio-temporal cross-correlation function is calculated with a data set length of 7 ms, corresponding to roughly 20000 probe characteristics per channel at a sweep frequency of 1.4 MHz. The visualisation of such a function usually reveals a noise peak in the origin of the Δy-Δt plane on top of a fluctuation induced cross-correlation structure. If there is significant phase shift between the two different quantities, then the crest of the underlying structure is displaced from the origin.

Following the technique introduced in section 4.3.2, the corrected cross-correlation functions are generated by ignoring the central peak and replacing the values by those of a fitted two-dimensional model function. It turned out, that it is sufficient to apply this on the time lag interval $|\Delta t| < 4\,\mu s$ and the $\Delta y = 0$ distance exclusively.
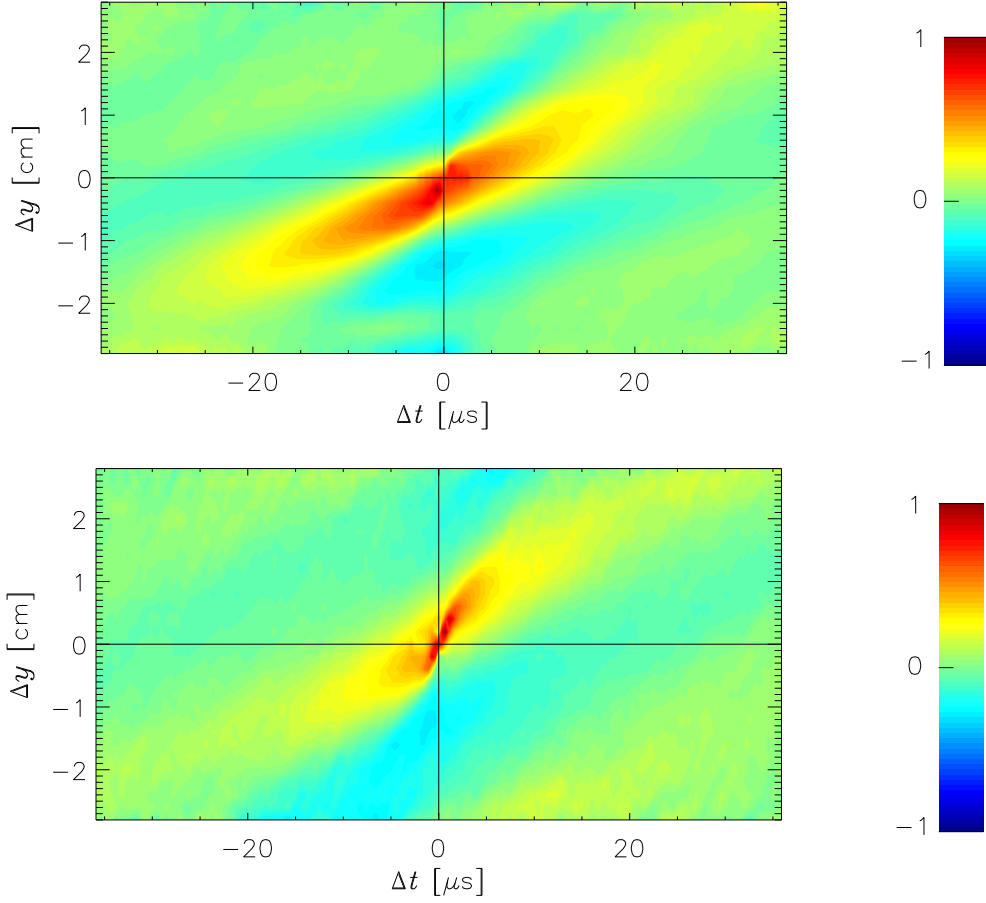
Figure 5.19: *Corrected cross-correlation functions between $\tilde{T}_e$ and $\tilde{n}_0$, on top for a probe position in the SOL, bottom for a probe position close to the separatrix. The correlation value is colour-coded and normalised to the absolute maximum value.*

The cross-correlation function is not to be normalised to the autopower, since the autopower noise peaks are up to one order of magnitude higher than the crest of the underlying correlation structure, depending on the considered quantities and on the probe position. In order to make best use of the color range when displaying such data, the corrected cross-correlation function is simply normalised to the maximum absolute value within the region of interest.

Figures 5.18 and 5.19 display the cross-correlation functions U_{float}-T_e and T_e-n_0. When compared to the correlation functions within one quantity (section 5.2.1, figures 5.5 - 5.9) it is remarkable, that the shape of the correlation structure, lifetime and poloidal size are very similar. This means U_{float}, T_e and n_0 do not fluctuate independently but follow quasi-coherently, i.e. within the lifetime of the structure, a certain pattern. There is, however, a defined sequence for the three quantities with a non-zero temporal and spatial lag. Therefore, within any pair of quantities, the center of mass of the positive cross-correlation strucure is displaced from the origin.

Comparing the different probe positions within figures 5.18 and 5.19, the eye is caught by two distinctive features: First, the propagation velocity increases in

105
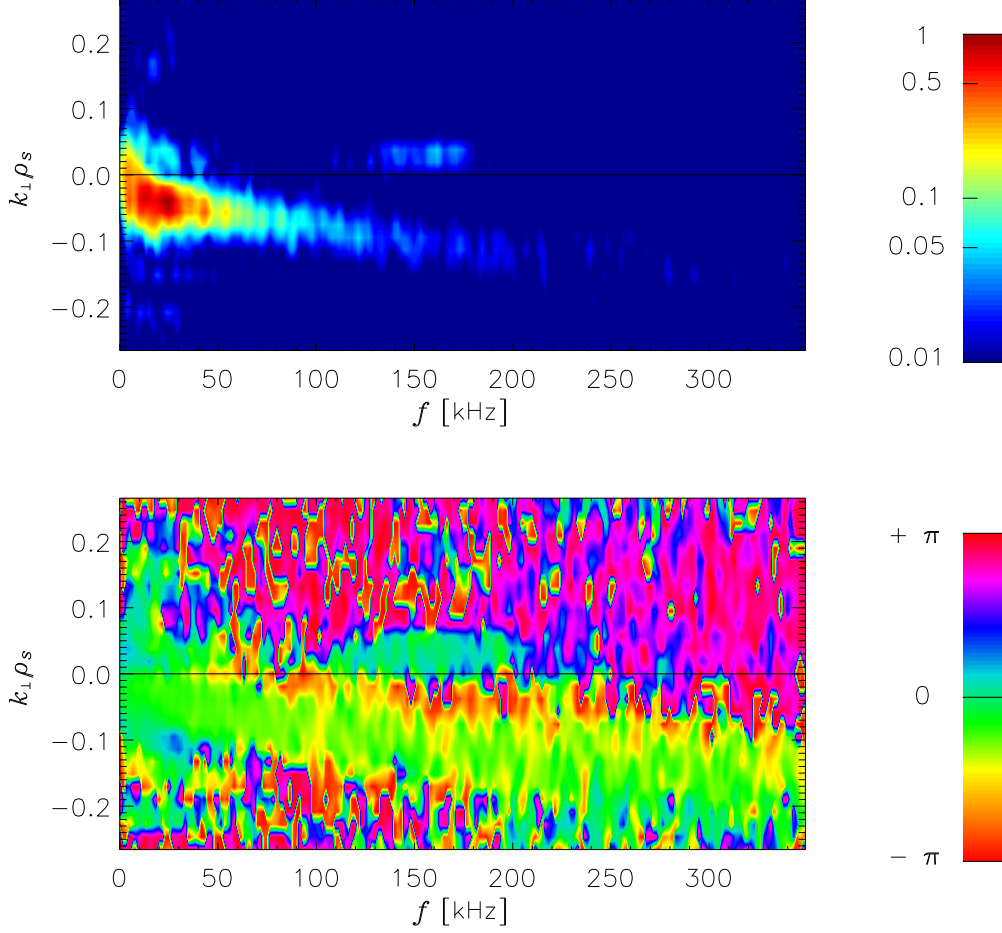
Figure 5.20: *Logarithmic cross power spectrum (top) and cross phase spectrum (bottom) between $\tilde{U}_{float}$ and $\tilde{T}_e$. Probe is positioned in the SOL. The power has been normalised to the absolute maximum value. For the cross phase a periodic colour chart is used, including a rapid change of the colours around 0 angle.*

the vicinity of the separatrix. This is the same for the correlation function of any quantity. Second, the displacement in time and space changes, since the center of mass of the positive cross-correlation structure moves to a different position. This is observed in both U_{float}-T_e and T_e-n_0, but with opposite sign. In the case of U_{float}-T_e the displacement is of particular interest with respect to the fact, that plasma potential fluctuations are often assumed to follow fluctuations of floating potential measured by probes. Depending on the position relative to the separatrix this assumption is not very good. For the evaluation of the plasma potential both T_e and U_{float} must be taken into account.

The cross-correlation T_e-n_0 in figure 5.19 displays a remarkable change of phase between the SOL and the separatrix location. While $\tilde{n}_0$ in the SOL is displaced relative to $\tilde{T}_e$ in electron diamagnetic direction, i.e. $\Delta y < 0$, it is different close to the separatrix, where the center of mass of the positive structure is slightly above $\Delta y = 0$. There is also a small scale anticorrelation at $\Delta t = 0$ and $\Delta y = \pm 0.2\,\mathrm{cm}$
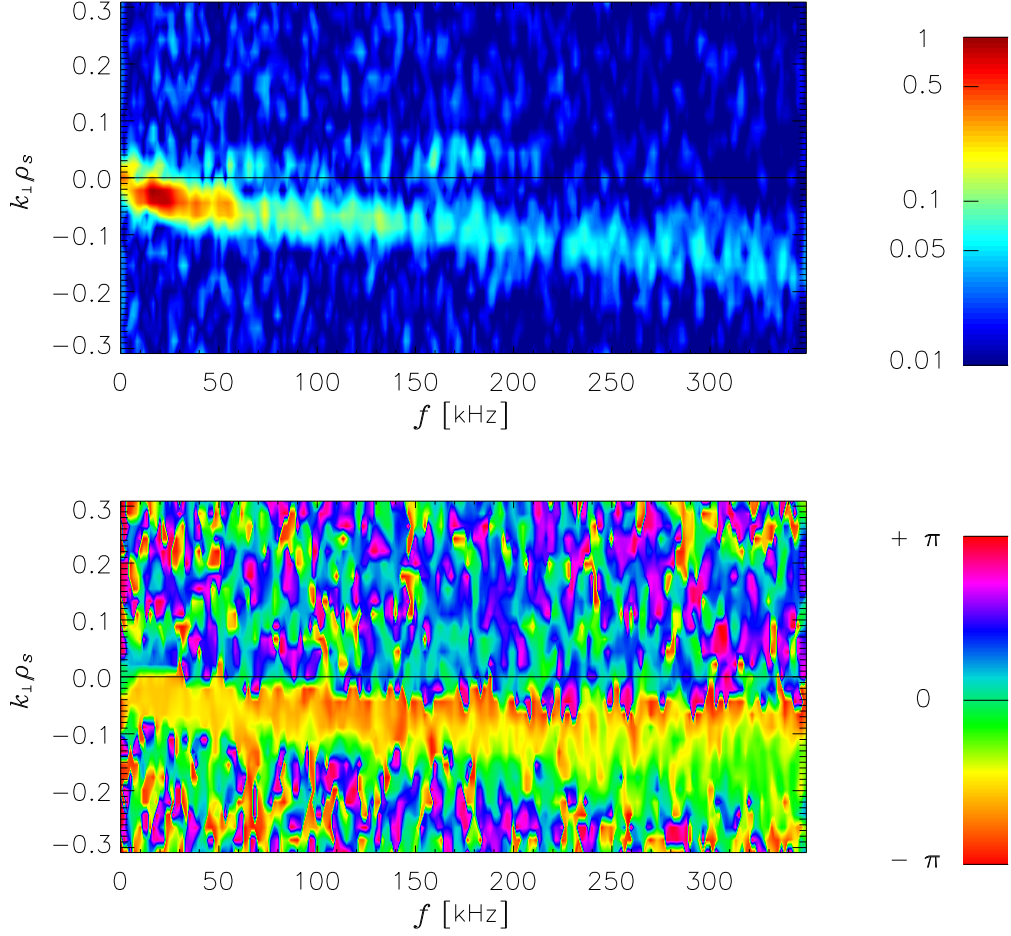
Figure 5.21: *Cross spectra between $\tilde{U}_{float}$ and $\tilde{T}_e$. On top: Normalised logarithmic cross power spectrum. Bottom: Cross phase spectrum. Probe is positioned close to the separatrix.*

when the probe is located close to the separatrix. The density is evaluated from two measured quantities, namely I_{sat} and T_e. Only the fluctuations of T_e display this particular anticorrelation (figure 5.8), so that it is just inherited from there.

5.2.3.2 Wavenumber-frequency spectra

The wavenumber-frequency or kf cross spectrum is the Fourier image of the cross-correlation function (section 2.1.3). Applied to the experimental data it reveals the common amplitude and the cross phase spectra of the fluctuations in two different quantities. The information is a convenient starting point in order to put the fluctuation properties into a theoretical context.

To avoid spectral leakage a two-dimensional Hanning window (section 2.1.3.2) was multiplied with the cross-correlation function before the transform. Wavenumbers were normalised to the inverse of the dispersion scale ρ_s, which depends on the probe position via the radial profile of the averaged T_e. The numerical value is

107
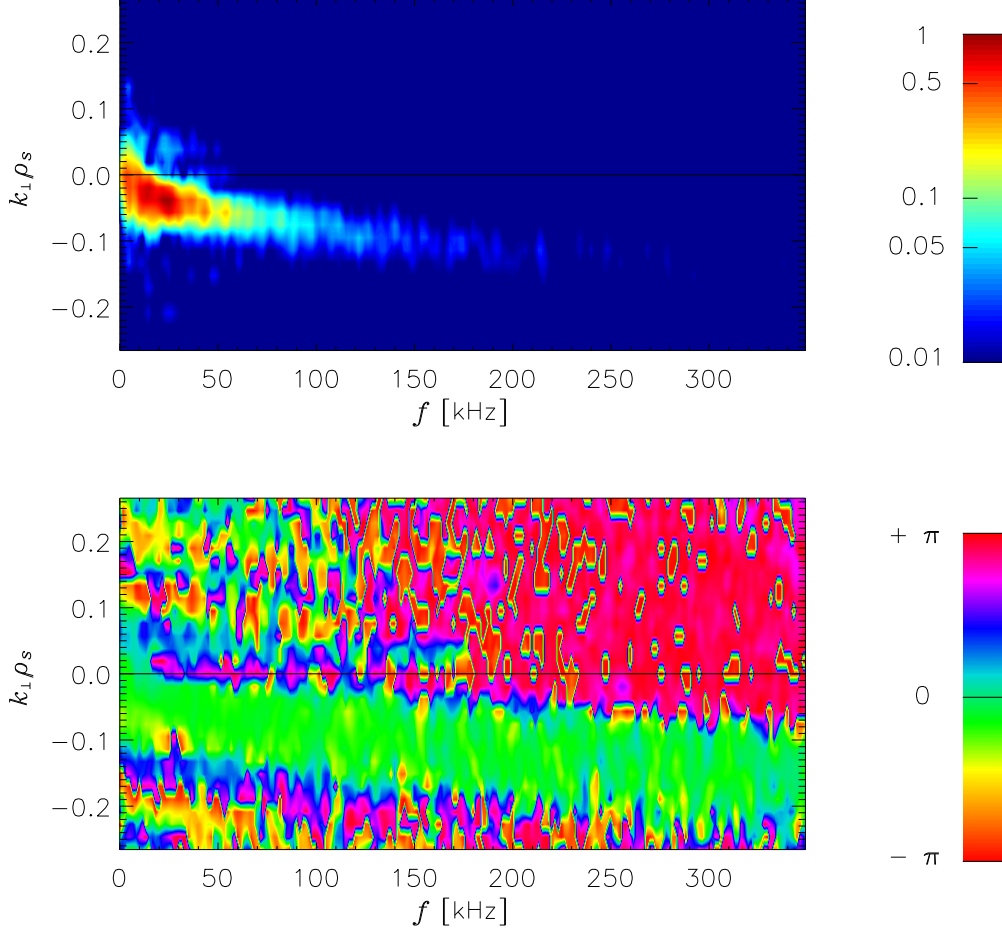
Figure 5.22: *Cross power spectrum (top) between $\tilde{T}_e$ and $\tilde{n}_0$, normalised to the absolute maximum value. Below is the corresponding cross phase spectrum. The probe was located in the SOL.*

always close to $\rho_s = 0.02\,\mathrm{cm}$.

The cross spectrum is complex and has a particular symmetry (appendix A.2.2), hence it is sufficient to display only the first and the fourth quadrant. These two quadrants contain positive frequencies and both signs of the wavenumber, which correspond to opposite propagation directions of the fluctuations. In the following both probe positions of the parameter pair U_{float}-T_e (figures 5.20 and 5.21) and of the pair T_e-n_0 (figures 5.22 and 5.23) are shown.

All figures of the cross power spectrum have in common, that the main part of the fluctuation power can be found in the quadrant with negative k as expected for the preferred direction of propagation in positive y direction (phase factor $e^{i(2\pi ft - |k|y)}$). The most prominent structures are found in both U_{float}-T_e and T_e-n_0 spectra.

Cross power spectra: The cross power of any pair has got a broad maximum in the kf plane. It is located at $f \approx 25\,\mathrm{kHz}$ and $k_\perp \approx -0.05\,\rho_s^{-1}$ when the probe is in the SOL (figures 5.20 and 5.22). Close to the separatrix the wavenumber localisation
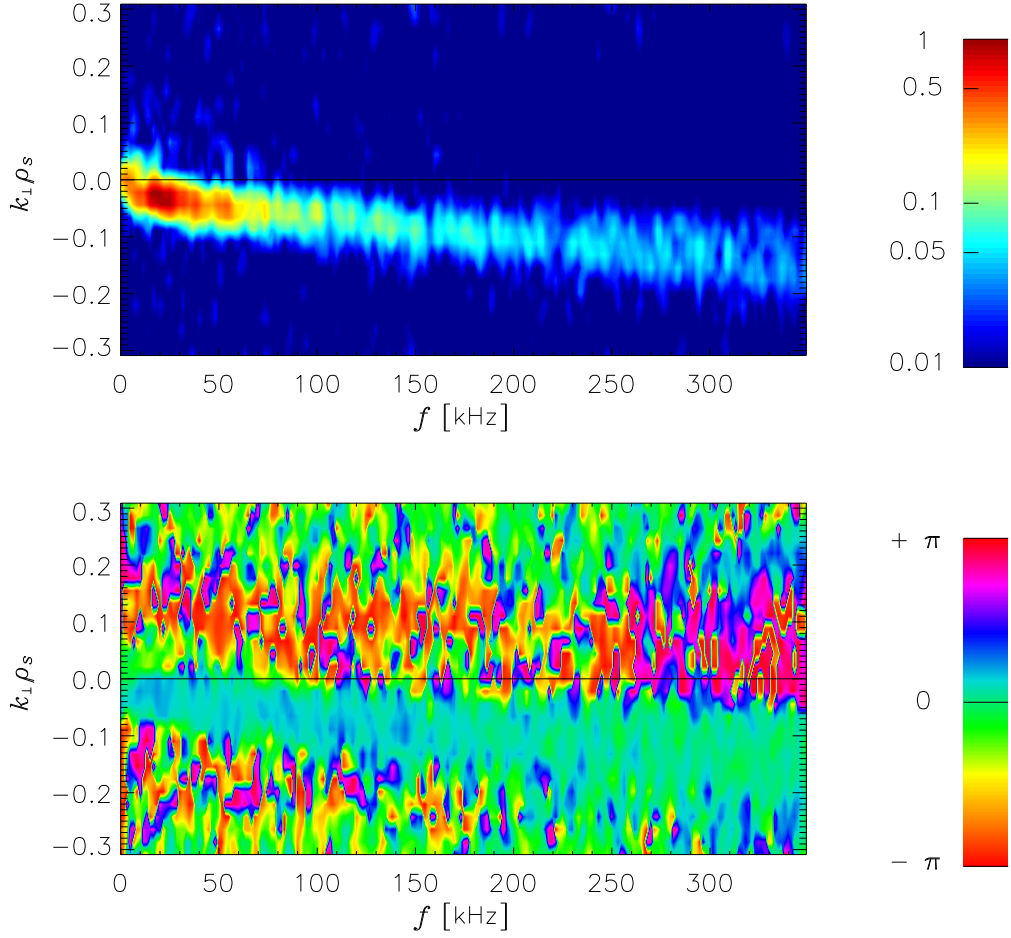
Figure 5.23: *Cross spectra between $\tilde{T}_e$ and $\tilde{n}_0$ for a probe position close to the separatrix. Top: Normalised logarithmic cross power spectrum. Bottom: Cross phase spectrum.*

slightly changes towards $k_\perp \approx -0.03\,\rho_{\mathrm{s}}^{-1}$, i.e. the most common structure size is larger than in the SOL. This is also observed in the correlation function, where the vertical size of the background pattern changed between the two probe positions (e.g. top and bottom of figure 5.19).

The full width of the spectral power in the frequency domain at one third of the maximum is approximately $40\,\mathrm{kHz}$ in the SOL and $70\,\mathrm{kHz}$ close to the separatrix. Most striking is the emerging of high frequency power ($f > 150\,\mathrm{kHz}$) close to the separatrix, which stems from the speed-up of poloidal plasma convection. As observed in figures 5.21 and 5.23, the high frequency power component of the fluctuations between $50\,\mathrm{kHz}$ and $200\,\mathrm{kHz}$ has got a wavenumber $k_\perp \approx -0.06\,\rho_{\mathrm{s}}^{-1}$.

In the U_{float}-T_e cross spectrum an additional cross power maximum is visible, which is located between $160\,\mathrm{kHz}$ and $180\,\mathrm{kHz}$ and at wavenumbers with opposite sign $k_\perp \approx 0.03\,\rho_{\mathrm{s}}^{-1}$ (figure 5.21). The corresponding structure in the spatio-temporal domain thus propagates opposite to the main structure and due to the elevated frequencies the propagation velocity is higher. Such counter propagation has been observed before in the U_{plasma} correlations (figure 5.12) and it is explained by the

fact, that the probe picks up high amplitude fluctuations from inside the confinement region. Near the separatrix the background radial electric field changes sign and thus the poloidal plasma convection is opposite. The additional maximum cannot be found in the T_e-n_0 cross spectra. This indicates that fluctuations of n_0 are radially stronger localised than those of T_e or U_{plasma}.

Cross phase spectra: Generally, the spectra display a well defined cross phase in those regions, where the cross power is significant. Furthermore the phase is relatively uniform there. If the cross power amplitude is at noise level, the phase is random and bears no physical meaning.

Comparing the two probe positions, a clear variation of the cross phase is observed in both cross spectra U_{float}-T_e and T_e-n_0. In the case of U_{float}-T_e the phase is small in the SOL (figure 5.20) and increases up to $\pi/2$ broadband at the separatrix (figure 5.21). Concerning T_e-n_0 (figures 5.22 and 5.23), a change of sign is clearly visible. This is compatible with the shift of the center of mass in the positive structure of the cross-correlation function (see figure 5.19).

The U_{float}-T_e cross phase of the counter propagating structure that corresponds to the additional maximum ($160\,\text{kHz} < f < 180\,\text{kHz}$, $k_\perp \approx 0.03\,\rho_\text{s}^{-1}$) is rather noisy in figure 5.21. It can be deduced, however, that this cross phase does not follow the tendency of the main structure. Instead, it remains close to zero.

5.2.3.3 Phase profiles in the scrape-off layer

In the next step of the analysis the stable phase within regions of significant cross power is utilised. It is adequate to define an average phase by weighting the cross phase spectrum with the cross power. Thus, the kf phase spectrum can be merged into a single number by taking the power weighted mean. The phase α between two quantities is multiplied with the associated cross power $|C|$ at the same values of k and f. This results in a power weighted phase spectrum, where an average phase $\bar{\alpha}$ is obtained by adding up a predefined range of k and f. The formula to be applied to a discrete spectrum reads with correct normalisation

$$\bar{\alpha} = \left(\sum_k \sum_f |C(k,f)|\,\alpha(k,f) \right) \Big/ \left(\sum_k \sum_f |C(k,f)| \right)\ .$$

The procedure can be repeated for several radial positions of the probe. This way, profiles of the average phase between fluctuating quantities are deduced.

In the following analysis a temporal length of $7\,\text{ms}$ in the primary time series was used to compute one kf spectrum. Only a small region in the fourth quadrant, i.e. positive f from 1 to $100\,\text{kHz}$ and negative k from -1 to $-4.3\,\text{cm}^{-1}$ were selected to average the phase. By convention the sign of the cross phase (figure 5.24) is inverted when compared to the complete kf spectra (figures 5.20 - 5.23). The selected set of wavenumbers corresponds roughly to the range $0.02\,\rho_\text{s}^{-1}\ldots 0.09\,\rho_\text{s}^{-1}$.
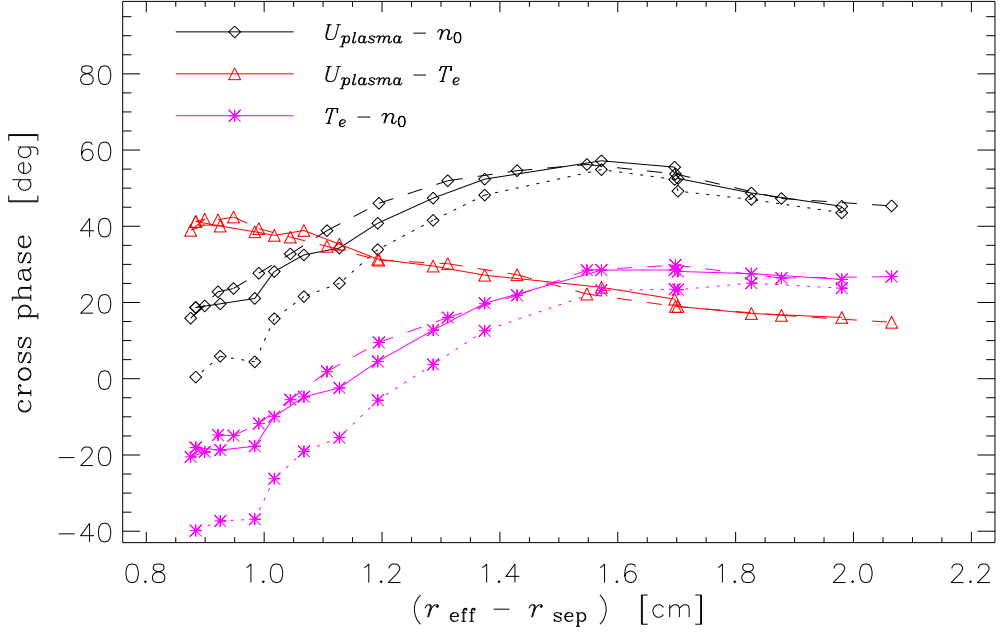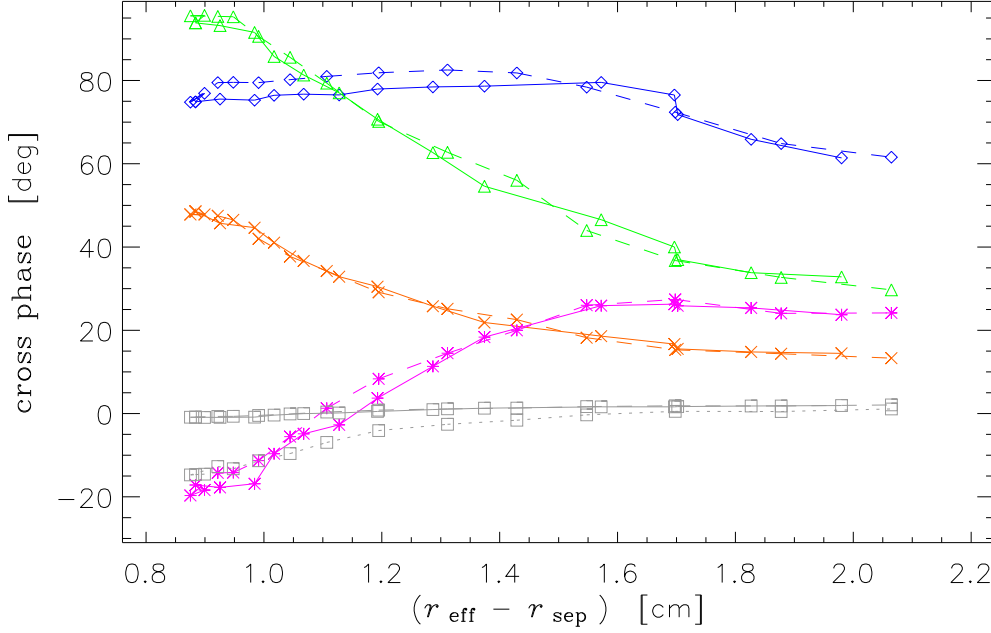
Figure 5.24: *Profiles of the power weighted cross phase between fluctuations of plasma quantities as a function of the distance to the separatrix ($r_{\mathrm{eff}} - r_{\mathrm{sep}}$): Black diamonds denote U_{plasma} versus n_0, red triangles U_{plasma} versus T_e and magenta asterisks T_e versus n_0. The profiles corresponding to the inward (solid) and the outward (dashed) movement of the probe are overplotted for the model $T_i = \bar{T}_e = const$, whereas the evaluation according to the model $T_i = T_e$ is overplotted with a single dotted line. In the case of U_{plasma} versus T_e (red triangles), the two models are indistinguishable.*

A positive phase between two quantities denotes a temporal delay of the second quantity with respect to the first one. In the particular geometry of the poloidal probe array the main propagation direction of the fluctuating structures is upward, and the cross product between $\mathrm{grad}\,p$ and $\boldsymbol{B}$, i.e. the electron diamagnetic drift points downward. Considering the propagation and the phase sign convention, this means that with a positive cross phase the second quantity is offset in electron diamagnetic direction.

Figure 5.24 shows that both pressure contributions $\tilde{T}_e$ and $\tilde{n}_0$ have an offset in electron diamagnetic direction with respect to $\tilde{U}_{plasma}$. This experimental result is consistent with the drift wave picture [Scott 1997]. Since the evaluation of the density n_0 depends on T_i, the models $T_i = \bar{T}_e = const$ and $T_i = T_e$ yield different results. The difference is at its maximum near the LCMS and vanishes in the SOL. Near the LCMS the cross phase U_{plasma}-n_0 is almost zero in the case $T_i = T_e$, whereas it remains positive ($\sim 20°$) if T_i is constant. Generally, cross phases that contain the density n_0 are decreased by $\lesssim 20°$ in the model $T_i = T_e$.

The interrelation between n_0, T_e, U_{plasma} and the primary fit parameters I_{sat} and U_{float} is displayed in figure 5.25. In the SOL, $\tilde{T}_e$ is closely in phase with both $\tilde{U}_{float}$ and $\tilde{I}_{sat}$, whereas near the LCMS the cross phase U_{float}-T_e even exceeds U_{float}-I_{sat}.

Figure 5.25: *Profiles of the power weighted cross phase between primary fit parameters and plasma quantities as a function of the radial position. Solid lines correspond to the inward and dashed lines to the outward movement of the probe. Blue diamonds: U_{float} versus I_{sat} . Green triangles: U_{float} versus T_e . Orange crosses: U_{float} versus U_{plasma} . Magenta asterisks: T_e versus I_{sat} . Grey squares: I_{sat} versus n_0 , where n_0 is evaluated with either assumption $T_i = \bar{T}_e$ (solid line), or $T_i = T_e$ (dotted line).*

If $\tilde{U}_{float}$ is compared to $\tilde{U}_{plasma}$, then a phase deviation is observed, which is largest (50°) near the LCMS and small (12°) in the SOL. The assumption on T_i has a minor effect on this cross phase: If $T_i = T_e$ then the cross phase decreases by 5° near the LCMS. In the SOL the difference is not significant.

Two conclusions can be drawn: First, $\tilde{I}_{sat}$ and $\tilde{n}_0$ are in phase closely. Depending on the model for T_i, excursions up to 15° are observed. Conventional $\tilde{I}_{sat}$ measurements therefore reflect the phase of density fluctuations within that precision. Second, the ubiquitous (e.g. see [Bleuel et al. 2002]) phase shift of approximately $\pi/2$ between $\tilde{U}_{float}$ and $\tilde{I}_{sat}$ is confirmed. It is even possible to refine it by identifying the interconnection to the electron temperature: The changing sign of the cross phase T_e-I_{sat} shifts T_e fluctuations away from U_{float} fluctuations near the LCMS, while further outside in the SOL the phase of T_e fluctuations is shifted towards the phase of U_{float} fluctuations.

5.3   Calculation of transport

The average radial flow of particles and energy is calculated from the measured fluctuations, following the method described in section 4.5.2. Additionally, the spectrum

of the transport is estimated by a decomposition into the contributions of different spatial scales. Finally, the total turnover of energy in the W7-AS is compared to the measured local flux by an extrapolation.
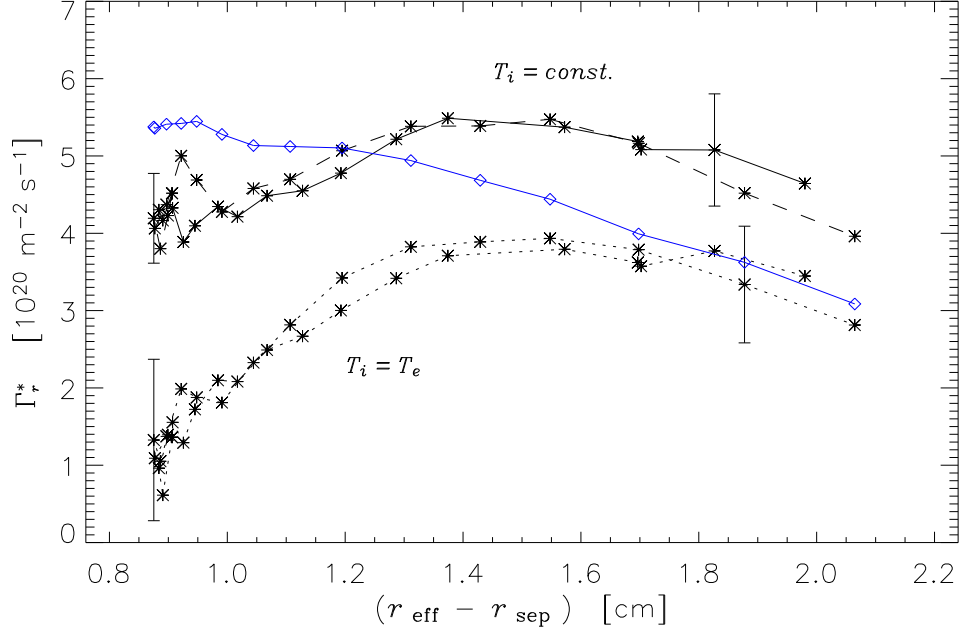
Figure 5.26: *Measured profile of the ambipolar radial particle flux driven by fluctuations. If the model $T_i = const$ is used to evaluate the density then the upper black curve (asterisk symbols) results. Both profiles corresponding to the inward (solid) and outward (dashed) movement of the probe are overplotted in this case. The dotted lines with asterisks represent the flux according to the model $T_i = T_e$. Additionally, the simplified calculation from I_{sat} and U_{float} fluctuations alone is overplotted with blue diamonds. Error bars are deduced from the deviation of the transport calculated by individual probe triplets.*

5.3.1 Transport of particles

The profile of the particle flux according to formula (1.27) is calculated from the cross-correlation function between U_{plasma} and n_0. Both models $T_i = const$ and $T_i = T_e$ have been used alternatively to evaluate n_0. In figure 5.26 the result is displayed and it can be compared with the traditional but simplified calculation, which uses fluctuations of U_{float} and I_{sat} together with the stationary profile of T_e. Each data point is the average over $7\,\mathrm{ms}$. Within this time interval the probe moved $0.3\,\mathrm{cm}$ at most. In order to deduce the experimental error, 13 individual probe triplets have been evaluated: the density measured by the middle tip of each probe triplet is multiplied with $\tilde{E}_{e\,\mathrm{dia}}$ calculated from two adjacent tips as in equation (4.8). This yields 13 individual profiles of the transport. The average of the individual results is in good agreement with the flux deduced from the cross-correlation. Numerically, they are not equal, since the correlation function at the

space lags $\pm d$ is the average of 14 tip pairs out of the 15 tips. The scatter of the 13 individual fluxes was used to calculate the standard deviation of the average value, which is shown exemplary for two radial positions as an error bar in figure 5.26. This error amounts to $\sim \pm 0.7 \cdot 10^{20}\,\mathrm{m}^{-2}\,\mathrm{s}^{-1}$ for the model $T_i = const$, whereas for $T_i = T_e$ the error is $\pm 1 \cdot 10^{20}\,\mathrm{m}^{-2}\,\mathrm{s}^{-1}$ near the LCMS, while in the SOL it is also $\sim \pm 0.7 \cdot 10^{20}\,\mathrm{m}^{-2}\,\mathrm{s}^{-1}$.

Independent of the model for the ion temperature the profile of the radial particle flux displays a remarkable variation with a maximum approximately in the middle between the extreme positions of the radial probe movement. This maximum is $\Gamma_r^* = 5.5 \cdot 10^{20}\,\mathrm{m}^{-2}\,\mathrm{s}^{-1}$ in the $T_i = const$ model and $\Gamma_r^* = 4 \cdot 10^{20}\,\mathrm{m}^{-2}\,\mathrm{s}^{-1}$, given $T_i = T_e$. Since the decrease towards the separatrix is not observed in the flux deduced from U_{float} and I_{sat} fluctuations, this is clearly an effect of the temperature fluctuations changing the sign of their cross phase relative to the density fluctuations. The effect of this cross phase is larger in the $T_i = T_e$ model. While in the SOL both models yield comparable results, $T_i = T_e$ reduces the calculated particle flux by a factor 3 near the LCMS.

The figures 5.27 (model $T_i = const$) and 5.28 (model $T_i = T_e$) display the spectral distribution of the flux according to the method described in section 4.5.2. The spectral distribution is shown within the wavenumber range that can be resolved by the probe array, and as a function of the probe position. In order to evaluate this, the corrected cross-correlation functions X_{En} of each probe position were multiplied with a Hanning window (section 2.1.3.2) using the two widths $\Delta t_H = 0.3\,\mathrm{ms}$ and $\Delta y_H = 2.8\,\mathrm{cm}$ before applying the Fourier transform. After the transform, corresponding quadrants were subsumed (see appendix A.2.2) to obtain a real quantity and all frequencies were added up to retain a wavenumber spectrum.

Note, that all wavenumber contributions are positive, i.e. the flux is directed radially outward. In the SOL a localised maximum for wavenumbers $k \approx 0.06\,\rho_\mathrm{s}^{-1}$ with a spectral width $\sim 4\,\mathrm{cm}^{-1}$ (FWHM) can be observed. The strong localisation disappears near the LCMS and the center of mass moves to higher wavenumbers $k \sim 5\,\mathrm{cm}^{-1}$, i.e. $k \sim 0.1\,\rho_\mathrm{s}^{-1}$. These properties are basically independent of the assumption on T_i. When compared to the model $T_i = const$, the transport evaluation using the model $T_i = T_e$ (figure 5.28) yields smaller values by an attenuation, which is basically uniform along the resolved range of wavenumbers. This is in accordance with the observation of broadband uniform cross phases between I_{sat}, U_{float} and T_e.

5.3.2 Transport of energy

The turbulent radial energy flux consists of the convective component Q_r^* and of the conductive component q_r^* (see section 1.4.1). The convective component is closely related with the particle flux. Neglecting the averaged center of mass kinetic energy, it is obtained by simply multiplying the particle flux with the factor $\frac{3}{2}\,k_B\,\bar{T}_e$ for the electron part, as introduced in equation (1.28). In figure 5.29 the profile of the energy flux convected by electrons is displayed. For the calculation of the density the model
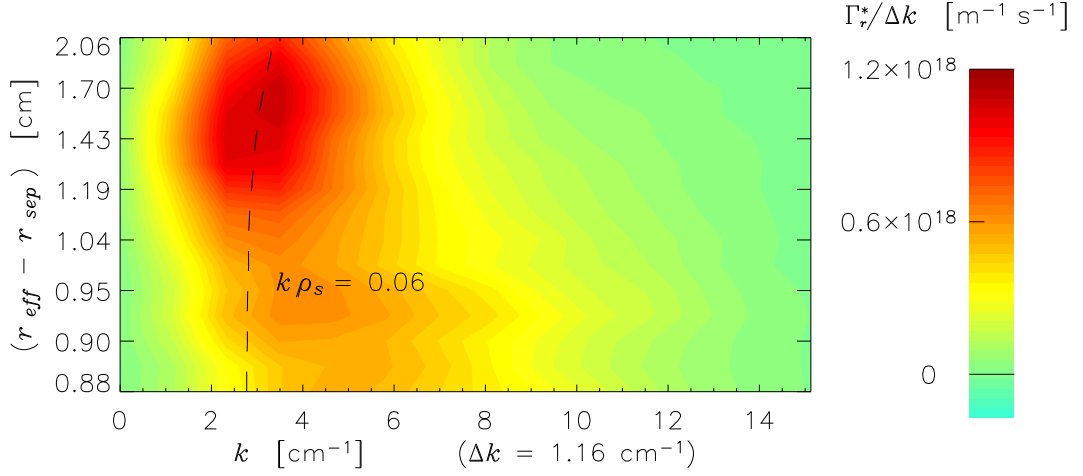
Figure 5.27: *Spectral distribution of the particle flux as a function of the wavenumber (horizontal axis) and of the probe position (vertical axis). The model to evaluate the plasma density assumes $T_i = const$ and the data corresponds to the outward movement of the probe. The spectral distribution of the particle flux is colour coded and has got a fixed resolution $\Delta k = 1.16\,cm^{-1}$ in the wavenumber domain. Along the vertical axis the discrete flux samples (denoted by asterisks in figure 5.26) are plotted using a constant binsize. Since there are more samples available near the LCMS, the mapping of the probe position is stretched in this region.*
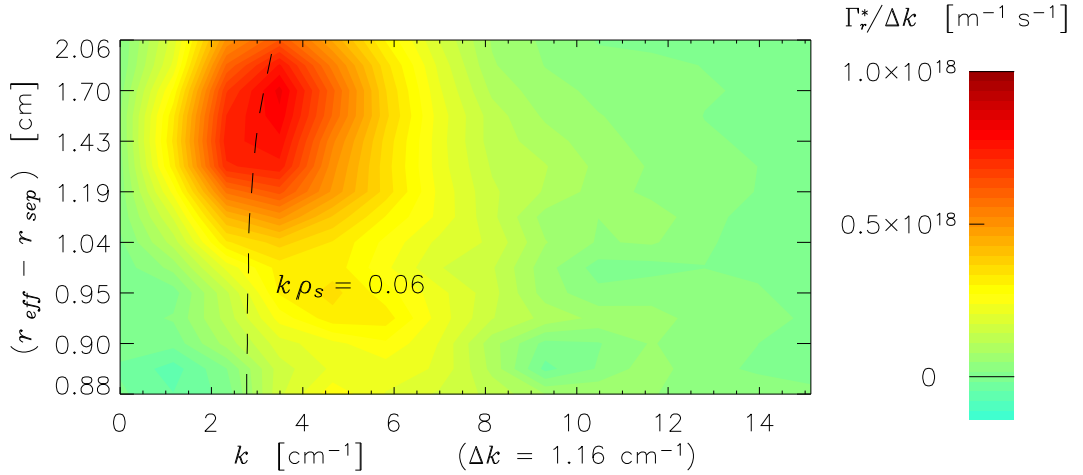
Figure 5.28: *Spectral distribution of the particle flux during the outward movement of the probe similar to figure 5.27, but using the model $T_i = T_e$ when evaluating the plasma density n_0.*

$T_i = const$ has been used. The profile is indeed very similar to the corresponding profile of the particle flux from figure 5.26. Contributions of ions were not measured and will be discussed later. Minor variations of the convected energy flux caused by the profile of the mean temperature are possible, for instance in the SOL towards large r_{eff}, the convected energy flux decreases more rapidly than the particle flux.

115
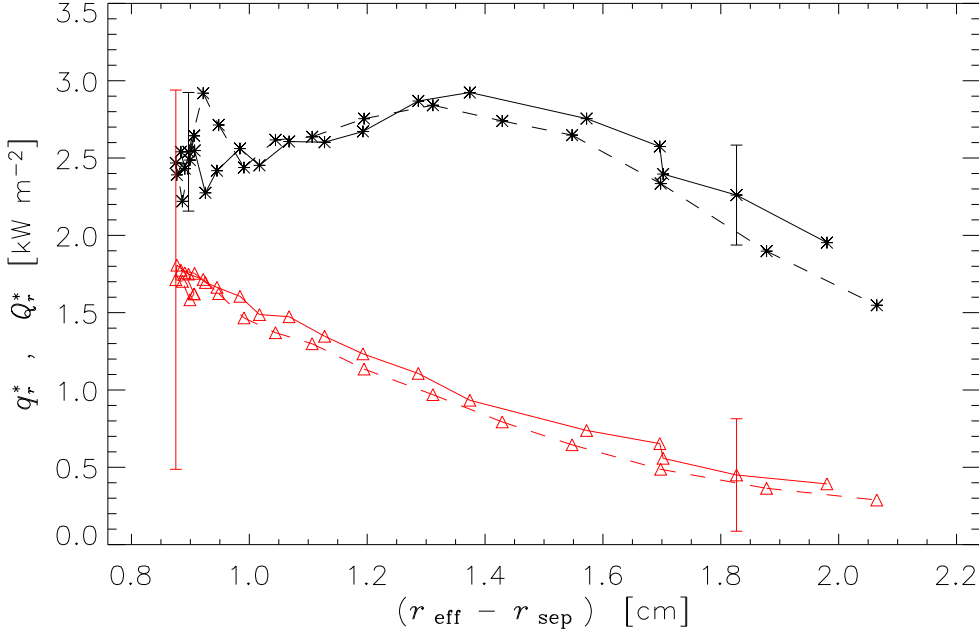
Figure 5.29: *Measured profiles of electron contributions to the turbulent energy flux, where U_{plasma} and n_0 have been evaluated according to the model $T_i = const$. Black asterisks: convected flux, red triangles: conducted flux. Both directions of the probe movement are overplotted, as solid lines (inward) and as dashed lines (outward). The error bars are estimated from the deviation of individual tip triplets (see section 5.3.1).*

The particular shape of the profile with the decline of the convection towards smaller r_{eff} is evidence, that convection alone cannot account for the total flux of energy. Since there is no energy source in the boundary plasma and in the SOL, a decrease of the total energy flux near the LCMS would be a contradiction. Therefore an additional mechanism must complement the energy transport.

5.3.2.1 Conduction of energy by temperature fluctuations

Temperature fluctuations can sustain an energy flux without transport of particles. This so-called conduction is quantified in equation (1.29). Evaluating the contribution of the electrons yields the radial profile, which is overplotted in figure 5.29. The visualisation suggests, that the reduced convection close to the separatrix is actually replaced by conduction. Furthermore the computing procedure reveals, that the triple product $\tilde{n}_0 \tilde{T}_e \tilde{v}_{E \times B}$ can be neglected in good approximation, thus $\tilde{T}_e \approx \tilde{T}_e^{\,*}$.

Similar to the case of the particle flux, the cross phase of the fluctuating quantities plays the decisive role. For conduction it is the U_{plasma}-T_e cross phase (cf. figure 5.24). Obviously, the rise in the conducted flux towards the separatrix follows the increasing cross phase.

If absolute values of convected and conducted energy flux are critically assessed, then a very sensitive dependency of the conduction on the bandwidth during the fit-

ting of probe characteristics must be conceded. Increasing the smoothing parameter k_{sm} from 10^{-5} to $4 \cdot 10^{-5}$ (see section 4.2.3) reduces the conducted energy flux by a factor of 2. This suggests that, when compared to convection, the high fluctuation frequencies are more important for the conduction. Nevertheless, the profile shape is robust, i.e. it does not change with the value of k_{sm}.

Finally, the corrected correlation function between potential and temperature is used to deduce the spectral composition of the conducted transport. The result is displayed in figure 5.30. All scales produce a radially outward conduction of energy
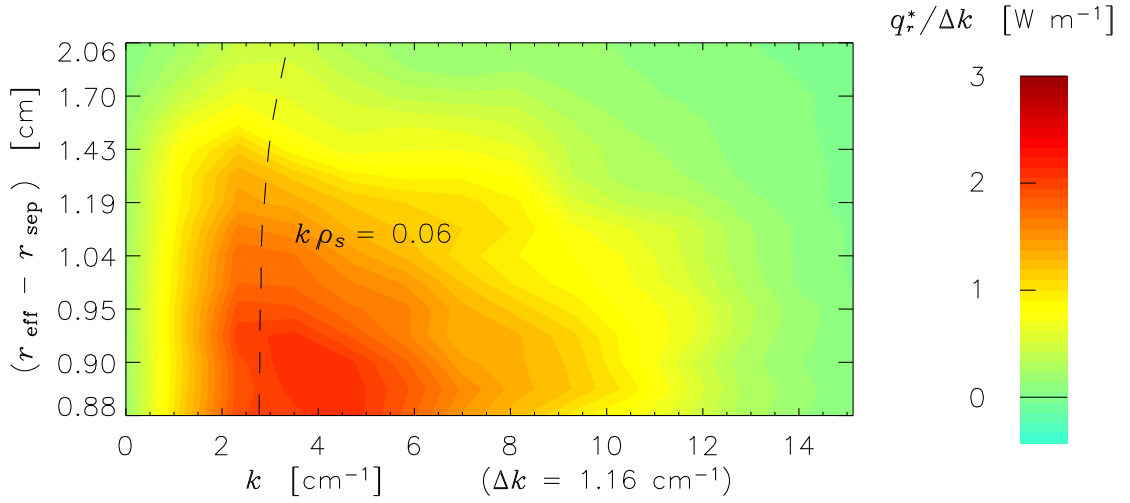
Figure 5.30: *Spectral distribution of the conducted energy flux during the outward movement of the probe. The description of the axes is the same as in figure 5.27. Both models that assume either $T_i = const$ or $T_i = T_e$ when evaluating the plasma potential yield essentially the result shown here.*

and the spectral shape hardly changes with the level of the total conducted transport. When compared to the spectrum of the particle flux (figure 5.27), the dominant scales are indeed smaller and the conduction is more broadband. The localisation of transport relevant power around $k \approx 0.06 \, \rho_s^{-1}$ is much less pronounced than for the particle flux. Approaching the separatrix it is rather replaced by a spectral plateau ranging up to $k \approx 0.1 \, \rho_s^{-1}$.

5.3.2.2 Uncertainty of the measured fluxes

Before discussing the details of experimental uncertainties, one must become aware, that the aim of the present analysis is to relate the local measurements to the overall confinement. Thus, the region of interest is the one close to the separatrix. The main contributions to the uncertainty of the average particle or energy flux are the statistical deviations of the transport along the extent of the array, and the uncertainty of the ion temperature plus its fluctuations. Additionally, the impact of

the coefficient for secondary electron emission is evaluated and discussed.

Algebraically, the statistical error can be calculated from the scatter of the local transport that is measured by individual probe triplets within the 15 tip array. Since the scatter is rather high for the case of conductive transport (including singular triplets with values around zero or slightly negative) the error bar is large. Close to the separatrix, this statistical error is typically 50% of the mean value. In the case of the convective transport, the scatter is much smaller and can be neglected with respect to the uncertainty introduced by the ion temperature model.

A different aspect is given by the uncertainty of T_i, its gradient and its fluctuations. Since there is no accurate measurement, both assumptions $T_i = \bar{T}_e = const$ (disregarding T_i fluctuations), and $T_i = T_e$ are investigated. An enhanced value T_i equal to 1.5 times the average electron temperature at the separatrix should now be assumed. Considerations that support such and even higher ratios are reported from the JET tokamak [Fundamenski et al. 2002]. The interrelation between density, saturation current, and the temperature ratio $\tau = T_e / T_i$ is supplied by probe theory. Taking this into account, the evaluated plasma density would decrease by the factor 0.89, as well as the particle flux and both energy fluxes conducted and convected by the electrons. The energy flux by the ions would rise by the factor 1.34, for the increased temperature outweighs the decrease of the density.

If there are significant fluctuations of the ion temperature, then a dramatic change is to be expected in the calculated flux of convected energy Q_r^*. For the extreme case $T_i = T_e$ the situation is shown in figure 5.31 and can be compared to the calculation with constant T_i in figure 5.29. Close to the separatrix the value of Q_r^* has dropped by a factor of ~ 3 from $2.4\,\mathrm{kW\,m^{-2}}$ to $0.8\,\mathrm{kW\,m^{-2}}$ for these assumptions. One reason was already anticipated in section 5.2.2: $T_i = T_e$ yields a reduced level of density fluctuations. Another reason is the behaviour of the cross phase T_e-n_0, which is more negative in the model $T_i = T_e$ when compared to the model $T_i = const$ (see figure 5.24). The change in the T_e-n_0 cross phase further diminishes the particle transport and the energy flux convected by electrons.

Despite these dramatic changes in particle and energy convection, the energy flux conducted by electrons is rather unaffected, naturally, by ion temperature fluctuations. It is notable, however, that the statistical error is smaller than in the computation with constant T_i. Obviously $T_i = T_e$ reduces the scatter of the conducted electron transport calculated from individual probe triplets.

Considering the influence of the coefficient for the emission of secondary electrons γ_e (see section 2.4.4), it turned out, that the uncertainty of its actual value plays a minor role compared to the other sources of uncertainty. The complete calculation of energy fluxes was carried out with values $\gamma_e \in \{0.4, 0.5, 0.6\}$. So far, the presented results were all obtained using $\gamma_e = 0.5$. Increasing γ_e from 0.5 to 0.6 enhances the convection by roughly 10% close to the separatrix, while other radial positions as well as the conducted energy flux are nearly unaffected.

To conclude, the uncertainty of the energy flux conducted by electrons is determined by the statistical deviation of individual probe triplets and amounts $\sim 50\%$,
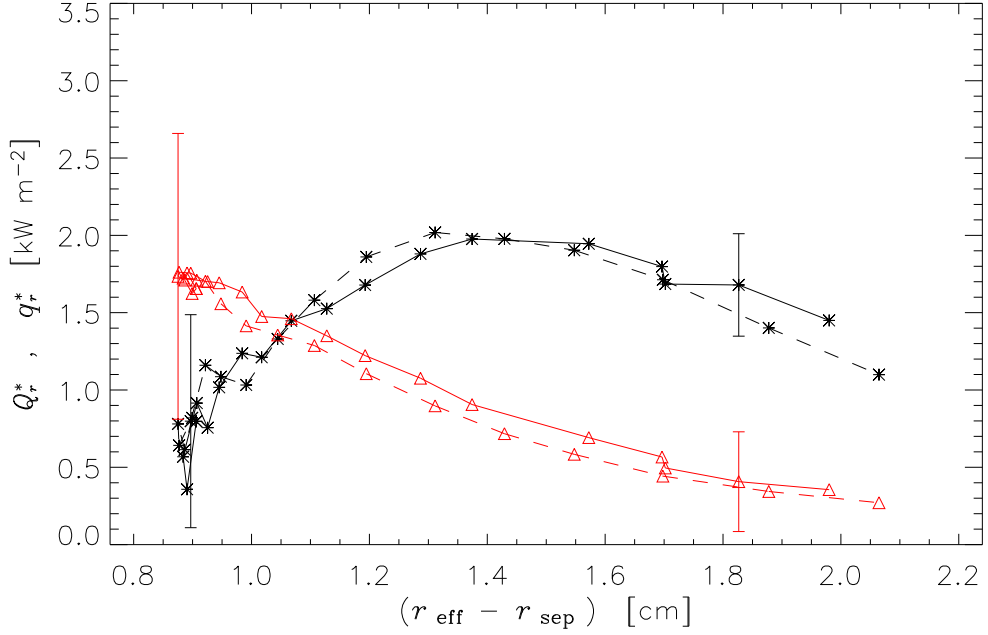
Figure 5.31: *Measured profiles of electron contributions to the turbulent energy flux with the model assumption $T_i = T_e$ also for the fluctuations. Asterisks stand for the convected flux (Q_r^*) and red triangles for the conducted one (q_r^*). Axes, linestyles, and the method to deduce the error bars are the same as in figure 5.29.*

while the average value $(1.8\,\text{kW}\,\text{m}^{-2}$ close to the separatrix) and the shape of the radial profile are robust with respect to the different assumptions on T_i. In contrast, particle and convected electron energy flux depend strongly on the T_i model. For the particle flux the uncertainty is more or less constant along the profile (in both T_i models) and amounts to $\sim 7 \cdot 10^{19}\,\text{m}^{-2}\,\text{s}^{-1}$. For the convected energy the uncertainty is mostly $0.4\,\text{kW}\,\text{m}^{-2}$, except when $T_i = T_e$ and the probe is located close to the separatrix. In that case the uncertainty is $0.7\,\text{kW}\,\text{m}^{-2}$.

5.3.2.3 Total energy flux

Neglecting the fact that the ion self collision time is comparable to the lifetime of the fluctuations, which could put the concept of an ion temperature into question, one may add the energy flux carried by ions in a straightforward way. In this case the dependence of the total energy flux on the ion model is not so serious: On one hand with $T_i = const = \bar{T}_e$ the total flux is twice the convected flux plus the conducted flux by electrons alone, altogether $(6.6 \pm 1.5)\,\text{kW}\,\text{m}^{-2}$ near the LCMS (figure 5.32). On the other hand the assumption $T_i = T_e$ requires to add two times the corresponding convected flux plus two times the conducted flux, altogether $(6.0 \pm 1.0)\,\text{kW}\,\text{m}^{-2}$ near the LCMS (figure 5.33).

The relative error of the total flux is smaller than that of the conductive flux. As before, 13 individual probe triplets have been used to calculate this error, but
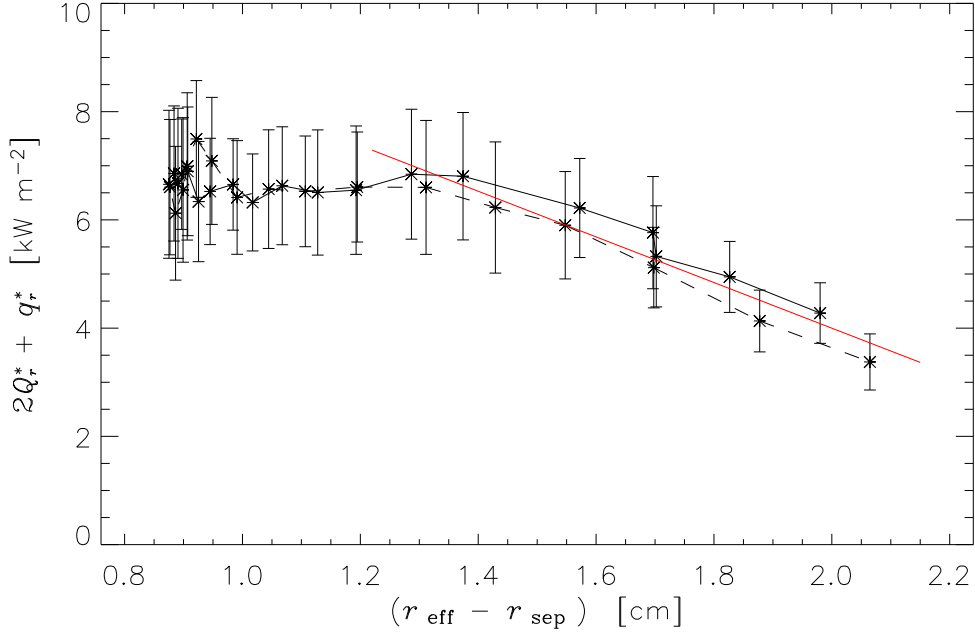
Figure 5.32: *Profile of the total turbulent energy flux according to the model $T_i =$ const. Both directions of the probe movement are overplotted, as a solid (inward) and a dashed line (outward). The error bars are estimated from the deviation of individual tip triplets. For values $r_{eff} > r_{sep} + 1.2$ cm the regression analysis yields the gradient (4.2 ± 0.4) kW m^{-2}/ cm (red line).*

this time evaluating temperature times density on the middle tip of each triplet, multiplied with the electric field fluctuations that are deduced from the adjacent tips. Obviously the scatter of these individual fluxes is smaller when compared to the scatter of conduction. This can be understood, since the product of temperature and density is equivalent to I_{sat} times $\sqrt{T_e}$, which reduces the impact of T_e being the fit parameter with the highest noise level.

From the magnitude of the total flux and its gradient (see figures 5.32 and 5.33) a gradient length can be estimated. This length is $\lambda = 1.6$ cm in the model $T_i = const$, and $\lambda = 1.5$ cm in the model $T_i = T_e$. Power decay lengths have been measured before in the SOL of the W7-AS, however without the divertor. For a similar magnetic configuration, 460 kW ECR heating and a volume averaged density of $2 \cdot 10^{19}$ m^{-3}, the reported power decay length was $\lambda_q \approx 1.4$ cm [Grigull et al. 1995], which is a reasonable agreement.
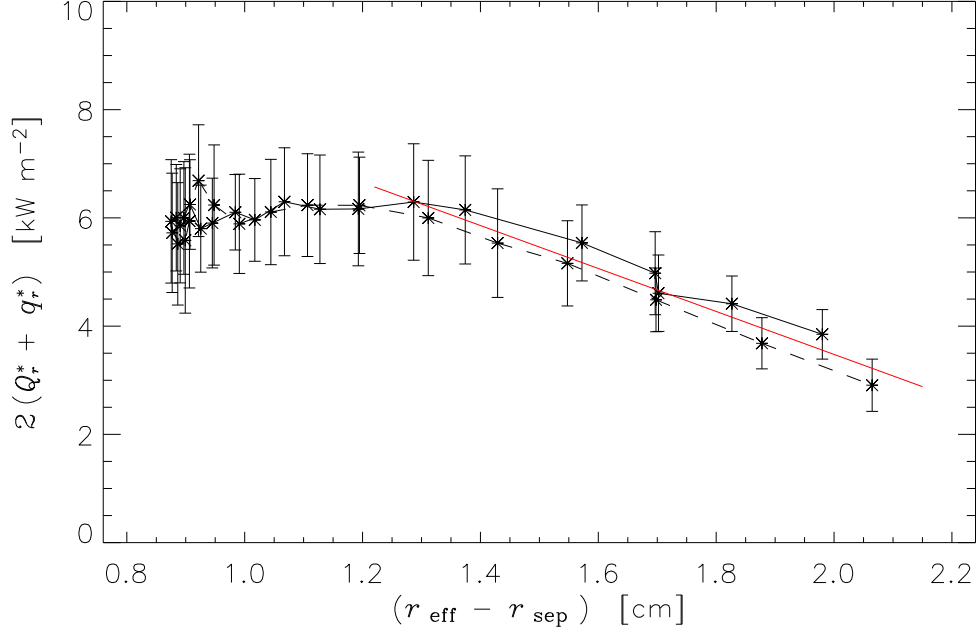
Figure 5.33: *Profile of the total turbulent energy flux similar to figure 5.32, but using the model $T_i = T_e$. The regression analysis in the SOL yields the gradient $(4.0 \pm 0.3)\,\mathrm{kW\,m^{-2}/\,cm}$ (red line).*

5.4 Comparison of the transport to the overall confinement in W7-AS

One may scale the measured local fluxes to the entire surface of the W7-AS and discuss the overall turnover of particles and energy. If the turbulent fluctuations are relevant for the average radial transport at least in the edge plasma, then the measured values should yield a significant ratio of the entire particle or energy turnover in the machine. According to equations (1.30) and (1.31), the comparison has the fewest unknown parameters when the data from near the LCMS is used. For the energy flux the method is simple, since the energy source inside the plasma bulk volume is well known. A detailed discussion of the particle flux, however, would require the exact recycling sources at the limiters and a computation of the neutral gas, and ionisation profiles, e.g. by the Monte Carlo code EIRENE [Reiter 1992]. This is beyond the scope of this work.

5.4.1 Impact of finite bandwidth

Examining the k-spectra of the transport in figures 5.27, 5.28 and 5.30, it is obvious that particularly the spectrum of conduction is broad compared to the bandwidth of the measurement. Since the contribution of conduction to the total energy flux is large near the LCMS, this puts the significance of the measurement into ques-
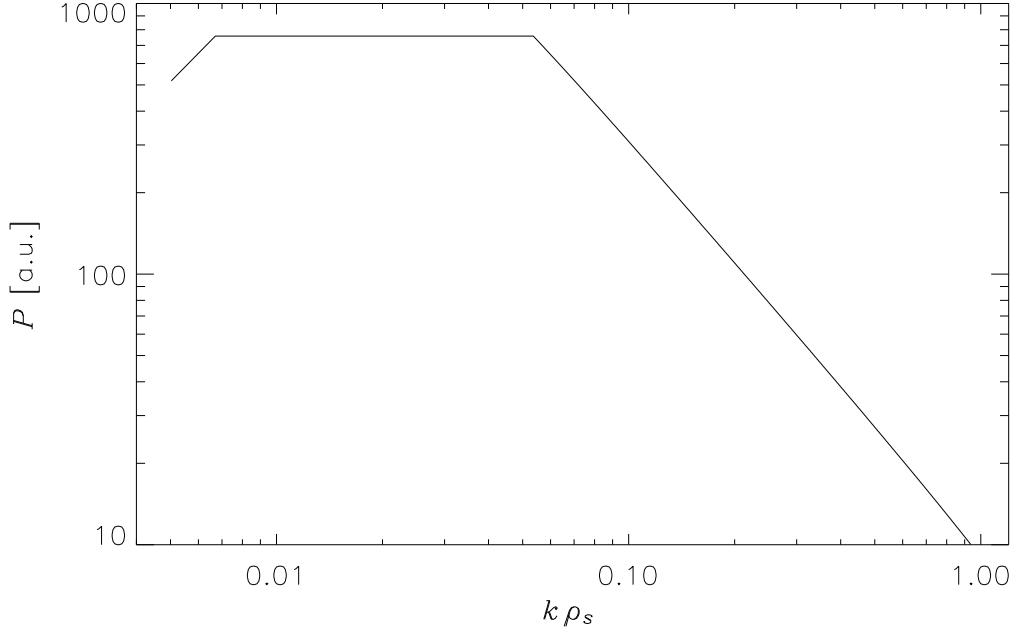
Figure 5.34: *Artificial power spectrum as a function of the normalised wavenumber. The transport relevant slope with exponent $-3/2$ models the experimentally obtained one.*

tion. A simulation of the measurement, where the observed spectral properties are extrapolated beyond the bandwidth, is considered to be helpful. Two questions can be tackled:

- Are the contributions of small wavenumbers to the transport measured correctly, if indeed the wave period is small compared to the recording time, but the wavelength is larger than the baseline of the probe array?

- Extrapolating the measured spectral properties to high wavenumbers: How large will the fraction of the transport actually be, that can be resolved properly with the given tip spacing?

One method to address these topics is to set up artificial spectra, spatio-temporal signals and transport numerically on a sufficiently fine grid. The data is numerically sampled on a more coarse grid corresponding to the tip spacing and the temporal grid.

Defining the temporal resolution $dt = 0.2 \, \mu s$ and the poloidal resolution $dy = 0.067 \, cm$ and using 50625×1125 grid points, the periodic simulation area has got side lengths $\sim 10 \, ms$ and $75 \, cm$, respectively. The length in time is equivalent to one packet, i.e. one probe position of the evaluated experimental data. Given $\rho_s = 0.02 \, cm$, the y spacing is chosen to match $k \approx \rho_s^{-1}$ as the maximum resolved wavenumber. This should be sufficient, since any numerical simulation of drift wave turbulence shows a strong drop-off in the spectral power above $k\rho_s = 1$ (e.g. [Scott 1997]).

122
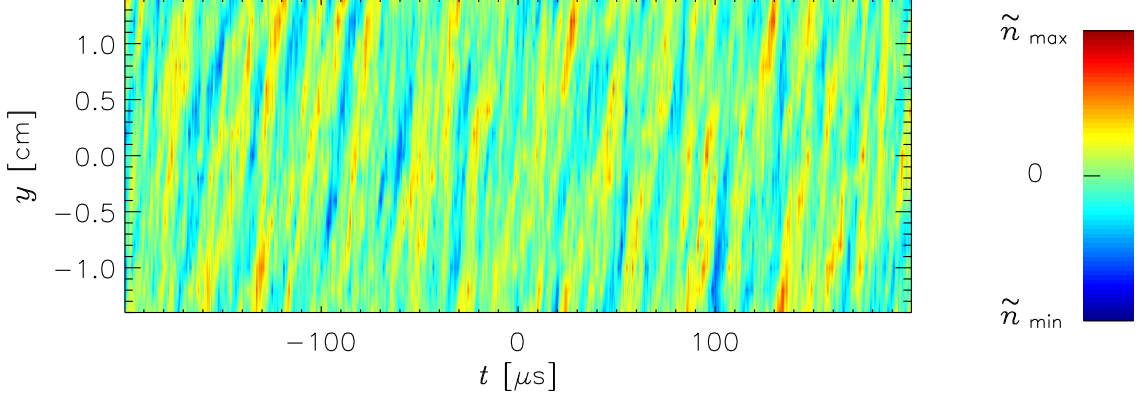
Figure 5.35: *Contour plot of the artificial data, sampled by a numerical 15 tip probe. The fluctuating part of the density is color coded and displayed as a function of time and space, where the latter corresponds to the poloidal coordinate in the real measurement. The primary data were calculated from the artificial amplitude kf spectrum and a random distribution of the phases.*

Within the kf plane an amplitude spectrum is selected that models the experimentally obtained ones for either $\tilde{T}_e$, $\tilde{n}_0$ or $\tilde{U}_{plasma}$. The artificial spectral power has got a plateau in the square region $0.251\,\mathrm{cm}^{-1} < k < 0.05\,\rho_\mathrm{s}^{-1}$ and $10\,\mathrm{kHz} < f < 50\,\mathrm{kHz}$. Beyond the plateau, lines of equal power display quadratic contours in the kf plane, where the amplitude decrement with the exponent $-5/4$ of either k or f is chosen to generate the experimentally observed $-3/2$ power law after integrating the f coordinate of the amplitude squared. The model power spectrum as a function of k alone is displayed in figure 5.34.

Thereafter the corresponding phase spectrum can be defined: For simplicity the phases of potential fluctuations are assumed to be randomly distributed. When calculating the density or temperature fluctuations, this random phase spectrum is reused, but the phases are shifted uniformly by 40° according to the experimental value close to the separatrix. In the following only the term "density" will be used in order to describe either density or temperature fluctuations.

Keeping in mind the guidelines written down in appendix A.2.2, the Discrete Fourier Transform is employed to produce the fluctuations in the spatio-temporal domain. Since the transform is a superposition of harmonic waves, electric field fluctuations can be evaluated from the potential exactly. The full transport wavenumber spectrum is obtained from the cross spectrum between the electric field fluctuations and the density by summing up all frequencies (see section 4.5.2).

Now an artificial probe measurement is performed in a 2.8 cm wide subset of the data. In several runs the location has been shifted along the spatial extent of the simulation area without significant change of the results. Defining a probe grid with 15 points, 2 mm spacing and 0.4 µs temporal resolution, the turbulence is "measured" artificially and a time slice of the "sampled" data can be displayed (figure 5.35).
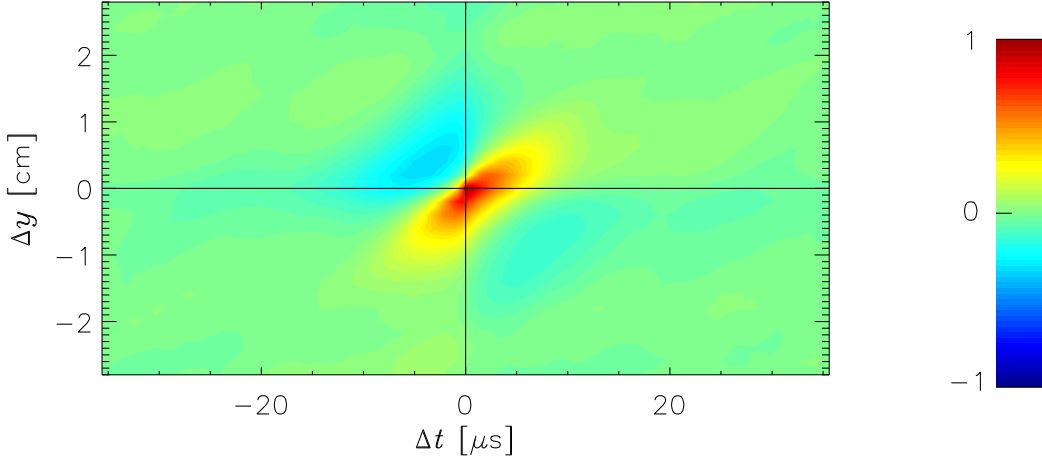
Figure 5.36: *Cross-correlation function between modelled potential and density fluctuations, calculated from the numerical probe measurement. The function is normalised to the absolute maximum of the displayed region.*

Analogue to the evaluation of experimental data, potential and density fluctuations are filtered by a 1 kHz highpass, the cross-correlation function is computed and averaged over equivalent tip pairs, and the electric field is approximated by taking finite differences. It is worth mentioning that the poloidal size of the cross-correlation in figure 5.36 is indeed similar to the experimentally obtained one. This scale is related to the location of the shoulder in the k-spectrum (see figure 5.34), i.e. where the plateau passes over to the spectral decay following a power law. If the numerical values are compared, then the poloidal size is roughly 0.37 times the wavelength associated with the wavenumber at the location of the shoulder.

There is one slight difference to the experimental results, that is the propagation velocity is less uniform. This is an effect of the weak proportionality between k and f in the model amplitude spectrum.

Finally, the transport spectrum as measured by the numerical probe and the exact spectrum are compared. With respect to the initial questions there are these findings:

- Contributions of wavelengths longer than the baseline of the probe are negligible. The spectral peak of the transport is located at the shoulder of the input wavenumber spectrum which is closely connected to the poloidal size.

- With the given $-3/2$ decay of fluctuation power extrapolated until the dispersion scale $k\rho_s = 1$, and assuming that the cross phase is stiff in that region, the probe misses approximately 70% of the total transport. The missing flux is carried by small scales, i.e. large wavenumbers. Even within the observable wavenumber range, the technique to use finite differences for the calculation of the electric field leads to significant leakage.

124
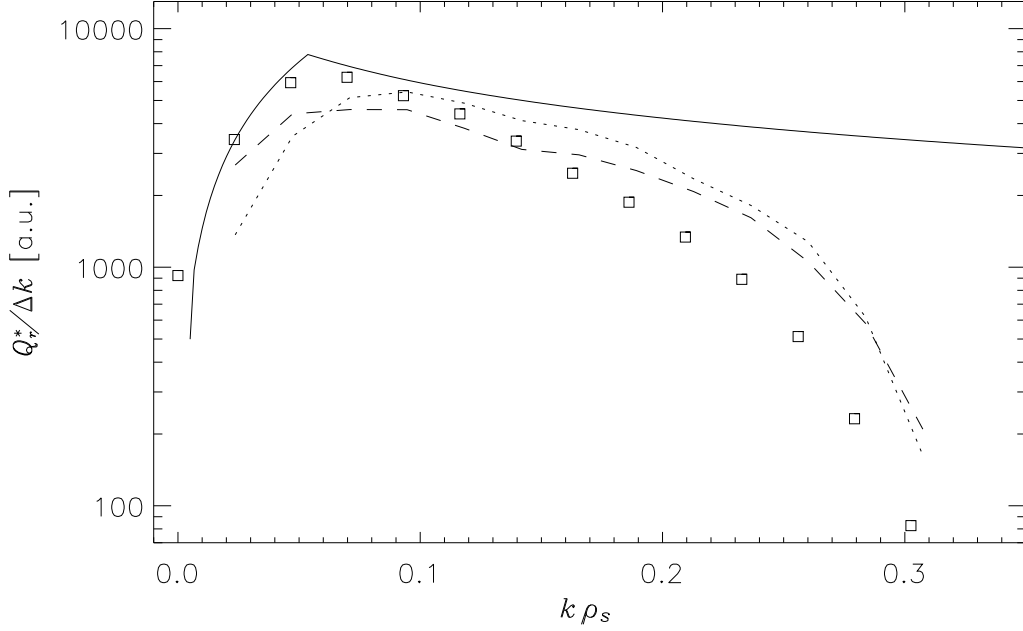
Figure 5.37: *Simulated and numerically sampled spectral density of the transport. The solid line is the exact calculation and the squares denote the result of the numerical probe measurement. Experimentally obtained transport spectra were scaled manually and overplotted with a dotted (convective) and a dashed (conductive) line.*

In order to substantiate these statements, figure 5.37 shows the spectral density of the transport from both the exact calculation and the numerical probe measurement. Note that the spectral decay of the (exact) transport is much slower than that of the power spectrum in figure 5.34. Additionally, two experimental transport spectra are overplotted, which were obtained close to the separatrix. Both the conductive and the convective part display a striking resemblance to the numerical probe measurement for $k\rho_s > 0.2$. Due to the fact that the natural spectrum of plasma fluctuations in the W7-AS is actually more smooth around the shoulder, the experimental spectra are more flat for $k\rho_s < 0.2$.

Concluding, an increased bandwidth particularly in the wavenumber domain is required, if one wants to measure a larger fraction of the actual turbulent transport. For future probe measurements this is equivalent to an array with more closely spaced tips.

5.4.2 Turnover of particles and energy in the W7-AS

In order to maintain a W7-AS plasma steady state, energy supply (in this case ECR heating) and neutral gas supply for particle refueling are necessary. The absolute values of the corresponding rates are available from the control signals. The balance inside the plasma volume requires that the total heating power is equal to the absorbed microwave power. For the particles it is more complicated, since recycling

neutrals from the wall diffuse into the plasma volume where they get ionised. This adds to the external supply of gas. A realistic treatment of the recycling is rather complex and will be omitted. Hence, the turnover of particles discussed here is only a lower limit, while the value for the energy is rather accurate.

The external particle fuelling rate of the W7-AS plasma during the probe measurement was $R_n = 4 \cdot 10^{20} \, \text{s}^{-1}$, and the absorbed heating power was $P_E = 0.48 \, \text{MW}$. Bolometry measurements suggest that the radiation losses inside the bulk plasma amount to $0.04 \, \text{MW}$. The additional energy sink defined by the volume integral over $W_{ion} S_n$ (see section 1.4.2) is negligible. This is given by the particle fuelling rate times the ionisation energy of hydrogen ($13.6 \, \text{eV}$) in the present case.

Since the area of the magnetic surface tangential to the probe is $A_\kappa(r_{\text{sep}}) = 15.1 \, \text{m}^2$ (see section 3.1.1), and since the radial transport at the location of the probe is decreased by a factor 1.22 due to the local flux expansion (see also section 3.1.1), the expected local radial flows are

$$\bar{\Gamma}_r^* \quad = \quad \frac{4 \cdot 10^{20} \, \text{s}^{-1}}{15.1 \, \text{m}^2 \cdot 1.22} \quad = \quad 2.2 \cdot 10^{19} \, \text{m}^{-2} \, \text{s}^{-1}$$

$$\text{and} \quad \bar{Q}_r^* + \bar{q}_r^* \quad = \quad \frac{(0.48 - 0.04) \, \text{MW}}{15.1 \, \text{m}^2 \cdot 1.22} \quad = \quad 24 \, \text{kW} \, \text{m}^{-2} \ ,$$

where the uncertainties of these values are small compared to those of the measured turbulent fluxes.

Chapter 6

Discussion

Before going into the interpretation of measurement results, it should be pointed out that the observed properties of fluctuations in the SOL of W7-AS ECRH plasmas are exemplary. They are not the average of a large database of various plasma experiments. However, discharges with ECR heating are highly reproducible in W7-AS with respect to radial profiles of temperature and density and to the total energy content. Therefore, an exemplary snapshot of edge fluctuations and their associated radial fluxes of particles and energy should also describe plasma edge turbulence under these experimental conditions in general.

6.1 Characteristics of W7-AS plasma edge turbulence

The simultaneous measurement of temperature, density and electric potential with sufficient resolution in both time and space allows one to determine properties of W7-AS plasma edge fluctuations in detail. Fluctuations are observed to be turbulent throughout the investigated region from near the LCMS into the SOL: From the measurements there is no evidence for long-range coherent periodicity of fluctuating plasma quantities, neither in time nor in the poloidal direction. Instead, using spatio-temporal correlation functions, the fluctuations appear to be localised features that can be characterized by a poloidal size d_{pol} and a lifetime τ_L (see section 5.2.1). In W7-AS SOL at full magnetic field $B = 2.5\,\text{T}$ typical values are $d_{pol} = 1\,\text{cm}$ and $\tau_L = 30\,\mu\text{s}$, respectively, for fluctuations of both n_0 and T_e.

Transforming the spatio-temporal correlation into Fourier space, these properties are corresponding to a mode spectrum of finite width. In the temporal domain, the total bandwidth is determined by poloidal $E \times B$ convection. The convection velocity is comparatively homogeneous along the extent of the Langmuir probe array, since the latter is aligned within one magnetic surface. The magnitude of the velocity depends on the distance to the LCMS. This was reported by Bleuel et al. [2002] and it is known from other machines, e.g. Ritz et al. [1984]. The poloidal convection is

induced by the stationary profile of the radial electric field that builds up depending on the total power and particle balance inside a plasma machine as can be described by neoclassical theory. Thus, since we cannot discuss the radial electric field within this frame, we do not rely on frequency spectra.

A more meaningful characterisation of the turbulence is possible by d_{pol} and the k spectrum, respectively. In this case, the spectral power as a function of normalised k is localised at low wave numbers with a slight maximum for values $k_\perp \rho_\mathrm{s} = 0.04 \ldots 0.05$ (section 5.2.2). Beyond the location of this maximum, the power spectrum decays proportional to k^x with an exponent $x \lesssim -1.5$ until the limit of resolution $k_\perp \rho_\mathrm{s} \approx 0.33$. The slowest decay ($x = -1.5$) is found near the LCMS and a more steep decline is found in the SOL. For density and potential, these poloidal scales in the W7-AS SOL have been reported before by Bleuel et al. [2002], who did meaurements in the SOL and show a power spectrum with $x = -3$. For T_e alone, there are measurements available inside the plasma confinement region of W7-AS by Sattler et al. [1994] and Bäumel et al. [2003]. Although in the latter reference the distance relative to our position in radial direction is about $8\,\mathrm{cm}$, the normalised poloidal scale is of the same order. Bäumel measured the poloidal evolution of the coherency. Given d_{pol} is two times the decay length of the coherency, his result is $d_{pol} = 1.6 \ldots 3\,\mathrm{cm}$, depending on the ECR heating power. This is a factor $1.6 \ldots 3$ higher compared to the edge, at the same time the normalisation parameter ρ_s, however, rises to ~ 3 times the edge value due to the electron temperature profile [Bäumel 2002]. Since $k_\perp$ scales with the inverse of the poloidal size, the product $k_\perp \rho_\mathrm{s}$ remains more or less unchanged (factor $1 \ldots 1.9$) inside the plasma.

Comparing the scales of density fluctuations measured with Langmuir probes in the SOL plasma of various tokamaks, the situation is very similar. For edge parameters $T_e = 20\,\mathrm{eV}$, $n_0 = 3 \cdot 10^{18}\,\mathrm{m}^{-3}$ and varying magnetic field strengths, Zweben and Gould [1985] ($B = 0.35\,\mathrm{T}$), Levinson et al. [1984] ($B = 0.8\,\mathrm{T}$), Ritz et al. [1984] ($B = 1\,\mathrm{T}$) and others report that the spectral power peaks below $k_\perp \rho_\mathrm{s} = 0.1$. More recently, frequency spectra of single point measurements, which are more easily to obtain, have been compared between different machines by Carreras et al. [1999]. Compensating for the $E \times B$ convection in the method of analysis, the authors find a universal similarity in the turbulence spectra.

6.2 Numerical simulation of plasma turbulence

Self consistency of particle dynamics and the relevant fields generated by these particles is achieved in numerical models for fully developed plasma turbulence. So far, the corresponding computer codes, however, are only applicable for the plasma confinement region. Present day's most advanced numerical simulations are three dimensional (3D) when using fluid representation of the plasma and five dimensional (5D), respectively, when applying a gyrokinetic model (i.e. neglecting the phase of the gyro motion). They are able to include magnetic geometry in detail. Scott [1997]

(3D) and Jenko [1998] (5D) provide simulations in flux tube geometry of a tokamak. For the simulated conditions at the plasma edge, but still within the LCMS, both find power spectra in density and potential with peak values at low wavenumbers and a rollover towards an exponential decay in the range $k_\perp \rho_s = 0.1 \ldots 0.2$. The fluid model has been adapted by Kendl [2000] to the flux tube geometry of a stellarator, including the W7-AS magnetic configuration. Kendl also compares the numerical results for different geometries and finds a dependence of the fluctuation induced transport level on the integrated modulus of the local shear, which is nonuniform within one magnetic surface of a stellarator. Normalized k spectra, however, are almost unaffected. Kendl's comparison of the k spectra, obtained from the simulation of turbulence in various stellarator and tokamak geometries is displayed in figure 6.1. One remark concerning the limit $k \rightarrow 0$ should be added: While the simulations usually show a white spectrum for small k values, this is not observed in the measurement due to the finite size of the observed volume.
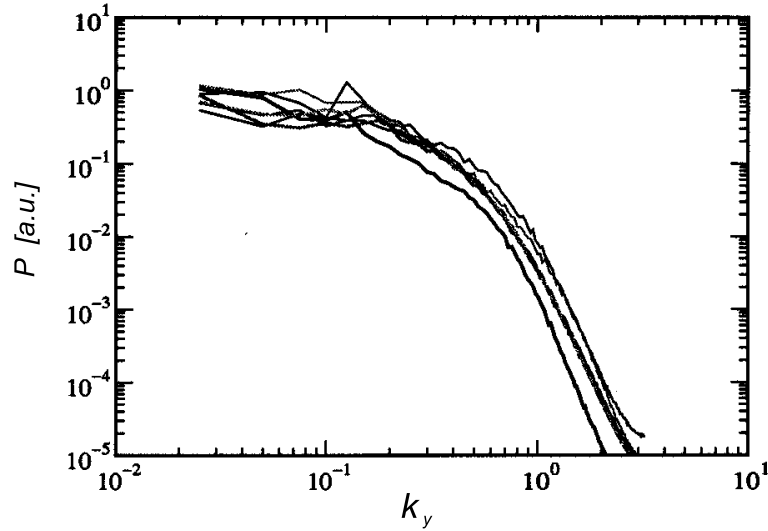
Figure 6.1: *Power spectra of density fluctuations as a function of the wavenumber k_y (perpendicular to the magnetic field) in units of $\rho_s{}^{-1}$ [Kendl et al. 2003]. The data are obtained from numerical simulations of drift-Alfvén turbulence in various stellarator and tokamak magnetic field configurations. The high degree of similarity indicates the universality of the turbulent spectrum.*

To conclude from the previous experimental and this theoretical section: The poloidal size d_{pol} and the corresponding location of the rollover in the k spectra of both temperature and density fluctuations are universal, when normalised to the drift scale ρ_s. This is confirmed by the W7-AS measurements at several positions in the SOL up to the LCMS. Compared with numerical simulations of drift wave turbulence on closed magnetic surfaces, the rollover of the k spectra measured in the SOL is located at wavenumbers, which are smaller by a factor ~ 2.

6.3 Phase relations between fluctuating quantities

It was pointed out in section 5.2.3, that the phase of the cross kf spectrum between two fluctuating quantities is independent of the values of k and f in good approximation. Therefore, it is sufficient to discuss scalar power weighted phases.

6.3.1 Measured properties

First of all it is remarkable, that the U_{float}-I_{sat} cross phase is close to 90° with marginal variation for different radial positions in the SOL. Along the direction of ion diamagnetic drift $\tilde{U}_{float}$ is always leading $\tilde{I}_{sat}$. Assuming that the negative gradient of U_{float} is equal to the transport relevant electric field (generally this is not a good assumption), then this phase shift yields the largest possible fluctuation induced radial transport directly opposed to the stationary gradient of the plasma pressure. The quantities U_{float} and I_{sat} were measured with non-sweeping probes on several devices and the observation of this characteristic phase shift is indeed universal. Levinson et al. [1984] found it at PRETEXT, Endler et al. [1995] at ASDEX, Lechte et al. [2002] at TJ-K, and it has already been documented at W7-AS by Bleuel [1998]. Taking into account the electron temperature T_e and its fluctuations, it becomes obvious that this stiff relation is composed of counteracting evolutions in the cross phases U_{float}-T_e and T_e-I_{sat}. Close to the confinement region the cross phase between fluctuations of T_e and I_{sat} is small and the U_{float}-I_{sat} phase shift is sustained by the displacement of $\tilde{U}_{float}$ with respect to $\tilde{T}_e$. Far out in the SOL the complementary behaviour is found: the U_{float}-T_e cross phase tends to small values (the minimum value that has been found was 30°) while the phase between the fluctuations of T_e and I_{sat} increases.

The phase of the density fluctuations $\tilde{n}_0$ deduced from $\tilde{I}_{sat}$ sensitively depends on the model assumption for T_i (section 5.2.3.3). Experimentally, it was not possible to distinguish between the two models $T_i = \bar{T}_e = const$ and $T_i = T_e$ within this work. In theory, on one hand the ions don't take part in the fast parallel dynamics of the electrons. This is an argument in favour of $T_i = const$. But on the other hand radial $E \times B$ drifts in a radial background gradient of T_i introduce a finite fluctuation level, which is an argument in favour of $T_i = T_e$. Hence, when evaluating the I_{sat}-n_0 cross phase with the two different model assumptions, the results can be interpreted as a lower and an upper boundary. The absolute deviation of the cross phase between the two models is $\sim 15°$ when evaluated close to the LCMS, whereas the deviation vanishes in the SOL.

Fluctuations of T_e and n_0 are highly correlated (see sections 5.2 and 5.2.3). Between the SOL location and the location near the LCMS there is a remarkable change of the cross phase: While in the SOL $\tilde{n}_0$ is displaced relative to $\tilde{T}_e$ in electron diamagnetic direction it is opposite close to the separatrix. The variation is larger

in the $T_i = T_e$ model than in the $T_i = \bar{T}_e = const$ model. This has a serious consequence for the radial transport of particles: Since T_e contributes significantly to the plasma potential (see the probe theory in section 2.4.4), the change of the cross phase sign leads to a reduction of the radial particle flux. The reduction is stronger pronounced in the $T_i = T_e$ model.

Data from other devices concerning the phase relation between $\tilde{T}_e$ and $\tilde{n}_0$ are very rare. Meier et al. [2001] supply a measurement at the LCMS of TEXT-U and deduce an in-phase fluctuation of T_e and n_0. This would be consistent with W7-AS for a probe position close to the LCMS. The T_e-n_0 cross phase was measured in the confinement region of W7-AS ECRH plasmas with a completely different diagnostic setup. Häse et al. [1999] used an ECE crossed sightline correlation radiometer combined with a broadband heterodyne reflectometer and they report in-phase correlation of $\tilde{T}_e$ and $\tilde{n}_0$, and a radial outward propagation of turbulent structures.

6.3.2 Theoretical approaches

Self consistent simulations of plasma edge turbulence are, as already pointed out, only available for the confinement region. Zeiler et al. [1997] find a significant correlation between $\tilde{T}_e$ and $\tilde{n}_0$ with fluctuations in phase, independent of the influence of the magnetic curvature. This is not surprising according to Scott [1997], since the basic characteristics of turbulence, i.e. the shape of the spectrum and the distribution of cross phases do not depend on the inclusion of single instability mechanisms. Fundamental is only the interplay between $E \times B$ drifts in a background pressure gradient on one hand, and the mode coupling and the dissipating parallel electron motion on the other. Scott additionally supplies the phase distribution between $\tilde{U}_{plasma}$ and $\tilde{n}_0$, which is generally independent of k and peaks at $\sim 20°$. The width of this distribution is also $\sim 20°$ and depends on the normalised parameter $\hat{\beta}$, that can be estimated to be close to 0.5 in the SOL of the W7-AS. When compared to the measurement near the LCMS, the most probable value of the cross phase obtained from the simulation is smaller by a factor ~ 1.5. Assuming that the simulation result is valid in the confinement region until the LCMS, and extrapolating the experimentally observed trend of a decreasing phase shift when approaching the LCMS from outside, then this finding is in accordance with the measurement. Summing up, there is remarkable agreement with respect to the sign and the order of magnitude of the cross phase, and with regard to the fact that also in the simulation results the phase distribution doesn't dependend on the wavenumber. In this way, the simplification to discuss a scalar power weighted phase is justified from both the measurement and the theoretical point of view.

In the SOL such detailed comparisons are not possible, because currently there are no simulations of fully developed turbulence available. Linear models by Nedospasov [1989], Garbet et al. [1991] and Endler [1994] are able to identify regions of unstable poloidal wavenumbers and predict growth rates. Endler studies the influence of both temperature and density gradient. For the case that the density

gradient is steeper than the temperature gradient, a "second instability mechanism" is reported. This mechanism affects mainly small poloidal wavenumbers and yields fluctuations of U_{plasma} and T_e in phase, while n_0 is shifted by 90°. Since U_{float} depends on U_{plasma} and T_e, it is clear that in this case U_{float} fluctuations have the same phase as U_{plasma} fluctuations. According to Endler, in this parameter range the boundary condition imposed by the sheath at the target plate dominates over the drift effects and gives strong and mutual feedback on the fluctuating quantities. Measurements for probe positions far out in the SOL, which indeed yield small cross phases U_{float}-T_e and U_{float}-U_{plasma} (section 5.2.3.3) approve this model. The density gradient measured by the probe is slightly steeper than the temperature gradient (see section 5.1), which is in compliance with the model requirements. One has, however, to keep in mind the simplification of a linear stability analysis. A self-consistent numerical treatment of the fully developed turbulence with correct sheath boundary conditions would be very valuable for detailed further comparison.

There is a phenomenological model for cross field transport by D'Ippolito et al. [2002], which presumes that an elongated (along $\boldsymbol{B}$) structure of a plasma density perturbation exists in the SOL. Such "blob" structure is in accordance with the result of the correlation analysis of the measured data (section 5.2.1), if it has got the poloidal size d_{pol} on average and if it has got a finite lifetime. Due to the boundary conditions in the SOL, each "blob" is terminated on both sides by a sheath. According to D'Ippolito, the charge separating magnetic curvature drift in combination with the sheath potential leads to a polarisation of the "blob". The polarisation can also be generated by the friction force between the "blob" and streaming neutral particles [Krasheninnikov and Smolyakov 2003]. The large phase shift between U_{plasma} and n_0 measured in the SOL (see figure 5.24) corresponds to the polarisation. Whether the observed cross phase T_e-n_0, which is comparatively large in the SOL, and the small cross phase U_{plasma}-T_e are reproduced by the "blob" model, however, requires further investigation.

6.3.3 Comparison of floating and plasma potential

In general the floating potential U_{float} in a magnetised plasma is a very sensitive quantity, depending on a large number of parameters. For instance, a significant impact on U_{float} by modifications in the probe geometry is reported [Höthker et al. 1999]. A complete theoretical treatment of U_{float} would require kinetic modelling of both ions and electrons, including the probe geometry in 3D. This is not within the frame of this work. Following equation (2.17), only the interrelations between U_{float}, T_e and U_{plasma} are discussed.

It has been shown (section 5.2.3.3) that the phase of U_{float} fluctuations differs from the phase of U_{plasma} fluctuations. The difference is small in the SOL and maximal in the vicinity of the LCMS. Given the aim of the measurement is to deduce transport relevant fluctuations of the poloidal electric field: In this case, U_{float} can nevertheless be used instead of U_{plasma} for the computation of the conductive en-

ergy transport, since the modification by T_e, namely the transport relevant product between the fluctuating poloidal gradient of T_e times the T_e fluctuations, is zero [Pfeiffer et al. 1998]. But in the case of the convective transport the usage of U_{float} fluctuations alone is not adequate (cf. figure 5.26). This is actually the consequence of the non-zero cross phase T_e-n_0.

At this point it should be noted, that the phase relation U_{plasma}-T_e deduced from the U_{float}-T_e cross phase data, and using probe theory, could be confirmed by Fink [2002], who measured fluctuations at the LCMS of W7-AS with emissive probes. Fink did a single point measurement and found significant spectral power in the frequency range $0 \ldots 100\,\text{kHz}$. From his data he deduces U_{plasma}-T_e cross phases around $45°$. For comparison, the measurement with the swept probes yields $40°$ near the LCMS (cf. figure 5.24).

The phase deviation between U_{float} and U_{plasma} is a natural consequence of the utilised probe theory. U_{plasma} fluctuations can be illustrated as the vector sum of U_{float} and T_e fluctuations, where the cross phase denotes the angle between them (figure 6.2). Consequently, if $\tilde{U}_{float}$ and $\tilde{T}_e$ are not in phase, as seen in the mea-
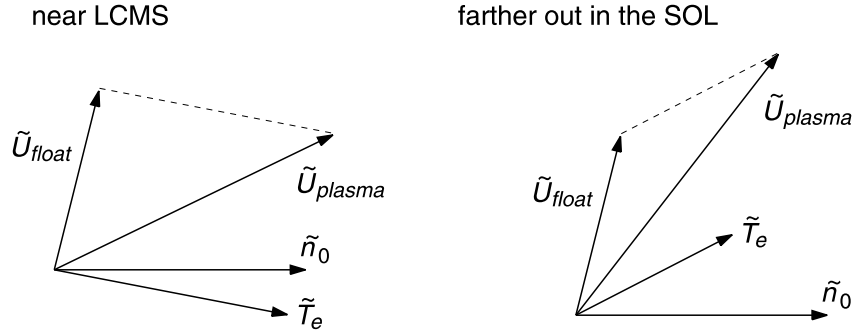
Figure 6.2: *Comparison of the relative phase between different fluctuating quantities (represented as arrows in the complex plane) at different radial positions in the SOL (schematically, amplitudes not to scale). The cross relation between $\tilde{U}_{float}$ and $\tilde{n}_0$ is the same in both figures, in compliance with the measurement results. According to probe theory, $\tilde{U}_{plasma}$ is the vector sum of $\tilde{U}_{float}$ and $\tilde{T}_e$ (plotted also with a dashed line).*

surements, then $\tilde{U}_{plasma}$ and $\tilde{T}_e$ won't be either. It can also be put the other way round: If numerical turbulence simulations in the confinement region yield a small but significant cross phase T_e-U_{plasma}, then probe theory demands a different, i.e. larger phase shift between T_e and U_{float}.

The applied probe theory is stationary in a sense that all transit times of electrons and ions through the presheath and the sheath are assumed to be small compared to the temporal scale of the turbulence. For both species in the sheath and for the electrons in the presheath this is uncritical. Regarding the transit time of the ions through the presheath (see section 2.4.5) this assumption is marginally fulfilled.

If the perpendicular diffusion, which refills the flux tube emptied by the probe, is modelled as a result of turbulent fluctuations, then the presheath size will fluctuate, too, and the presumption of a stationary probe measurement is not valid. Since the presheath determines the ion acceleration, this has a sensitive impact on the floating potential, whereas the measurement of T_e is not affected. Possibly that difference could explain the special properties of the U_{float} fluctuations, such as the extraordinary phase shift with respect to I_{sat}. One way to approach this problem, i.e. to study dynamic presheath effects, would be to carry out a kinetic simulation of both the plasma turbulence and the potential drop imposed by the boundary condition of a probe collecting ions. An additional outcome of such a simulation could be the influence of the yet neglected ion temperature fluctuations. This is, however, outside the frame of this work.

6.4 Electrostatic turbulent transport in the context of the global confinement

The fast swept Langmuir probe system at W7-AS is calibrated to absolute values, therefore it is possible to evaluate the turbulent particle and energy flux quantitatively. If the local measurement at the probe position is representative for the entire magnetic surface, one can evaluate the total turbulent flux by multiplying the local flux with the area of the magnetic surface. The total flux can be compared to the global energy and particle balance of W7-AS. Of course, the assumption of homogeneity within the magnetic coordinates of the flux surface is a rigorous simplification, based on the numerical simulations by Kendl (see section 2.3). In order to make a better extrapolation, one would have to measure at different poloidal positions, in the 3D field of a stellarator even at several toroidal positions.

6.4.1 Energy transport

The calculation of the turbulent radial energy flux has been simplified by using the equations (1.28) and (1.29) for both electrons and ions. These formulas were derived for isotropic pressure and for turbulent flow velocities much smaller than the thermal velocities. Both conditions are only marginally fulfilled for the ions. Keeping these problems in mind, probe data evaluation yields energy fluxes up to $(6.6 \pm 1.5)\,\mathrm{kW\,m^{-2}}$ near the LCMS. Farther outside in the SOL the turbulent radial energy flux decreases with a scale length $\sim 1.5\,\mathrm{cm}$, in accordance with the power decay length of the W7-AS SOL (section 5.3.2.3). The expected energy flux, calculated from the ratio of the total deposited heating power and the flux surface area, is $24\,\mathrm{kW\,m^{-2}}$, where the effect of the local flux expansion is already included (section 5.4.2).

Although the magnitude of the radial flux actually measured is only $\sim 28\%$ of the expected value, it cannot be excluded that turbulent fluctuations account for

the radial SOL transport in total: A simulation of the probe measurement in a fluctuating background shows that the missing percentage can be carried by small scales which are unresolved by the probe (section 5.4.1). This result relies on the extrapolation of the observed spectral properties near the LCMS, namely the power law for the fluctuation amplitude and the stiffness of the cross phase, beyond the resolution limit ($k_\perp \rho_s \approx 0.33$) until the dispersion scale ($k_\perp \rho_s = 1$).

Alternatively, one can argue with the observed power decay lengths: According to the fluctuation spectra (e.g. figure 5.16) the fluctuation bandwidth is reduced in the SOL, so that a larger fraction of the transport relevant fluctuations is resolved there. The flattening of the calculated energy flux for $r_{\mathrm{eff}} < r_{\mathrm{sep}} + 1.2\,\mathrm{cm}$ is, therefore, due to a change of the fluctuation bandwidth. Using the measured radial gradient in the SOL ($\approx 4\,\mathrm{kW\,m^{-2}\,cm^{-1}}$, see figures 5.32 and 5.33), and extrapolating the turbulent energy flux to the separatrix position $r_{\mathrm{eff}} = r_{\mathrm{sep}}$ yields also a larger fraction of the total energy flux.

Uncertainties of the measurement

Extrapolating the values measured in the SOL to the separatrix position depends on the calibration of the coordinate r_{eff}. The position of the separatrix $r_{\mathrm{sep}} = 17.5\,\mathrm{cm}$ was deduced from the appearance of counter propagating structures in the correlation function of measured fluctuations in U_{float}. With respect to the nominal position there is a discrepancy of $1.35\,\mathrm{cm}$, since field line tracing in the vacuum magnetic configuration yields $r_{\mathrm{sep}} = 16.15\,\mathrm{cm}$. The deviation is larger than the geometrical uncertainty of the probe alignment. Deviations of this order were already reported by Bleuel [1998]. The tendency is always the same for probe measurements in W7-AS: If the separatrix position is determined by the velocity shear layer then it is of the order of $1\,\mathrm{cm}$ farther outside than the nominal position. In the present case, the multiplication of the radial deviation with the gradient of the power decay in the SOL suggests, that the turbulent radial energy flux at the nominal separatrix position is larger by $+5.4\,\mathrm{kW\,m^{-2}}$. This value can be regarded as an additional uncertainty of the measured flux, when it is compared with the total heating power.

The evaluated turbulent energy flux is influenced by the assumption on the magnitude of T_i, which could not be measured near the LCMS. Following the considerations in section 5.3.2.2, the assumption $\bar{T}_i = 1.5\,\bar{T}_e$ reduces the energy fluxes via the electrons and enhances the energy fluxes via the ions. Altogether in the model $T_i = \bar{T}_e = const$ the energy flux calculated from measurement data near the LCMS increases by $+0.4\,\mathrm{kW\,m^{-2}}$, and in the model $T_i = T_e$ by $+0.7\,\mathrm{kW\,m^{-2}}$. Obviously the effect of the T_i uncertainty is much smaller than the effects of the measurement bandwidth and the r_{eff} calibration.

The impact of secondary electron emission on the evaluated turbulent fluxes is negligible, which was addressed in section 5.3.2.2 by using different values for γ_e during the computation.

6.4.2 Particle transport

Concerning the particle flux, a detailed comparison is not possible, since the total turnover of particles is unknown in W7-AS. The total particle rate from external sources, divided by the LCMS area and compensated for the local flux expansion at the probe position, yields the flux $2.2 \cdot 10^{19} \, \mathrm{m^{-2} s^{-1}}$. Recycling sources, however, are not considered. I.e., neutral atoms (invisible to the probe) from recombination at the wall diffuse into the plasma, they are ionised and effuse as plasma, this time recognised by the probe. Hence, probe measurements indicate fluxes up to $5 \cdot 10^{20} \, \mathrm{m^{-2} s^{-1}}$ (see section 5.3.1), which is more than one order of magnitude higher than the flux calculated from external injection. If one examines the radial profile of the turbulent particle flux (figure 5.26), one notices that the peak value is measured approximately $1.5 \, \mathrm{cm}$ outside the LCMS. Towards the separatrix, the particle flux decreases significantly. Depending on the model for T_i, the reduction factor can be as small as one third. On the contrary, the energy flux does not display such behaviour. The results can be interpreted in a way, that the recycling neutral particles from the wall are ionized already within the SOL and are transported outward by the turbulence. Since there are no energy sources within the SOL, the situation is different for the energy flux.

Interpretation of the particle flux profile

Two questions may arise with respect to the measured profile of the particle flux (figure 5.26): The first is, which property of the turbulence changes in order to cause this peculiar radial variation? The second: Can the shape of the profile be understood?

The answer to the first question was anticipated in section 6.3.1, and the conclusion is that the decrease towards the separatrix is due to the changes in the phase of the T_e fluctuations. In principle it is unnecessary to argue with U_{float} and T_e, since the main point is the cross phase U_{plasma}-n_0 (cf. figure 5.24). The profile of this cross phase and the profile of the particle transport are essentially the same (indicating that the change in the fluctuation amplitudes plays a minor role). Nevertheless, it is helpful to disentangle the contributions to U_{plasma}, which are U_{float} and T_e, in order to put the results into the context of former investigations. For example, Lechte et al. [2002] and LaBombard [2002] neglected the effects of T_e fluctuations. It seems probable, that a part of LaBombard's criticism could be resolved by the inclusion of T_e and its fluctuations. Pfeiffer et al. [1998] already reported a significant overestimate of the particle flux, if one does not account for $\tilde{T}_e$.

Turning to the second question, whether one can understand the shape of the profile. It is helpful to remember the continuity equation (1.21) for particles and its application to the SOL (see section 1.4.2). Since the scale length of the particle flux variation is much smaller than the effective plasma radius $r_{\mathrm{eff}} \approx 18 \, \mathrm{cm}$, the particle flux divergence can be approximated as the partial derivative with respect to the

radial direction. At the maximum of the radial particle flux at $(r_{\text{eff}} - r_{\text{sep}}) \approx 1.5\,\text{cm}$ the effective particle source S_{eff} is zero, i.e. the volume source S_n balances the parallel losses $\text{div}\,\boldsymbol{\Gamma}_\parallel$. Under the assumption that the volume source due to ionisation of recycling neutrals is constant in this region, an alternative formulation of the second question is: Do the parallel losses change with the radial coordinate?

Field line tracing in the vacuum magnetic field configuration (see section 3.1.1) shows that there is a strong change in the connection length at $(r_{\text{eff}} - r_{\text{sep}}) \approx 1.5\,\text{cm}$, cf. figure 6.3. In the direction opposite to the magnetic field the length is constant and connects to the lower divertor of the W7-AS. Along the field vector the connection jumps from one module of the upper divertor to a more distant one. The situation is illustrated in figure 6.4. Given the parallel loss scales with the inverse of the connection length, it can be concluded that for probe positions $(r_{\text{eff}} - r_{\text{sep}}) > 1.5\,\text{cm}$ the parallel loss is indeed enhanced.
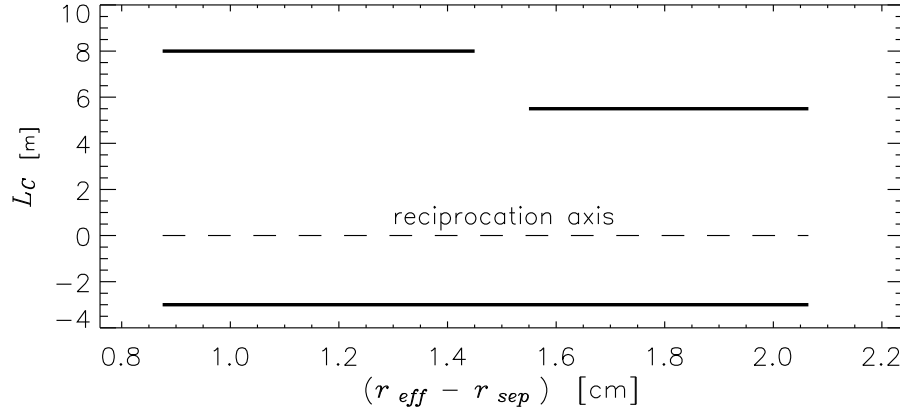
Figure 6.3: *Connection lengths (L_C) in the W7-AS SOL from the probe to the limiters as a function of the radial probe position. The edge rotational transform in the magnetic configuration is $\iota = 0.345$. Positive L_C corresponds to the direction in parallel with the magnetic field. At the location $r_{\text{eff}} - r_{\text{sep}} \approx 1.5\,\text{cm}$ the connection jumps to a different limiting component.*

6.4.3 Interplay of conduction and convection

From the spectral representation one obtains insight into the composition of the energy flux. This way, different properties can be observed in conduction (figure 5.30) and convection (figures 5.27 and 5.28). Most notably, particle and convected energy flux are sustained by smaller wavenumbers $k_\perp \rho_s \lesssim 0.1$, while the conduction spectra are inherently broader and cover the range $k_\perp \rho_s \lesssim 0.2$. The ranges are estimates for the e^{-1} widths of the spectral flux density. One can assume that both the convective transport, predominantly found in the SOL, and the conductive transport, which is dominating near the LCMS, are sustained by "blobs" [D'Ippolito and Myra 2003].
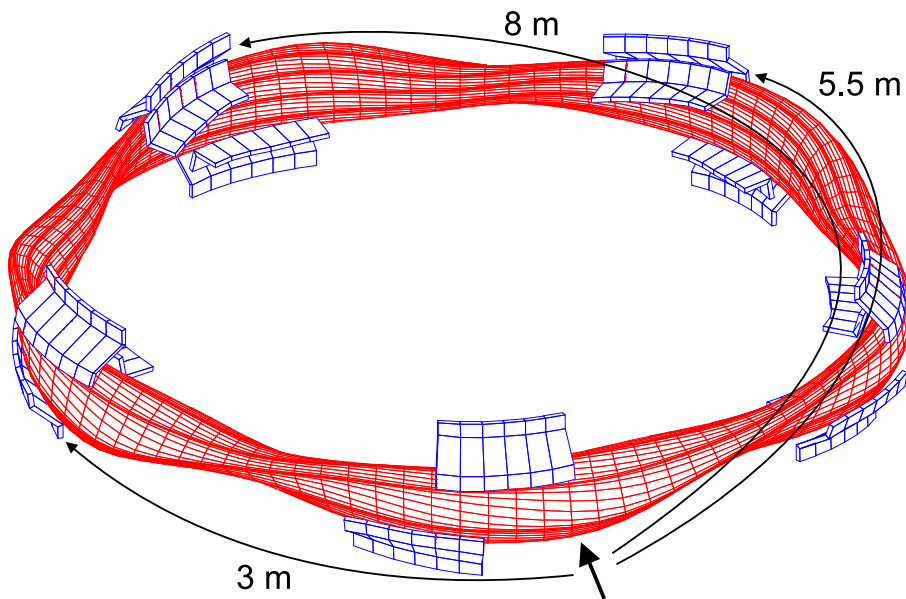
Figure 6.4: *Probe position (solid arrow), connection lengths (slim arrows) and plasma limiting divertor modules at W7-AS. The connection is drawn only schematically. Figure courtesy of J.Kisslinger, IPP Garching.*

In this case, although the details on "blob" stability in the particular W7-AS magnetic geometry would require further investigation, D'Ippolito's remark that large blobs (low k) will break into smaller ones (high k) on their way from the LCMS into the SOL cannot be supported.

Following the fact that in the SOL the fluctuation power generally increases when approaching the separatrix, the observed transition between conduction and convection is only possible because of changes in the cross phases between the fluctuating quantities. Hence, the cross phases seem to be the most important degrees of freedom, which allow the turbulence to sustain both the recycling particle flux and the steady energy flux.

Conclusions and Outlook

Using the sweeping technique for a poloidal multi-tip Langmuir probe array, the set of transport relevant fluctuations of T_e, n_0 and U_{plasma} was measured at different radial positions in the W7-AS edge plasma. The achieved space and time resolution has broadened the experimental view of plasma turbulence. Furthermore, the measurements provide detailed insight into the properties of the plasma fluctuation dynamics, which allows one to do a comprehensive comparison with numerical simulations of plasma turbulence.

To evaluate the data, the fit model with continuous evolution of the fit parameters I_{sat}, U_{float} and T_e turned out to be adequate in a sense, that the deviation between the measured and the fitted model data is small. Near the last closed magnetic surface (LCMS), where the bandwidth of the fluctuations is not small when compared to the sweep frequency, the fit parameters become covariant. Thus, the measuring method is at its limit for such probe positions.

In the scrape-off layer (SOL) of the W7-AS, profiles of the radial heat transport have been measured, and the contributions of convection and conduction could be clearly separated. When approaching the LCMS from outside, the convected part of the energy flux and the radial particle flux decrease, whereas the total energy flux is maintained by increased conduction. This condition is due to the cross over of the phase between T_e and n_0 fluctuations. The previously known power decay length in the SOL is confirmed by the present work. Only 28% of the total energy flux near the LCMS were measured. Calculations show that this is due to the limited bandwidth in both the frequency and the wavenumber domain. Hence, for future measurements further extension of both bandwidths is desirable but very demanding.

In the SOL the measurements suggest large cross phases (U_{plasma}, n_0) up to $\wp(60°)$. If that is to be compared to a numerical model, a self-consistent treatment of the fully developed turbulence with correct sheath boundary conditions would be necessary. Near the LCMS the comparison is possible: The amplitude and phase of T_e fluctuations provide the missing link between the previously obtained $\pi/2$ phase shift (U_{float}, I_{sat}) and the theoretical predictions of small cross phases (U_{plasma}, n_0) from drift-wave turbulence simulations.

Appendix A

Formulas and Constants

The following topics are referred to in various literature. Some subtle distinctions, however, are often neglected and the reader might have to inquire several references to find the exact background. The basics of a couple of items, which have been elaborately used in the previous chapters are reviewed in this appendix.

A.1 Small Plasma Formulary

A.1.1 The Coulomb Logarithm

The value of the Coulomb Logarithm is needed when the electrostatic interaction during particle encounters has to be taken into account in a plasma. For instance to do a computation of the parallel electric resistivity or of thermal relaxation times or of the slowing down of fast particles. Following Spitzer [1962] the Coulomb Logarithm is the natural logarithm of the ratio between Debye and Landau length.

$$\ln \Lambda = \ln \frac{\lambda_D}{\lambda_L}$$

The Landau length λ_L is the impact parameter of a collision with 90° deflection

$$\lambda_L = \frac{Z Z_f \, e^2}{4\pi\epsilon_0 \, m \, v^2} \quad .$$

Since the Coulomb Logarithm is derived for a test particle moving in an ensemble of field particles, Z is the charge number of the test particle and Z_f is the charge number of the field particles. The precise Landau length should contain the reduced mass m and the relative velocity v. There are, however, the following simplifications:

- Given a thermal distribution, then $m \, v^2$ is replaced by $3 \, k_B T$. If collisions among ions are regarded then $T = T_i$. If electrons are involved either as test or as field particles then $T = T_e$ (see [Golant et al. 1980]).

- In the numerator of $\ln \Lambda$, λ_D is used as a function of the electron temperature alone. According to Golant et al. [1980] this is valid if an electron is the test particle, because the ions cannot take part in the screening within the collision time. If the test particle is an ion, then λ_S (see section 2.4.1) may be used. Yet this particular distinction is neglected.

The approximations have only a marginal effect on the value of $\ln \Lambda$. They may change the argument of the logarithm by a factor of around 2. Since in a fusion plasma the argument is of the order 10^6, the result of the Coulomb Logarithm is affected by $\pm 5\%$.

When the Landau length drops below the critical value $(4\pi)^{-1} \lambda_{DeBroglie}$, effects from quantum mechanics come into play and the Coulomb Logarithm must be modified:

$$\ln \Lambda = \ln \frac{\lambda_D}{\lambda_L} \frac{e^2}{2\pi\epsilon_0 \hbar v} = \ln \frac{\lambda_D 2 m v}{Z Z_f \hbar} \ .$$

The critical velocity and temperatures (from the root mean square velocity) are:

$$v_{crit} = \frac{Z Z_f e^2}{2\pi\epsilon_0 \hbar} \ , \qquad k_B T_{e,i\ crit} = \frac{m_{e,i} Z^2 Z_f^2 e^4}{12\pi^2 \epsilon_0^2 \hbar^2} \ .$$

Assuming a plasma that consists of electrons and protons, the temperatures correspond to $k_B T_{e\ crit} = 36.28\,\text{eV}$ and $k_B T_{i\ crit} = 66.62\,\text{keV}$, respectively.

In present-day fusion machines the operating temperature is below $T_{i\ crit}$, therefore no quantum mechanical modification is applied to ion-ion collisions.

To conclude, using $\lambda_D = \sqrt{\epsilon_0 k_B T_e / e^2 n_0}$ and $v_{e,i} = \sqrt{3 k_B T_{e,i} / m_{e,i}}$ the Coulomb logarithm is calculated from:

- with electrons involved

$$\ln \Lambda_{e-x} = \ln \frac{12\pi}{Z_x} \left(\frac{k_B T_e}{\sqrt[3]{n_0}\ e^2 \epsilon_0^{-1}} \right)^{\frac{3}{2}} \ , \qquad \text{if} \quad T_e \leq T_{e\ crit} \ ,$$

$$\ln \Lambda_{e-x}^{>} = \ln \frac{2\sqrt{3}}{Z_x} \frac{k_B T_e}{\sqrt{n_0\ \hbar^2 m_e^{-1}\ e^2 \epsilon_0^{-1}}} \ , \qquad \text{if} \quad T_e > T_{e\ crit}$$

- and with collisions among ions

$$\ln \Lambda_{i1-i2} = \ln \frac{12\pi}{Z_{i1} Z_{i2}} \frac{(k_B T_e)^{\frac{1}{2}} k_B T_i}{(\sqrt[3]{n_0}\ e^2 \epsilon_0^{-1})^{\frac{3}{2}}} \ .$$

It is convenient to utilise the properties of the logarithm:

$$\ln \Lambda_{e-x} = \ln(12\,\pi) - \ln(Z_x) + \tfrac{3}{2}\ln(\tfrac{\epsilon_0\,[\mathrm{Vm}]}{e}) + \tfrac{3}{2}\ln(\tfrac{k_B}{e\,[\mathrm{V}]}\,T_e) - \tfrac{1}{2}\ln(n_0\,[\mathrm{m}^3])$$
$$\approx 30.37 \;-\; \ln(Z_x) \;+\; \tfrac{3}{2}\ln(\tfrac{k_B}{e\,[\mathrm{V}]}\,T_e) \;-\; \tfrac{1}{2}\ln(n_0\,[\mathrm{m}^3])$$

$$\ln \Lambda^{>}_{e-x} = \ln(2\sqrt{3}) - \ln(Z_x) + \tfrac{1}{2}\ln(\tfrac{\epsilon_0\,m_e\,[\mathrm{V}^2\mathrm{m}^3]}{\hbar^2}) + \ln(\tfrac{k_B}{e\,[\mathrm{V}]}\,T_e) - \tfrac{1}{2}\ln(n_0\,[\mathrm{m}^3])$$
$$\approx 32.17 \;-\; \ln(Z_x) \;+\; \ln(\tfrac{k_B}{e\,[\mathrm{V}]}\,T_e) \;-\; \tfrac{1}{2}\ln(n_0\,[\mathrm{m}^3])$$

$$\ln \Lambda_{i1-i2} \approx 30.37 \;-\; \ln(Z_{i1}\,Z_{i2}) \;+\; \ln(\tfrac{k_B}{e\,[\mathrm{V}]}\,T_i) \;-\; \tfrac{1}{2}\ln(n_0\,[\mathrm{m}^3]) \;+\; \tfrac{1}{2}\ln(\tfrac{k_B}{e\,[\mathrm{V}]}\,T_e)$$

A.1.2 Collision Times

The "collision time" can only be defined in combination with a particular process and, therefore, several terms are utilised. Following Spitzer [1962] the "deflection time", the "energy exchange time" and the "equipartition time" will be introduced.

A.1.2.1 Deflection Time

The deflection time $t_{90°}$ characterises the velocity spread of so-called test particles within an ensemble of field particles. For example, if electrons move in a bulk of heavy and comparatively motionless ions, then $t_{90°,\,e-i}$ is the time until on average the actual velocity vector of an electron is perpendicular to its initial direction. If the initial relative velocity between test (x) and field particles is denoted by v, and indicating quantities that belong to the field particles by the subscript f, the expression is

$$t_{90°,\,x-f} = \frac{2\,\pi\,\epsilon_0^2\,m^2\,v^3}{k_{corr.}(s)\,(Z\,Z_f\,e^2)^2\,n_f\,\ln \Lambda_{x-f}} \quad .$$

The correction factor $k_{corr.}$ depends on s, which is the ratio between v and the thermal velocity of the field particles:

$$s = \frac{v}{v_{th,\,f}} \;, \qquad v_{th,\,f} = \sqrt{\frac{2\,k_B T_f}{m_f}} \;,$$

$$k_{corr.} = \frac{\exp(-s^2)}{s\,\sqrt{\pi}} + \left(1 - \frac{1}{2\,s^2}\right) \frac{2}{\sqrt{\pi}} \int_0^s \exp(-u^2)\,du \;.$$

For the particular example with electrons in a motionless field of ions, s approaches infinity and $k_{corr.}$ becomes unity.

An important case is the isothermal ensemble of both test and field particles: v can be replaced by $\sqrt{3\,k_B T\,/\,m}$ and s^2 is equal to $3\,m_f/2\,m$. From that follows the characteristic dependence of the collision time on the temperature

$$t_{90°,\,x-f} = \frac{6\,\pi\,\sqrt{3}\,\epsilon_0^2\,\sqrt{m}\,\left(\tfrac{k_B T}{e}\right)^{3/2}}{k_{corr.}\,e^{\,5/2}\,(Z\,Z_f)^2\,n_f\,\ln \Lambda_{x-f}} \quad .$$

Furthermore, if test and field particles are the same species, then $m = m_f$, the velocity ratio s is equal $\sqrt{3/2}$ and $k_{corr.}$ is approximately 0.714. The corresponding deflection time $t_{90°,\,x-x}$ is also called "self-collision time" $t_{c,\,x}$.

A.1.2.2 Energy Exchange Time

Similar to deflection an energy exchange time t_E can be defined, which provides the duration until the initial kinetic energy has been exchanged with the field. This is different from deflection, since acceleration or deceleration parallel to the initial velocity transfers energy, too. Only two special cases are presented, more details are provided by Spitzer [1962].

- $v \ll v_{th,\,f}$ (e.g. ions in an electron bulk): Here applies in good approximation $t_E = 0.5\,t_{90°}$. The error is below 1%, whenever $v < 0.2\,v_{th,\,f}$. At the same time, series expansion can be used to calculate $k_{corr.}(s) \approx 4\,s\,/\,3\,\sqrt{\pi}$.

$$t_{E,\,x-f} = \frac{3\,\pi\,\sqrt{\pi}\,\epsilon_0^2\,m^2\,v_{th,\,f}\,v^2}{4\,(Z\,Z_f\,e^2)^2\,n_f\,\ln\Lambda_{x-f}}$$

  If both test and field particles are thermalised then

$$t_{E,\,x-f} = \frac{9\,\pi\,\sqrt{\pi}\,\epsilon_0^2}{2\,\sqrt{2}\,(Z\,Z_f\,e^2)^2\,n_f} \cdot \frac{m}{\sqrt{m_f}} \cdot \frac{k_B T\,\sqrt{k_B T_f}}{\ln\Lambda_{x-f}}\quad.$$

- $m = m_f$ and $v \approx v_{th,\,f}$: This case supplies within one particle species the relaxation time of a slightly perturbed Maxwellian distribution. It is evaluated by multiplying $t_{90°,\,x-x}$ with roughly 0.880. Hence, self-collision time $t_{c,\,x}$ and relaxation time $t_{E,\,x-x}$ are nearly identical.

A.1.2.3 Equipartition time

If there are two groups of particles with different temperatures, they will approach the equilibrium temperature on the timescale of the equipartition time. For the test particles the change rate is

$$\frac{d}{dt}\,T = \frac{T_f - T}{t_{eq}}\quad,\quad\text{with}$$

$$t_{eq} = \frac{3\sqrt{2}\,\pi\,\sqrt{\pi}\,\epsilon_0^2\,m\,m_f}{(Z\,Z_f\,e^2)^2\,n_f\,\ln\Lambda_{x-f}} \cdot \left(\frac{k_B T}{m} + \frac{k_B T_f}{m_f}\right)^{3/2}\quad.$$

This depends on the density of the field particles alone. Conservation of energy requires

$$n\,\frac{d}{dt}T = -n_f\,\frac{d}{dt}T_f\quad,$$

which can easily be verified.

Summing up, the order of various collision times in a plasma with equal ion and electron charge densities and with similar temperatures of the two species is roughly

$$t_{90°,\,e-i} \,:\, t_{c,\,e} \,:\, t_{c,\,i} \,:\, t_{E,\,i-e} \,:\, t_{eq} \,=\, 1 \,:\, 1 \,:\, \sqrt{\frac{m_i}{m_e}} \,:\, \frac{m_i}{m_e} \,:\, \frac{m_i}{m_e} \;.$$

More background can also be found in [Trubnikov 1965].

A.1.3 Resistivity

The plasma resistivity η is calculated as a modification of the so-called Lorentz gas. In a Lorentz gas, ions are at rest and electrons do not interact with each other. The solution η_L is in SI units:

$$\eta_L = \frac{\sqrt{m_e\,e}\; Z\; \ln \Lambda_{e-i}}{64\,\sqrt{2\,\pi}\,\epsilon_0^2} \left(\frac{k_B T}{e}\right)^{-3/2} .$$

When applied to a plasma, there is a modification depending on the ion charge Z: $\eta = \eta_L \,/\, \gamma_Z$ [Spitzer 1962], where γ_Z is provided in table A.1. Conveniently, these numerical formulas can be utilised:

$$\eta_L \quad = \quad 38.0\,\Omega\mathrm{m}\; \frac{Z\; \ln \Lambda_{e-i}}{(T_e \cdot \mathrm{K}^{-1})^{3/2}}$$

$$\eta\,(Z=1) \;=\; 65.2\,\Omega\mathrm{m}\; \frac{\ln \Lambda_{e-i}}{(T_e \cdot \mathrm{K}^{-1})^{3/2}} \;=\; 5.22 \cdot 10^{-5}\,\Omega\mathrm{m}\; \frac{\ln \Lambda_{e-i}}{(T_e \cdot (\mathrm{eV})^{-1})^{3/2}} \quad .$$

Z	1	2	4	16	∞
γ_Z	0.582	0.683	0.785	0.923	1

Table A.1: *Ratio between the resistivity of an ideal Lorentz gas and the one of a plasma.*

A.2 Mathematical Formulas

A.2.1 Integrating the Distribution Function

A useful identity when evaluating the integrals of a Maxwellian distribution function is this relation between the definite integral and the Gamma function.

$$\int_0^\infty x^n \, exp(-x^2/a^2)\, dx = \tfrac{1}{2}\, a^{n+1}\, \Gamma(\tfrac{n+1}{2})$$

$$\Gamma(\tfrac{1}{2}) = \sqrt{\pi} \;, \quad \Gamma(1) = 1 \;, \quad \Gamma(x+1) = x \cdot \Gamma(x)$$

A.2.2 Discrete Fourier Transform in Two Dimensions

If the algorithm of the Discrete Fourier Transform (DFT) is used together with real signals, some attention must be paid to the correct implementation. The link between the complex DFT and a representation in terms of the trigonometric functions is shown in this section and it is exemplarily solved for two-dimensional data.

It is assumed that there is a set of time space data $X(t, y)$ as a result of the superposition of waves with different wavenumbers k and frequencies f. Individual wave amplitudes are denoted $A_{\hat{f}\hat{k}}$ and their phases $p_{\hat{f}\hat{k}}$. For equidistant f and k the superposition reads

$$
\begin{aligned}
X(t, y) = A_{00} &+ \sum_{\hat{f}=1}^{n_f} A_{\hat{f}0} \cos(2\pi\,\Delta f\,\hat{f}\,t + p_{\hat{f}0}) + \sum_{\hat{k}=1}^{n_k} A_{0\hat{k}} \cos(\Delta k\,\hat{k}\,y + p_{0\hat{k}}) \\
&+ \sum_{\hat{k}=1}^{n_k}\sum_{\hat{f}=1}^{n_f} A_{\hat{f}\hat{k}}^{(+)} \cos(\Delta k\,\hat{k}\,y - 2\pi\,\Delta f\,\hat{f}\,t + p_{\hat{f}\hat{k}}^{(+)}) \\
&+ \sum_{\hat{k}=1}^{n_k}\sum_{\hat{f}=1}^{n_f} A_{\hat{f}\hat{k}}^{(-)} \cos(\Delta k\,\hat{k}\,y + 2\pi\,\Delta f\,\hat{f}\,t + p_{\hat{f}\hat{k}}^{(-)}) \ ,
\end{aligned}
$$

where the actual frequency and wavenumber values are

$$
f = \Delta f \cdot \hat{f}\,, \quad \hat{f} = 1 \ldots n_f \quad \text{and} \quad k = \Delta k \cdot \hat{k}\,, \quad \hat{k} = 1 \ldots n_k\,.
$$

The signal is split into five terms, which are: the average value (A_{00}), spatially uniform fluctuations ($A_{\hat{f}0}, p_{\hat{f}0}$), stationary patterns ($A_{0\hat{k}}, p_{0\hat{k}}$), waves propagating in the positive spatial direction ($A_{\hat{f}\hat{k}}^{(+)}, p_{\hat{f}\hat{k}}^{(+)}$) and waves in the opposite direction ($A_{\hat{f}\hat{k}}^{(-)}, p_{\hat{f}\hat{k}}^{(-)}$). Observing the formula of trigonometric addition the phase $p_{\hat{f}\hat{k}}$ can be separated and $X(t, y)$ is accordingly composed of cosine and sine series.

$$
\begin{aligned}
X(t, y) = A_{00} &+ \sum_{\hat{f}=1}^{n_f} A_{\hat{f}0} \Big(\cos p_{\hat{f}0}\,\cos(2\pi ft) - \sin p_{\hat{f}0}\,\sin(2\pi ft) \Big) \\
&+ \sum_{\hat{k}=1}^{n_k} A_{0\hat{k}} \Big(\cos p_{0\hat{k}}\,\cos(ky) - \sin p_{0\hat{k}}\,\sin(ky) \Big) \\
&+ \sum_{\hat{k}=1}^{n_k}\sum_{\hat{f}=1}^{n_f} A_{\hat{f}\hat{k}}^{(+)} \Big(\cos p_{\hat{f}\hat{k}}^{(+)}\,\cos(ky - 2\pi ft) - \sin p_{\hat{f}\hat{k}}^{(+)}\,\sin(ky - 2\pi ft) \Big) \\
&+ \sum_{\hat{k}=1}^{n_k}\sum_{\hat{f}=1}^{n_f} A_{\hat{f}\hat{k}}^{(-)} \Big(\cos p_{\hat{f}\hat{k}}^{(-)}\,\cos(ky + 2\pi ft) - \sin p_{\hat{f}\hat{k}}^{(-)}\,\sin(ky + 2\pi ft) \Big) \quad \text{(A.1)}
\end{aligned}
$$

It will be shown that each addend belongs to a particular area in the complex representation which is suitable for DFT.

A.2.2.1 Discrete Fourier Transform algorithm

The Discrete Fourier Transform maps the regularly gridded time space domain data $X_{\hat{t}\hat{y}}$ and the complex kf domain data $C_{\hat{f}\hat{k}}$ onto each other. The transform is

$$C_{\hat{f}\hat{k}} = \frac{1}{MN} \sum_{\hat{y}=0}^{N-1} \sum_{\hat{t}=0}^{M-1} X_{\hat{t}\hat{y}} \, \bar{F}_{\hat{f}\hat{t}, \hat{k}\hat{y}} \qquad \text{(in forward direction)}$$

$$X_{\hat{t}\hat{y}} = \sum_{\hat{k}=0}^{N-1} \sum_{\hat{f}=0}^{M-1} C_{\hat{f}\hat{k}} \, F_{\hat{f}\hat{t}, \hat{k}\hat{y}} \qquad \text{(backward)} \qquad \text{(A.2)}$$

$$F_{\hat{f}\hat{t}, \hat{k}\hat{y}} = e^{i\varphi} = e^{i\, 2\pi \left(\frac{\hat{f}\hat{t}}{M} + \frac{\hat{k}\hat{y}}{N} \right)} \, ,$$

where F and $\bar{F}$ are phase factors and $\bar{F}$ is the complex conjugate of F. Time and space are defined by

$$t = \Delta t \cdot \hat{t} \, , \quad \hat{t} = 0 \ldots M - 1 \quad \text{and} \quad y = \Delta y \cdot \hat{y} \, , \quad \hat{y} = 0 \ldots N - 1 \, .$$

By a convention frequently used in commercial DFT modules (e.g. [RSI 1997]), the normalisation is applied during the forward transform. There are the following identities within the set of phase factors:

$$\begin{aligned} F_{(M-\hat{f})\hat{t}, \, (N-\hat{k})\hat{y}} &= \bar{F}_{\hat{f}\hat{t}, \, \hat{k}\hat{y}} \\ F_{\hat{f}\hat{t}, \, (N-\hat{k})\hat{y}} &= \bar{F}_{(M-\hat{f})\hat{t}, \, \hat{k}\hat{y}} \, . \end{aligned} \qquad \text{(A.3)}$$

The phase factors are constant whenever $\hat{k}$ is offset by N or $\hat{f}$ is offset by M. Applied to a real signal $X_{\hat{t}\hat{y}}$, the DFT yields coefficients $C_{\hat{f}\hat{k}}$ with similar properties

$$\begin{aligned} C_{(M-\hat{f})(N-\hat{k})} &= \bar{C}_{\hat{f}\hat{k}} \\ C_{\hat{f}(N-\hat{k})} &= \bar{C}_{(M-\hat{f})\hat{k}} \, . \end{aligned} \qquad \text{(A.4)}$$

If $(M - \hat{f})$ and $(N - \hat{k})$ are associated with $-\hat{f}$ and $-\hat{k}$, respectively, the interrelations (A.3) and (A.4) characterise a Hermitian form (see Bracewell [1986]).

The dimensions are chosen such that $M = 2n_f + 1$ and $N = 2n_k + 1$. In this way the sampling theorem will be fulfilled and the DFT can be split into different quadrants. Observing (A.3) and (A.4) the first and the third quadrant can be subsumed and in the same manner the second and the fourth.

$$\begin{aligned} X_{\hat{t}\hat{y}} = \; C_{00} &+ \sum_{\hat{f}=1}^{n_f} \left(C_{\hat{f}0} F_{\hat{f}0} + \bar{C}_{\hat{f}0} \bar{F}_{\hat{f}0} \right) + \sum_{\hat{k}=1}^{n_k} \left(C_{0\hat{k}} F_{0\hat{k}} + \bar{C}_{0\hat{k}} \bar{F}_{0\hat{k}} \right) \\ &+ \sum_{\hat{k}=1}^{n_k} \sum_{\hat{f}=1}^{n_f} \left(C_{\hat{f}\hat{k}} F_{\hat{f}\hat{k}} + \bar{C}_{\hat{f}\hat{k}} \bar{F}_{\hat{f}\hat{k}} \right) \\ &+ \sum_{\hat{k}=1}^{n_k} \sum_{\hat{f}=1}^{n_f} \left(C_{(M-\hat{f})\hat{k}} F_{(M-\hat{f})\hat{k}} + \bar{C}_{(M-\hat{f})\hat{k}} \bar{F}_{(M-\hat{f})\hat{k}} \right) \qquad \text{(A.5)} \end{aligned}$$

Since

$$CF + \bar{C}\bar{F} = (C + \bar{C})\cos\varphi + i(C - \bar{C})\sin\varphi$$

the formulation (A.5) is equivalent to (A.1), provided that there are the following relations between the complex DFT coefficients and the real amplitude and phase parameters:

$$A_{00} = C_{00} \qquad\qquad \hat{f} = 1\ldots n_f \qquad\qquad \hat{k} = 1\ldots n_k$$

$$C_{\hat{f}0} = \tfrac{1}{2} A_{\hat{f}0}\left(\cos p_{\hat{f}0} + i\sin p_{\hat{f}0}\right) \qquad\qquad C_{0\hat{k}} = \tfrac{1}{2} A_{0\hat{k}}\left(\cos p_{0\hat{k}} + i\sin p_{0\hat{k}}\right)$$

$$C_{\hat{f}\hat{k}} = \tfrac{1}{2} A^{(-)}_{\hat{f}\hat{k}}\left(\cos p^{(-)}_{\hat{f}\hat{k}} + i\sin p^{(-)}_{\hat{f}\hat{k}}\right) \qquad C_{(M-\hat{f})\hat{k}} = \tfrac{1}{2} A^{(+)}_{\hat{f}\hat{k}}\left(\cos p^{(+)}_{\hat{f}\hat{k}} + i\sin p^{(+)}_{\hat{f}\hat{k}}\right) \ .$$

One must not forget to set up the remaining elements of C, namely the quadrants $(M - \hat{f})(N - \hat{k})$ and $(\hat{f})(N - \hat{k})$ according to the relations (A.4). Hence the spectral power of the real signal is split into opposite quadrants of the complex domain.

Comparing the arguments of the trigonometric functions in (A.1) and the definition of the phase factors F, it is evident that the k and f grids are linked to the t and y grids:

$$2\pi\left(\frac{\hat{f}\hat{t}}{M} + \frac{\hat{k}\hat{y}}{N}\right) = \Delta k\,\hat{k}\,\Delta y\,\hat{y} + 2\pi\,\Delta f\,\hat{f}\,\Delta t\,\hat{t} \qquad \text{(for the } A^{(-)} \text{ waves)}$$

$$2\pi\left(\frac{(M - \hat{f})\hat{t}}{M} + \frac{\hat{k}\hat{y}}{N}\right) = \Delta k\,\hat{k}\,\Delta y\,\hat{y} - 2\pi\,\Delta f\,\hat{f}\,\Delta t\,\hat{t} + 2\pi\hat{t} \qquad (A^{(+)} \text{ waves}) \ .$$

The term $2\pi\hat{t}$ is irrelevant, because of the trigonometric periodicity. In any case the resolutions are connected via

$$\Delta y \cdot \Delta k = \frac{2\pi}{N} \ , \quad \Delta t \cdot \Delta f = \frac{1}{M} \ .$$

A.3 Model Functions

A.3.1 Fit Function for the Autocorrelation

In the analysis of turbulent fluctuations two-dimensional correlation functions of various plasma quantities are calculated. Although the term "autocorrelation" is normally assigned to the temporal evolution only, in this context it is used for the spatio-temporal correlation function within one quantity, in order to distinguish it from the cross-correlation, where two different quantities are involved. It has been observed that the main properties of the spatio-temporal autocorrelation function can be modelled by this formula:

$$X_{m,\,auto}(\Delta t, \Delta y, \boldsymbol{p}) = p_0 + \frac{p_1 \cdot \cos(p_2(\Delta y - p_4 \Delta t))}{\cosh(p_5 \Delta t) \cdot \cosh(p_6(\Delta y - p_7 \Delta t))}$$

$$+ \frac{p_{11} \cdot \cos(p_{12}(\Delta y - p_{14}\Delta t))}{\exp(p_{15}\Delta t^2) \cdot \cosh(p_{16}(\Delta y - p_{17}\Delta t))} \ ,$$

where Δt and Δy are time and space lag. The symbol $\boldsymbol{p}$ denotes a parameter vector. Note that not all successive indices of $\boldsymbol{p}$ are used. The reason is a practical one: Since the model function for cross-correlations is of a similar form, but contains more parameters, the additional parameters are simply set zero and left out in the autocorrelation model. The function is derived from the ones that were introduced by Endler [1994] and Bleuel et al. [2002].

A.3.2 Fit Function for the Cross-correlation

In order to calculate the cross-correlation, the product of two different quantities is evaluated. Since the shape of the experimentally observed cross-correlation function bears resemblance to the autocorrelation, a similar form has been used to model it. The two quantities, however, will not necessarily fluctuate in phase, so that additional parameters must be introduced that model a phase shift in the spatio-temporal plane.

$$X_{m,\,cross}(\Delta t, \Delta y, \boldsymbol{p}) = p_0 + \frac{p_1 \cdot \cos(p_2(\Delta y + p_3 - p_4\Delta t))}{\cosh(p_5\Delta t) \cdot \cosh(p_6(\Delta y - p_7\Delta t))}$$
$$+ \frac{p_{11} \cdot \cos(p_{12}(\Delta y + p_{13} - p_{14}\Delta t))}{\exp(p_{15}\Delta t^2) \cdot \cosh(p_{16}(\Delta y - p_{17}\Delta t))} .$$

The phase shifts p_3 and p_{13} denote a temporal delay if the corresponding parameters for the wave frequency p_4 and p_{14} are positive. A propagation of fluctuations in the negative spatial direction would change the sign of both phase shift and frequency.

A.4 Physical Constants

Some frequently used constants with a relative precision of at least $2 \cdot 10^{-5}$, as recommended by NIST [Mohr and Taylor 2005]:

k_B	Boltzmann's constant	$1.38065 \cdot 10^{-23}\,\mathrm{J\,K^{-1}}$
$\hbar$	Planck constant $\div 2\pi$	$1.05457 \cdot 10^{-34}\,\mathrm{J\,s}$
e	elementary charge	$1.60218 \cdot 10^{-19}\,\mathrm{A\,s}$
m_e	electron mass	$9.1094 \cdot 10^{-31}\,\mathrm{kg}$
m_p	proton mass	$1.67262 \cdot 10^{-27}\,\mathrm{kg}$
m_p/m_e	proton-electron mass ratio	1836.15
c_0	vacuum speed of light	$2.99792 \cdot 10^8\,\mathrm{m\,s^{-1}}$
ϵ_0	electric constant	$8.8542 \cdot 10^{-12}\,\mathrm{A\,s\,V^{-1}\,m^{-1}}$

Appendix B

Annotations to data analysis

B.1   Emmert and Stangeby compared

A very common method to evaluate the perturbation of a probe is provided by Stangeby [1986]. In this model ions enter the Debye sheath with the sound speed

$$c_s = \sqrt{\frac{k_B \left(T_i + Z\, T_e \right)}{m_i}} \quad .$$

Note, that the electron temperature should be weighted with the ion charge Z [Hutchinson 1987]. Stangeby proposed to use 0.5 times the unperturbed electron density as the plasma electron density at the sheath edge. The ion current density on the probe is therefore

$$j_{i,\,sat}^{\text{Stangeby}} = \frac{1}{2}\, e\, n_0\, c_s \quad .$$

If the probe is at floating potential, then $j_{i,\,sat}$ is balanced by the electron current
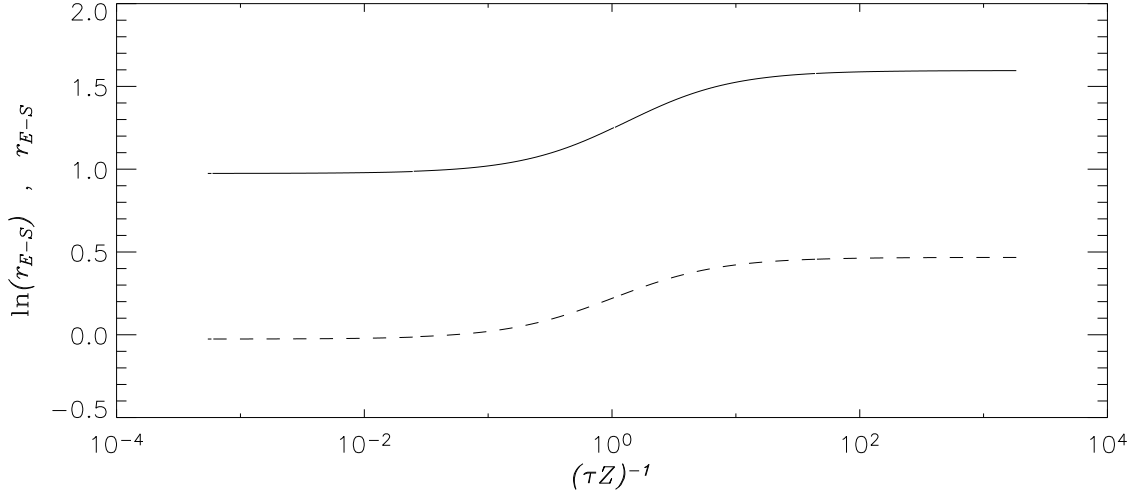
$$j_e = \frac{1}{4}\, n_0\, (1 - \gamma_e)\, \sqrt{\frac{8\, k_B T_e}{\pi\, m_e}}\, \exp\left(\frac{e\, \Phi_W}{k_B T_e} \right) \quad .$$

Altogether the formula reads

$$\Phi_W^{\text{Stangeby}} = -\frac{k_B T_e}{e}\, \ln\left(\frac{(1 - \gamma_e)}{\sqrt{(1 + \frac{1}{\tau Z})}}\, \sqrt{\frac{2\, m_i}{\pi\, Z\, m_e}} \right) \quad . \tag{B.1}$$

Comparing the Stangeby (B.1) and the Emmert model (2.17), it turns out that they differ by a characteristic expression r_{E-S}:

$$r_{E-S} = \quad j_{i,\,sat}^{\text{Emmert}} \, / \, j_{i,\,sat}^{\text{Stangeby}} \quad = \quad \exp\left(-\frac{e}{k_B T_e} \left(\Phi_W^{\text{Stangeby}} - \Phi_W^{\text{Emmert}} \right) \right)$$

$$= \frac{4\sqrt{2}}{\pi}\, \hat{D}\left(\sqrt{\psi(\tau Z)} \right) \sqrt{1 + \frac{1}{\tau Z}} \quad . \tag{B.2}$$

Figure B.1: *Ion flux density (solid line) of the Emmert model divided by the density according to Stangeby, curve label r_{E-S}. The independent variable is the ratio of the ion temperature to Z times T_e ($\tau = T_e / T_i$). Also shown is the difference of normalised floating potentials (dashed line), curve label $\ln(r_{E-S})$.*

 If there is a significant ion temperature, i.e. τZ is finite, then r_{E-S} is greater than one, see figure B.1.

A typical experimental application is to measure $j_{i,\,sat}$ in order to deduce the unperturbed density n_0. Using the Stangeby model this yields a density that is larger than the density according to the Emmert model. When the plasma potential U_{plasma} is calculated from the measured floating potential U_{float} and electron temperature T_e, the situation is similar: The difference $U_{plasma} - U_{float}$ in the Stangeby model is larger than for the Emmert model. The effect, however, is slightly attenuated by the natural logarithm. With $\tau Z = 1$ numerical values are: $\psi = 0.404$, $r_{E-S} = 1.246$, $\ln r_{E-S} = 0.2199$. The normalised potential drop ψ in the Emmert presheath is smaller than in the Stangeby presheath ($\ln 2 \approx 0.693$).

Concluding, the Stangeby model overestimates the density at given $j_{i,\,sat}$ by roughly 25%. Additionally the difference between U_{plasma} and U_{float} is increased by

$$\Delta U = 0.2199\, k_B T_e\, /e \ .$$

If the coefficient for the emission of secondary electrons is $\gamma_e = 0.5$, then ΔU corresponds to a 10% deviation of the plasma potential evaluated from U_{float} and T_e relative to the value from the Emmert model, where

$$U_{plasma} - U_{float} \approx 2.272\, k_B T_e\, /e \ .$$

B.2 Displaying the 2D correlation

If the two dimensions of this sheet of paper are used to display both independent variables Δt and Δy, and the dependent value of the two-dimensional correlation
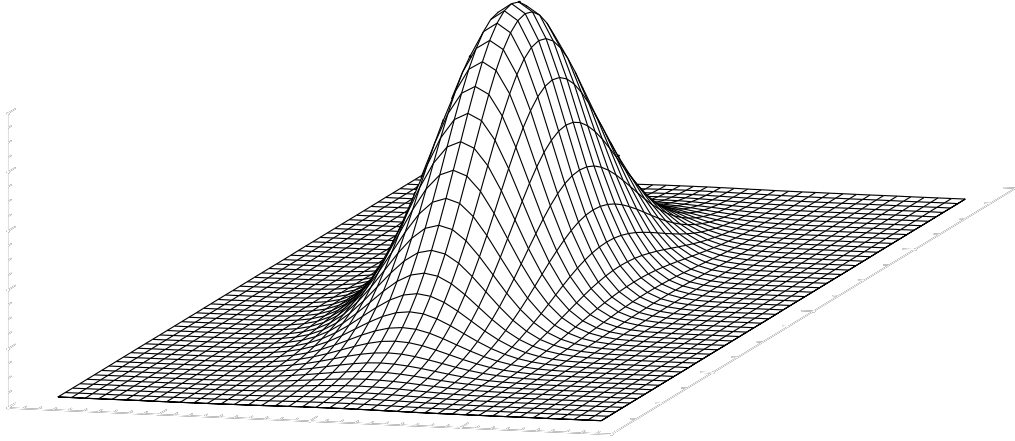
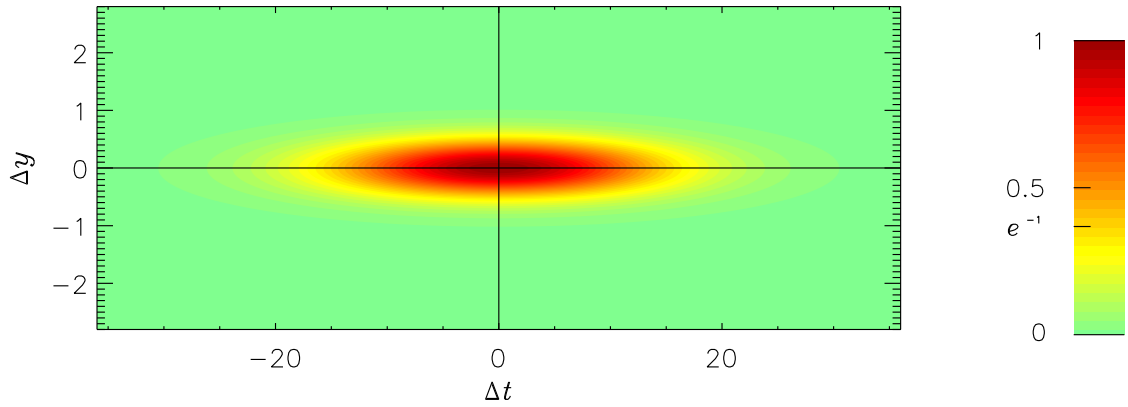**Figure B.2:** *Two-dimensional Gaussian function. The Δt axis is oblique and points to the upper right, and the Δy axis is nearly horizontal from right to left.*

Figure B.3: *Contour plot of the two dimensional Gaussian function.*

function, then a three-dimensional encoding must be utilised. The contour technique is preferred in this case: correlation values will be color coded and plotted against the independent variables on the horizontal and vertical axes. An example should illustrate this: Assume a Gaussian-shaped autocorrelation

$$X_{AA}(\Delta t, \Delta y) = e^{-\left(\frac{\Delta t}{15}\right)^2} \cdot e^{-\left(\frac{\Delta y}{0.5}\right)^2} \ .$$

If the function is plotted as a surface in space, i.e. the spatial coordinate that is perpendicular to the $\Delta t - \Delta y$ plane is assigned to the function value, then it can be projected into the plane of the paper. This will result in figure B.2 for an oblique line of sight. The projection is well suited to get a good idea of the shape but it is of minor use to extract any proportions quantitatively. For comparison, the same function is displayed using filled contours in figure B.3. With the aid of the formula one can deduce that the function value will drop to e^{-1} on an ellipse passing through $\Delta t = \pm 15$ and $\Delta y = \pm 0.5$. That is easily verified utilising the color chart. Note that the color changes from orange to yellow close to this particular function value.

Appendix C

# Electronics for the probe measurements

There are two tasks in the design of the electronics: One is miniaturisation in order to put the amplifiers into the front end of the probe system. The second is to achieve sufficient common mode rejection at the high frequency of the sweep. It was proposed by Pfeiffer [1997] to distribute these two tasks to separate units. When both are finally brought together, they must pass a detailed balancing procedure.

C.1 Differential amplifier design

Individual tip currents are measured as differential voltages across shunt resistors. In this case it is possible to use a common voltage source for all tips (see figure C.1). Since the voltages on both sides of the shunt are by far too high for any integrated differential amplifier circuit, voltage dividers are necessary. The latter must have the required bandwidth, therefore they are compensated by appropriate capacitors (see figure C.1). Altogether these devices are used:

- Shunt resistor $R_{sh} = 20\,\Omega$, maximum ohmic loss of $20\,\mathrm{W}$ allows for a tip current of $1\,\mathrm{A}$.

- High ohmic part of the voltage divider $R_h = 51\,\mathrm{k\Omega}$, SMD installation size 1206, compound of four individual devices (two in parallel, two in series) to increase the power dissipation. Maximum voltage $230\,\mathrm{V}$ (power limited). Given a stray capacitance of $1\,\mathrm{pF}$, the "natural" bandwidth of this device is $\sim 3\,\mathrm{MHz}$ without any compensation.

- Low ohmic part $R_l = 5.1\,\mathrm{k\Omega}$. Choosing this value yields a differential signal at the amplifier input of $1/11$ times the voltage across the shunt, e.g. for a tip current of $100\,\mathrm{mA}$ the amplifier input is $\sim 180\,\mathrm{mV}$. In order to achieve a current precision of $1\,\mathrm{mA}$ (differential shunt voltage $20\,\mathrm{mV}$) at a tip voltage of $\sim 100\,\mathrm{V}$, the relative accuracy of the resistors must be $\mathcal{o}(2\cdot10^{-4})$. Hence,
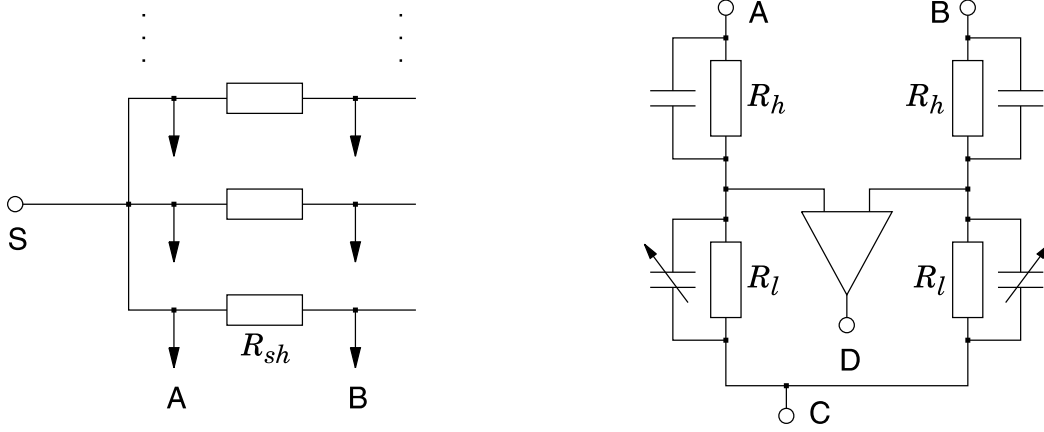
Figure C.1: *Scheme of the multi-tip current measurement. On the left, the split of the common voltage (input S) to individual tips via shunt resistors is shown. On the right, one channel for the current measurement is displayed, that is connected to one shunt (A, B). The differential amplifier (output D) measures the voltage across the resistor bridge. Note that point C is not at ground potential, but connected to an appropriate ratio of the signal −S (phase shift π). This will be discussed in section C.2.*

    both resistors R_h and R_l were selected from a large, pre-aged and precisely measured set. Distribution functions of R_h and R_l were compared and it has been found that the largest amount of resistor pairs could be utilised with a divider ratio of $R_l / R_h = 0.099795$.

- Capacitive compensation: Parallel to R_h a value of $1/3$ pF (three 1 pF capacitors in series) proved to be sufficient, i.e. this clearly dominated over the observed stray capacities. Parallel to R_l trimming capacitors with 3.3 ± 1.5 pF were attached.

- Differential amplifier: Type MAXIM 436 (MAX436), wideband transconductance amplifier, bandwidth-gain product ~ 200 MHz, both inputs are high omic (700 kΩ). Maximum output current 20 mA, i.e. driving a 50 Ω line with gain 1, the tip current range is ± 0.55 A .

There are two additional channels which are not connected to a probe tip: One channel is slightly modified to measure the common mode level directly. This is achieved by omitting the shunt and the divider at point B (figure C.1), and connecting the corresponding amplifier input B to ground. The second of the two additional channels is used to measure the common tip voltage. Only in that case, point C is grounded, both shunt and the B divider are omitted, and the amplifier B input is also grounded. In order to adjust this amplifier's input voltage range, the values of R_l and its capacitive compensation are changed to 220 Ω and 70 pF, respectively. Hence, this amplifier can measure voltage amplitudes up to 230 V.

C.2   Active common mode rejection

If the tip voltage is continuously swept, then both shunt contacts A and B (figure C.1) will undergo the voltage oscillations. In the case of zero tip current the oscillations are identical. This is called a common mode, and by definition it should be rejected in a differential amplifier. Nevertheless, a real differential amplifier is always sensitive to common mode, which is quantified by the device's common mode rejection rate (CMRR): The CMRR is the ratio between differential gain and common mode gain. It is supplied in decibel, is a function of the common mode frequency, and generally it strongly degrades towards high frequencies. The voltage dividers at both differential amplifier inputs (cf. figure C.1) have little effect on the CMRR, provided the precision and the bandwidth of the (passive) components is high enough. With increasing divider ratio it becomes more difficult to maintain the bandwidth, therefore the comparatively small ratio ($\approx 1/10$) was used.

In principle the MAX436's CMRR is large enough ($\sim 70\,\mathrm{dB}$ at $1\,\mathrm{MHz}$), to distinguish the differential voltage of $20\,\mathrm{mV}$ (corresponding to a tip current of $1\,\mathrm{mA}$) from the common mode signal $\sim 60\,\mathrm{V}$ at both points A and B. But the input voltage range of the MAX436 is restricted to $\pm 5\,\mathrm{V}$ ($\pm 50\,\mathrm{V}$ at the points A and B), which imposes a close limit on the applied tip voltage. The situation can be improved, however, if the properly scaled and inverted signal S, namely $-k \cdot \mathrm{S}$, is fed into point C [Pfeiffer 1997]. Ideally k is equal to the divider ratio R_l / R_h, so that both inputs of the differential amplifier are actively kept at $0\,\mathrm{V}$ (current free tip). Any differential voltage across the shunt due to a non-zero tip current is preserved.

How to provide $-k \cdot \mathrm{S}$? A comparatively high amplitude in combination with the bandwidth from DC to $\mathcal{o}(1\,\mathrm{MHz})$ is needed. Readily available monolithic operational amplifiers with a maximum supply voltage $\pm 15\,\mathrm{V}$ can only generate amplitudes up to $13\,\mathrm{V}$ (corresponding to $130\,\mathrm{V}$ at A and B), which is considered to be insufficient. Therefore a hybrid inverting module was designed, consisting of a low frequency (LF) and a high frequency (HF) band (figure C.2). The hybrid inverting module can produce amplitudes $\mathcal{o}(10\,\mathrm{V})$ in each frequency band. Additionally, the phase characteristic of the HF band can be shifted and, thus, optimised for the projected sweep frequency without influencing the bias.

The threshold frequencies in the hybrid inverting module are $2.5\,\mathrm{kHz}$ for the HF band and $70\,\mathrm{kHz}$ for the LF band. Hence, there is an overlap in the intermediate region, which is important in order to avoid large excursions of the phase, since voltage fluctuations with intermediate frequencies generated by the plasma turbulence will couple into the system via the tip voltage line (point S). The output coupling of the two branches is ohmic for the LF and capacitive for the HF component. Due to the ohmic LF coupling and the corresponding voltage loss, the LF output stage must be oversized, and additionally the correct bias can only be produced for a well defined load impedance. The latter is determined by the values R_l of all tip amplifiers in parallel. In the case of the 15 channel front end it amounts to $140\,\Omega$.
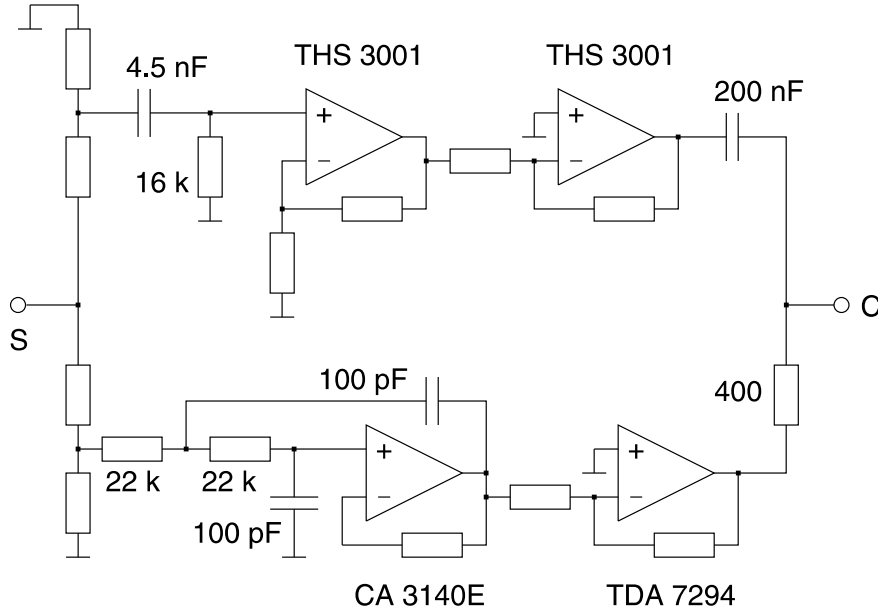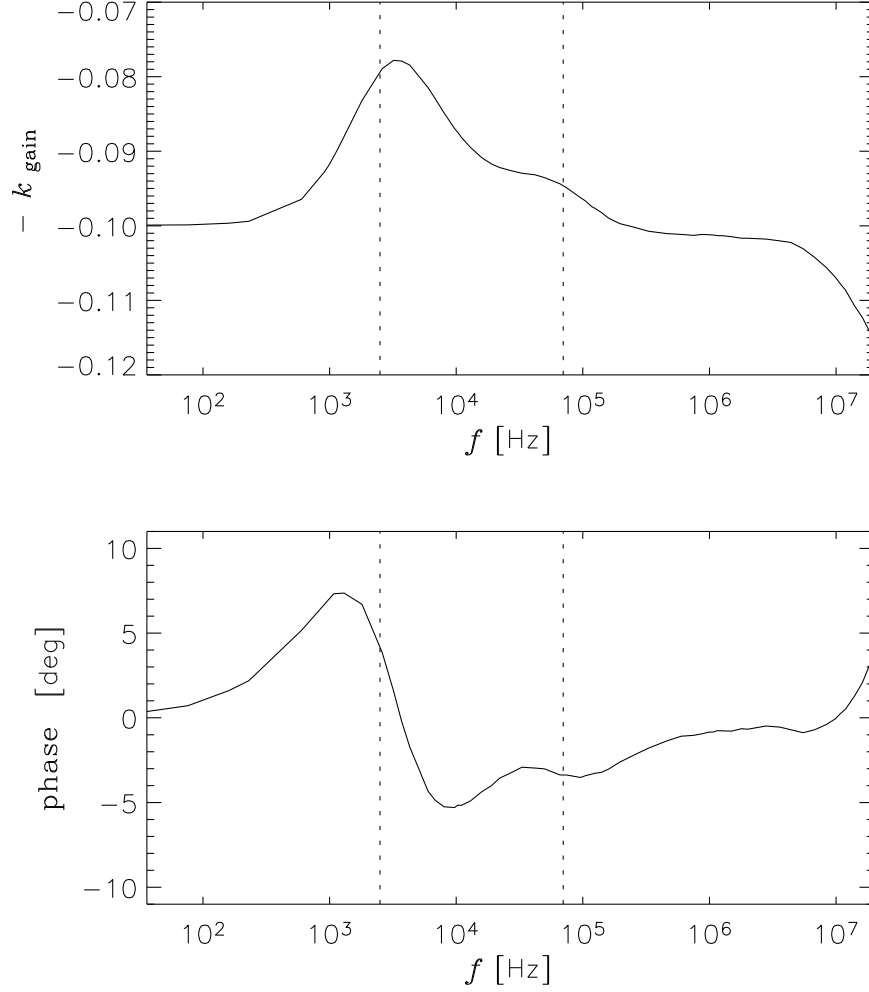
Figure C.2: *Hybrid inverting module, optimised for the generation of both an antiphase sweep signal ($\sim 1\,\text{MHz}$, $\sim 10\,\text{V}$) into output C (load impedance $140\,\Omega$), and an inverted bias ($\sim 8\,\text{V}$). Output C $\approx -1\,/\,10\cdot$S broad-band. High input impedance is achieved, since each branch has got a non-inverting pre-stage. The devices that determine the cross-over frequencies are specified ($f_{\min} = 2.5\,\text{kHz}$ for the HF part on top, $f_{\max} = 70\,\text{kHz}$ for the LF part at the bottom). The high speed IC THS3001 (Texas Instruments) and the LF pre-stage CA3140E (Harris) operate with $\pm 15\,\text{V}$ supplies, whereas the HIFI IC TDA7294 (SGS Thomson) operates at $\pm 35\,\text{V}$. Frequency compensation and the fine tuning of the gain by trimmers are omitted in the drawing.*

Measured amplitude and phase characteristics of the hybrid inverting module are displayed in figure C.3. There are small excursions of the amplitude (20%) and of the phase ($\pm 7°$) in the intermediate frequency region. Note that both amplitude and phase are stable for the two main constituents of the voltage: at DC ($f = 0$) and at $f \sim 1\,\text{MHz}$.

The design of the hybrid inverting module, however, could not be made small enough to allow the placement in the front end. Therefore the module was mounted outside the reciprocation system, tapping the common tip voltage line $\sim 3\,\text{m}$ away from the tip current amplifiers. Whenever there is no correct termination of the transmission line between S and the front end, reflected waves superpose. This effect must be considered during the gain adjustment of the hybrid inverting module under measurement conditions.

The output C of the hybrid inverting module must be transmitted into the front end. In order to improve the impedance matching, a $100\,\Omega$ transmission line is utilised. Since this line impedance is close to the load impedance ($140\,\Omega$), reflections can be neglected.

Figure C.3: *Frequency characteristic of the hybrid inverting module, operating with the nominal load $140\,\Omega$. On top the amplitude ratio and below the phase of the output relative to the input. Overplotted with dotted lines are the theoretical threshold frequencies of the two amplifier branches. At DC and around the projected sweep frequency ($\sim 1\,\text{MHz}$) both amplitude ratio and phase are close to their nominal values ($-0.1\,$, $0°$).*

C.3   Calibration and high frequency properties

In this section an overview on the required balancing procedure is given. The adjustment must be done carefully, since the evaluation of plasma parameters and of the electron temperature in particular depends very sensitive on the frequency characteristics. It can be demonstrated that the signal flow without plasma is well understood and in good agreement with high frequency theory.
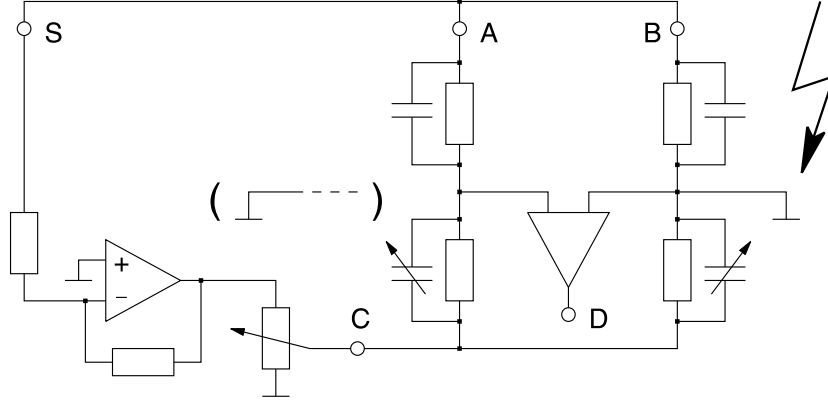
Figure C.4: *Balancing procedure for the voltage dividers. In advance, the output of a simple broad-band inverter (bottom left) must be connected to point C. One of the two differential amplifier inputs is grounded (jagged arrow) and a small amplitude square signal is fed into S. The gain of the simple inverter is adjusted with the trimming resistor, nulling the differential amplifier signal (output D) at low source frequencies $\mathcal{O}(10\,\text{kHz})$. Subsequently the source frequency can be increased up to the projected sweep frequency ($\sim 1\,\text{MHz}$), and the trim capacitor of the voltage divider can be fine tuned. If this procedure is completed for the A divider, the grounding (jagged arrow) is transferred to the opposite side and the B divider can be balanced in the same way.*

C.3.1   Current amplifier balance

The bandwidth of the differential amplifier is much higher than the natural bandwidth of the ohmic voltage dividers when taking into account typical stray capacities. Hence, the main task is to adjust the two voltage dividers per channel correctly. Stray capacities can be modeled and balanced adequately by the capacitors displayed in figure C.1.

Before starting, the shunt resistor R_{sh} must be bypassed and one of the two differential amplifier inputs must be grounded (cf. figure C.4). Small amplitudes are used for the balancing procedure, therefore it is not necessary to employ the hybrid inverting module. Instead, the signal $-k \cdot S$ can be provided with adequate bandwidth ($> 10\,\text{MHz}$) by a simple inverter (operational amplifier, low input impedance). The gain of this operational amplifier must be fine tuned using low frequencies.

Measuring the output at point D, one should encounter a signal similar to one of those displayed in figure C.5. In this case a $2\,\text{MHz}$ square wave has been applied to point S, so that different states of compensation can be clearly distinguished. The ideal response is a straight line, corresponding to a perfect inverting module and a fully compensated divider. The procedure must be repeated with the divider at the other input of the differential amplifier.

Given the two dividers of one channel are balanced, then the achieved CMRR can be controlled. The grounding must be removed, thus putting both differential amplifier inputs into operation, but the shunt resistor R_{sh} is still bypassed. Note
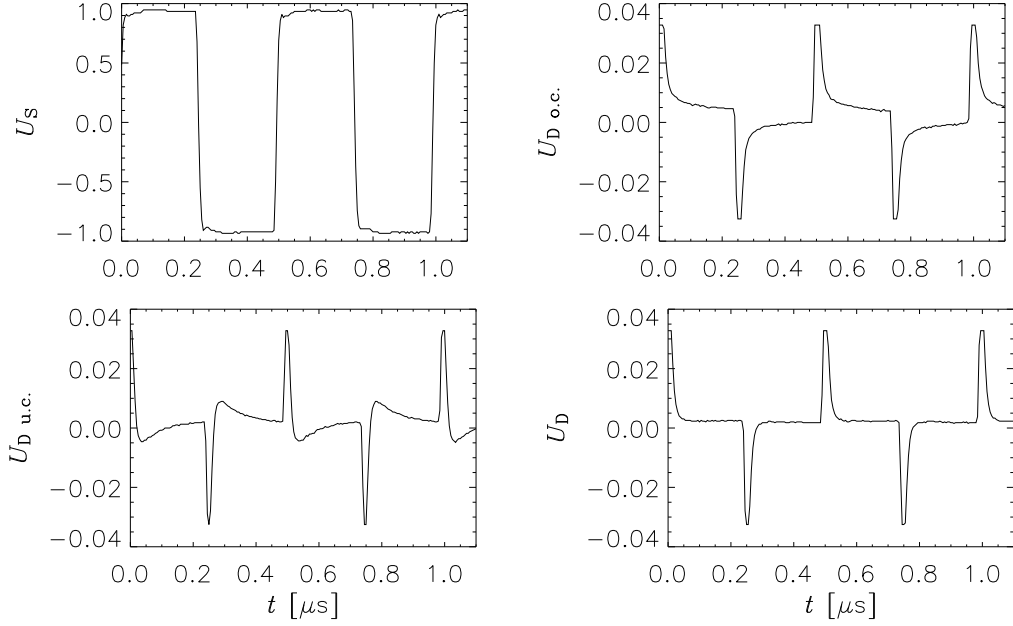
Figure C.5: *Different states of compensation as a function of the trim capacitor adjustment. Top left is the input voltage, top right is the response (output* D*) of an overcompensated divider, i.e. when the trim capacity is too large. In the bottom row on the left the divider is undercompensated and on the right it is balanced. The remaining spikes are due to the finite slew rate of the simple inverter (which is connected to input* C*).*

that now there are two stages of common mode rejection: the simple inverter and the differential amplifier. Exemplary the response to a 4 MHz square is shown in figure C.6. After a settling time of $\sim 0.05\,\mu s$ the output peak to peak amlitude is $\sim 3 \cdot 10^{-4}\,mV$. Observing the divider ratio, the voltage across the shunt R_{sh} that would produce the same output is $\approx 3.3\,mV$. Since the applied peak to peak amplitude is $U_S = 1.8\,V$, the real CMRR is $3.3 \cdot 10^{-3}\,/\,U_S$ or $-55\,dB$ at 4 MHz.
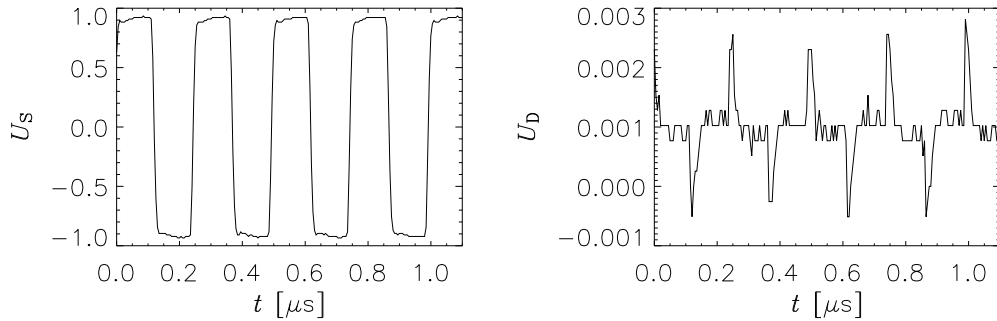
Figure C.6: *Common mode rejection of a differential amplifier with balanced voltage dividers operating in combination with the simple inverter. On the left the applied voltage and on the right the amplifier response.*

161

C.3.2 Balance of the hybrid inverting module

The gain of the hybrid inverting module (figure C.2) must be adjusted under measurement conditions in order to match the ratio of the voltage dividers in the front end. As already pointed out, the length of the voltage line between the front end and the hybrid inverting module is $\sim 3\,\mathrm{m}$ (see also figure 3.6 in section 3.3.1). Without plasma there is an open loop at the probe tips, thus the source wave is reflected and the reflection superposes in the common tip voltage line. The hybrid inverting module receives both the source wave and the reflection and, consequently, a perfect compensation of the common mode in the front end is not possible. The only way to achieve the nominal gain adjustment is to employ high frequency theory for the transmission and reflection of the source wave, and to compare the frequency characteristics of the tip voltage and the common mode, both measured in the front end. During plasma operation there will be a finite load at the tips, which causes the amplitude of the reflected wave to decrease.

At first the correct open loop probe head impedance $Z_L(\omega)$ has to be determined. All voltage dividers, shunts, cables and compensation capacitors in the front end must be taken into account. $Z_L(\omega)$ is complex.

Subsequently the transfer function between the common tip voltage and the common mode measurement in the front end must be set up. This function consists of three parts:

- Transformation from the front end along the common voltage line to the position of the hybrid inverting module. Given the complex Fourier spectra are $U_m(\omega, 0)$ in the front end and $U_m(\omega, -l_W)$ at the inverting module, this reads

$$U_m(\omega, -l_W) = U_m(\omega, 0) \left(\cos(\omega\,\tau_W) \;+\; \frac{i\,Z_W}{Z_L(\omega)}\,\sin(\omega\,\tau_W) \right) \quad [\text{Russer 1993}]\,,$$

  where the length of the transmission line l_W (impedance Z_W) is included in $\tau_W = l_W\,/\,c_W \approx\, l_W\,/\,0.7\,c_0$.

- Frequency characteristic of the hybrid inverting module. That was discussed in section C.2 and displayed in figure C.3.

- Transformation from the hybrid inverting module output to the front end through the $100\,\Omega$ line. Since this line is terminated almost correctly, the voltage at point C of the dividers in the front end is in good approximation

$$U_C(\omega, 0) = U_C(\omega, -l_W)\,\exp(-i\,\omega\,\tau_W)\;.$$

  Note that τ_W is the same as for the common voltage line.

The complete calculation was carried out and compared to the measured frequency characteristic. In the figures C.7 and C.8 the results are displayed. Due to the interplay of the cable length l_W and the head impedance $Z_L(\omega)$ a phase cross-over

162
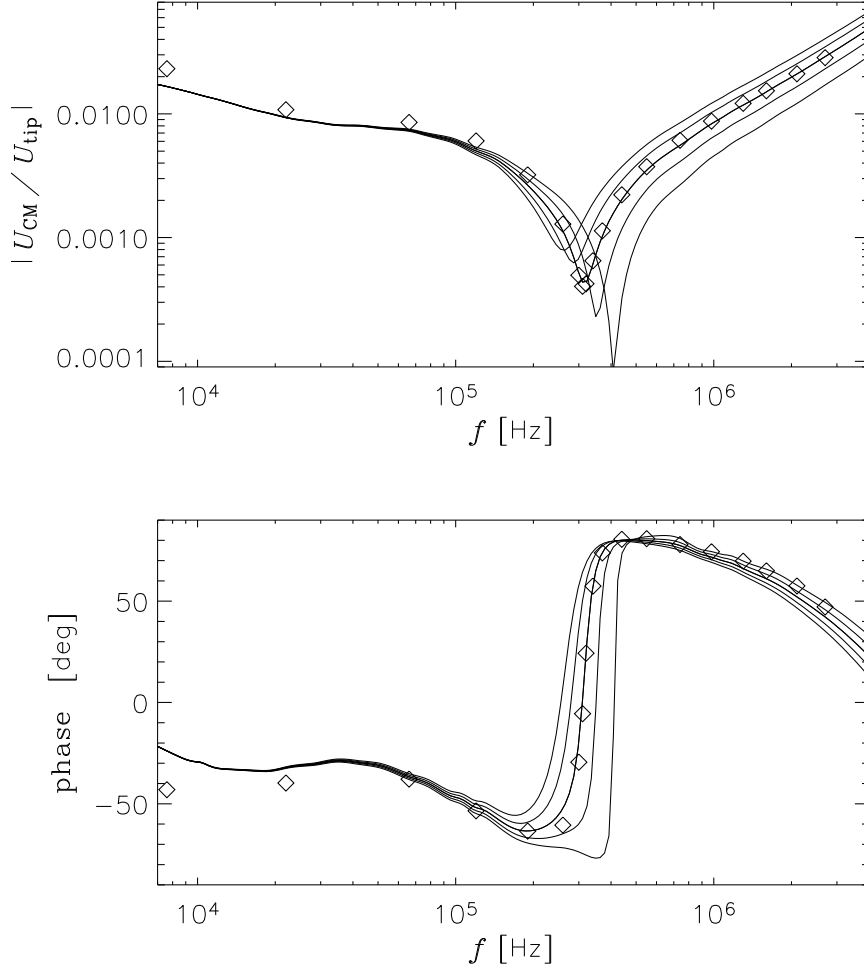
Figure C.7: *Comparison of the theoretical and the measured amplitude and phase characteristic between the common tip voltage and the common mode signal. The curves are obtained without plasma. Several lines are displayed that correspond to different cable lengths between front end and inverting amplifier in the theoretical calculation. Values are $2.2\,\mathrm{m}, 3\,\mathrm{m}, 3.7\,\mathrm{m}, 4.4\,\mathrm{m}$ and $5.1\,\mathrm{m}$, and the cross-over frequency decreases with increasing cable length. The experimental values (diamonds) fit well with a cable length of $3.7\,\mathrm{m}$.*

appears at several $100\,\mathrm{kHz}$. Since $Z_L(\omega)$ is well known, the precise value of l_W can be determined (figure C.7).

At the cross-over frequency the common mode amplitude has got a minimum, but even for the correct gain adjustment it remains finite (figure C.8). The signal most sensitive to the gain is the magnitude of the phase excursion below and above the cross-over frequency. For a correctly aligned module values of $-60°$ and $+70°$ are found theoretically. Since the experimental amplitude and phase characteristics are in good agreement with the theory, the method is considered reliable. The accuracy of the gain can be estimated to $\pm 2 \cdot 10^{-3}$. If the gain mismatch was larger, then the theoretical phase characteristic would not fit the measured phase values.
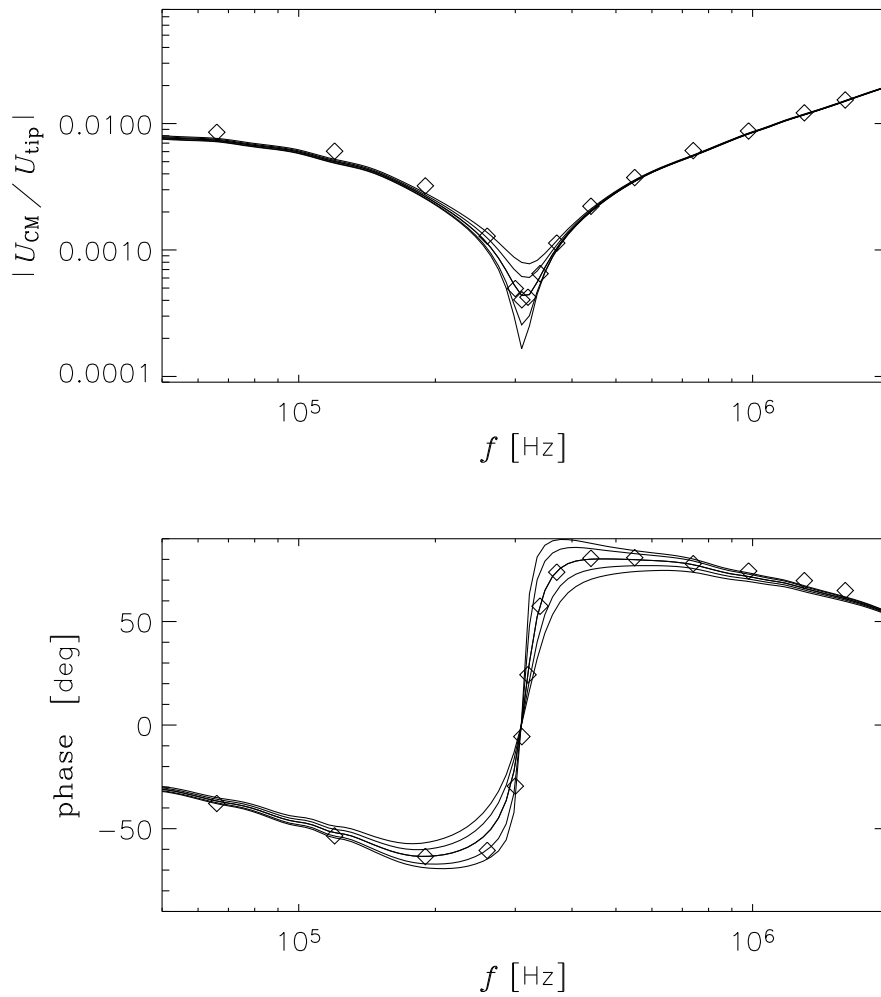
Figure C.8: *Amplitude and phase characteristic similar to figure C.7, this time varying the inverting module gain in the theoretical calculations. The nominal gain is modified by the factors $0.996, 0.998, 1, 1.002, 1.003$, where for higher magnitudes of the gain the amplitude ratios decrease and the phase excursions increase. Plotted with diamonds is the experimental characteristic, which fits the nominal case closely.*

164

Bibliography

R. Balbín, C. Hidalgo, M.A. Pedrosa, I. García-Cortés, and J. Vega. Measurement of density and temperature fluctuations using a fast-swept Langmuir probe. *Review of Scientific Instruments*, 63(10):4605–4607, 1992.

S. Bäumel. *Zweidimensionale Charakterisierung von Elektronentemperaturfluktuationen an W7-AS*. PhD Thesis, Ernst-Moritz-Arndt-Universität Greifswald, 2002.

S. Bäumel, G. Michel, H.J. Hartfuss, M. Rodriguez-Girones Arboli, and H.L. Hartnagel. Two-dimensional correlation measurements of electron cyclotron emission fluctuations on the stellarator Wendelstein 7-AS. *Review of Scientific Instruments*, 74(3):1441–1444, 2003.

R.C. Bissel. The application of the generalized Bohm criterion to Emmert's solution of the warm ion collisionless plasma equation. *Physics of Fluids*, 30(7):2264–2265, 1987.

R.C. Bissel and P.C. Johnson. A review of models for collisionless one-dimensional plasma flow to a boundary. *Phys. Fluids B*, 1(5):1133–1140, 1989.

J. Bleuel. *Elektrostatische Turbulenz am Plasmarand des Stellarators Wendelstein 7-AS*. PhD Thesis, Technische Universität München, 1998. IPP report III/235, Max-Planck-Institut für Plasmaphysik, Garching bei München.

J. Bleuel, M. Endler, H. Niedermeyer, M. Schubert, H. Thomsen, and W7-AS Team. The spatial structure of edge fluctuations in the Wendelstein 7-AS stellarator. *New Journal of Physics*, 4:38.1–38.38, 2002.

J.A. Boedo, D. Gray, R.W. Conn, P. Luong, M. Schaffer, R.S. Ivanov, A.V. Chernilevsky, G. van Oost, and TEXTOR Team. On the harmonic technique to measure electron temperature with high time resolution. *Review of Scientific Instruments*, 70(7):2997–3006, 1999.

D. Bohm. Minimum ionic kinetic energy for a stable sheath. In A. Guthrie and R.K. Wakerling, editors, *The Characteristics of Electrical Discharges in Magnetic Fields*, National Nuclear Energy Series, pages 77–86. McGraw-Hill, New York, Toronto, London, 1949.

A.H. Boozer. Physics of magnetically confined plasmas. *Reviews of Modern Physics*, 76(4):1071–1141, 2004.

R.C. Bracewell. *The Fourier Transform and Its Applications*. McGraw-Hill, New York, 2nd edition, 1986.

S.I. Braginskii. Transport processes in a plasma. In M.A. Leontovich, editor, *Reviews of Plasma Physics*, volume 1, pages 205–311. Consultants Bureau, New York, 1965.

R. Brakel. Confinement in W7-AS and the role of radial electric field and magnetic shear. *Plasma Physics and Controlled Fusion*, 39:B273–B286, 1997.

E.O. Brigham. *The Fast Fourier Transform and its Applications*. Prentice-Hall, New Jersey, 1988.

M. Bruchhausen. *Aufbau und Erprobung eines repetierenden Laser-Blow-Off-Systems zur Untersuchung elektrostatischer Elektronendichtefluktuationen in der Rand- und Abschälschicht von TEXTOR und Wendelstein 7-AS*. PhD Thesis, Heinrich-Heine-Universität Düsseldorf, 2002. report Jül-3993, Institut für Plasmaphysik, Forschungszentrum Jülich GmbH, D-52425 Jülich.

B.A. Carreras, R. Balbín, B. van Milligen, M.A. Pedrosa, I. García-Cortés, E. Sanchez, C. Hidalgo, J. Bleuel, M. Endler, H. Thomsen, A. Chankin, S. Davies, K. Erents, and G.F. Matthews. Characterization of the frequency ranges of the plasma edge fluctuation spectra. *Physics of Plasmas*, 6(12):4615–4621, 1999.

F.F. Chen. Electric probes. In R.H. Huddlestone and S.L. Leonard, editors, *Plasma Diagnostic Techniques*, volume 21 of *Pure and Applied Physics*, chapter 4, pages 113–200. Academic Press, New York, London, 1965.

F.F. Chen. *Introduction to Plasma Physics*. Plenum Press, New York and London, 1974.

P.M. Chung, L. Talbot, and K.J. Touryan. *Electric Probes in Stationary and Flowing Plasmas: Theory and Application*, volume 2 of *Applied Physics and Engineering*. Springer Verlag, Berlin, Heidelberg, New York, 1975.

D.A. D'Ippolito and J.R. Myra. Blob stability and transport in the scrape-off-layer. *Physics of Plasmas*, 10(10):4029–4039, 2003.

D.A. D'Ippolito, J.R. Myra, and S.I. Krasheninnikov. Cross-field blob transport in tokamak scrape-off-layer plasmas. *Physics of Plasmas*, 9:222–233, 2002.

D.F. Düchs. 3/2 or 5/2 for convective thermal transport? Technical Report 13, JET Joint Undertaking Report JET-R, July 1989.

G.A. Emmert, R.M. Wieland, A.T. Mense, and J.N. Davidson. Electric sheath and presheath in a collisionless, finite ion temperature plasma. *Physics of Fluids*, 23 (4):803–812, 1980.

M. Endler. The poloidal variation of the radial transport due to electrostatic fluctuations in toroidal magnetic confinement experiments. *Plasma Physics and Controlled Fusion*, 41:1431–1440, 1999.

M. Endler. *Experimentelle Untersuchung und Modellierung elektrostatischer Fluktuationen in den Abschälschichten des Tokamaks ASDEX und des Stellarators Wendelstein 7-AS*. PhD Thesis, Technische Universität München, 1994. IPP report III/197, Max-Planck-Institut für Plasmaphysik, Garching bei München.

M. Endler, H. Niedermeyer, L. Giannone, E. Holzhauer, A. Rudyj, G. Theimer, N. Tsois, and ASDEX Team. Measurements and modelling of electrostatic fluctuations in the scrape-off layer of ASDEX. *Nuclear Fusion*, 35(11):1307–1339, 1995.

User Manual FI30xx. FAST ComTec GmbH, Oberhaching Germany, 2001.

M. Fink. Untersuchung der Fluktuationen des Plasmapotentials mit emissiven und nichtemissiven elektrostatischen Sonden. Master's thesis, Ernst-Moritz-Arndt-Universität Greifswald, November 2002. IPP report 15/3, Januar 2003, Max-Planck-Institut für Plasmaphysik, Teilinstitut Greifswald.

U. Frisch. *Turbulence: The Legacy of A.N.Kolmogorov*. University Press, Cambridge, 1995.

W. Fundamenski, S. Sipilä, G.F Matthews, V. Riccardo, P. Andrew, T. Eich, L.C. Ingesson, T. Kiviniemi, T. Kurki-Suonio, and V. Philipps. Interpretation of recent power width measurements in JET MkIIGB ELMy H-modes. *Plasma Physics and Controlled Fusion*, 44:761–793, 2002.

A.A. Galeev and R.Z. Sagdeev. Theory of neoclassical diffusion. In M.A. Leontovich, editor, *Reviews of Plasma Physics*, volume 7, pages 257–343. Consultants Bureau, New York and London, 1979.

X. Garbet, L. Laurent, J.-P. Roubin, and A. Samain. A model for the turbulence in the scrape-off layer of tokamaks. *Nuclear Fusion*, 31(5):967–972, 1991.

A. Geier. Transientes Verhalten von Langmuirsonden in einem magnetischen Plasma. Master's thesis, Technische Universität München, August 1997. IPP report III/224, Max-Planck-Institut für Plasmaphysik, Garching bei München.

J.E. Geiger, A. Weller, M.C. Zarnstorff, C. Nührenberg, A. Werner, Y.I. Kolesnichenko, W7-AS Team, and NBI Group. Equilibrium and stability of high-beta

plasmas in Wendelstein 7-AS. *Fusion Science and Technology*, 46(1):13–23, 2004. Special Issue 14th International Stellarator Workshop.

L. Giannone, R. Balbín, R., H. Niedermeyer, M. Endler, G. Herre, C. Hidalgo, A. Rudij, G. Theimer, and Ph. Verplanke. Density, temperature, and potential fluctuation measurements by the swept langmuir probe technique in Wendelstein 7-AS. *Physics of Plasmas*, 1:3614–3621, 1994.

V.E. Golant, A.P. Zhilinsky, and I.E. Sakharov. *Fundamentals of Plasma Physics*. John Wiley & Sons, New York, 1980.

C. Gourdon and W. Lotz. *Optimiertes Programm für Numerische Rechnungen in Toroidalen Magnetfeld-Konfigurationen.* Max-Planck-Institut für Plasmaphysik, Garching bei München, 1970. revised 1983.

P. Grigull, F. Sardei, Y. Feng, G. Herre, D. Hildebrandt, G. Kocsis, G. Kühner, and W7-AS Team. Edge transport studies on the W7-AS stellarator. In *Tenth International Conference on Stellarators*, Madrid, 1995. CIEMAT.

P. Grigull, K. McCormick, J. Baldzuhn, R. Burhenn, R. Brakel, H. Ehmler, Y. Feng, F. Gadelmeier, L. Giannone, D. Hartmann, D. Hildebrandt, M. Hirsch, R. Jänicke, J. Kisslinger, J. Knauer, R. König, G. Kühner, H. Laqua, D. Naujoks, H. Niedermeyer, N. Ramasubramanian, N. Rust, F. Sardei, F. Wagner, A. Weller, U. Wenzel, and W7-AS Team. First island divertor experiments on the W7-AS stellarator. *Plasma Physics and Controlled Fusion*, 43:A175–A193, 2001.

E. Grimsehl, W. Schallreuter, and R. Gradewald. *Elektrizitätslehre*, volume 2. Teubner, Leipzig, 1988.

G.A. Hallock, A.J. Wootton, and R.L. Hickok. Space-potential and density fluctuations in the ISX-B tokamak. *Physical Review Letters*, 59(12):1301–1304, 1987.

E.R. Harrison and W.B. Thompson. The low pressure plane symmetric discharge. *Proceedings of the Physical Society London*, 74(2):145–152, 1959.

M. Häse, M. Hirsch, and H.J. Hartfuss. Temperature fluctuations and their correlation with density fluctuations in W7-AS. *Review of Scientific Instruments*, 70(1): 1014–1017, 1999.

A. Hasegawa and K. Mima. Pseudo-three-dimensional turbulence in magnetized nonuniform plasma. *Physics of Fluids*, 21(1):87–92, 1978.

A. Hasegawa and M. Wakatani. Plasma edge turbulence. *Physical Review Letters*, 50(9):682–686, 1983.

C. Hidalgo, R. Balbin, M.A. Pedrosa, I. Garcia-Cortes, and M.A. Ochando. Experimental evidence of significant temperature fluctuations in the plasma edge region of the TJ-I tokamak. *Physical Review Letters*, 69(8):1205–1208, 1992.

E. Holzhauer, ASDEX Team, and W7-AS Team. Turbulence in the separatrix region associated with the L-H transition in the ASDEX tokamak and the W7-AS stellarator. *Plasma Physics and Controlled Fusion*, 38:1267–1271, 1996.

K. Höthker, H.A. Claassen, H. Gerhauser, and W. Bieger. On the measurement of electric fields in magnetised plasmas by means of probes. *Czechoslovak Journal of Physics*, 49:167–180, 1999. Suppl. S3.

I.H. Hutchinson. A fluid theory of ion collection by probes in strong magnetic fields with plasma flow. *Physics of Fluids*, 30(12):3777–3781, 1987.

ITER Physics Basis Editors and ITER Physics Expert Groups Chairs and Co-Chairs. Overview and summary. *Nuclear Fusion*, 39(12):2137, 1999.

F. Jenko. *Numerische Modellierung von stoßfreier Driftwellenturbulenz.* PhD Thesis, Technische Universität München, 1998. IPP report 5/82, Max-Planck-Institut für Plasmaphysik, Garching bei München.

A. Kendl. *Driftwellen in Helias-Konfigurationen.* PhD Thesis, Technische Universität München, 2000. IPP report 5/95, Max-Planck-Institut für Plasmaphysik, Garching bei München.

A. Kendl and B.D. Scott. Magnetic shear damping of dissipative drift wave turbulence. *Physical Review Letters*, 90(3):035006, 2003.

A. Kendl, B.D. Scott, R. Ball, and R.L. Dewar. Turbulent edge structure formation in complex configurations. *Physics of Plasmas*, 10(9):3684–3691, 2003.

S.I. Krasheninnikov and B. Smolyakov. On neutral wind and blob motion in linear devices. *Physics of Plasmas*, 10(7):3020–3021, 2003.

B. LaBombard. An interpretation of fluctuation induced transport derived from electrostatic probe measurements. *Physics of Plasmas*, 9(4):1300–1311, 2002.

J.G. Laframboise and J. Rubinstein. Theory of a cylindrical probe in a collisionless magnetoplasma. *Physics of Fluids*, 19(12):1900–1908, 1976.

C. Lechte, S. Niedner, and U. Stroth. Comparison of turbulence measurements and simulations of the low-temperature plasma in the torsatron TJ-K. *New Journal of Physics*, 4:34, 2002.

S.J. Levinson, J.M. Beall, E.J. Powers, and R.D. Bengtson. Space time statistics of the turbulence in a tokamak edge plasma. *Nuclear Fusion*, 24(5):527–539, 1984.

P.C. Liewer. Measurements of microturbulence in tokamaks and comparisons with theories of turbulence and anomalous transport. *Nuclear Fusion*, 25(5):543–621, 1985.

P.C. Liewer, J.M. McChesney, S.J. Zweben, and R.W. Gould. Temperature fluctuations and heat transport in the edge regions of a tokamak. *Physics of Fluids*, 29 (1):309–317, 1986.

B. Lipschultz, I. Hutchinson, B. LaBombard, and A. Wan. Electric probes in plasmas. *Journal of Vacuum Science & Technology A*, 4:1810–1816, 1986.

H. Maaßberg, R. Brakel, R. Burhenn, U. Gasparino, P. Grigull, M. Kick, G. Kühner, H. Ringler, F. Sardei, U. Stroth, and A. Weller. Transport in stellarators. *Plasma Physics and Controlled Fusion*, 35:B319–B332, 1993.

K. McCormick and ASDEX Team. Measurement of the scrape-off layer density profile on ASDEX via an energetic neutral lithium beam. *Review of Scientific Instruments*, 56(5):1063–1065, 1985.

M.A. Meier, R.D. Bengtson, G.A. Hallock, and A.J. Wootton. Adiabatic electron thermal pressure fluctuations in tokamak plasmas. *Physical Review Letters*, 87 (8):085003, 2001.

P.J. Mohr and B.N. Taylor. CODATA recommended values of the fundamental physical constants: 2002*. *Reviews of Modern Physics*, 77(1):1–107, 2005. http://physics.nist.gov/constants.

R. Müller and W. Heywang. *Rauschen*, volume 15 of *Halbleiter-Elektronik*. Springer Verlag, Berlin, Heidelberg, New York, 2nd edition, 1990.

LabVIEW. National Instruments, Austin, Texas USA, 2000.

A.V. Nedospasov. Turbulence near wall in tokamaks. *Soviet Journal of Plasma Physics*, 15(10):659–661, 1989.

A.V. Nedospasov and D.A. Uzdensky. On dynamical effects on I-V characteristic of Langmuir probes in tokamak edge plasma. *Contributions to Plasma Physics*, 34: 478–483, 1994.

H. Niedermeyer, M. Endler, L. Giannone, A. Rudyj, G. Theimer, ASDEX Team, and W7-AS Team. Langmuir probe measurements in fluctuating plasmas. *Contributions to Plasma Physics*, 36:131–138, 1996. Special Issue.

J. Nührenberg and R. Zille. Stable stellarators with medium β and aspect ratio. *Physics Letters A*, 114(3):129–132, 1986.

NAG Fortran Library Mark 19. The Numerical Algorithms Group Ltd, Oxford UK, 1999.

J.M. Pedgley, G.M. McCracken, H. Farhang, and B.H. Blott. Measurements of secondary electron emission for fusion related materials. *Journal of Nuclear Materials*, 196-198:1053–1058, 1992.

U. Pfeiffer. Messung von Elektronentemperatur, Potential und Dichte in einem Plasma mit hoher Zeitauflösung mittels Langmuirsonde. Master's thesis, Technische Universität München, September 1997. IPP report III/226, Max-Planck-Institut für Plasmaphysik, Garching bei München.

U. Pfeiffer, M. Endler, J. Bleuel, H. Niedermeyer, G. Theimer, and W7-AS Team. Density, temperature and potential fluctuation measurements with multiple fast swept langmuir probes on W7-AS. *Contributions to Plasma Physics*, 38:134–144, 1998. Special Issue.

J. Raeder, I. Cook, and F.H. Morgenstern. Safety and environmental assessment of fusion power (SEAFP). Commission of the European Communities, Brussels(BE). Directorate General XII - Fusion Programme, 1995. report EUR-FU-BRU XII-217/95.

D. Reiter. *The EIRENE Code, version: Jan. 92 - Users Manual*. Forschungszentrum Jülich GmbH, Institut für Plasmaphysik, D-52425 Jülich, 1992. report Jül-2599.

K.-U. Riemann. The Bohm criterion and sheath formation. *J.Phys.D: Appl.Phys.*, 24:493–518, 1991.

K.-U. Riemann. The Bohm criterion and boundary conditions for a multicomponent system. *IEEE Transactions on Plasma Science*, 23(4):709–716, 1995.

Ch.P. Ritz, R.D. Bengtson, S.J. Levinson, and E.J. Powers. Turbulent structure in the edge plasma of the text tokamak. *Physics of Fluids*, 27(12):2956–2959, 1984.

D.C. Robinson and M.G. Rusbridge. Turbulent density fluctuations in Zeta. *Plasma Physics*, 11:73–100, 1969.

D.W. Ross. On standard forms for transport equations and quasilinear fluxes. *Plasma Physics and Controlled Fusion*, 34:137–146, 1992.

D.W. Ross. On standard forms for transport equations and fluxes. *Comments on Plasma Physics and Controlled Fusion*, 12:155–163, 1989.

IDL Reference Guide. RSI Research Systems, Inc., Boulder, Colorado, March 1997. IDL Version 5.0.

P. Russer. *Hochfrequenztechnik*, volume 1. Lehrstuhl für Hochfrequenztechnik der Technischen Universität München, München, 6th edition, 1993.

G.B. Rybicki. Dawson's integral and the sampling theorem. *Computers in Physics*, 3(2):85–87, 1989.

F. Sardei and M. Richter-Glötzl. *Transformation package TRANS for W7-AS*. Max-Planck-Institut für Plasmaphysik, Garching bei München, 1988. revised 1995.

S. Sattler and H.J. Hartfuss. Intensity interferometry for measurement of electron temperature fluctuations in fusion plasmas. *Plasma Physics and Controlled Fusion*, 35:1285–1306, 1993.

S. Sattler, H.J. Hartfuss, and W7-AS Team. Experimental evidence for electron temperature fluctuations in the core plasma of the W7-AS stellarator. *Physical Review Letters*, 72(5):653–656, 1994.

C. Schröder. *Experimental investigations on drift waves in linear magnetized plasmas.* PhD Thesis, Ernst-Moritz-Arndt-Universität Greifswald, 2003. IPP report 15/5, Max-Planck-Institut für Plasmaphysik, Garching bei München.

U. Schumacher. *Fusionsforschung.* Wissenschaftliche Buchgesellschaft Darmstadt, Darmstadt, 1993.

B. Scott. Three-dimensional computation of drift Alfvén turbulence. *Plasma Physics and Controlled Fusion*, 39:1635–1668, 1997.

B. Scott. *Low Frequency Fluid Drift Turbulence in Magnetised Plasmas.* Habilitation thesis, Heinrich-Heine-Universität Düsseldorf, 2000. IPP report 5/92, March 2001, Max-Planck-Institut für Plasmaphysik, Garching bei München.

Operator's Manual, PDA12-MEM500. Signatec Inc., Corona, California USA, 1997.

P.L. Similon and P.H. Diamond. Nonlinear interaction of toroidicity-induced drift modes. *Physics of Fluids*, 27(4):916–924, 1984.

L. Spitzer. *Physics of Fully Ionized Gases.* Wiley Interscience, New York and London, 2nd edition, 1962.

L. Spitzer. The stellarator concept. *Physics of Fluids*, 1(4):253–264, 1958.

P.C. Stangeby. The plasma sheath. In D.E. Post and R. Behrisch, editors, *Physics of Plasma-Wall Interactions in Controlled Fusion*, number 131 in NATO ASI, pages 41–97. Plenum Press, New York and London, 1986.

U. Stroth. Transport in toroidal plasmas. In A. Dinklage, T. Klinger, G. Marx, and L. Schweikhard, editors, *Plasma Physics - Confinement, Transport and Collective Effects*, volume 670 of *Lecture Notes in Physics*, chapter 9, pages 213–267. Springer, Berlin and Heidelberg, 2005.

U. Stroth, J. Baldzuhn, B. Brañas, V. Erckmann, T. Estrada, L. Giannone, M. Hirsch, H.J. Hartfuss, M. Kick, G. Kühner, ECRH Group, and W7-AS Team. Transport experiments in W7-AS. In *Tenth International Conference on Stellarators*, Madrid, 1995. CIEMAT.

J. Svensson, A. Dinklage, J. Geiger, A. Werner, and R. Fischer. Integrating diagnostic data analysis for W7-AS using Bayesian graphical models. *Review of Scientific Instruments*, 75(10):4219–4221, 2004.

P.W. Terry and P.H. Diamond. Theory of dissipative density-gradient-driven turbulence in the tokamak edge. *Physics of Fluids*, 28(5):1419–1439, 1985.

P.W. Terry and P.H. Diamond. Theory of dissipative density gradient driven turbulence in the tokamak edge. Technical Report 114, Institute for Fusion Studies, University of Texas, April 1984.

G. Theimer. *Charakterisierung transportrelevanter turbulenter elektrostatischer Fluktuationen in der Abschälschicht des Tokamaks ASDEX mittels Darstellung als Superposition von raum-zeitlich lokalisierten Ereignissen.* PhD Thesis, Technische Universität München, 1997. IPP report III/223, Max-Planck-Institut für Plasmaphysik, Garching bei München.

G. Theimer. Methoden zur Untersuchung der räumlichen Struktur von Dichtefluktuationen in der Randschicht von Fusionsexperimenten demonstriert am Divertortokamak ASDEX. Master's thesis, Technische Universität München, December 1990. IPP report III/169, Max-Planck-Institut für Plasmaphysik, Garching bei München.

U. Tietze and Ch. Schenk. *Halbleiter-Schaltungstechnik.* Springer Verlag, Berlin, Heidelberg, New York, 5th edition, 1980.

B.A. Trubnikov. Particle interactions in a fully ionized plasma. In M.A. Leontovich, editor, *Reviews of Plasma Physics*, volume 1, pages 105–204. Consultants Bureau, New York, 1965.

P. Verplancke. *Langmuir probes at high frequencies in a magnetized plasma: a theoretical and experimental study.* PhD Thesis, University of Ghent, 1996. IPP report 4/275, January 1997, Max-Planck-Institut für Plasmaphysik, Garching bei München.

F. Wagner. Topics in toroidal confinement. *Plasma Physics and Controlled Fusion*, 39:A23–A50, 1997.

F. Wagner and H. Wobig. Magnetic confinement. In A. Dinklage, T. Klinger, G. Marx, and L. Schweikhard, editors, *Plasma Physics - Confinement, Transport and Collective Effects*, volume 670 of *Lecture Notes in Physics*, chapter 7, pages 137–172. Springer, Berlin and Heidelberg, 2005.

F. Wagner, S. Bäumel, J. Baldzuhn, N. Basse, R. Brakel, R. Burhenn, A. Dinklage, D. Dorst, H. Ehmler, M. Endler, V. Erckmann, Y. Feng, F. Gadelmeier, J. Geiger, L. Giannone, P. Grigull, H.J. Hartfuss, D. Hartmann, D. Hildebrandt, M. Hirsch,

E. Holzhauer, Y. Igitkhanov, R. Jänicke, M. Kick, A. Kislyakov, J. Kisslinger, T. Klinger, and al. W7-AS: One step of the Wendelstein stellarator line. *Physics of Plasmas*, 12(7):072509, 2005.

M. Wakatani and A. Hasegawa. A collisional drift wave description of plasma edge turbulence. *Physics of Fluids*, 27(3):611–618, 1984.

M. Weinlich. *Elektrostatische Sonden in starken Magnetfeldern*. PhD Thesis, Technische Universität München, 1995. IPP report 5/64, Max-Planck-Institut für Plasmaphysik, Garching bei München.

E.W. Weisstein. *Cross-Correlation Theorem*. MathWorld - A Wolfram Web Resource, http://mathworld.wolfram.com/Cross-CorrelationTheorem.html, 2005a.

E.W. Weisstein. *Ellipse*. MathWorld - A Wolfram Web Resource, http://mathworld.wolfram.com/Ellipse.html, 2005b.

E.W. Weisstein. *Wiener-Khinchin Theorem*. MathWorld - A Wolfram Web Resource, http://mathworld.wolfram.com/Wiener-KhinchinTheorem.html, 2005c.

J. Wesson. *Tokamaks*. Clarendon Press, Oxford, 2nd edition, 1997.

H. Wobig. Magnetohydrodynamik. Technische Universität München, 1997. lecture notes.

A. Zeiler, J.F. Drake, and D. Biskamp. Electron temperature fluctuations in drift-resistive ballooning turbulence. *Physics of Plasmas*, 4(4):991–1001, 1997.

A. Zeiler, D. Biskamp, J.F. Drake, and B.N. Rogers. Transition from resistive ballooning to η_i driven turbulence in tokamaks. *Physics of Plasmas*, 5(7):2654–2663, 1998.

S. Zoletnik, S. Fiedler, G. Kocsis, K. McCormick, J. Schweinzer, and H.P. Winter. Determination of electron density fluctuation correlation functions via beam emission spectroscopy. *Plasma Physics and Controlled Fusion*, 40:1399–1416, 1998.

S.J. Zweben and R.W. Gould. Structure of edge-plasma turbulence in the Caltech tokamak. *Nuclear Fusion*, 25(2):171–183, 1985.

Acknowledgements, Danksagung

First of all, I would like to thank **Prof.F.Wagner** for the possibility to realise this project and also for the permanent encouragement to bring it to a successful end.

Many thanks to **Prof.T.Klinger** who always kept an eye on this work. His comments and in particular the final correction of the manuscript were very helpful.

My supervisor **Dr.M.Endler** is the only one, who went with me through all the details of this thesis. I am deeply grateful, thank you very much!

Dr.R.Brakel and **Dr.R.Jaenicke** very patiently set up the W7-AS discharges that were necessary to realise the probe measurements. Thank you.

Beim Aufbau des Messsystems musste ich an die Grenzen des handwerklich und technisch Machbaren gehen. Ohne die Zuarbeit zahlreicher Kollegen wäre der erfolgreiche Abschluss nicht möglich gewesen. Ich danke ganz besonders **S.Siche** für die Präzision, Zuverlässigkeit und Ausdauer bei Aufbau und Wartung der Sondentechnik. In der Elektronikwerkstatt in Garching hatten **H.Huber**, **A.Jenning** und **F.Beibl** viel Geduld mit mir und meinen Sonderwünschen. Frau **J.Ahmels**, **H.Holitzner**, **K.H.Knauer** und **H.Scholz** kümmerten sich um Vakuum, Schaltpläne und elektrische Verdrahtung. **P.Schötz** und **G.Zangl** standen wohlwollend als Ansprechpartner zur Verfügung, sogar nach dem offiziellen Feierabend.

Die schrecklichen Launen unterschiedlicher Computersysteme mussten unter Kontrolle gebracht werden. **Dr.W.Nagel**, **Dr.H.Reuter**, **Dr.N.Ruhs** und **A.Schott** waren dabei eine große Hilfe.

I thank all people of the former **W7-AS team**, also the colleagues of the scientific, technical and administrative staff in Greifswald.

Thank you **Francesco** for the never-ending refreshment by e-mail and for the invitations to Oxford and Napoli. During the exhausting time of writing up, this brought new life to me.

Gerne war ich mit den netten Menschen im **Garchinger Sinfonieorchester** zusammen. Das gemeinsame Musizieren, die Probenarbeit und die gemeinsame Freizeit sind mir immer eine schöne Erinnerung.

In Greifswald spielte für mich die Freundschaft mit **Thomas**, **Andrea**, **Henning**, **Aniela**, **Jens**, **Jakob** und **Kyu-Dong** eine entscheidende Rolle, um mich wohl zu fühlen.

Zu guter Letzt danke ich ganz besonders meinen Eltern. Für die bedingungslose Unterstützung im Allgemeinen und ganz speziell für den äusserst hilfreichen Taxi-Dienst zum Berliner Flughafen Tegel im Sommer 2004 ...